Tropospheric ozone from IASI : regional and global assessment

Sarah Safieddine

▶ To cite this version:

HAL Id: tel-01158420

https://theses.hal.science/tel-01158420v2

Submitted on 1 Jun 2015

Université Pierre et Marie Curie

Ecole doctorale de Sciences de l'Environnement (ED129)

Laboratoire Atmosphères, Milieux, Observations Spatiales (LATMOS)

TROPOSPHERIC OZONE FROM IASI : REGIONAL AND GLOBAL ASSESSMENT

Sarah Safieddine

Thèse de doctorat en Sciences de l'Environnement

Dirigée par Cathy Clerbaux

Presentée et soutenue publiquement le 10 février 2015

Devant un jury composé de :

M. François Ravetta	Président
M. Brice Barret	Rapporteur
M. David Edwards	Rapporteur
M. Pierre-François Coheur	Examinateur
Mme. Jennie Thomas	Examinatrice
Mme. Carole Deniel	Examinatrice-Invitée

II

Acknowledgement

Résumé

L'ozone troposphérique (O_3) est un gaz à effet de serre et un polluant atmosphérique majeur. Il est la source principale du radical hydroxyle OH, l'oxydant le plus important dans l'atmosphère, fortement réactif avec les composés organiques et inorganiques. Les concentrations globales d'ozone troposphérique ont augmenté considérablement depuis l'époque pré-industrielle en raison de l'accumulation des émissions anthropiques de précurseurs d'ozone. Mon travail de thèse consiste à étudier la variabilité spatiale et temporelle de l'ozone troposphérique aux échelles globale et régionale telle qu'elle est mesurée par le sondeur IASI (Infrared Atmospheric Sounding Interferometer). Deux instruments IASI ont été lancés à bord des satellites MetOp-A et MetOp-B en 2006 et 2012.

La première partie de mon travail consiste en l'étude des mesures O_3/IASI : sa sensibilité dans la troposphère, sa variabilité saisonnière et ses modes de transport. Le deuxième volet de mon travail de thèse repose sur des études ciblées. Celles-ci comprennent une première étude sur l'ozone, urbain et rural, et sa relation complexe avec le dioxide d'azote (NO_2) mesuré depuis l'espace par GOME-2 (Global Ozone Monitoring Experiment) au-dessus de différentes villes de l'hémisphère nord. Une deuxième étude s'attache à expliquer la source des pics d'ozone observés en région méditerranéenne en été, en utilisant IASI et le modèle de chimie-transport WRF-Chem (Weather Research and Forecasting model coupled with Chemistry). Enfin, en utilisant ces deux jeux de données, je présente en troisième étude l'analyse de la mousson d'été en Asie de l'Est ainsi que son effet sur l'ozone troposphérique.

v

Abstract

Tropospheric ozone (O_3) is an important greenhouse gas and air pollutant. It is the primary source of the most important oxidant in the atmosphere, the hydroxyl radical OH, that is highly reactive with organic and inorganic compounds. Global tropospheric O_3 concentrations have been rising considerably since pre-industrial times as a result of the increase in the anthropogenic emissions of O_3 precursors. In this thesis, I will study the temporal and spatial variability of tropospheric O_3 on a global and regional scale as measured by IASI (Infrared Atmospheric Sounding Interferometer). The IASI instruments have been launched on-board the MetOp-A and MetOp-B satellites in 2006 and 2012.

I first discuss the IASI/O_3 measurements, their sensitivity in the troposphere and their seasonal variation and the transport processes of O_3 in the troposphere. I then perform more detailed and focused studies. Those include studying the urban and rural O_3 and its relationship with nitrogen dioxyde (NO_2) measured from GOME-2 (Global Ozone Monitoring Experiment) over different cities in the Northern Hemisphere; investigating the summertime tropospheric O_3 maxima over the Mediterranean region using IASI and the WRF-Chem (Weather Research and Forecasting model coupled with Chemistry) data; and finally, using both satellite and model data, I present my analysis of the East Asian monsoon variability and its effect on the tropospheric O_3 column.

VIII

Contents

CONTENTS

Chapter 1

Introduction

Ozone (O_3) was discovered by C.F. Schönbein in the middle of the nineteenth century [Schoenbein, 1840]. In his laboratory, he suggested the presence of a gas with a peculiar smell (in Greek, "to smell" is *ozein*). In Earth's atmosphere, (Fig. 1.1), O_3 is found in the stratosphere and troposphere. Panel (a) of Fig. 1.1 shows an average profile of temperature of the bottom 100 km of Earth's atmosphere. The troposphere is the region between the surface and the tropopause (the upper layer of the troposphere), in which the temperature decreases in average with increasing altitude. The lowermost part of the troposphere is the boundary layer which is typically between 500 and 3000 m above sea surface, and is therefore the region the most affected by human activity and in which air pollution and O_3 buildup is of most concern. In the troposphere, O_3 is a well-known pollutant and a greenhouse gas, the third most effective (besides water vapor), after carbon dioxide (CO_2) and methane (CH_4). It also plays a significant role in the chemistry as its photolysis leads to the production of the hydroxyl radical OH, the most important tropospheric oxidizing agent. Even with the European Union (EU) regulations for decrease in anthropogenic O_3 precursors emissions, O_3 concentrations and trends in Europe are still not clearly decreasing [EEA, 2012]. The stratosphere is where most of the atmospheric O_3 resides. Stratospheric O_3 abundance is essential to life on Earth as it absorbs UV radiation that can cause cancer for humans and damage plants and crops.

This chapter will focus on the troposphere and stratosphere and in particular on the O_3 behavior in each. I will present an overview on our current understanding and measurement

techniques of O_3 in each of these two layers, with a focus on the tropospheric O_3, the main subject of this thesis work.
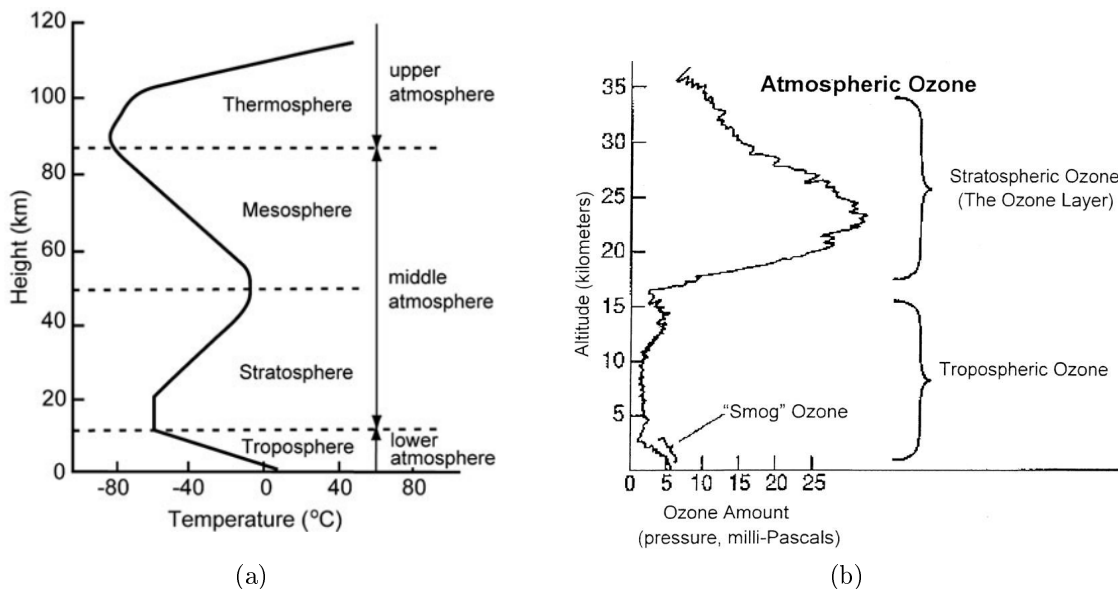
Figure 1.1: (a) Temperature structure of the Earth's atmosphere. (b) Distribution of O_3 in the atmosphere. Figure from [WMO, 1994]

1.1 Stratospheric Ozone

Ozone is generated in the stratosphere when solar ultraviolet radiation is absorbed by molecular oxygen, breaking the molecular bond and yielding two free oxygen atoms. A free oxygen atom can then combine with an oxygen molecule to form O_3. Ozone itself undergoes photo-dissociation (as well as other loss processes), yielding a net balance between O_3 formation and O_3 destruction. This balance leads to a quasi-steady-state concentration of atmospheric O_3 that is greatest in the lower stratosphere, between about 15 and 30 km of altitude (Fig. 1.1, panel (b)). Although the total amount of stratospheric O_3 is very small of only about 10 molecules of O_3 per million molecules of air, O_3 blocks much of the ultraviolet radiation that would otherwise damage all sort of life on Earth. The temperature inversion (Fig. 1.1) in this layer is caused by O_3 which absorbs much of the near ultraviolet radiation of the Sun and re-emits infrared radiation which heats the stratosphere.

1.1.1 Discovery of the Ozone Hole

Stolarski and Cicerone [1974] suggested that catalytic cycles with chlorine are a possible O_3 sink. Attention was shifted in the same year, to the industrially used Chlorofluorocarbons (CFCs) when Molina and Rowland [1974] presented their famous theory of CFCs induced O_3 depletion, predicted to occur roughly uniformly at all latitudes. Surprisingly, a severe O_3 drop, causing the so-called Antarctic O_3 hole, was detected above Halley Bay, Antarctica [Farman et al., 1985]. This large O_3 depletion, was found to be caused by heterogeneous chemistry involving anthropogenic emissions of chlorine and bromine-containing species, which are highly reactive and involved in catalytic O_3 destruction cycles throughout the stratosphere [Molina and Rowland, 1974, Stolarski and Cicerone, 1974, Wofsy et al., 1975]. Polar stratospheric clouds (PSCs) support this process by providing surfaces for heterogeneous chemical reactions [Solomon et al., 1986, Molina and Molina, 1987]. The Southern Hemisphere winter is about five degrees Celsius colder than the winter in the Northern Hemisphere favoring the development of PSCs, and the subsequent destruction of O_3 when the Sun begins to rise. Accordingly, a more severe O_3 depletion is seen over the Antarctic. Two years after the discovery of the Antarctic O_3 hole, the Montreal Protocol was signed to regulate emissions of ozone-depleting substances. Due to the long lifetimes of CFCs and other ozone-depleting substances in the stratosphere, the Antarctic O_3 hole continues to form during late winter and early spring. The 2014 World Meteorological Organization (WMO) Ozone Assessment [WMO, 2014] predicts the success of the Montreal Protocol and its amendments: the O_3 concentrations will increase over the next few decades with estimates to recover to its pre-1980 levels around mid of this century due to the decline of ozone-depleting substances emissions.

1.1.2 The Brewer-Dobson Circulation

Over the poles, O_3 variability is governed primarily by the transport of O_3 via the Brewer-Dobson circulation and temperatures inside the polar vortex [1]. The Brewer-Dobson circula-

---

1. During winter, the polar region cools due to lack of sunlight and a large latitudinal temperature gradient forms. At the edge of this temperature gradient, a westerly flow, or winter jet develops. The region inside the winter jet is called the polar vortex.

tion, proposed by Brewer [1949] and Dobson [1956], involves the tropospheric rise of air from the tropics followed by poleward transport. For mass conservation, stratospheric air must then return to the troposphere mainly in mid and high latitudes. The overall circulation allows therefore the transport of trace gases, such as O_3 and CFCs from the tropics. The Brewer-Dobson circulation is driven in the extra-tropics by stationary planetary waves propagating from the troposphere to the stratosphere. Since these planetary waves require westerly winds to propagate upward, the Brewer-Dobson circulation only occurs in winter, when the stratospheric polar vortex has formed. The Brewer-Dobson circulation transports O_3 rich tropical air to the winter pole and O_3 poor air, from beneath the O_3 maximum, away from the winter pole. In the Northern Hemisphere, the Brewer-Dobson circulation is strengthened by planetary waves, which originate over large land masses and mountain ranges. Contrarily, in the Southern Hemisphere, limited topography leads to reduced Brewer-Dobson circulation. Therefore, more O_3 is transported to the Arctic than Antarctic.

1.2   Tropospheric Ozone

Tropospheric O_3 is a direct man-made greenhouse gas. It is also the primary source (through photolysis by solar UV radiation) of hydroxyl radicals (OH) which, in turn, provide the mechanism by which pollutants such as carbon monoxide (CO) and methane (CH_4) are removed from the lower atmosphere. Sources of O_3 in the troposphere are either downward transport from the stratosphere or the *in situ* production through the photolysis of nitrogen dioxide (NO_2). The first long term observations and experimental evidence that tropospheric O_3 may be increasing was reported from balloon-sonde observations made between 1967 and 1982 at the meteorological station in Hohenpeissenberg in southern Germany [Attmannspacher et al., 1984]. Present day surface measurements are a factor of 2-4 larger than those of pre-industrial times [Volz and Kley, 1988, EMEP, 2011]. The following subsections are therefore a general introduction to highlight the importance of the study of tropospheric O_3. More details on tropospheric O_3 chemistry, transport and distribution will be provided in the following chapters.

1.2.1 Effects of Tropospheric Ozone on Health and Agriculture

Humans can be adversely affected by exposure to air pollutants in ambient air. In response, the European Union has developed an extensive body of legislation which establishes health based standards and objectives for a number of pollutants in air. The standards and objectives for O_3 are summarized in Table 1.1. For example, for health protection, a daily maximum eight hour average threshold of 120 $\mu g/m^3$ of O_3 is set. The threshold should not be exceeded at a monitoring station on more than 25 days per year, determined as a three year average starting 2010.

Table 1.1: Air quality standards for O_3 as defined in the Air Quality Directive [EEA, 2012]

Objective	Period	Threshold value ($\mu g/m^3$)
Human health	Daily maximum 8-hour mean [2]	120
Information	One hour	180
Alert [3]	One hour	240

The estimation of the urban exposure of the European population to exceedances of the O_3 target value (of 120 $\mu g/m^3$, applicable starting 2010) for the protection of human health estimation is shown in Fig. 1.2 for the period 2001-2010.

The exposure is estimated based on O_3 measured at all urban background monitoring stations from the AirBase database (http://www.eea.europa.eu/). For each city an average concentration is calculated and it is considered that the entire population of a city is exposed to this average concentration. In 2010 about 17 % of the EU population in urban areas was exposed to O_3 concentrations above the target value. The extent of exposure above the target value has varied between 15% and 61% since 2001 partly reflecting variations caused by meteorology. Interestingly, there is no apparent trend over this period [EEA, 2012]. The EU urban population that is exposed to O_3 levels exceeding the World Health Organization (WHO) air quality guidelines value (8-hour mean of 100 $\mu g/m^3$) is significantly higher, representing more than 97% of the total urban population in 2010.

Exposure to high levels of O_3 is associated with reduced lung function and chronic respiratory diseases as well as premature mortality. During moderate exercise, even healthy people

---

2. Not to exceed 25 days per year averaged over three years.
3. To be measured over three consecutive hours.

% of urban population
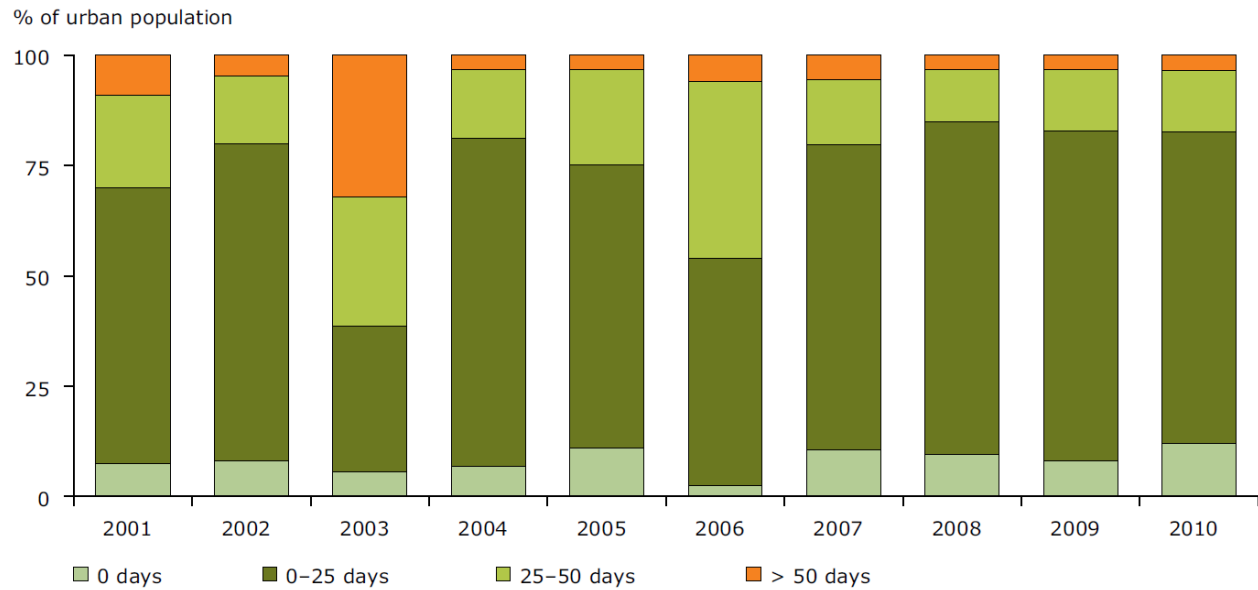
Figure 1.2: Percentage of the EU urban population exposed to O_3 concentrations over the target value threshold set for protection of human health, 2001-2010. Figure from EEA [2012].

can suffer from chest pain, coughing, nausea and pulmonary congestion [Ebi and McGregor, 2008, Jhun et al., 2014, Chen et al., 2015].

Because O_3 formation requires sunlight, periods of high O_3 concentration coincide with the growing season. Studies have shown that O_3 reduces crops production and yield [Schaub et al., 2005, Karnosky et al., 2007, Yue and Unger, 2014, Feng et al., 2014]. Figure 1.3 shows the effect of O_3 on vegetation. The two leaves on the left-hand side grew in control chambers, and the two leaves on the right-hand side grew in chambers with moderately elevated O_3 concentrations. Purple and blue in ozone-exposed leaves indicate that the leaves are carrying out photosynthesis less efficiently than leaves in the control chambers, where deeper red and yellow appear. The right assessment of O_3 effect on crops is essential in order to increase the sustainability of agricultural land management to the change in tropospheric O_3 concentrations, and to eventually secure food supply in regions with rapidly growing populations [Fuhrer and Booker, 2003].
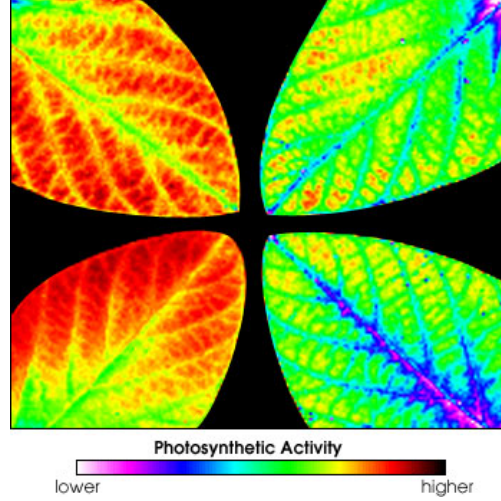
Figure 1.3: Fluorescence imaging technology captures soybean plant responses to change in levels of ozone. On the left: control chamber, and on the right: high exposure to ozone. Figure from Kim et al. [2001].

1.2.2 Net Global Radiative Forcing

The IPCC report of 2013 ([IPCC, 2013]), reports the net total positive forcing due to human activities since 1750 to be $+2.3 \pm 1 \ Wm^{-2}$. Fig. 1.4 shows the global mean radiative forcings (RF) and effective radiative forcing (ERF)[4] and their 90% confidence intervals in 2011 for various agents and mechanisms. The net anthropogenic radiative forcing and its range are also shown.

The O_3 contribution which affects the climate in two ways. The depletion of stratospheric O_3 is estimated to have had a cooling effect of -0.15 $\pm$ 0.15 Wm^{-2} and increasing tropospheric O_3 has had a warming effect estimated to be about +0.50 $\pm$ 0.20 Wm^{-2}. The RF of tropospheric O_3 is still quite uncertain and based on model simulations, due to the limited spatial and temporal coverage of observations.

---

4. The RF concept has been used for many years and in previous IPCC assessments for evaluating and comparing the strength of the various mechanisms affecting Earth's radiation balance and thus causing climate change. Whereas in the RF concept all surface and tropospheric conditions are kept fixed, the ERF calculations presented here allow all physical variables to respond to perturbations except for those concerning the ocean and sea ice. The inclusion of these adjustments makes ERF a better indicator of the eventual temperature response.
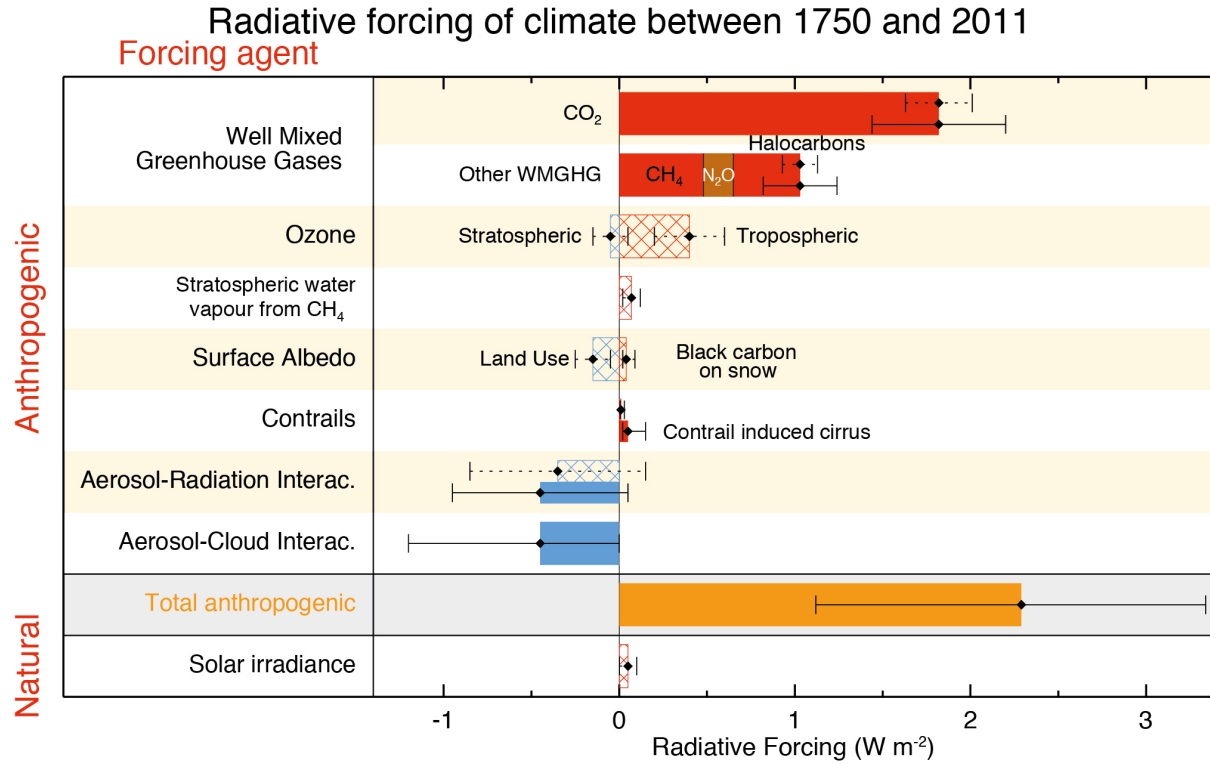
Figure 1.4: Bar chart for radiative forcing (RF-hatched) and effective radiative forcing (ERF-solid) for the period 1980–2011. Uncertainties (5 to 95% confidence range) are given for RF (dotted lines) and ERF (solid lines). Figure from IPCC [2013].

1.3 Ozone Sounding Methods

To study atmospheric composition in general, and O_3 in the stratosphere and troposphere in particular, few methods are available. Hereafter is a brief review on the main observation methods available.

1.3.1 Ground Observations

Ground observation measurements have the advantage of precise measurements with relatively low maintenance cost. They allow the measurements of many geophysical properties including O_3 abundances. The O_3 vertical distribution measurement is performed with ozonesondes with a high vertical resolution, of 100 meters. In the Northern Hemisphere, the Network for the Detection of Atmospheric Composition Change (NDACC) (http://www.

`ndsc.ncep.noaa.gov/`) [Leblanc et al., 2004] and the World Ozone and Ultraviolet Data Center (WOUDC) (`http://www.woudc.org/`) provide long time series of O_3 sounding. In the Southern Hemisphere, the time series starts in 1997 with the Southern Hemisphere Additional Ozone Sondes (SHADOZ) program (`http://croc.gsfc.nasa.gov/shadoz`) [Thompson et al., 2004]. To remotely measure atmospheric O_3, passive spectrophotometry (the Dobson network) and active Light Detection and Ranging (LIDAR) techniques are used. While ozoneondes are quite useful, they require significant infrastructure and are consequently limited in overall global coverage.

1.3.2 Aircraft-based Observations

Scientific aircraft missions or commercial airplanes can carry instruments to measure atmospheric composition. They provide an important source of information for profiles during take-off and landing and more importantly (and generally) at the cruising altitudes (between 9-12 km), providing information on the upper troposphere and/or on the transport between the stratosphere and the troposphere. Since dedicated scientific flights are expensive, commercial flights provide airbone *in situ* measurements at a regular and steady flow. The In-service Aircraft for a Global Observing System (IAGOS) (2011-today), previously Measurements of OZone and water vapor by in-service AIrbus airCraft (MOZAIC) program (1994-2014), (`http://www.iagos.fr/`), provide measurements of O_3, water vapor, carbon monoxide, and total nitrogen oxides. Measurements are geo-localized (latitude, longitude and pressure) and come with meteorological observations (wind direction and force, temperature).

1.3.3 Satellite Observations

Ground, aircraft or even balloon observations (not discussed here), provide geographically limited observations. Atmospheric sounding methods from space on the other hand, provide the means to achieve a global coverage. Techniques of atmospheric remote sensing from space measure electromagnetic radiation at different wavelengths from radio to the ultraviolet. Satellites commonly fly on Low Earth Orbit (LEO), between 160 and 2000 km from Earth,

or on Geostationary Earth Orbit (GEO) where the satellite is placed around 36000 km above the Earth's equator and with a period equal to the Earth's rotational period. GEO satellites are mostly used for communications and weather satellites. Since an object in a geostationary orbit appears motionless to ground observers, the GEO satellite antennas that communicate with them do not have to move to track them. On the other hand, most Earth observation satellites are found in LEO which can also take advantage of sun-synchronous orbits at an altitude of about 800 km and near polar inclination. The main remote sounding techniques involve nadir sounders which are those that measure the signal from a field of view that is generally downward, and limb sounders that look through the edge of the atmosphere (Fig. 1.5). For tropospheric O_3 studies, nadir view instruments are currently widely used since they provide a better sensitivity to the troposphere and a good spatial resolution.
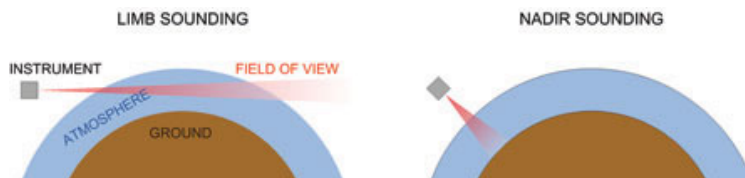
Figure 1.5: Limb and nadir sounding from space.

In nadir mode, the first O_3 distributions (stratospheric and to a lesser extent tropospheric) in the ultra-violet and visible (UV-vis) range were obtained from the Total Ozone Mapping Spectrometer (TOMS) [Heath et al., 1975] starting 1978, flown on four satellites. More recently, O_3 monitoring has been performed from the Global Ozone Monitoring Experiment (GOME) launched in 1996 [Munro et al., 1998, Burrows et al., 1999], Ozone Monitoring Instrument (OMI) launched in 2004 [Levelt et al., 2006, Liu et al., 2010] to provide data continuity of the TOMS O_3 record, and GOME-2 (to provide continuity to GOME) launched in 2007 [Loyola et al., 2011].

The thermal infrared range can provide specific information on the troposphere. First measurements of tropospheric and total O_3 in the thermal infrared were performed with Interferometric Monitor Greenhouse gases (IMG) in 1996 during a period of only 10 months [Turquety et al., 2002]. Currently, few other instruments are able to provide a good global coverage and time series of tropospheric O_3. Those are: the Atmospheric Infrared Sounder (AIRS) [Aumann et al., 2003], the Tropospheric Emission Spectrometer (TES) [Beer, 2006, Bowman

et al., 2006] and the Infrared Atmospheric Sounding Interferometer (IASI) [Clerbaux et al., 2009].

1.4 Planning and Goals of This Thesis

The goal of my PhD work, performed at the Laboratoire Atmosphère Milieux Observations Spatiales (LATMOS), is to study the tropospheric O_3 seasonal variation at different regions of the globe in order to improve our understanding of this trace gas and pollutant on a regional and global scale using observations from IASI.

After this introduction, this thesis will be planned as follows: Chapter 2 will explain the tropospheric chemistry leading to the production and destruction of O_3 and then it will discuss the modes of long-range and intercontinental transport of O_3 in the troposphere. A special focus on the Meteorological Operational satellite programme (MetOp) satellites carrying the IASI instruments to monitor atmospheric composition is provided in Chapter 3. Chapter 4 will provide an overview on thermal infrared absorption and emission, the radiative transfer equation and code used to retrieve O_3 abundance from the IASI data. Results of this study will be presented in Chapters 5, 6, 7 and 8. These results will focus on the tropospheric O_3 product from IASI, to show the seasonal variability and the sensitivity of O_3 to its precursors during 2008 to 2013, and over different regions in the world. I will attempt to investigate the effect of urban pollution on O_3 in rural areas; I will look and discuss O_3 maxima seen over particular regions of the world, in particular the Mediterranean basin and East Asia, as well as the effect of the East Asian monsoon on the reduction in the tropospheric O_3 column. Conclusions, discussions and some perspectives for future work will be listed in Chapter 9.

Chapter 2

Tropospheric Ozone: Chemistry and Transport

Tropospheric ozone is a reactive oxidant gas produced in trace amounts in the troposphere. Since most of the O_3 resides in the stratosphere, it was previously thought that the tropospheric O_3 sources are mainly the downward transport of stratospheric air masses. In the early 1970's, Chameides and Walker [1973] and Crutzen [1974] were the first to assess the *in situ* tropospheric O_3 production. Fig. 2.1 provides the schematic of gas-phase O_3 chemistry in the troposphere emphasizing the coupling between the cycles of O_3, the hydrogen oxide radicals [1] (HO_x=OH+H+peroxy radicals), and the nitrogen oxides (NO_x=NO + NO_2). The ozone budget in the troposphere is therefore determined as follows: it is supplied to the troposphere by the transport from the stratosphere and the chemical production within the troposphere; it is removed by deposition and tropospheric chemical consumption. The total chemical production of tropospheric O_3 is estimated as 3420 $\pm$ 770 Tg/yr with a mean lifetime of 24 $\pm$ 2 days [IPCC, 2007].

In this chapter, I will first provide an overview of the tropospheric chemistry, in particular focusing on the role of the hydroxyl radical chemistry to introduce tropospheric O_3 sources

---

1. In chemistry, a *radical* (more precisely, a free radical) is an atom, molecule, or ion that has unpaired valence electrons or an open electron shell, and therefore may be seen as having one or more "dangling" covalent bonds. With some exceptions, these "dangling" bonds make free radicals highly chemically reactive towards other substances, or even towards themselves.

and sinks. The next part of this chapter discusses the various modes and dynamical processes leading to the long-range and intercontinental transport of O_3 in the troposphere.
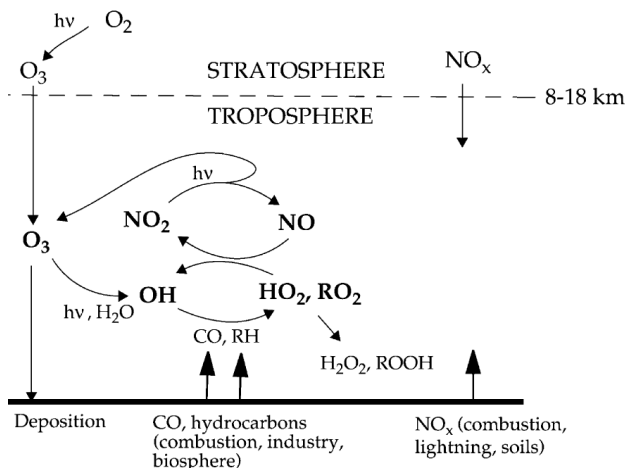
Figure 2.1: Schematic of tropospheric O_3 chemistry illustrating the coupling between the chemical cycles of O_3, HO_x, and NO_x. RO_2 refers to the ensemble of organic peroxy radicals. Figure from [Jacob, 2000].

2.1 The Hydroxyl Radical and the Peroxy Radicals

The formation of OH is the initiator of radical-chain oxidation of the atmospheric photochemistry. One of the roles of atmospheric radical chemistry, driven by OH, is to "clean" the troposphere from a wide-range of organic compounds. The OH radical is known to react with most trace gases. In many situations and chemical reactions, it initiates and determines the rate of production of various chemical species. Thus, OH can control the removal and, therefore, the tropospheric concentrations of many trace gases, in particular O_3.

In order to understand O_3 production and destruction in the troposphere, one should therefore start by understanding the peroxy radicals (HO_2, RO_2, and CH_3O_2) behavior. The peroxy radicals can be thought of as the intermediates between the hydroxyl (OH) radical and O_3 formation or destruction [Monks, 2005]. These radicals are responsible of removal of primary pollutants such as NO_x and volatile organic compounds (VOCs). The main sources of NO_x are either anthropogenic, such as the result of the combustion of fossil fuels and biomass burning, or natural from wildfires, soil emissions, and lighting. Most of the NO_2 in urban air results from the rapid oxidation of NO which is the major nitrogenous product

emitted from combustion [Finlayson-Pitts and Pitts, 1997, Klonecki and Levy, 1997, Jacob, 2000, Seinfeld and Pandis, 2006, Jacobson, 2012]. VOCs sources are various and include biogenic non-methane hydrocarbons (NMHC) and oxygenated NMHC (e.g., alcohols, aldehydes and organic acids). VOCs influence climate through their production of organic aerosols and their involvement in photochemistry. The largest source, by far, is natural emission from vegetation, mainly from isoprene (C_5H_8) [Guenther et al., 1995, 2006].

Photolysis of O_3 by ultraviolet light in the presence of water vapor is the main source of hydroxyl radicals in the troposphere.

$$O_3 + h\upsilon(\lambda < 320 \ nm) \to O_2 + O(^1D) \tag{2.1}$$

$$O(^1D) + H_2O \to OH + OH \tag{2.2}$$
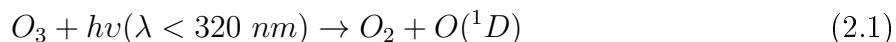
The hydroxyl radical lifetime, under the majority of conditions (polluted or not), is less than a second. So why is OH critical to the atmosphere? First, its high reactivity, and second -and given this high reactivity- its relatively high concentration in the troposphere, given the abundance of O_3 and water vapor in the troposphere.

Hydroxyl radical chemistry cannot be treated in isolation as it is part of a closely coupled system involving HO_x, NO_x, and O_3. In relatively unpolluted regimes (low NO_x) the main fate for the hydroxyl radical is reaction with either carbon monoxide (CO) or methane (CH_4) to produce peroxy radicals such as HO_2 and CH_3O_2.

$$OH + CO \xrightarrow{O_2} CO_2 + HO_2 \tag{2.3}$$

And,

$$OH + CH_4 \to CH_3 + H_2O \tag{2.4}$$

$$CH_3 + O_2 + M \to CH_3O_2 + M \tag{2.5}$$
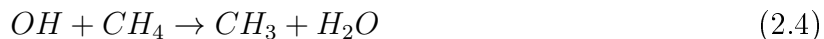
where M is a third body that acts only to stabilize the association complex.

HO_2, the major peroxy radical, has a lifetime of about a minute in clean air and much less than a minute in polluted air. In low NO_x conditions, HO_2 from reaction 2.3 can react with O_3 leading to its further destruction in a chain sequence involving the production of hydroxyl radicals:

$$HO_2 + O_3 \rightarrow OH + 2O_2 \tag{2.6}$$

$$OH + O_3 \rightarrow HO_2 + O_2 \tag{2.7}$$

In more polluted conditions (high NO_x), the peroxy radical catalyzed oxidation of NO to NO_2 is as follows:

$$HO_2 + NO \rightarrow OH + NO_2 \tag{2.8}$$
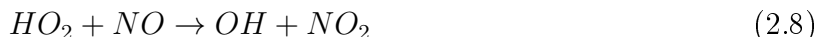
Leading to the production of O_3 from the subsequent photolysis of NO_2 where the oxygen atom (O) rapidly recombines with molecular oxygen (O_2) to produced O_3 .

$$NO_2 + h\upsilon(\lambda < 420 \ nm) \overset{O_2}{\rightarrow} NO + O(^3P) \tag{2.9}$$

$$O(^3P) + O_2 + M \rightarrow O_3 + M \tag{2.10}$$
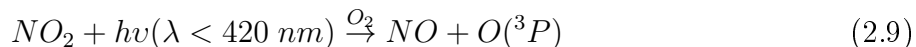
These 2 last reactions occur rapidly (in the order of 200 seconds or less) and establish a near-steady state between NO and NO_2. However there are 2 distinct situations in which these 2 equations actually result in a net loss of O_3: during nighttime since reaction 2.9 stops and during daytime in the vicinity of large NO emission sources (such as in the plumes of power plants), where removal of O_3 can occur. Since ambient NO_x originates mostly from NO emissions, the rapid inter-conversion of O_3, NO and NO_2 (reaction 2.9 and 2.10) results in a photochemical equilibrium with a significant O_3 loss, also called NO_x titration.

Hydroxyl radicals produced in reaction 2.8 can go on to form more peroxy radicals (e.g. via reactions 2.3, 2.4 and 2.5).

Similarly to HO_2, CH_3O_2 can also oxidize NO to NO_2 which then proceeds to produce O_3,

as:

$$CH_3O_2 + NO \rightarrow CH_3O + NO_2 \tag{2.11}$$
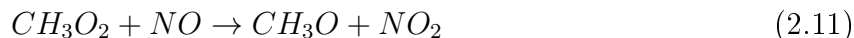
The resulting radical product reacts rapidly with O_2 to form formaldehyde (HCHO) and HO_2 as:

$$CH_3O + O_2 \rightarrow HCHO + HO_2 \tag{2.12}$$
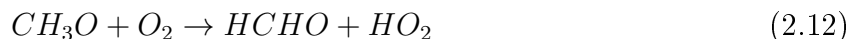
The OH radical may have another fate, depending on the concentration of NO_2, in that it can react with NO_2 to form nitric acid (HNO_3) as:

$$OH + NO_2 + M \rightarrow HNO_3 + M \tag{2.13}$$

The formation of HNO_3 represents an effective loss mechanism for both HO_x and NO_x. There are a number of other potential sources of HO_x in the atmosphere, such as the photolysis of carbonyl compounds produced from the (partial) oxidation of hydrocarbon species. The simplest and most common of these is formaldehyde, which is produced from CH_4 oxidation:

$$HCHO + hv(\lambda < 334\ nm) \rightarrow H + HCO \tag{2.14}$$

$$HCO + O_2 \rightarrow HO_2 + CO \tag{2.15}$$

$$H + O_2 + M \rightarrow HO_2 + M \tag{2.16}$$
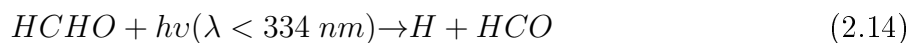
2.2 Fate of Peroxy Radicals: Photochemical Production and Destruction of Ozone

The fate of the peroxy radicals can have a marked effect on the ability of the atmosphere either to produce or to destroy O_3. Photolysis of NO_2 and the subsequent reaction of the photo-product $O(^3P)$ with O_2 (reactions 2.9 and 2.10) are the only known ways of producing O_3 in the troposphere. One can see from the reactions listed thus far that there is a balance

between photochemical production of O_3 and O_3 loss depending on the concentrations of HO_x and NO_x. Figure 2.2 shows the net O_3 production dependence on NO_x availability in a clean environment.
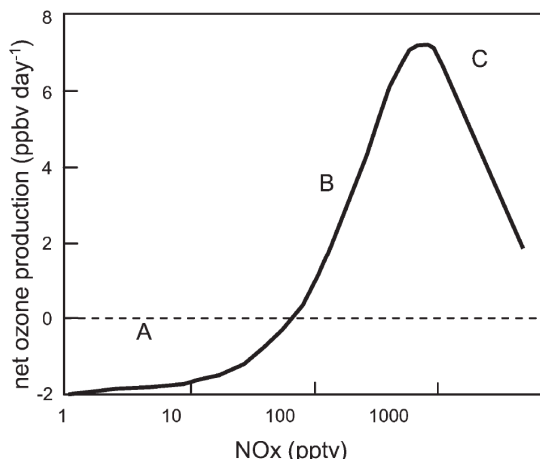
Figure 2.2: Dependence of the production of O_3 on NO_x taken from a numerical model. Figure from [Monks, 2005].

The figure shows that for low NO_x concentrations (region A), we have net O_3 loss. In region B, the O_3 production rate increases with increasing NO_x concentration to reach a maximum production rate for O_3 . Region B is also know as NO_x limited with respect to the production of O_3 . In region C, the net production rate begins to decrease, due to the increased competition for NO_2 by reaction 2.13.

However, reality is different and the situation presented in Fig. 2.2 is somewhat more complicated by the presence of increased levels of non-methane hydrocarbons (NMHCs) at high concentrations of NO_x, especially in places with urban atmospheric conditions. The oxidation of NMHCs, in common with much of tropospheric oxidation chemistry, is initiated by reaction with OH, leading to the rapid sequence of chain reactions. An example of hydrocarbons (RH) undergoing oxidation that involves organic peroxy radicals RO_x (to eventually produce O_3) is:

$$RH + OH \xrightarrow{O_2} RO_2 + H_2O \tag{2.17}$$

$$RO_2 + NO \rightarrow RO + NO_2 \tag{2.18}$$

$$RO + O_2 \rightarrow R'CHO + HO_2 \tag{2.19}$$

$R'CHO$ is the carbonyl compound and HO_2 will eventually react as reaction 2.8 predicts to produce OH and NO_2 and therefore O_3 via reactions 2.9 and 2.10.

With the involvement of VOC (*e.g.* through the NMHC reactions above), one should update Fig. 2.2 as Fig. 2.3 shows.
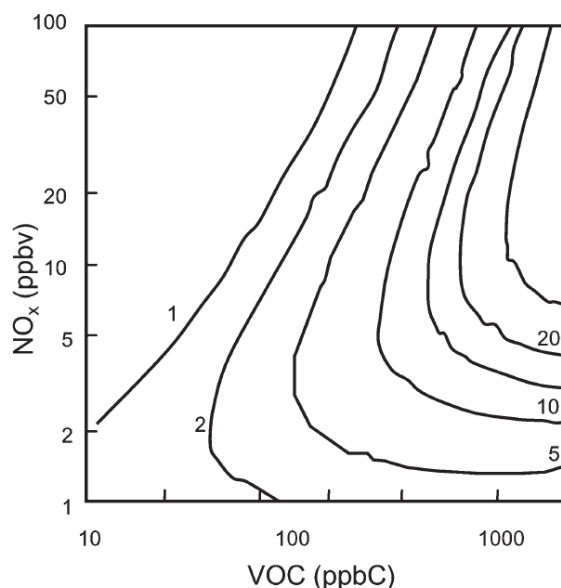
Figure 2.3: Isopleths giving net rate of O_3 production (ppb/h) as a function of VOC (ppbC^2) and NO_x (ppbv) for mean summer daytime meteorology and clear skies under urban conditions. Figure from [Monks, 2005].

The peak initial concentrations of O_3 generated from a range of initial concentrations of NO_x and VOCs are usually represented as an "O_3 isopleth diagram", an example of which is shown in Fig. 2.3. In an O_3 isopleth diagram, initial mixture compositions giving rise to the same peak O_3 concentration are connected by the appropriate isopleth. This plot shows that O_3 production is a highly nonlinear process in relation to NO_x and VOC. As shown in the figure, it is possible to identify two regimes with different O_3-NO_x-VOC sensitivity. In the NO_x-sensitive regime (with relatively low NO_x and high VOC, at the right side of the plot), O_3 increases with increasing NO_x and changes little in response to increasing VOC. In

---

2. "$ppbC$" signifies parts per billion carbon, which is equal to parts per billion by volume (ppbv) times the number of carbon atoms in the molecule. $ppbC$ is a very common unit of measurement for VOC in regards to ozone formation

the NO_x-saturated or VOC-sensitive regime O_3 decreases with increasing NO_x and increases with increasing VOC (left part of the plot).

2.3 Long-Range Transport of Tropospheric Ozone

Given the O_3 lifetime, another source -besides chemistry- of tropospheric O_3 in a certain region, is transport. This transport might be within the troposphere or from the stratosphere. To illustrate this, I will present in the rest of this chapter the different dynamical mechanisms responsible of O_3 transport across the oceans, between the continents, from the downward motion from the stratosphere and the vertical transport within the troposphere.

Typical O_3 intercontinental transport times are of the order of 5-10 days [Wild and Akimoto, 2001] suggesting that the transport of pollutants, such as tropospheric O_3, its precursors and reservoir species, with a lifetime larger than this transport time, should be considered on a global scale. Studying the long-range transport of O_3 cannot be done without studying the wind patterns and dynamical processes responsible of the vertical and horizontal/lateral transport, which will be done and discussed in the following subsections.

2.3.1 Transatlantic Transport

Many studies have discussed the effect of the transatlantic transport of anthropogenic pollution on the pollution budget over Europe and Northern America. In fact, 30% of the surface O_3 response in a receptor region is shown to result from changes outside that region. This has strong implications for O_3 trend assessments [HTAP, 2010, and references therein]. Transported pollution from one side will make air quality standards much more difficult on the other side [Jonson et al., 2001]. The westerlies general flow from the North American continent acts as the primary mechanism of pollution transport into the North Atlantic. In the North Atlantic, the movement of those pollutants and in particular O_3 can come under flow patterns that are modulated by the North Atlantic Oscillation (NAO)[3]. The North

---

3. The North Atlantic Oscillation (NAO) can be defined as "the tendency for pressure to be low near Iceland when it is high near the Azores and vice versa". The Icelandic Low is a semi-permanent center of low atmospheric pressure found between Iceland and southern Greenland and the Azores High is a large subtropical semi-permanent center of high atmospheric pressure typically found south of the Azores in the

Atlantic "oscillation" refers to the swing in the atmospheric pressure between the Icelandic Low and the Azores High (see Fig. 2.4) and thus plays an important role in determining intercontinental transport of air from North America to Europe and the sub-tropics. An NAO index is defined by Hurrell [1995] to help the assessment of the circulation. It is determined by the difference in pressure between the Azores High and the Icelandic Low. The clockwise rotation of the Azores High and the counterclockwise rotation of the Icelandic Low, as shown in Fig. 2.4, directs air eastward to Europe. The strength of this flow depends on the pressure difference between the two. A well-developed Azores High (strong high pressure) and a well-developed Icelandic Low (very low pressure) corresponds to the NAO positive (NAO+) phase. The NAO negative (NAO-) phase occurs when both systems are weak.
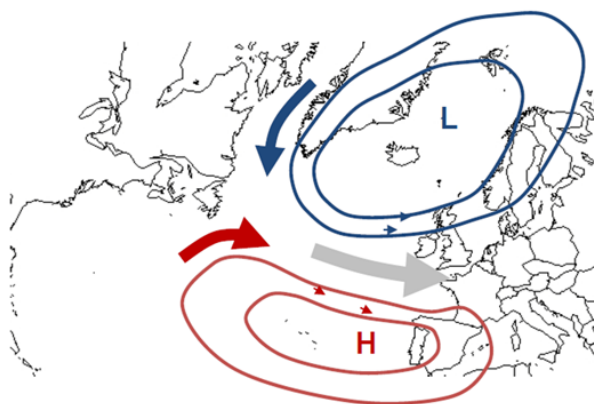
Figure 2.4: The pressure difference between the Azores High and the Icelandic Low determines the phase of the NAO and influences the flow of westerly winds toward Europe. Figure from http://www.air-worldwide.com/.

In mid-latitudes, the NAO is the leading mode of variability across the North Atlantic and dictates the strength and pathways of the westerly movement of air across this region. The NAO is recognized as a major factor in inter-annual variability in temperature and precipitation over Europe. Meteorological observations show that a strong Icelandic Low is usually accompanied by a strong Bermuda Azores High [van Loon and Rogers, 1978].

During the positive phase of the NAO, the increased difference sets up a greater north-south pressure gradient which produces an enhanced zonal (west to east) flow, causing air to move quickly with less impedance from west to east across the North Atlantic. Meteorological effects are above normal precipitation and mild temperatures over northern Europe and drier

Atlantic Ocean, at the Horse latitudes [Walker and Bliss, 1932, Tucker and Barry, 1984].

weather conditions in the Mediterranean area. The North American influence on western Europe surface O_3 is strongly correlated with the NAO especially in spring [Li et al., 2002, Creilson et al., 2003] and Pausata et al. [2012] found a positive correlation in all seasons except fall suggesting that the positive trend in O_3 over the last decade could be related to the prevailing positive phase of the NAO during this time period.

During the negative phase, the Icelandic Low and the Azores High both weaken causing the circulation across the North Atlantic to be altered. This altered flow is less conductive to transport of air parcels from North America to Europe. On the other hand, the meridional (north to south) atmospheric mass exchange is enhanced [Hurrell, 1995, Li et al., 2002, Creilson et al., 2003, Pausata et al., 2012]. The weather related to low NAO phases is characterized by drier conditions in northern Europe and above normal precipitation in southern Europe. As a summary, one should know that in the Northern Hemisphere, the prevailing westerlies are the main source of transatlantic transport of North American pollution to Europe but other dynamical effect, of a smaller importance, might favor the transport of pollutants from Europe to North America.

From US to Europe

Parrish et al. [1993] have shown that during North Atlantic summer, the amount of photochemically generated O_3 transported from North America appears to be greater than the amount injected from the stratosphere as it was previously thought [Oltmans and Levy, 1992]. This supported the speculations that the transport of pollution from North America can have a strong effect on down-wind regions. Over eastern North America (between 30 and 60N in particular), the westerly winds extend to the surface allowing the transport in the lower troposphere of North American pollution to the North Atlantic and/or to Europe [Li et al., 2002]. This can be seen in the boundary layer wind patters presented in Fig. 2.5. The Figure provides the spatial distribution of the winds patterns during January and June 2013 (taken as an example year) at 875 hPa representing the near-surface/boundary layer.

The wind directions plotted in Fig. 2.5 (and later on in Fig. 2.6) are extracted from the u and v component of horizontal wind from the ECMWF Re-Analysis (ERA)-Interim archive. Data are provided as daily (4 observations per day) or monthly means over a grid size of 0.75
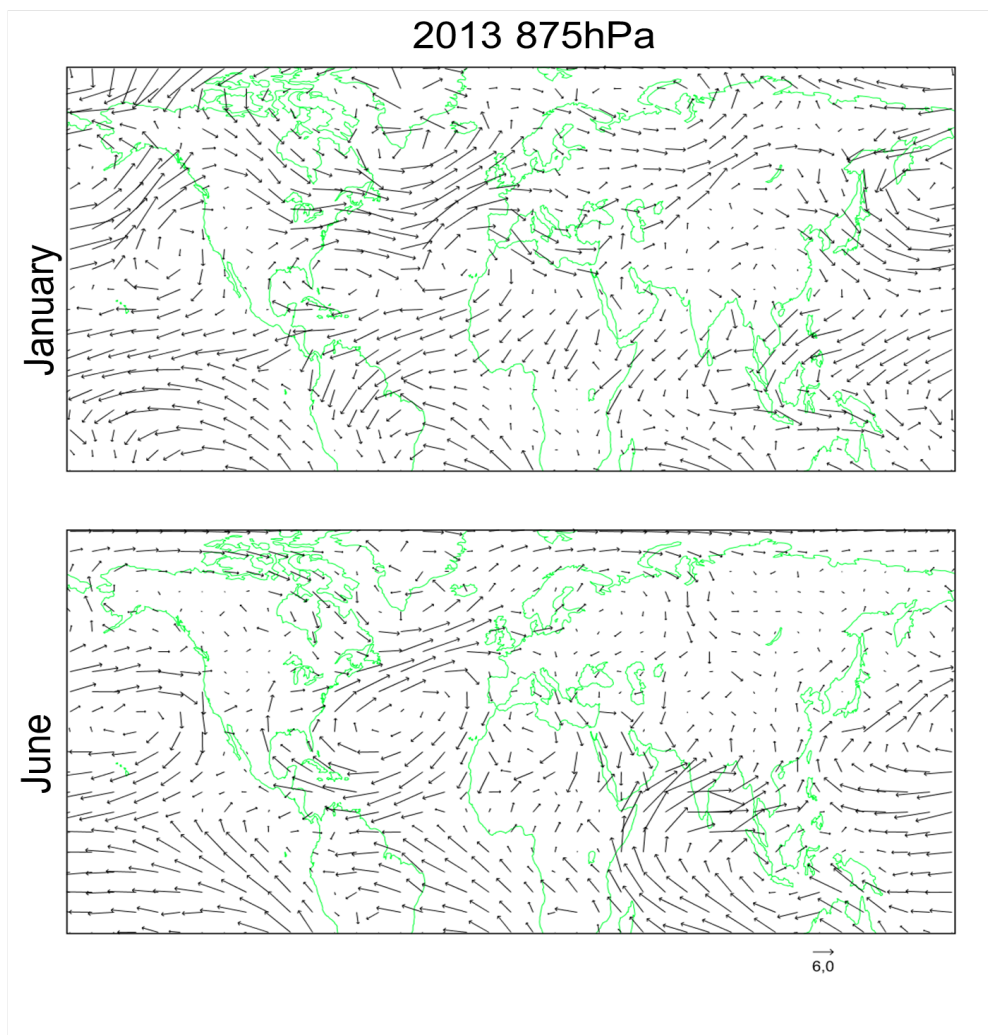
Figure 2.5: Monthly averaged wind speed and direction (from ERA-interim) at 875 hPa, upper panel: January 2013, lower panel: June 2013.

x 0.75 degree and 37 pressure levels from 1000 to 1 hPa.

Another pathway for transatlantic transport involves strong convection (section 2.5 provides more information on deep convection) over the central and eastern United States, especially in summer. This causes the uplift of O_3 and its precursors to the middle and upper troposphere. There, they are exported by westerlies [Jacob et al., 1993]. This export by westerlies during the different months of the year is represented by the winds at 500 hPa in Fig. 2.6. The figure shows the wind patterns during January and June 2013, representing the free troposphere at 500 hPa. The long-range transport of pollutants in general, and of tropospheric O_3 in particular, in the free troposphere, is more efficient since the winds are

stronger. Moreover, the O_3 will survive longer than in the lower troposphere where its lifetime is shorter and its sources are complex. The uplift by a warm conveyor belt[4], associated with cyclonic pressure systems allowing tropospheric O_3 to be lifted into the free troposphere over the western North Atlantic, is responsible for a long-range transport of O_3 by winds in the free troposphere (Fig. 2.6) via the westerlies to Europe [Stohl, 2001, Stohl et al., 2002, Cooper et al., 2002]. In summer, the values of tropospheric O_3 are the highest, making the export fluxes of North American O_3 to Europe more important.
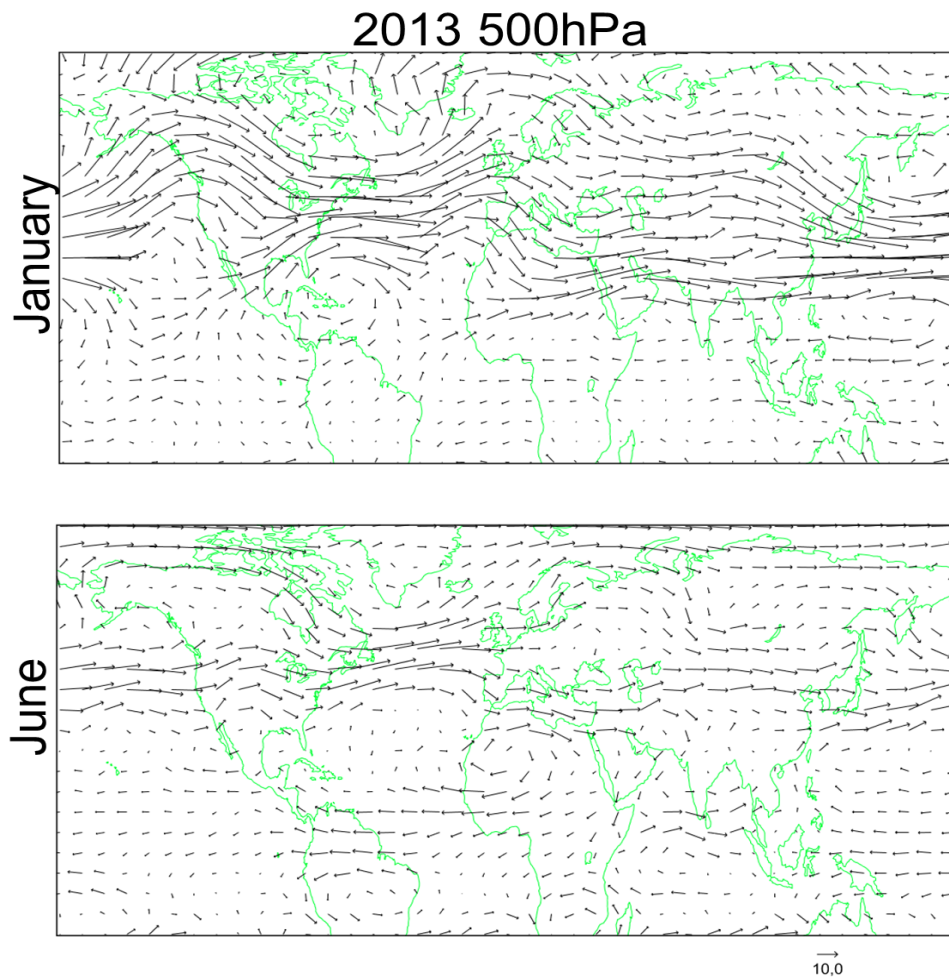
Figure 2.6: Monthly averaged wind speed and direction (from ERA-interim) at 500 hPa, upper panel: January 2013, lower panel: June 2013.

---

4. A Warm Conveyor Belt is defined as a layer of air which originates in a relative easterly to southeasterly flow within the lower levels of the troposphere in the ridge area ahead of the front, generally ascends poleward forming clouds then changes to descending motion where cloud dissolution takes place.

From Europe to the US

A more general route for transatlantic transport of European pollution involves circulation around the southern branch of Bermuda Azores High. This transport has been detected particularly in summer for aerosols when the High extends far to the north and east [Hamelin et al., 1989], though not for O_3 due to the weak circulation and its rather short lifetime; the combination of which makes the transport negligible. This weak circulation could actually be seen in Fig. 2.5 at 875 hPa especially for the month of June. European pollution is also suggested to be transported to North America by circulation around the Icelandic Low [Li et al., 2002]. This is seen for example during January 2013 at 875 hPa in Fig. 2.5.

2.3.2 Transpacific Transport

The transpacific transport of East Asian pollution to North America takes place mostly in the free troposphere since the westerlies do not extend to the surface and therefore the uplifting of the pollutants from the boundary layer to the free and upper troposphere is necessary [Yienger et al., 2000, Fiore et al., 2002]. To support this claim, the winds patterns presented in Fig. 2.5 at 875 hPa are indeed very weak above land in East Asia, and show that the general flow over the Pacific is not straight to the American continent. On the other hand, at 500 hPa as in Fig. 2.6, this transport is much stronger and better directed towards the coasts of North America.

If NO_x is uplifted to the free troposphere, even in small quantities, it can lead to large O_3 production in the continental free troposphere, and downwind of it [Jacob et al., 1993, Thompson et al., 1994]. PAN (peroxyacetylnitrate), could be for example, uplifted and transported in the free troposphere, then subsided and decomposed to release NO_x and thus leading to a potential high O_3 production. This is found to be a major source of the O_3 enhancement in the Asian plumes across the transpacific [Heald et al., 2003, Hudman et al., 2004], though Jacob et al. [1999] found that Asian influence on surface O_3 in the US is driven by long range transport of O_3 itself rather than that of its precursors. East Asian regions have the greatest potential to affect the regional and global O_3 budget due the efficient vertical transport, though in comparison, Europe experiences the greater intercontinental

effect due to the shorter distance through the Atlantic [Wild and Akimoto, 2001]. Asian pollution enhanced surface O_3 concentrations by 5–7 ppbv over western North America in spring 2006 [Zhang et al., 2008]. The export of Asian pollution is done through boundary layer ventilation, frontal uplifting [5] (typically in warm conveyor belts), lifting of air particles due to convection, orographic lifting (by mountains for example over central and eastern China) [Liu et al., 2003] and in typhoons [Liang et al., 2007]. Once in the free troposphere, it can be transported across the Pacific during a period of 5 to 10 days [Yienger et al., 2000]. Figure 2.6 shows that this transport will be more frequent in winter (January, but also during spring, not shown here) due to the strong westerly winds, and smaller in summer (June in Fig. 2.6). When the air reaches the west coasts of North America, the mean transport time to the surface is around 2-3 weeks [Liu and Mauzerall, 2005]. In general, Asian O_3 influence on Europe (from the winds seen in Figs. 2.5 and 2.6) is negligible, though under certain circumstances, it could be important.

2.4 Transport from the Stratosphere

The stratosphere and the troposphere are separated by the tropopause. The latter has many definitions and a good review is found in Hoinka [1997]. The *thermal* tropopause is defined by the WMO as the lowest level at which the temperature lapse rate decreases to 2 kelvins/km or less, and the lapse rate averaged between this level and any level within the next 2 km does not exceed 2 kelvins/km. The WMO defines the *dynamical* tropopause as the atmospheric layer corresponding to a potential vorticity of 1.6 PVU [WMO, 1986] where "PVU" stands for potential vorticity unit$= 10^{-6}$ m^2 s^{-1} K kg^{-1}, while values between 2 and 3 were also suggested [Danielsen et al., 1987]. The advantage of the dynamical definition of the tropopause is that the PV is a conserved entity that is not affected by adiabatic convergence and divergence. The thermal definition, however, possesses a major operational advantage in that it allows the determination of the tropopause height from a single temperature profile. Another tropopause definition in use is based on a threshold O_3 mixing ratio, which shows

---

5. A **front** is where two different air masses meet, so frontal lifting is when one air mass along a front gets lifted up over the other. A cold front occurs when a cold air mass advances onto a warm air mass. A warm front is the opposite: when a warm air mass advances onto a cold air mass.

a sharp transition from low concentrations in the troposphere to high concentrations in the stratosphere. Bethan et al. [1996] noticed that this so-called *chemical* tropopause is somehow lower than the thermal one. In his definition, he suggests that the tropopause would be the level at which the O_3 VMR exceeds 110 ppbv. In common tropospheric chemistry models, the value of 150 ppbv is used (as done using 26 chemistry models by Stevenson et al. [2006] for example). Figure 2.7 shows the tropopause height based on the chemical definition from IASI[6]. The tropopause will be the first atmospheric level where the volume mixing ratio of O_3 is higher than 150 ppbv. The figure shows that the highest values are around the Equator with a tropopause height around 16 km, and 13-14 km height in the subtropical regions, and less than 12 km elsewhere. In midlatitudes (northern and southern), this value is larger in summer and smaller in winter.
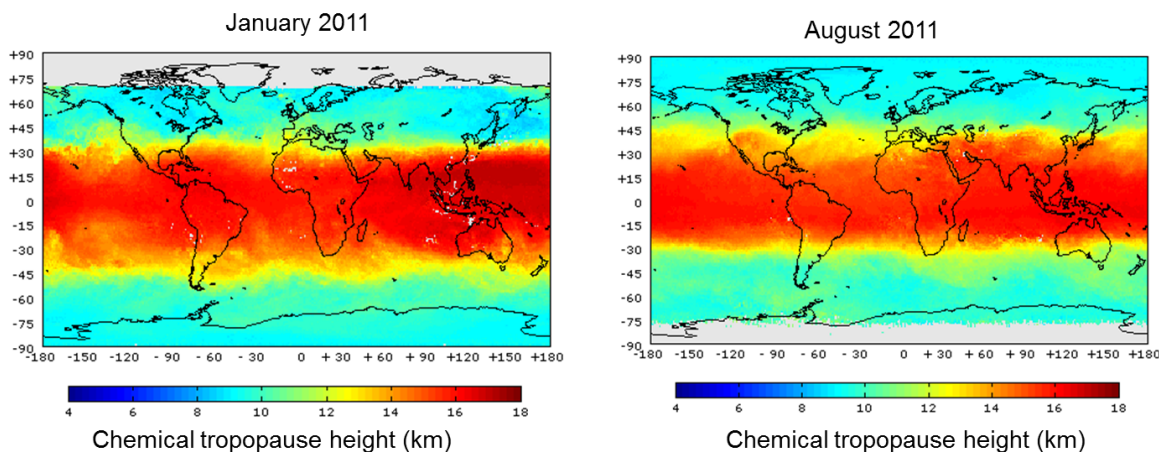
Figure 2.7: Chemical tropopause ($O_3 < 150$ ppbv) height from IASI data.

Various dynamic mechanisms are responsible for the transport of O_3 enriched strato-spheric air into the troposphere [Stohl et al., 2003]. In general, stratosphere-troposphere exchange (STE) is driven by the Brewer-Dobson circulation with upward motion across the tropopause at the equator and downward motion in the extra-tropics. Extratropical STE is associated with synoptic-scale (horizontal length scale of the order of 1000 km) and mesoscale processes (horizontal length scale from around 5 to several hundred kilometers). The contribution to the annual mean O_3 mixing ratios across Europe due to stratospheric-tropospheric

---

6. Though I haven't introduced measurements by IASI *yet*, this figure is used here for mere illustration.

exchanges is in the range of 5.7 to 10.6 ppbv [Collins et al., 2003, Derwent et al., 2004]. The downward transport of stratospheric air into the troposphere has been observed to occur in:

– Tropopause folds, both in the vicinity of the polar jet [Lamarque and Hess, 1994] and the subtropical jet [Baray et al., 2000]. The polar and subtropical jet are represented in Fig. 2.8.
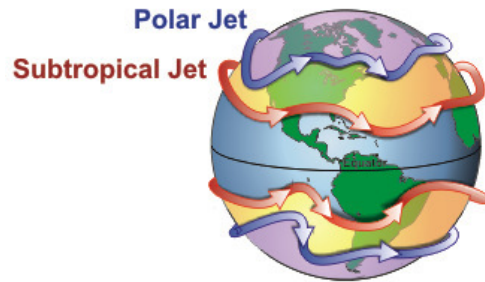
Figure 2.8: Polar and subtropical jet. Figure from http://www.srh.noaa.gov/jetstream/global/jet.htm

– Cutoff low pressure systems: those are closed upper tropospheric systems that are completely detached (and thus "cut off") from their polar sources and extend to the south of the mid-latitude westerly flow. A cutoff low usually maintains its polar characteristics with low temperature and high potential vorticity (PV) [Palmén, 1949].
In an intense cut off low, there could be a tropopause funneling causing pronounced stratospheric intrusions into the troposphere [Ancellet et al., 1994, Holton et al., 1995]. An example is shown in Fig. 2.9 where a deep stratospheric intrusion event over Europe during June 2001 took place. A large cut-off low with high PV started developing over southeastern Europe and propagating slowly eastwards during the 20th and 21st of June as the upper panels show. The respective GOME total column ozone measurements show high values on 20 June (Fig. 2.9c) resembling the hook-shaped streamer of high PV on 20 June while the high total ozone values on 21 June (Fig. 2.9d) are clearly associated with the developed cut-off low over southeastern Europe.

– Thunderstorms and mesoscale convective complexes, which are considerably larger than individual thunderstorms but producing a similar effect on a larger scale [Poulida et al., 1996].

– Breaking gravity waves [Langford et al., 1996]. A gravity wave is a vertical wave
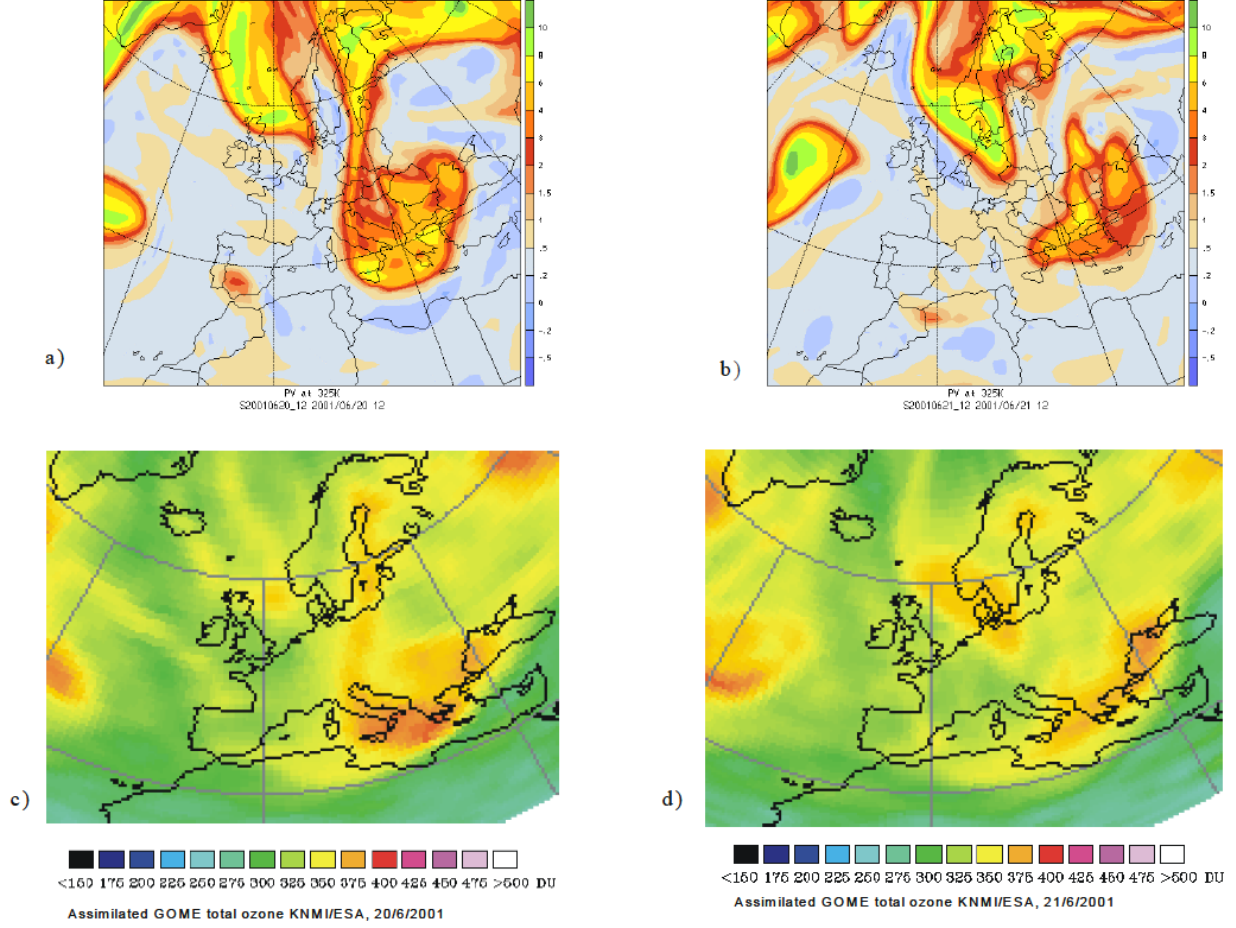
Figure 2.9: Isentropic PV on the 325K surface on 20 June 2001 12:00UTC (a) and on 21 June 2001 12:00UTC (b) based on the ECMWF global analysis data. The assimilated GOME total O_3 fields for 20 June 2001 (c) and 21 June 2001 (d) are additionally shown for comparison with the PV fields. Figure from Zanis et al. [2003].

triggered by mountains and thunderstorm updrafts for example. If air is forced to rise up in stable air, the natural tendency will be for the air to sink back down over time creating a wave pattern. Gravity waves break through setting up either convective or shear instability, generating turbulence and mixing and thus the transport of air parcels from the stratosphere to the troposphere. Lamarque et al. [1996b] have also showed that topographically excited gravity waves that break at the tropopause are responsible of an irreversible downward transport of O_3 from the stratosphere.

2.5 Deep Convection of Tropospheric Ozone and its Precursors

Over polluted continental areas, the transport of O_3 and its precursors, through deep convection, plays an important role for the upper tropospheric ozone budget. Deep convection can also bring O_3-rich air from the lower stratosphere to the troposphere. Early work on the role of convection on the tropospheric O_3 budget showed that the upward transport of O_3 and its precursors can lead to an enhancement of the tropospheric O_3 column over urban areas since the lifetime of these tends to increase with altitude [Pickering et al., 1990]. Recent works show different results, but nevertheless suggest that deep convection plays a significant role in the budget of O_3 in the troposphere. A study by Lawrence et al. [2003] suggests that the upward transport of precursors (primarily driven by the transport of NO_x) is the main source of the increase in the O_3 amount in the troposphere of clean and polluted regions. This effect outweigh the effect of vertical mixing of O_3 itself. On the other hand, a study by Doherty et al. [2005] using a different model suggests the opposite result: the effect of O_3 vertical transport is larger than the effect of precursor mixing changes.

Chapter 3

IASI on MetOp

Satellites provide a variety of data about atmospheric properties. In 1960, TIROS-1, or Television Infrared Observation Satellite, was the first satellite that was capable of remote sensing of the Earth for weather forecasting purposes. Ever since, a variety of different instruments on board of satellites served to improve weather forecasting and our understanding of atmospheric composition.

This chapter will be dedicated to the MetOp satellites and to the IASI instruments on board. Using an online software, *IXION* (http://climserv.ipsl.polytechnique.fr/ixion.html), I will generate time series plots of different properties and introduce some relevant details on the MetOp satellites (Capderou [2012] is used as a reference). In the second part, I will introduce IASI and some of its technical properties, measurements technique and processing levels.

3.1   MetOp Orbit Properties

The MetOp is a series of three polar orbiting meteorological satellites which form the space segment component of the overall EUropean Organisation for the Exploitation of MEteorological SATellites (EUMETSAT) Polar System (EPS). MetOp-A and B were launched on a Soyuz-2-1A (Soyuz-2/Fregat) launch vehicle on October 19, 2006 and September 17, 2012 from the Baikonur Cosmodrome, Kazakhstan. MetOp-A and B operate in a co-planar orbit, 180 degrees out of phase. Metop-C is due to be launched in 2018. The Metop satellites

(with a model shown in Fig. 3.1) carry each a payload of eight instruments for observing the planet, together with a range of communications and support services to provide detailed observations of the global atmosphere, oceans and continents.

Figure 3.1: 1:1 model of the MetOp Satellite.

3.1.1 Inclination and Altitude

Figure 3.2 shows the inclination i and the altitude of MetOp-A over the period 2006-2014. The inclination is measured relatively to the equatorial plane of Earth and defines the nature of the orbit. If i is between 80° and 100° (MetOp is around 98.8^o) the orbit is called (quasi)-polar as the satellite can see both poles of Earth. On the other hand, MetOp, at 817 km, is said to be in Low Earth Orbit (LEO), a nomenclature for satellites with orbits less than 1500 km.

This figure also shows that the inclination and altitude both drift with time, due to atmospheric friction. They are pushed back to the desired values every few months. *NOR* (in the legend, and in all the legends of this section), refers to NORAD, or, the North American Aerospace Defense Command center, giving real radar observations of all orbital properties of satellites that are officially unclassified, and the database source that *IXION* uses.
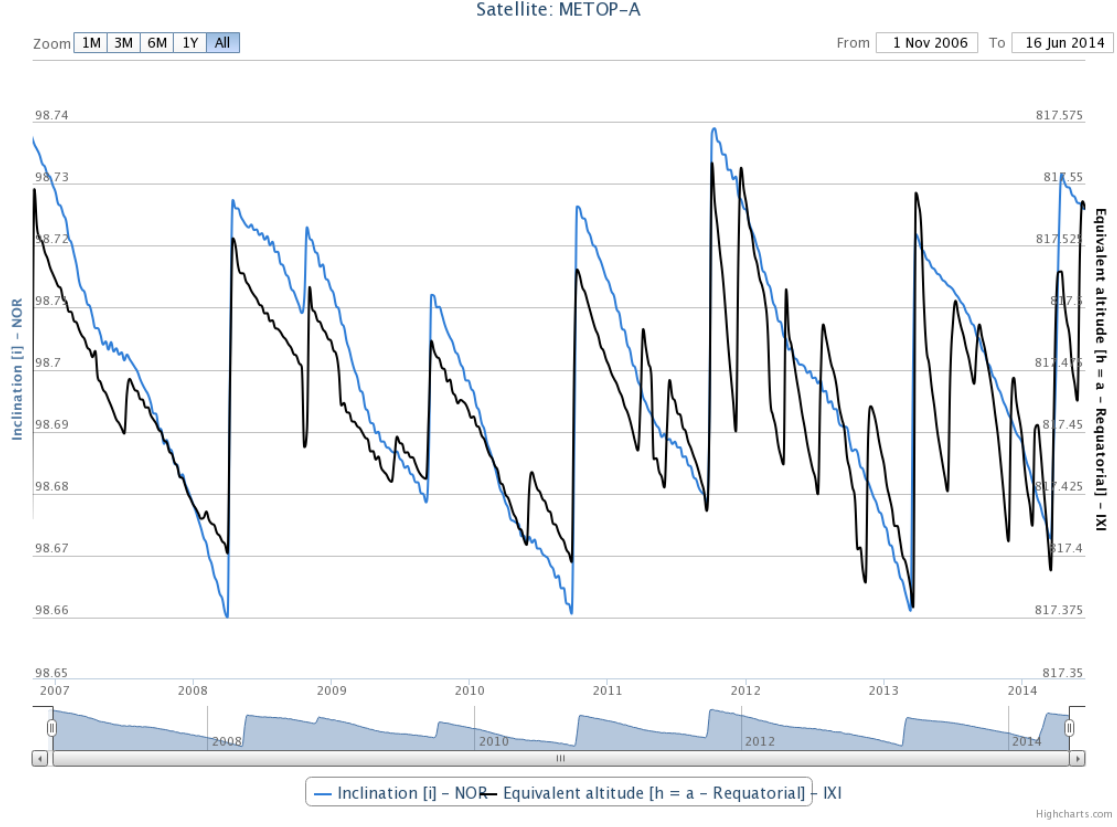
Figure 3.2: Time series of: left axis, MetOp-A inclination (in degrees) and right axis, altitude (in km).

3.1.2 Crossing Time

To understand the crossing time of any satellite, two properties need to be introduced. First, the local time, also call the mean solar time (MST) defined as: MST=UT+$long$/15, where UT is the universal time (at the Greenwich meridian) in hours, and $long$ is the longitude in degrees. Second, the nodes, which are the intersection points between the orbit and the equatorial plane of Earth. Two nodes are defined: the ascending node, the point at which the satellite passes from the Southern Hemisphere to the Northern one, and descending nodes, when the satellite passes from the Northern Hemisphere to the Southern Hemisphere. For MetOp-A, and as Fig. 3.3 shows, the satellite crosses the Equator at around 21:30 local time (or MST). The descending node (not shown here) passes 12 hours later, at 9:30 local time.
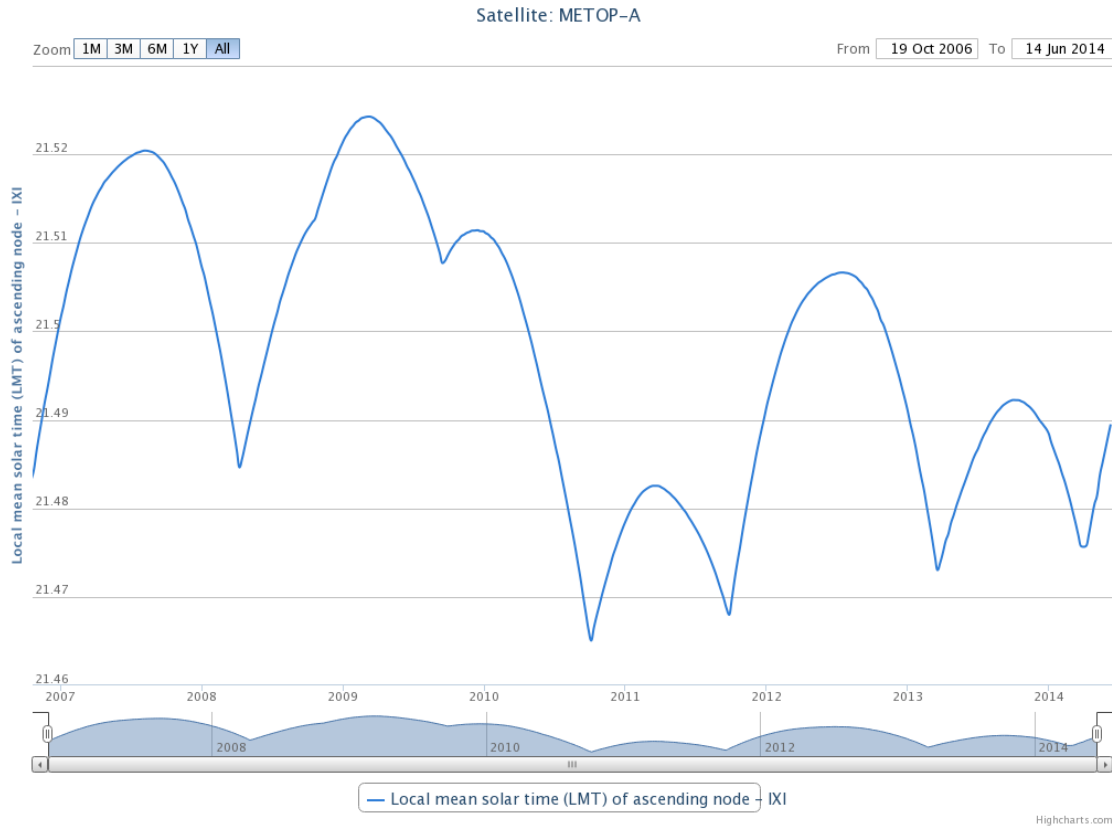
Figure 3.3: Time series of MetOp-A time of ascending node (in mean solar time). Note that the change is small, of amplitude around 5 minutes only.

3.1.3 Anomalistic Period

The anomalistic period is the time that the satellite needs to come back to its perigee (Fig. 3.4). Figure 3.5 shows that the orbit period for the MetOp satellites is approximately 101 minutes (seen on the left axis). This means that during one day, MetOp will perform around 14 anomalistic periods as seen on the right axis of Fig. 3.5. The MetOp mission requires a repeat orbit of 412 revolutions every 29 days.
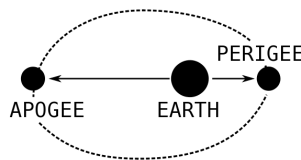
Figure 3.4: Apogee and perigee in an elliptic orbit.
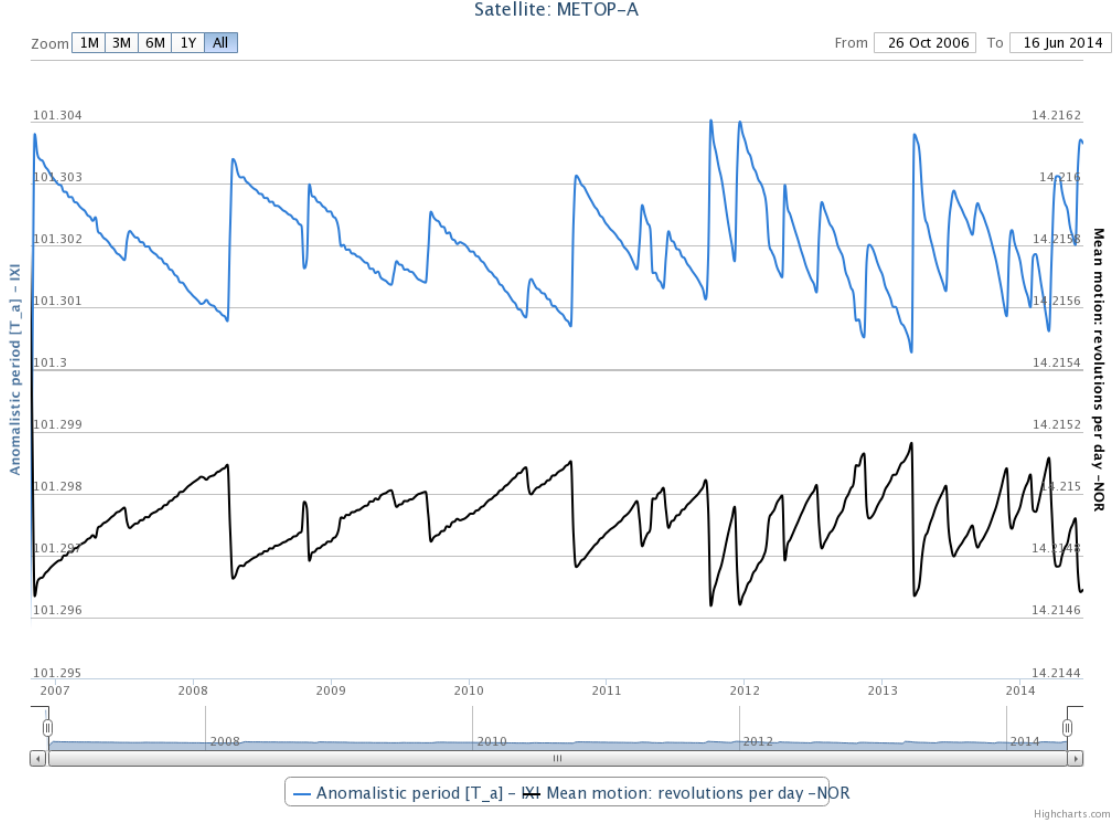
Figure 3.5: Time series of: left axis, MetOp-A time anomalistic period (in minutes) and right axis, number of revolution per day.

3.2   The IASI Instrument

Developed by Centre National d'Etudes Spatiales (CNES) in the framework of a co-operation agreement with EUMETSAT, the IASI instrument (Figs. 3.6 and 3.7) is a key payload element of the MetOp series of European meteorological polar-orbit satellites.

3.2.1   IASI Measurement Technique

Passive IR remote sensing is used for measurement by IASI. It is composed of a precisely calibrated Fourier Transform Spectrometer operating in the spectral range of 3.6 μm to 15.5 μm (645 to 2760 cm^{-1}) associated with an infrared imager operating in the 10.3-12.5 μm region. It is important to note that more often used in spectroscopy is the wavenumber $\nu = 1/\lambda$ in cm^{-1}. The wavenumber notation will be also used in the rest of the this chapter
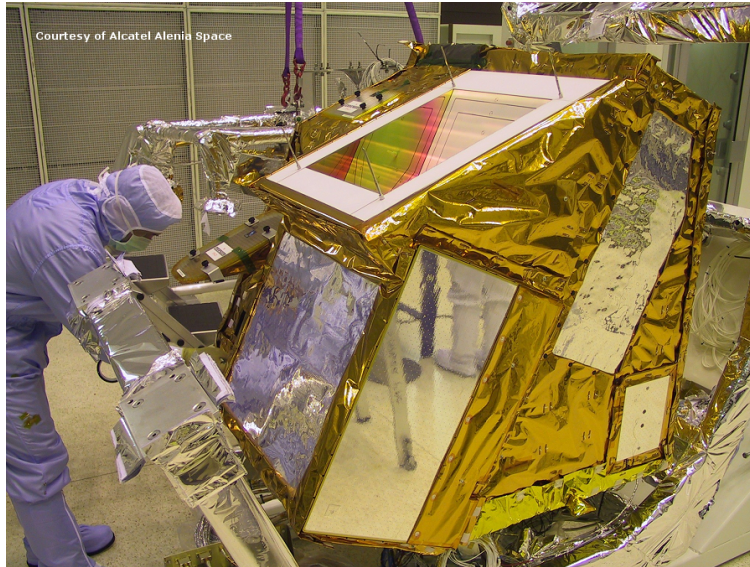
Figure 3.6: The IASI instrument. Figure taken from www.cnes.fr/iasi.

(and thesis). The Fourier Transform Spectrometer is based on a Michelson interferometer, focal planes and cold optics are passively cooled to 93 K; on-board digital processing includes inverse Fourier Transform and radiometric calibration. The integrated infrared imager allows the co-registration of the IASI sounder with the MetOp's imager Advanced Very High Resolution Radiometer (AVHRR) for cloud detection.

3.2.2   The Swath of IASI

The instruments on board of satellites, could have a fixed detector sensor or a moving one. IASI with a moving sensor, uses an *orthogonal* mode of sweeping. This means that the sweeping happens perpendicularly to the movement, as Fig. 3.7 shows. Moreover, IASI orthogonal sweeping happens on both sides of the swath, with 4 simultaneous pixels at a time each with a diameter of 12 km. In total, the whole swath has 120 pixels (30 observations, 15 from each side), meaning we have a full swath width of 2200 km. Fig. 3.7 also shows the swath (or scan) angle of IASI. By definition, this angle is measured between the line of sight from the satellite and the nadir, also called the instrument's Field Of View (FOV). For IASI it is around ± 48.3 degrees and scanned in 8 seconds. Figure 3.8 generated from *IXION* shows how the swath looks like along the IASI track line to sound the Earth atmosphere during half a day. One can see how the swath line (and therefore pixels) are deformed with
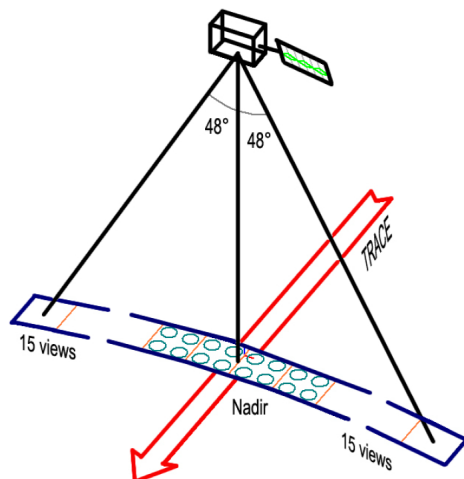
Figure 3.7: IASI observing mode: swath width of around 2200 km, every 50 km at nadir (with 4 footprints of 12 km in diameter). Figure taken from Clerbaux et al. [2009].
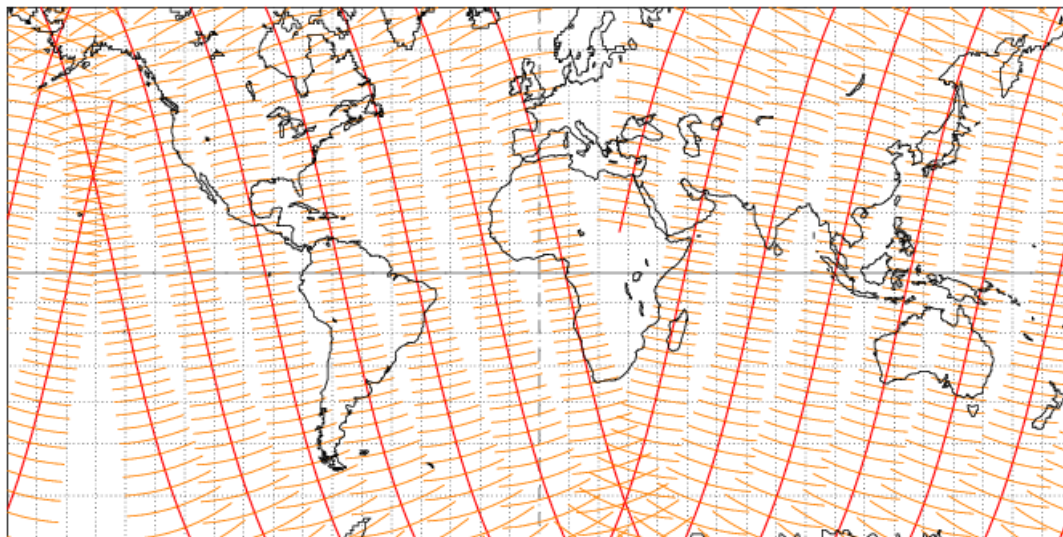
Figure 3.8: Orthogonal swath of IASI/MetOp-A during half a day. One scan per minute represented.

latitude due to Earth's curvature. The figure also shows how a global coverage is achieved twice a day, with some gaps between orbits around the equator.

3.2.3   The Interferometer

In general, the main function of the interferometer, is to create interferograms which will be eventually recorded by a detection unit. In IASI, the interferometer is based on a variant of the Michelson interferometer as shown in Fig. 3.9. The flat mirrors have been replaced by hollow cube-corner reflectors designed to minimize sensitivity to angular measurements. The mobile corner cube shown in the figure, is displaced along the optical axis in order to create a variable optical path difference which is set to be between ± 2 cm. A reference LASER source is also injected into the interferometer to serve as a precise reference indicating the exact value of the optical path difference (OPD). The interferometer's optics are in a thermal enclosure regulated at 20 degrees that is almost decoupled from the rest of the instrument by multi-layers insulation [Simeoni et al., 2004]. The input light (the orange arrow in Fig. 3.9) will hit the separating plate and will be divided into 2 beams which are reflected by the fixed corner cube mirror and the mobile corner cube mirror with the OPD. They both recombine in the receiver and enter the detection system.

3.2.4   Fourier Transform Spectroscopy

The Fourier transform spectrometer does not directly record the spectrum, but instead, its Fourier transform, called the interferogram. During the recombination of the two beams, there is therefore alternately constructive and destructive interference, resulting in the oscillation of the detected signal. By making measurements of the signal at many discrete positions of the moving mirror, the resulting signal, representing the intensity of the radiation as a function of the optical path difference, is the interferogram. For a continuous spectrum, the intensity is given by:

$$I(x) = \frac{1}{2} \int_{-\infty}^{\infty} S(\nu)(1 + cos(2\pi\nu x))d\nu \tag{3.1}$$

x being the OPD and ν the wavenumber ($\nu = 1/\lambda$). The intensity $I(x)$ is then equal to a
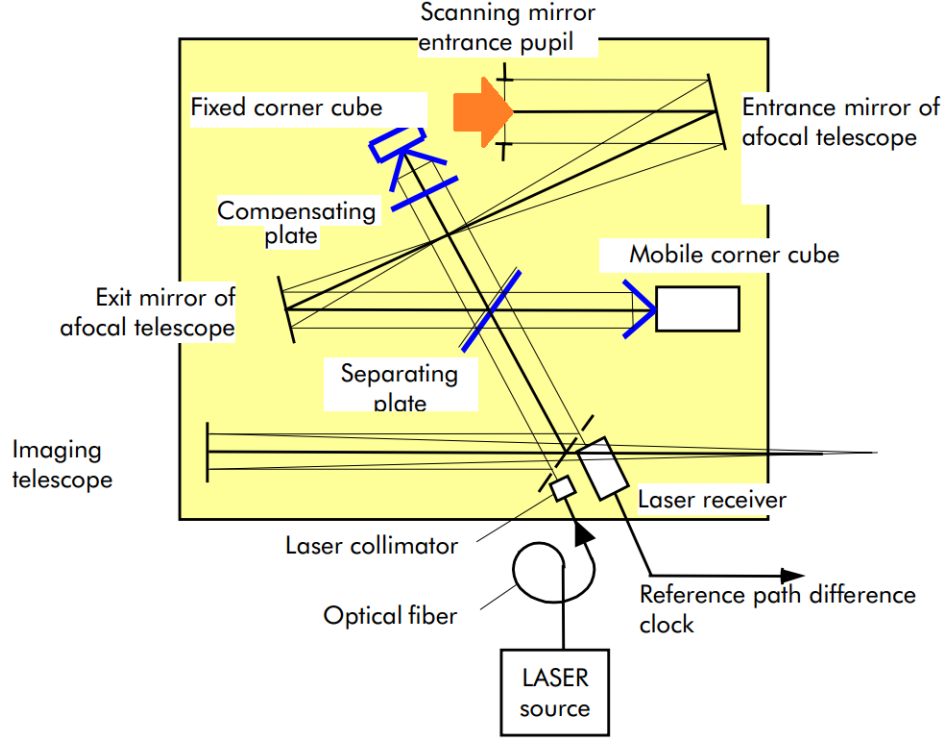
Figure 3.9: Schematic view of the Michelson interferometer of IASI. Figure from [Simeoni et al., 2004].

constant term ($\int S(\nu)d\nu$) and to the real part of the direct Fourier Transform (F) of $S(\nu)$ [1]. The first term is of no use for spectroscopy but the second term can be used to retrieve the spectrum S of the incident light by taking the *Inverse Fourier Transform* as:

$$F^{-1}(I(x)) : \nu \to S(\nu) = \int_{-\infty}^{\infty} I(x)cos(2\pi\nu x)dx \qquad (3.2)$$

In practice, interferograms can only be measured out to finite optical path differences. In this case, the interferogram must be sampled at very stable and regularly spaced known positions of the moving mirror. The sampling is triggered by a reference laser signal clock ("LASER source" in Fig. 3.9) with fixed frequency which is injected in the interferometer beams, and transformed in an electrical signal. It serves as a precise reference indicating the OPD during the motion of the moving mirror. Thus the interferogram is only known for a finite number of discrete values limited by the maximum optical path difference $\Delta L = \pm 2\ cm$

---

1. The Fourier Transform of a function $S(\nu)$ is given by:
$F(S(\nu)) = \int_{-\infty}^{\infty} S(\nu)e^{-2i\pi\nu x}d\nu = \int_{-\infty}^{\infty} S(\nu)(cos2\pi\nu x - isin2\pi\nu x)d\nu.$

allowed by the moving mirror mechanism. The computation used to retrieve the spectrum is thus a Discrete Fourier Transform and as a consequence, the spectrum is known with a sampling $\Delta\nu = 1/(2L_{max}) = 0.25\ cm^{-1}$ and only for wave numbers below the wavenumber of the LASER.

Eq. 3.2 becomes:

$$S(\nu) = \int_{-L}^{L} I(x)cos(2\pi\nu x)dx \tag{3.3}$$

which is equivalent to multiplying Eq. 3.2 by the rectangular (or normalized boxcar) function:

$$\Pi(x) = 1, \quad |x| \le L$$
$$\Pi(x) = 0, \quad |x| > L \tag{3.4}$$

In order to perform the multiplication to solve Eq. 3.3, one should know that Fourier Transform of a product is the convolution of the corresponding transforms. The effect of measuring the interferogram out to finite path differences is thus equivalent to convolving the input spectrum with the Fourier Transform of the rectangular function:

$$\begin{aligned} F(\Pi(x)) &= \int_{-L}^{L} cos(2\pi\nu x)dx \\ &= 2L\frac{sin(2\pi\nu x)}{2\pi\nu x} \\ &= 2Lsinc(2\pi\nu x) \end{aligned} \tag{3.5}$$

The *sinc* function (Fig. 3.10 and panel a, Fig. 3.11) is characterized by a series of secondary lobes (or the phenomena called "ringing") of slowly decreasing amplitude, the amplitude of the first minimum being -21.7% of the main lobe. The full width at half maximum (FWHM) of this function is called the spectral resolution and is equal to 0.603/L. For an ideal Fourier Transform spectrometer, *sinc* is the instrumental spectral response function (ISRF) and it does not change its functional form as ν moves along the wavenumber axis. However, because of the phenomenon of self-apodization, an instrumental effect that is mainly due to the finite extent of the field of view of the spectrometer such as IASI, the ISRF is less than ideal and not wavenumber invariant. IASI's ISRF dependence on the wavenumber is shown in Fig. 3.10.
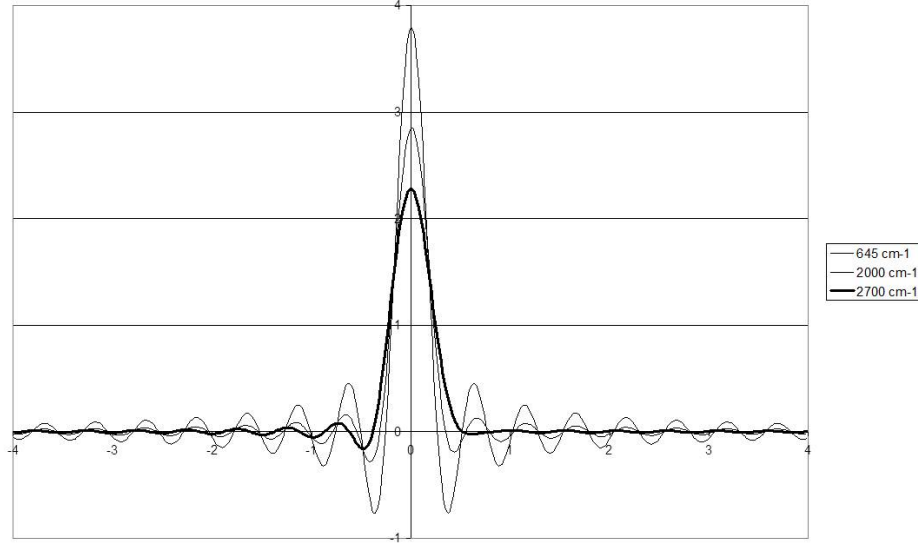
Figure 3.10: IASI instrument spectral response function (ISRF) dependence on the wavenumber. Figure from Tournier et al. [2002].

3.2.5 Apodization

The goal of apodizing is to decrease the amplitudes of the sidelobes associated with the *sinc* function at the cost of increasing the FWHM of the ISRF (i.e., decreasing the spectral resolution). Apodizing is readily accomplished by multiplying the interferogram with an apodizing function. For IASI, the apodization is done with a Gaussian function with half-width at half-height equal to 0.5 cm^{-1} and the effect is seen in Fig. 3.11. The resolution slightly degrades due to apodization, leading to 0.5 cm^{-1} resolution for the apodized spectrum. The resulting spectrum will be closer to the true spectrum than the unapodized spectrum.

3.2.6 Processing Levels

Global data products are categorized according to instrument and product level. For IASI those are as follows:

Level 0

The Level 0 product contains the raw instrument data. It is done on board of IASI then
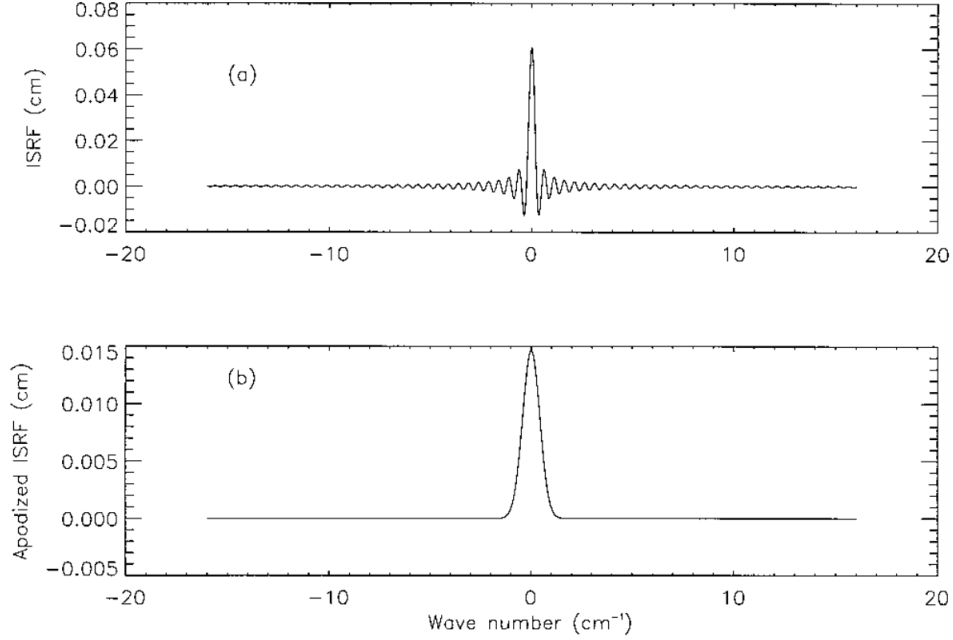
Figure 3.11: Nominal IASI instrumental spectral response function (ISRF) for a (a) the central wavenumber at 650 cm^{-1}. (b) The same function but but after apodization with a Gaussian function with half-width at half-height equal to 0.5 cm^{-1}. Figure from Amato et al. [1998].

transmitted to MetOp. The main function of the on-board processing is to compress and reduce the data rate by from about 45 Mbit/s to about 1.5 Mbit/s. IASI transmits to MetOp the calibrated spectra calculated after the inverse Fourier Transform. The calibration is done by applying proper calibration coefficients allowing the flagging of wrong measurements and merging the three spectral bands (Table 3.1). The resulting signal is then coded and transmitted.

Table 3.1: IASI's three spectral bands.

Band	Wavenumbers (cm^{-1})	Wavelength (μm)
1	645.0 - 1210.0	8.26 -15.50
2	1210.0 - 2000.0	5.00 - 8.26
3	2000.0 - 2760.0	3.62 - 5.00

Level 1a

Spectral calibration and apodization functions are computed. A spectral calibration function is applied to Plank's function on-board and an appropriate correction is applied to the

spectra. Since the internal black body reference source is not exactly unity, a hot black body emissivity function is also applied. The impact of the scanning mirror reflectivity at different angles and its temperature dependency is accounted for. Finally, the correlation between two other instrument onboard Metop, the IASI Integrated Imager (ISS) and Advanced Very High Resolution Radiometer (AVHRR) allows the geo-localization of IASI.

Level 1b

The estimated spectral calibration functions are applied to the spectrum. Calibrated, Earth located and quality controlled products are provided. A resampling of Level 1a data is done on a constant wave number basis ($0.25\ cm^{-1}$). The spectra are finally interpolated on a new equidistant spectral grid by using a cubic spline interpolation.

Level 1c

The IASI Level 1b spectra are apodised using the apodisation function estimated. Level 1C data are used to retrieve level 2 ozone profiles and columns.

Level 2

The objectives of the IASI Level 2 ground processing is the derivation of geophysical parameters from the radiance measurements. The following parameters are derived during IASI Level 2 processing such as the temperature and humidity profiles, surface temperature, surface emissivity, fractional cloud cover, cloud top temperature, cloud top pressure, cloud phase, as well as total and partial columns of trace gas amounts, and processing and quality flags.

Chapter 4

Atmospheric Radiative Transfer and Inverse Theory

The theory of radiative transfer provides the means for describing interaction between radiation which passes on its way to final detection and matter (gases, aerosols, cloud droplets). The thermal infrared radiation emitted from the surface of Earth is therefore attenuated after passing through the Earth's atmosphere, following three key processes: emission, absorption and scattering[1] by atmospheric constituents (corresponding to a redistribution of the radiative energy in all the directions). Under the photon theory of light, a photon is a discrete or quantum bundle of electromagnetic radiation. Photons, like all quantum objects, exhibit both wave-like and particle-like properties. Fig. 4.1 shows the radiation spectrum that can be divided into wavelength regions. We note in particular the infrared region with its three regions: near infrared, mid infrared and far infrared. The mid infrared is known as the thermal infrared, which is the region of interest to this chapter.

In this chapter, I will go through the atmospheric radiative transfer in the infrared range of the spectrum and the inversion undergone to get the vertical profile of temperature and gas concentrations. The explanation presented hereafter are from McCartney [1983], Lenoble [1993], Rodgers [2000], Burrows et al. [2011] and Hurtmans et al. [2012].

---

1. The **infrared** scattering cross-section for molecules is much smaller than the absorption cross-section; such that scattering can be neglected at the wavelengths of interest to IASI, and won't be therefore treated here.
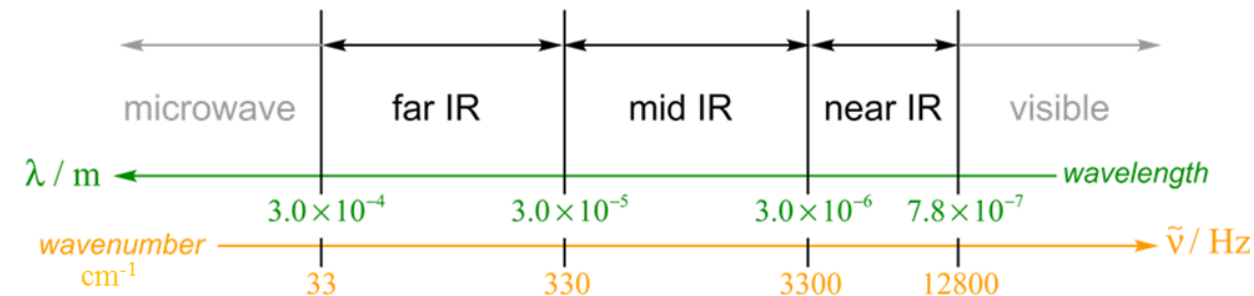
Figure 4.1: Decomposition of the electromagnetic spectrum with a focus on the infrared range.

4.1 Energy Transitions

Depending on the molecule present, every part of the atmosphere absorbs and re-emits infrared photons. The strongest spectral features are due to rotational-vibrational transitions allowed by the quantum selection rules. Quantum mechanics describes electromagnetic radiation as a stream of photons. The energy E of a photon depends on the wavelength of the radiation as follows:

$$E = h\upsilon = hc/\lambda \tag{4.1}$$

So that the energy of the re-emitted or absorbed photon is:

$$h\Delta\upsilon = E_2 - E_1 \tag{4.2}$$

Where υ is the frequency of the radiation and h is the Planck constant $= 6.626$ x 10^{-34} Js. The transition between the discrete internal energy state of atoms or molecules provides the basis for the interaction with electromagnetic radiation. In the thermal infrared, the transitions allowed are called ro-vibrational: each of the normal modes of vibration of heteronuclear diatomic or larger molecules in the gas phase also contains closely-spaced (1-10 cm^{-1} difference) energy states attributable to rotational transitions that accompany the vibrational transitions. A molecule's rotation can be affected by its vibrational transition because there is a change in bond length, so these rotational transitions are expected to occur. Since vibrational energy states are on the order of 1000 cm^{-1}, the rotational energy states can be superimposed upon the vibrational energy states.

4.1.1 Ro-Vibration Selection Rules

When a molecule is vibrationally and rotationally excited (at room temperature), each vibration state splits into a series of ro-vibrational states.

Selection Rules for Vibrational Transition

Vibration of a molecule is treated as harmonic oscillator movement [2], which is quantum mechanically described by the following energy levels:

$$E_n = \left(n + \frac{1}{2} \right) h\upsilon_0 \tag{4.3}$$

Where n denotes the vibrational quantum number or level, and $(1/2)h\upsilon_0$ is the zero point energy of the molecular oscillator. At room temperature, most molecules are in the n = 0 state. Upon absorption of vibration energy, this vibrational quantum number can change by +1 unit. Molecules will absorb in the infrared if they have a permanent dipole moment or if the vibration generates a dipole moment. Thus symmetrical diatomic molecules like nitrogen, oxygen and hydrogen, do not absorb infrared radiation, because they are homonuclear diatomic molecules with no permanent dipole moment and lack a mechanism of interacting with the electric field of the light.

Selection Rules for Rotational Transitions

When the angular momentum of the entire molecule changes, rotational energy states rise. The rotational energy levels are given by:

$$E_j = B \cdot J(J+1) \; with \; B = \frac{h}{8\pi^2\Theta c} \tag{4.4}$$

---

2. To a first approximation, the motion in a normal vibration can be described as a kind of simple harmonic motion. In this approximation, the vibrational energy is a parabola with respect to the atomic displacements and the first state has twice the frequency of the fundamental. In reality, vibrations are **anharmonic** and the first state has a frequency that is slightly lower than twice that of the fundamental. Excitation of the higher states involves progressively less and less additional energy and eventually leads to dissociation of the molecule, as the potential energy of the molecule is more like a **Morse** potential.

J is the rotational or angular quantum number, B is the rotational constant, expressed in cm^{-1}, and Θ is the moment of inertia with respect to the rotation mode.

Rotational transitions occur when:

1- The molecule have a dipole moment (an unevenly distributed charges), and

2- The difference in angular momentum quantum number ΔJ between the initial and final state $=\pm 1$.
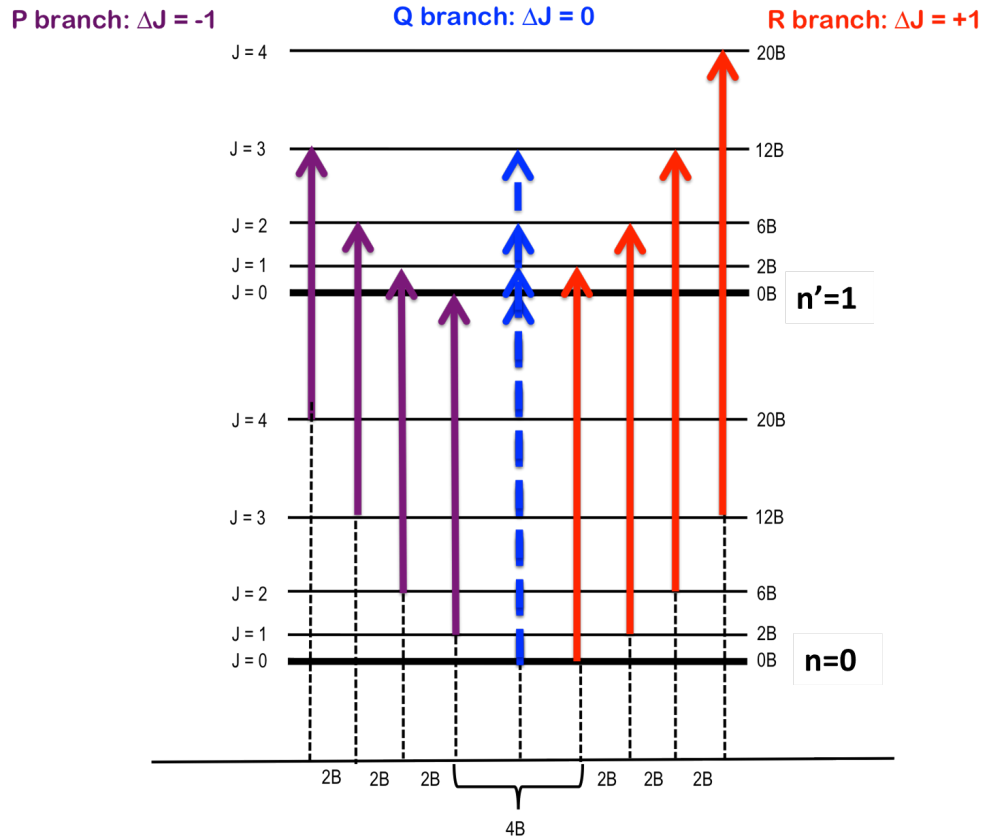
Figure 4.2: Depiction of rotational energy levels, J, imposed on vibrational energy levels, n. The transitions between levels that would result in the P- and R-branches are depicted in purple and red, respectively, in addition to the theoretical Q-branch line in blue.

ΔJ=-1 are called P-branch transitions, ΔJ=+1 R-branch, and ΔJ=0 Q-branch. Given Eq. 4.4, the photon energy ΔE of allowed transitions is:

$$\Delta E_j = E_{j+1} - E_j = B[(J+1)(J+2) - J(J+1) = 2B(J+1)] \tag{4.5}$$

Thus the observed rotational transitions consist of equally spaced lines of difference 2B

as seen in Fig. 4.2. The lines of the P-branch (represented by purple arrows) and R-branch (represented by red arrows) are separated by specific multiples of B (2B). Most molecules are in excited rotational states at room temperature, since these energies are of the order of the thermal kinetic energy of molecules at ambient conditions.

4.1.2 Ro-Vibrational Spectrum of Ozone

The number of vibrations mode is 3N-6 for a molecule of N atoms and 3N-5 for a linear molecule of N atoms (diatomic molecules have one normal mode of vibration). Ozone is a triatomic non-linear molecule and therefore it possesses 3 vibration modes denoted ν_1 (centered at 1110 cm^{-1}), ν_2 (centered at 701 cm^{-1}) and ν_3 (centered at 1042 cm^{-1}). These 3 modes are active in the infrared, with the ν_3 being the strongest with P, Q, and R allowed rotational transitions. The ro-vibrational spectra of O_3 is shown in Fig. 4.3 over the whole absorption spectral bands. In the lower panel, a zoom over the infrared region, in particular that of ν_1 and ν_3.
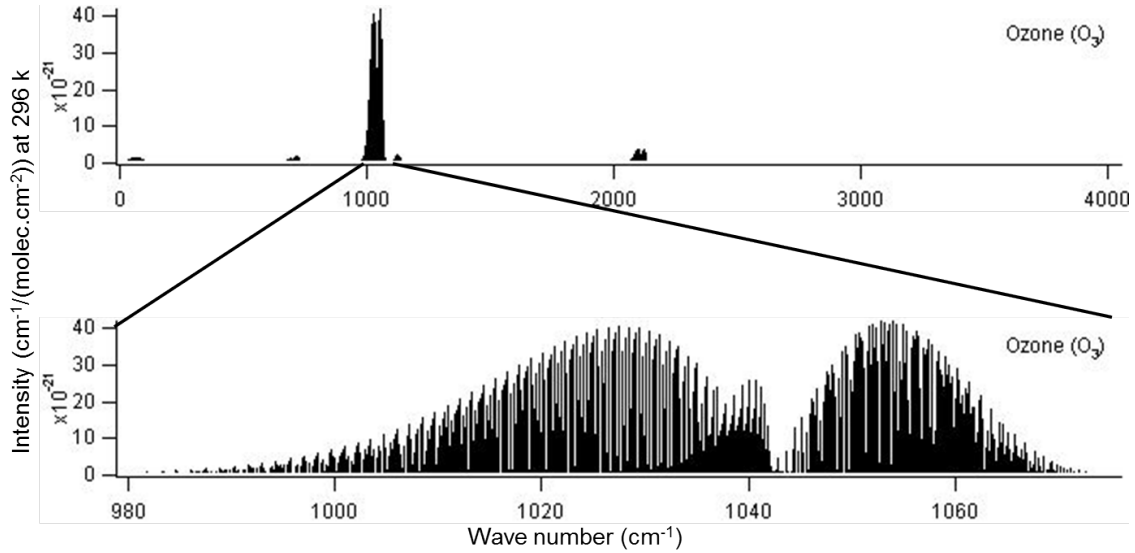
Figure 4.3: Ro-vibrational spectra of O_3 from the HITRAN database with a zoom over the infrared region with v_1, v_3 modes, the latter being the strongest and used in the inversion of O_3.

4.2 Emission

4.2.1 Black Body Emission

The thermal or heat radiating from the Earth's surface or from the atmosphere belongs to the thermal infrared region of the electromagnetic spectrum. The Fourier transform spectrometer of IASI, described in the previous chapter, provides infrared spectra with high resolution between 645 and 2760 cm^{-1}. The Earth's thermal emission is present during the day and the night, giving the advantage to thermal infrared remote sensors. Originally proposed in 1900, Planck's law (Fig. 4.4) describes the electromagnetic radiation emitted by a black body in thermal equilibrium at a definite temperature and is described by:
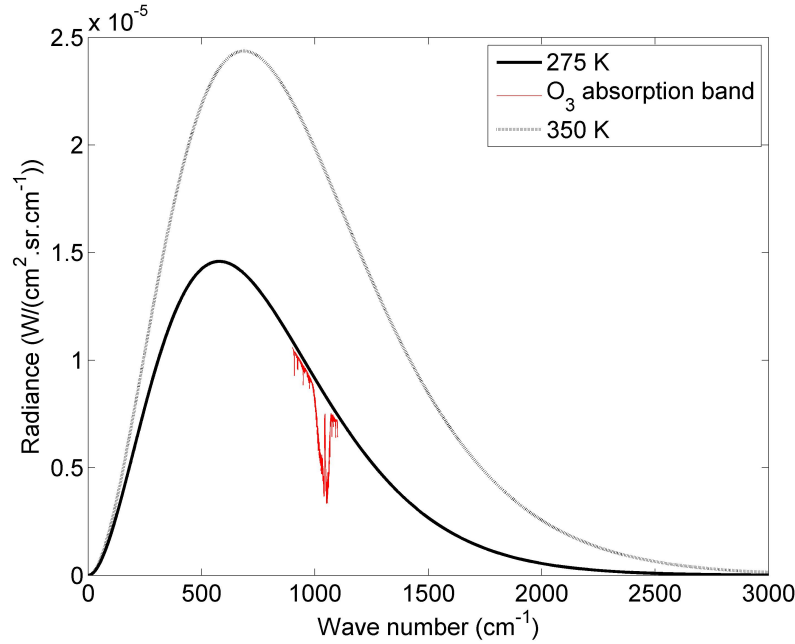
Figure 4.4: Black body emission spectrum at 275 and 350 K. In red, the O$_3$ absorption band location.

$$B_\nu(T) = \frac{2h\nu^3 c^2}{\left(exp\left(\frac{h\nu c}{kt}\right) - 1\right)} \tag{4.6}$$

With, $k = 1.38 \times 10^{-23} J \cdot K^{-1}$ the Boltzmann constant and ν is the wavenumber.

Wien's Displacement Law

Planck's distribution is an increasing function with respect to temperature(T) and is a con-cave function of the wavenumber(ν) as Fig. 4.4 shows. The wavenumber of the maximum (at fixed T) can be found by calculating $\partial B/\partial \nu = 0$, which yields to:

$$\nu_{max} \approx (1.96 \ cm^{-1}/K) \cdot T \tag{4.7}$$

The so-called Wien's displacement law states that when the temperature of a black body increases, the overall radiated energy increases and the peak of the radiation curve moves to higher wavenumbers. One can clearly see the direct relationship between the wavenumber of the peak of the emission of a black body ν_{max} and its temperature in Eq. 4.7 and Fig. 4.4.

Stefan-Boltzmann Law

The Stefan–Boltzmann law, describes the power radiated from a black body in terms of its temperature. This can be achieved by integrating the Planck's function over the entire wavenumber domain, such as:

$$B(T) = \int_0^\infty B_\nu(T) d\nu = \sigma T^4 \ W.m^{-2} \tag{4.8}$$

With,
$\sigma = 2\pi^5 k^4/15c^2h^3 = 5.670373 \times 10^{-8} W \cdot m^{-2} \cdot K^{-4}$. The law basically states that the radiative energy emitted by a black body is an increasing function proportional to the fourth power of the temperature.

4.2.2 Emissivity

Since neither Earth including land and oceans or the atmosphere are perfect black bodies, a correction factor, the emissivity, should be used. Eq. 4.6 is corrected and the radiative energy that is actually emitted by a medium or atmospheric component at temperature T, for a given wavenumber ν is:

$$E_\nu = \epsilon_\nu B_\nu(T) \tag{4.9}$$

Where $B_\nu(T)$ is the black-body Planck function at the ground temperature T, and emissivity ϵ_ν ranges between 0 and 1 (unitless). White snow in forests [3] behaves similarly to a black body, with $\epsilon_\nu \approx 1$. On the other hand, the urban environment has a lower emissivity, with with ϵ_ν between 0.7-0.9 (concrete) and 0.9 for an average urban environment [Jacobson, 2005].

4.3 Absorption

Radiance [4] and spectral radiance are measures of the quantity of radiation that passes through or is emitted from a surface and falls within a given solid angle in a specified direction. It responds to Planck's equation and emits radiation isotropically, in all directions. The portion of radiation absorbed by a uniform gas layer thickness ds in the atmosphere as seen in Fig. 4.5 can be expressed by the Beer-Lambert Law which governs the reduction in the radiance, called L_ν, the at a wavenumber ν.

Beer-Lambert Law

If ds is the gas thickness oriented in the direction of radiation propagation, the evolution of the radiation intensity is given by:

$$A_\nu = k_\nu(s)\rho(s)L_\nu ds = \sigma_\nu(s)L_\nu ds \tag{4.10}$$

$\sigma_\nu = k_\nu(s)\rho(s)$ (in cm^{-1} if s is in cm) is the spectral **absorption or attenuation coefficient** of the gas, where $k_\nu(s)$ is the mass absorption coefficient or opacity, and $\rho(s)$ is the molecular density of the atmospheric component at altitude s.

The change in the radiance of the radiation entering an atmospheric component dL_ν will

---

3. In the infrared, snow is a good absorber and emitter. In the vicinity of a tree, it behaves like a black body: the tree's trunk absorbs the Sun's radiation and emits energy in the infrared that will be partially absorbed by the snow. During absorption, the infrared radiation is converted to internal energy and the snow melts around the tree trunk, producing a small depression that encircles the tree.

4. In French, radiance is called *luminance*, which should not be confused with the English luminance, which is a photometric measure of the luminous intensity per unit area of light traveling in a given direction and is expressed in candela per square meter (cd/m^2).

be equal to the emission from it E_ν defined in Eq. 4.9 along the path ds minus the absorption A_ν defined in Eq. 4.5, namely:

$$dL_\nu = \epsilon_\nu B_\nu(T) - k_\nu(s)\rho(s)L_\nu ds \qquad (4.11)$$
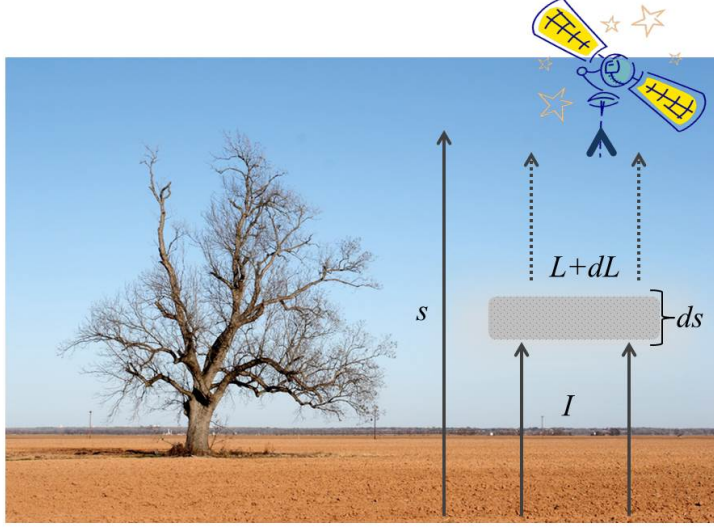
Figure 4.5: Nadir remote sensing illustration of an incident radiation traversing the atmosphere.

Kirchoff's Law

Kirchhoff's law of thermal radiation (1859) connects the absorptivity and the emissivity of a medium (here the atmospheric gas) at local thermodynamic equilibrium[5] as:

$$\epsilon_\nu = \rho k_\nu ds$$

---

5. Local Thermodynamic Equilibrium (LTE) means that over time scales of interest, all independent degrees of freedom in the system are in equilibrium with each other. The atmosphere, in particular the troposphere and lower stratosphere, could be thought as in local thermal equilibrium where collisions are numerous. For a medium in LTE, the emission coefficient and absorption coefficient are functions of the kinetic temperature, as defined by the Maxwell-Boltzman equation, and density only.

4.4   Radiative Transfer Equation and the Direct Problem

The full equation of radiative transfer simply says that as a beam of radiation travels, it loses energy to absorption, gains energy by emission, and redistributes energy by scattering (not considered in infrared region). At local thermodynamic equilibrium and taking into account the absorption and emission of the radiation found in previous sections, the evolution of the radiance could be re-written as:

$$\frac{dL_\nu}{ds} = \rho k_\nu(s)(B_\nu(T) - L_\nu) \tag{4.12}$$

Equation 4.12 couples emission and absorption and is the differential form of the radiative transfer equation in the infrared.

The solution of Eq. 4.12 is given in Eq. 4.13. Since Earth's infrared radiation propagates from the bottom to the top of the atmosphere, the temperature T is a function of the altitude. We therefore get the complete form of the radiative transfer equation, also called as the Schwarzchild's Equation:

$$L_\nu(\theta, s) = L_\nu(\theta, 0)Tr_\nu(\theta, 0, s) + \int_0^s B_\nu(T)\frac{\partial}{\partial s'}Tr_\nu(\theta, s', s)ds' \tag{4.13}$$

Tr is the transmittance, which is defined by:

$$Tr(s, \theta) = e^{(-\int_{s'}^{s} k_\nu(s'')\rho(s'')ds'')} \tag{4.14}$$

I introduced in Eq. 4.13 the dependence of the radiation received by the instrument on the satellite on the ground zenith angle (Fig. 4.6). In fact, the path s depends on the zenithal angle of the beam and Earth's curvature. Parallel plane approximation [6] could be applied for IASI observations at nadir where properties depend only on altitude, but for large viewing angles, as for IASI's field of views, the sphericity of the Earth should be taken into account.

In the first term $L_\nu(\theta, 0)$ is the radiance at the Earth's surface at ν with a ground zenith angle of θ and is calculated as follows:

---

6. The flat-Earth (or, the plane-parallel) model of the atmosphere is satisfactory near the zenith/nadir (Fig. 4.6) where ds is equal to $sec(\theta)$.
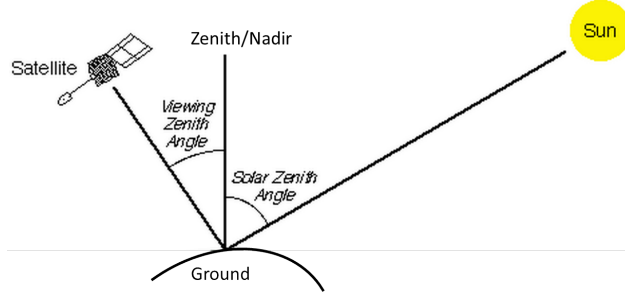
Figure 4.6: Viewing (ground) zenith angle and the solar zenith angle.

$$L_\nu(\theta, 0) = \epsilon_\nu B_\nu(T_{skin}) + (1 - \epsilon_\nu)L_{down} + \alpha_\nu L_{down} \qquad (4.15)$$

Where $B_\nu(T_{skin})$ is the ground black-body Planck function at the ground temperature T_{skin}. The rest of the terms take into account the reflected thermal radiation: assuming reflection by a Lambertian surface, L_{down} is the mean radiance associated to the total downward flux reaching the surface at the wavenumber ν, integrated up on all the geometries; and the last term $\alpha_\nu L_{down}$ is the fraction of sunlight that is retro-reflected in the direction of the sounding beam, which depends on the sun azimuthal angle and the surface effective reflectivity α_ν.

The second term of equation 4.13 (in the integral) is composed of 2 decoupled terms, one a function of the vertical distribution of temperature (T) through the Planck's function, and the second a function of the absorption coefficient associated with the density profile of the relevant absorbing gases. If all of these geophysical parameters in this equation are found, the radiance can be then calculated for every wavenumber. This is called the direct problem.

One should note here that all this formulation was done using a specific ν, i.e. for a monochromatic light. To integrate over all the spectral domain, the transmittance should be known across the spectral domain of interest to the sensor measurement.

4.4.1   The IASI Atmospheric Spectra

Figure 4.7 shows an example of normalized radiance spectrum (normalized with Plank's function) measured by IASI in the infrared range with a spectral resolution of $0.5 \ cm^{-1}$. The brightness temperature on the y-axis is defined as the temperature a black body would be in order to produce the radiance perceived by the sensor. The brightness temperature is

obtained by applying the inverse of the Planck function to the measured radiation.
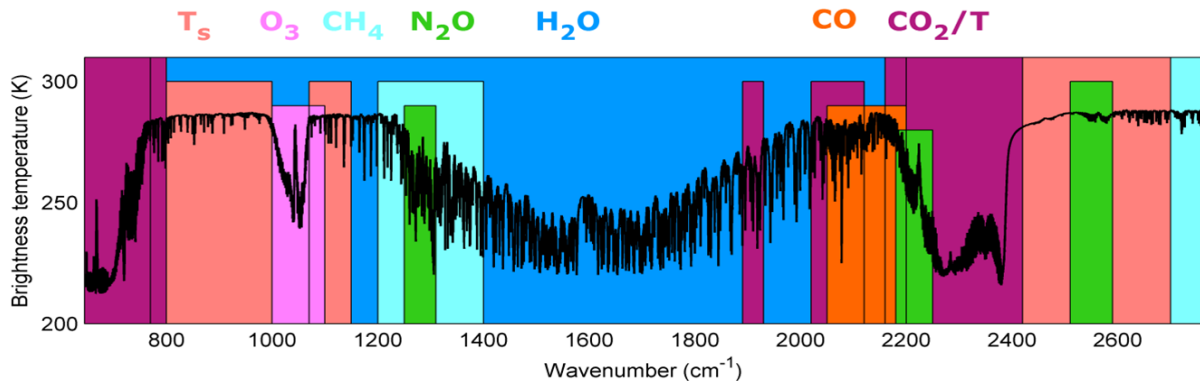
Figure 4.7: The recorded radiance spectra of IASI. It exhibits signatures associated with spectroscopic absorption/emission lines of molecules present along the optical path between the Earth's surface and IASI, from which geophysical data such as temperature profiles and atmospheric concentrations can be derived in selected spectral windows.

This spectrum, assuming an Earth temperature of around 288 k, contains the spectral signatures of many atmospheric molecules. One can notice the water vapor absorption band covering most of the spectral range. The absorption bands of CO_2, CH_4, O_3, CO, N_2O are also easily identified. Lower spectral signatures (not shown on the figure) corresponding to the absorption of HNO_3, OCS, CFC-12, CFC-11, SO_2, PAN, NH_3, CH_3OH, HCOOH and C_2H_4 could also be detected. Some of these molecules can only be detected above emission sources or plumes such as SO_2 in the vicinity of volcanoes [Clarisse et al., 2012] and volatile organic compounds such as HCOOH, CH_3OH, C_2H_4, and the PAN in the vicinity of biomass burning [Coheur et al., 2009]. Nitric acid (HNO_3) can be also detected as shown by Wespes et al. [2009, 2012]. The absorption band of O_3 is better highlighted in Fig 4.8.

Figure 4.8 represents a part of the IASI spectrum where the atmospheric O_3 absorbs. The morning and the evening spectra show the effect of diurnal change in temperature on the IASI retrieved brightness temperature.

4.4.2 Spectral Features

Absorption lines are characterized by three spectroscopic parameters: position, width and intensity.
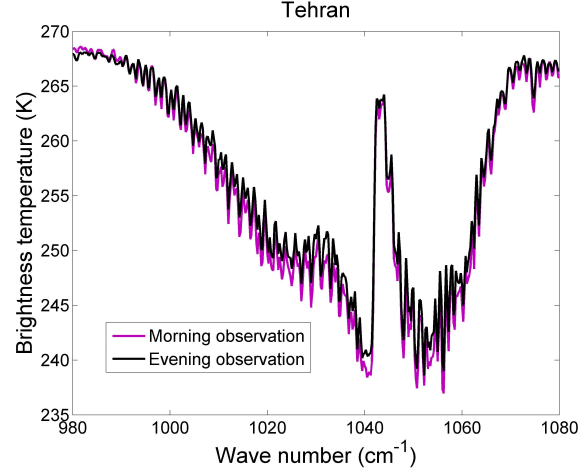
Figure 4.8: Clear-sky IASI radiance spectra around the intense ozone absorption band at $9.6\mu m$ (1040 cm^{-1}) recorded over Tehran on the morning and evening of 01/01/2011.

Position   Each molecule is characterized by its spectral absorption line(s) determined by the energy step of the rotational-vibrational transitions of Eq. 4.2.

Width   Observed spectral lines are always broadened, partly due to the finite resolution of the spectrometer and partly due to intrinsic physical causes. The principal physical causes of spectral line broadening in the IR are Doppler and pressure or collisional broadening which depend on pressure and temperature. Since these vary at the different altitude, this is where the height information on the concentration of the retrieved species at different altitudes comes from. More information on broadening effects can be found in Appendix B.

Intensity   corresponds to the integrated area under the spectral absorption line, directly related to the absorption coefficient and therefore to the availability and concentration of the molecule. For large heavy molecules (such as PAN, methanol, CFC11 and CFC12), single line parameters fail to represent very dense spectral features. Heavy molecules have large moments of inertia, therefore the spacing between ro-vibrational lines of heavy molecules is very small, and the band structure is a blending of numerous individual spectral features. For gases whose line parameters are not yet available, cross-sections derived from laboratory spectra measurements at different atmospheric pressures and temperatures are used.

4.5   Retrieval Algorithm

To derive the vertical profiles, one should start by analyzing the atmospheric radiance. This is called the **inverse problem**. Given the non-linearity of the radiative transfer equation, relating the gaseous concentration profile to the spectral radiance is not an easy task. The density values are hidden in the exponent of an integral which is further complicated by the spectral integration. Because of these complications, retrieval of the gaseous density profile is very difficult. Statistical and numerical assumptions should be taken into account (that is why this inverse problem is called ill-posed).

In this work, I use the Fast Optimal/Operational Retrieval on Layers for IASI (FORLI), a dedicated radiative transfer and retrieval software for IASI. Currently, it is used to retrieve O_3, HNO_3 and CO. In this work, I will focus on the FORLI-O_3 retrievals and product. It was developed at the Université Libre de Bruxelles (ULB; Hurtmans et al. [2012]) in collaboration with LATMOS, with the objective to provide global concentration distributions of atmospheric trace gases in near real time. To solve the radiative transfer equation, the atmosphere is discretized into layers of 1 km width, so that the whole atmosphere can be described by N levels from the surface to the top of the atmosphere (TOA). For each layer, average parameters (e.g. of temperature and pressure) are computed. For the inversion step, it relies on a scheme based on the widely used Optimal Estimation theory [Rodgers, 2000].

4.5.1   Look-up Tables for Fast Calculation

In FORLI, and to speed up the radiative transfer calculation, the line by line integrated absorption sections are pre-calculated at various temperatures and pressures and then stored in tables (also known as the *Look Up Tables* or LUTs) for future reference. In FORLI, the LUTs are computed using The HIgh resolution TRANsmission (HITRAN) spectroscopic database version 2004, with updates up to 2006 [Rothman et al., 2005]. The spectral range for LUTs used in FORLI is 960-1075 cm^{-1} for O_3. One should note here that in addition to modeling individual spectral lines and absorption cross sections in FORLI, special care is taken to account for *absorption continua* of molecules most importantly those of H_2O and CO_2. These are slowly varying components of absorption that are present, though with

lesser atmospheric importance, in the absorption bands. In many atmospheric applications (in weather forecasting and climate prediction models, and in remote sensing applications), an adoption of a semi-empirical representation of the continuum is used. FORLI uses that of Clough et al. [2005].

4.5.2   Auxiliary Parameters

Temperature and Pressure Profiles

In order for atmospheric temperatures to be determined by measurements of thermal emission, the source of emission must be a gas of known and uniform distribution. Otherwise, the uncertainty in the abundance of the gas will make ambiguous the determination of temperature from the measurements. There are two gases in the Earth's atmosphere which have uniform abundance, and which also show emission bands in the spectral regions that are convenient for measurement. Oxygen, a major constituent satisfies the requirement of a uniform mixing ratio and has a microwave spin-rotational band and carbon dioxide (CO_2), which has infrared vibrational-rotational bands and is used in thermal emission spectrometers such as IASI to measure temperature. The detailed absorption characteristics of CO_2 in the infrared region are relatively well-understood and its absorption parameters are well known. Consequently, the measurements of the upwelling radiance in the CO_2 absorption band contain information regarding the temperature values. The temperature and pressure profiles are used as state parameters in FORLI and are retrieved from IASI level 2 data (discussed in the previous chapter) by the operational processor [Schlüssel et al., 2005], and disseminated in near-real-time through the EUMETCast system [7], including ground temperature and relative humidity profiles.

Fractional Cloud Cover

The cloud detection is performed with three concurrent cloud detection methods using AVHRR collocated cloud mask, the NWP forecasts and IASI measurements. In these IASI L2 Version 6 products, the cloud characterization solely comes from the exploitation of IASI

---

7. EUMETCast is a multi-service dissemination system based on standard Digital Video Broadcast (DVB) technology. It uses commercial telecommunication geostationary satellites to multi-cast files (data and products) to a wide user community. EUMETCast also delivers a range of third-party products.

measurements, through the CO_2-slicing method and chi-square methods used to estimate the fractional cloud cover and the cloud top pressure for the IASI IFOVs. The CO_2-slicing method is based upon a fixed, pre-selected number of CO_2 channels and a reference channel. The effective cloud amount is estimated from the radiance within a window channel and by making use of the previously-retrieved cloud top pressure. The chi-square method is described in [August et al., 2012]. In FORLI, the cloud cover is used as an input parameters and a threshold is specified for the different molecules with 13% for O_3. These numbers were chosen after a series of tests, which have shown that scenes below this threshold could be treated as cloud free without significant impact on the column retrievals. Above this value, a more specific treatment of clouds would be needed and data are disregarded for the moment.

Emissivity and Orography

For oceans, a single standard emissivity is used. For continental surfaces, a wavenumber dependent surface emissivity ϵ_ν is considered. FORLI uses a climatology built by Zhou et al. [2011], and the MODIS climatology of Wan [2008]. Orography in FORLI is based on the GTOPO30 global digital elevation model accessible online.

One should note here that errors from all these input parameters are propagated in the FORLI trace gas product error.

4.5.3 Forward Radiative Transfer

Given the general radiative transfer equation derived previously, the measurement y can be expressed as the vector of measured radiances. The direct radiative transfer equation can be then written as:

$$y = F(x, b) + \eta \tag{4.16}$$

y is the measured vector of radiances: it refers to the quantities actually measured in order to retrieve x.

F is the forward radiative transfer function, with x being the vector of atmospheric states, for example, the trace gas concentration at different altitudes. b represents all the other fixed

parameters influencing the measurement (temperature, pressure, instrumental parameters...), which are known to some accuracy, but are not intended as quantities to be retrieved. η includes forward model error, and the measurement or detector noise or random error, since measurements are made to a finite accuracy.

4.5.4 Optimal Estimation

The inverse problem of getting x in Eq. 4.16 is solved in FORLI using the widely used Optimal Estimation method which relies on finding an optimal solution of a state vector denoted $\hat{x}$ (the circumflex indicating an estimated quantity rather than a true state), starting from relevant *apriori* information (a certain prior knowledge of the atmospheric state), composed of a mean state x_a. The measured radiances y are combined with the *apriori* state x_a and both are weighted by covariance matrices, S_a(n x n)[8], the covariance matrix of x_a, associated with an independent set of data used to generate the *apriori* state x_a, meant to represent the natural variability of the gas considered. The elements of this covariance matrices can be expressed as follows:

$$S_a(i,j) = E[(x_i - x_{a,i})(x_j - x_{a,j})] \tag{4.17}$$

Where E is the expected value operator[9].

Table 4.1: Summary of the input parameters used to construct x_a, S_a and $\bar{S}_\eta$ in FORLI-O$_3$.

	FORLI-O$_3$
$\Delta\nu_{LUTs}(cm^{-1})$	960-1075
$\Delta\nu_{retrieved}(cm^{-1})$	1025-1075
x_a, S_a	McPeters/Labow/Logan ([McPeters et al., 2007])
$\bar{S}_\eta(W/(cm^2cm^{-1}sr))$	2x10^{-8}

Table 4.1 shows that the spectral range used to retrieved O$_3$ is $\Delta\nu_{retrieved}$=1025-1075 cm^{-1}. The IASI-O$_3$ spectra over this region can also be seen in Fig. 4.8. This range is mainly dominated by O$_3$ line signature, with few water lines of moderate intensity and a small

---

8. The covariance matrix is often also called variance-covariance matrix, to stress the variance, i.e. the diagonal elements of S_a.

9. The expected value is a key aspect of how one characterizes a probability distribution. The expected value is also known as the expectation, mathematical expectation, EV, mean, or first moment.

contribution of methanol. The *apriori* covariance matrix S_a is constructed from a climatology of O_3 profiles which combines long term satellite limb measurements and measurement from ozonesondes. $\bar{S}_\eta$ is the approximate average noise in the retrieval spectral range and has an average value of 2 x 10^{-8} $W/(cm^2 cm^{-1} sr)$, which is close to the IASI instrumental noise.
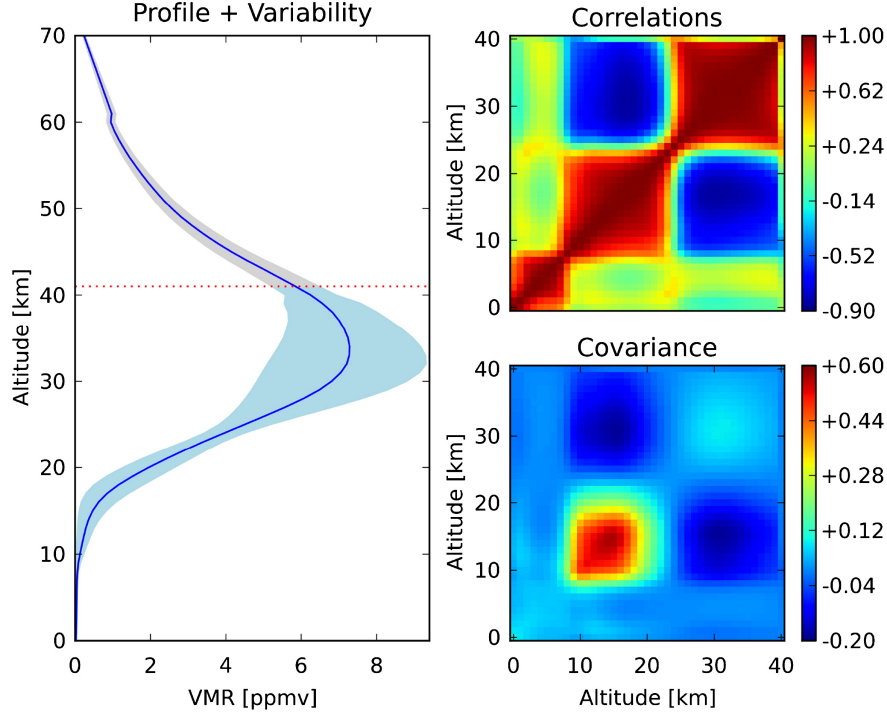
Figure 4.9: Left: Global O_3 *apriori* profile (blue line) with its variability (shaded blue, square root of the diagonal elements of the O_3 *apriori* covariance matrix). Right: correlation and global O_3 *apriori* covariance matrix constructed from climatology O_3 profiles. Figure from Hurtmans et al. [2012].

Figure 4.9 shows the profile of the *apriori* x_a with its associated variance in shaded blue. This profile is fixed and is unique for all the globe. From the surface up to around 10 km, one can notice how the profile changes slowly and reaches its maximum in the middle stratosphere. S_a on the right, is associated to x_a. It represents the allowed variability around the *apriori* profile during the inversion. The variability or the square root of the variance on the diagonal elements is the highest in the UTLS region (0.6 or 60%).

4.5.5 Linear and Non-Linear Inverse Problems

A problem is called linear problem when the forward model can be put in the form $y = F(x) + \eta = Kx + \eta$, and any *apriori* is Gaussian. The retrieved state solution $\hat{x}$, solution of the Optimal Estimation is given by:

$$\hat{x} = x_a + (K^T S_\eta^{-1} K + S_a^{-1})^{-1} K^T S_\eta^{-1}(y - Kx_a) \tag{4.18}$$

$\hat{x}$ is then the best estimation of x. It is a linear function of x_a and y. K is the Jacobian of the forward model function F. It represents the matrix of measurement sensitivity to model parameters.

In fact, very few practical problems are linear. In our problem, the solution of the inverse radiative transfer is moderately non linear and hence the problem can be linearized to a certain extent. In a non-linear case, as in a linear case, the solution is to find the best estimate $\hat{x}$ and its associated error. In order to do so, Eq. 4.18 is iteratively repeated using a Gauss-Newton method until convergence is achieved as follows:

$$x_{i+1} = x_a + (K_i^T S_\eta^{-1} K_i + S_a^{-1})^{-1} K_i^T S_\eta^{-1}[y - F(x_i) + K(x_j - x_a)] \tag{4.19}$$

The Gauss-Newton method consists of linearizing, at each iteration $i + 1$, the non-linear problem in the vicinity of the solution of the previous iteration i. The convergence can be achieved by imposing a maximum limit for the difference between $x_{i+1} - x_i$. After convergence, the covariance matrix can be found in exactly the same manner as in the linear case.

4.5.6 The Averaging Kernels

Let us consider the general case of a vector y with m degrees of freedom. The most probable state in the Gaussian linear case is the one which minimizes

$$\chi^2 = (x - x_a)^T S_a^{-1}(x - x_a) + \eta^T S_\eta^{-1} \eta \tag{4.20}$$

Where $\eta = y - Kx$. The minimum of Eq. 4.18 is at:

$$\hat{x} - x_a = (K^T S_\eta^{-1} K + S_a^{-1})^{-1} K^T S_\eta^{-1} (y - K x_a) = G(y - k x_a) \tag{4.21}$$

Where G is defined as:

$$G = (K^T S_\eta^{-1} K + S_a^{-1})^{-1} K^T S_\eta^{-1} \tag{4.22}$$

G is called the gain matrix, or contribution function matrix. The averaging kernels matrix is defined as:

$$A = GK = (K^T S_\eta^{-1} K + S_a^{-1})^{-1} K^T S_\eta^{-1} K \tag{4.23}$$

For a linear model, $y = Kx + \eta$. Replacing y and G in the retrieved state of a linear problem (Eq 4.18) we get:

$$\begin{aligned} \hat{x} &= x_a + G(Kx + \eta - K x_a) \\ &= Ax + (I - A)x_a + G\eta \end{aligned} \tag{4.24}$$

Where I is the identity matrix. The averaging kernel matrix A is a very useful quantity which plays a significant role in various descriptions of the information content. It represents the sensitivity of the retrieval to the true state. Eq. 4.24 shows that the retrieved profile at each altitude is the true profile weighted by the sensitivity, i.e. the averaging kernels at that altitude (the row of A). Figure 4.10 shows in panel (a), the ideal case of an observation. The different colors depict the different altitudes. In the ideal inverse method, A would be a unit matrix and the real profile would be exactly that retrieved from the instrument measurement. In panel (b), a more realistic situation where the instrument's observation is sensitive only over a certain altitude. Since different instruments have different sensitivities, in reality, each row of A is a function, with a peak at a certain level indicating the altitude of maximal retrieval sensitivity, with a half-width equal to the spatial resolution of the instrument. The plot shows that there is little or no sensitivity towards the surface. At this altitude all/most of the information comes from the *apriori*. On the other hand, the averaging kernels in the lower troposphere (surface, 850 and 700 hPa) peak towards 500 hPa (~ 5 km).
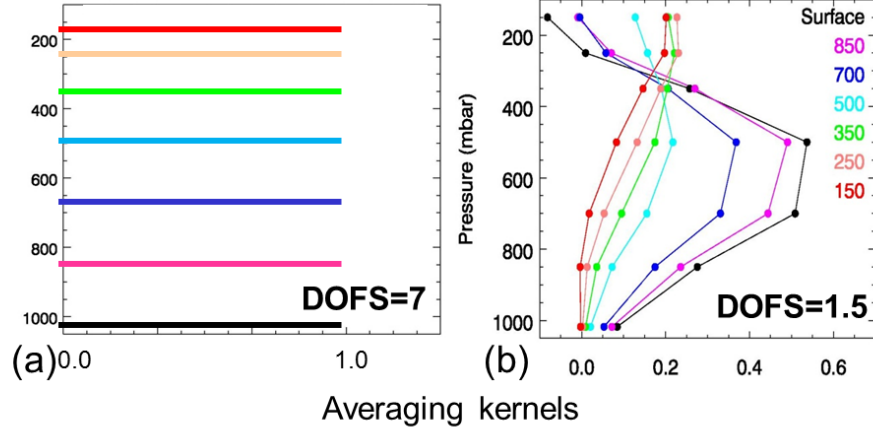
Figure 4.10: Averaging kernels function for (a) an ideal observation case and (b) a more realistic observation where the DOFS are =1.5.

4.5.7   Degrees of Freedom for Signal

The degree of freedom is defined as the number of independent pieces of information in a retrieval, more precisely how many of those are related to the signal. At the minimum, the expected value of χ^2 (Eq. 4.20) is equal to the number of degrees of freedom (or the number of m independent measurements), which can be divided into two parts: degrees of freedom for signal, and degrees of freedom for error. The first term can be described as:

$$DOFS = E[(x - x_a)^T S_a^{-1}(x - x_a)] \qquad (4.25)$$

Thus the DOFS term is attributable to a state vector and is a measure of information as can be seen in Fig. 4.10: it describes the number of useful independent quantities there are in a particular retrieval of a measurement. It could be a positive decimal or integer.

Rodgers [2000] shows that the relationship between the DOFS and the averaging kernel matrix is given by:

$$\begin{aligned}
DOFS &= tr(S_{\hat{x}} S_a^{-1}) \\
&= tr[K^T S_\eta^{-1} K + S_a^{-1})^{-1} K^T S_\eta^{-1} K] \\
&= tr(GK) \\
&= tr(A)
\end{aligned} \qquad (4.26)$$

Chapter 5

Tropospheric Ozone from IASI

After introducing the ozone chemistry in the troposphere, the remote sensing of atmospheric composition from space, and the methods used to retrieve concentrations of trace gases in the previous three chapters, this chapter will provide an overview and a general summary on what can be accomplished by IASI for O_3 measurement. In this thesis, I do not show any validation of the IASI profiles and partial column products. This has been accomplished before by our group at LATMOS as well as by others. Comparison between FORLI-O_3 and ozonesondes is shown in Table 5.1. The comparison shows a good agreement in the troposphere and middle stratosphere ($<$30 km) at mid-latitudes and tropics, where the differences are lower than 10% on average. However, at high latitudes, a significant positive bias is found both for the [0-8] km column (-25 to -15 %) and for profiles between 10 and 25 km (about 10-26%).

In this chapter, I will show and analyze the tropospheric O_3 product from IASI-A and IASI-B and use each of the two products separately or combined and look at tropospheric O_3 variability over different regions. I will also compare the IASI-A and IASI-B products globally and locally. To support my analysis, I use the ERA-interim reanalysis to retrieve wind pattern and the IASI-L2 temperature profile product to analyze surface temperature and thermal contrast and their effect on the retrieval. The different sections might be somewhat disconnected from one another, as this chapter gathers all the unpublished information and small analysis and studies done during my thesis. More focused and extended studies will be presented in the following 3 chapters.

Table 5.1: FORLI-O_3 and ozonesondes bias at different latitudes for different partial columns and profiles. Data are from Dufour et al. [2012][1], Pommier et al. [2012][2], Gazeaux et al. [2012][3], Scannell et al. [2012][4].

	Mid-latitudes[1] (in %)		Tropics[1] (in %)		High-latitudes (in %)	
Partial columns	$[0-6]$km	-8±16.6	$[0-8]$km	-6.7±10.6		
	$[0-11]$km	1.6 ±15.3	$[0-16]$km	3.6±9.2		
	$[8-16]$km	10.6±15.1	$[11-20]$km	13.5±15.6	$[0-8]$km[2]	-25 to -15
	$[16-30]$km	2.4±5.4	$[16-30]$km	5.7±5.8		
	$[0-30]$km	3.3±5.1	$[0-30]$km	4.7±5.4		
Profiles					$[0-10]$km[3]	<10
					$[10-25]$km[3]	10 to 26
					$[25-40]$km[3]	<10
					$[0-40]$km[4]	<30

5.1 Retrievals from IASI-A and IASI-B

Before looking at the O_3 product, I will show first the spatio-temporal probing of the atmosphere by IASI, then discuss the sensitivity of the O_3 vertical distribution to these spatial and temporal variations.

5.1.1 Number of Observations per Day

In order to know how many times IASI will "see" a specific location on Earth per day, I plot in Fig. 5.1 the number of O_3 observations seen during one day (morning and evening) with IASI-A and IASI-B, as calculated by FORLI. I separate between day and night observation using the sun zenithal angle (sza). $sza < 90^o$ corresponds to day observation and $sza > 90^o$ are the night observations. One can see that there are more frequent overpasses around the poles both in the Northern and Southern Hemisphere. MetOp, with its polar orbit, makes 14 revolutions per day (anomalistic period, see section 3.1.3), and therefore will pass by the poles on each revolution. In the regions of small cloud cover, the IASI observation count is higher. Around the Equator, and due to the Intertropical Convergence Zone (ITCZ), this count is smaller. The plot also shows the added value and the advantage of using coupled IASI-A and IASI-B data to have (almost) twice more data.
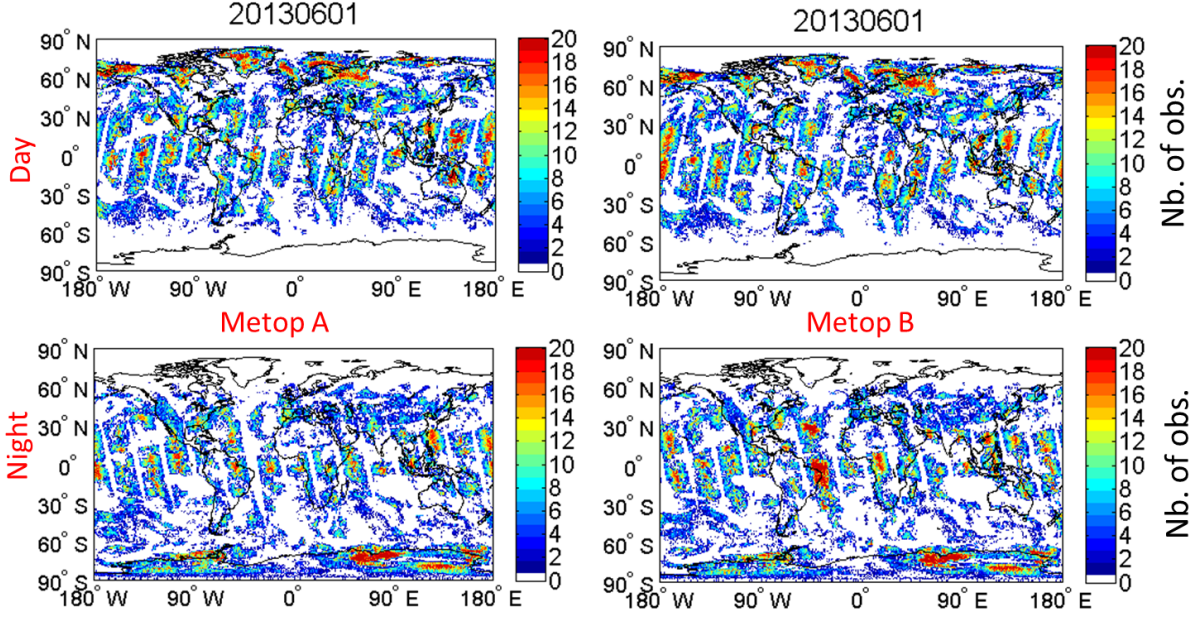
Figure 5.1: Number of IASI-O_3 observations per day (upper panel) and night (lower panel), for MetOp-A (left) and MetOp-B (right), over a grid of 1x1 degree.

5.1.2 IASI-A and IASI-B Crossing Time

Figure 5.2 shows the IASI crossing time during JJA 2013 over Madrid. Take for example, the first of July 2013. MetOp-A passed at 10:45 am, while MetOp-B passed around 50 minutes later at 11:35 am (UT). On the other hand, this effect is reversed on August first, 2013: MetOp-B passed 50 minutes before MetOp-A. Since the 2 satellites are 180 degrees out of phase, this is expected, and one satellite might be before or after the other.

5.1.3 IASI-A and IASI-B Local Ground Track

Comparison of the tropospheric O_3 product from IASI-A and IASI-B is not straightforward as the time and location of the observation vary and as a result, the pixels are not geographically co-localized. Moreover, the IASI product is subject to a cloud flag, so one observation seen at a certain location with IASI-A might be discarded during the retrieval whereas it might be taken into account by IASI-B if the cloud contamination is smaller than 13% (see section 4.5). Fig. 5.3 shows how part of the morning observation (till the time shown in the title of each plot) looks like above the region of Madrid. An easy way out to compare
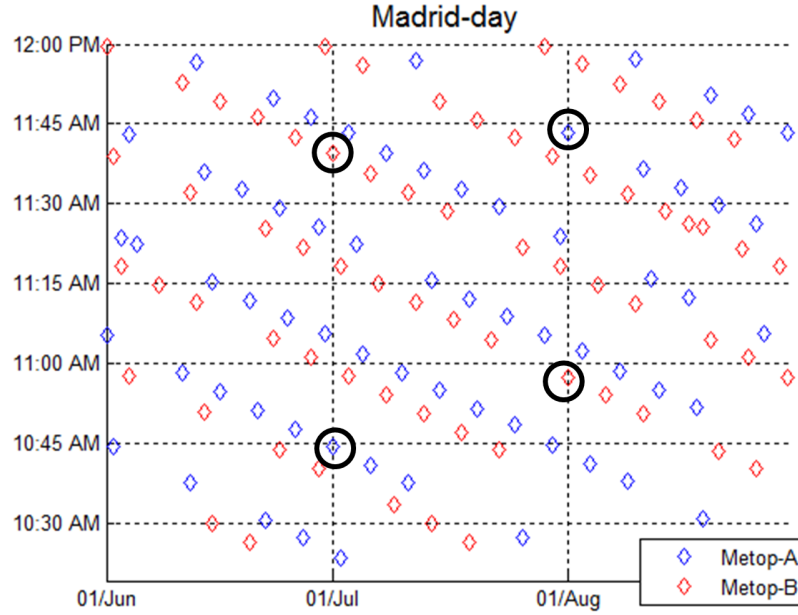
Figure 5.2: Crossing time of MetOp-A and MetOp-B morning orbit over Mardid during summer 2013. Black circles corresponds to the crossing time of July 1st and August 1st discussed in the text.

the two products would be taking averaged observations during one day for example, over a finite grid such as 0.5 x 0.5 or 1 x 1 degrees, which will be applied for the comparison of the two products in the following sections hereafter.

(a)   (b)
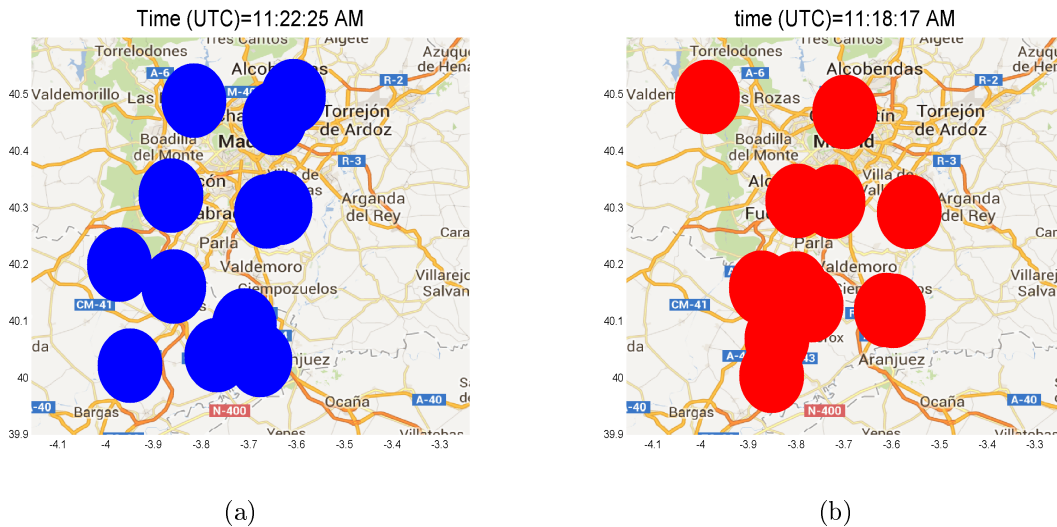
Figure 5.3: Ground track of part of the morning orbit (until the hour shown in the title of each figure) of the O_3 product from (a)IASI-A and (b)IASI-B on 09/07/2013.

5.2   Sensitivity of IASI-Ozone in the Troposphere

The averaging kernel (AK) functions, as shown in section 4.5.6, represent the sensitivity of the retrieval to the true state. These AK are highly variable in space and time. The shape of the AKs can change to peak to lower altitudes in certain conditions. The AKs and their shape sensitivity is described hereafter.

5.2.1   Tropospheric Averaging Kernel Functions

Fig. 5.4 shows the global sensitivity of the IASI instrument to the O_3 in the troposphere averaged over the month of August 2013.
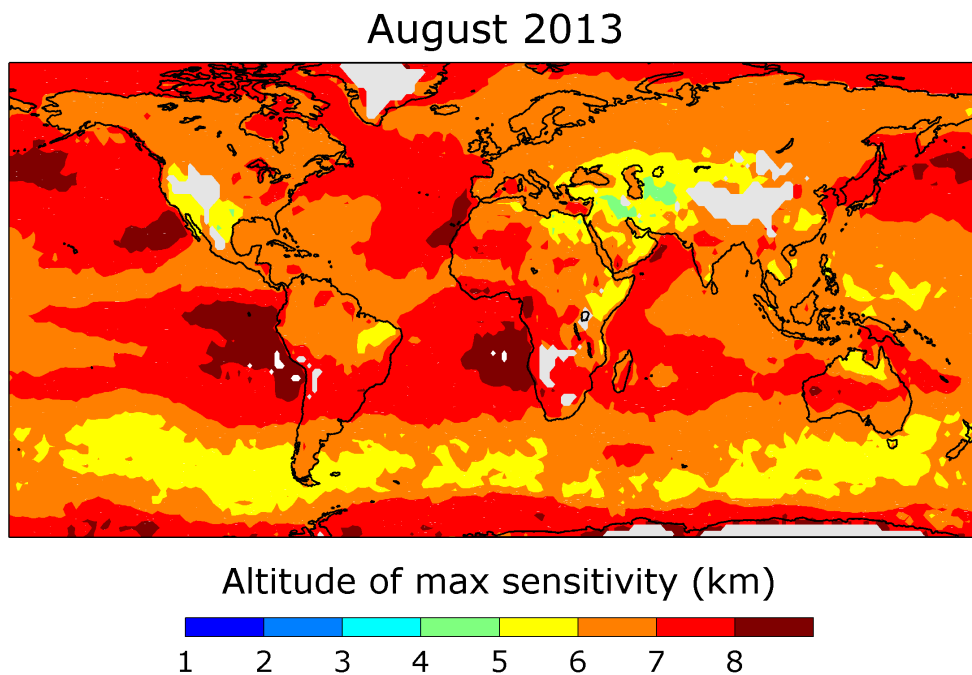
Figure 5.4: The altitude corresponding to the first peak in the O_3 averaging kernels function summed over the [0-8] km column of IASI and averaged over the month of August. No data (in white pixels) correspond to high altitudes or regions with emissivity issues (desert, snow).

The daily values were found by calculating the first local maximum in the kernel summed function over the [0-8] km column. The result was then averaged for the month of August 2013 over a grid of 2x2 degrees as shown here. The plot shows that on average, the altitude of maximal sensitivity is in general from 5 to 8 km, making the average maximal sensitivity of IASI-O$_3$ in the free to upper free troposphere. One can notice how the sensitivity is lower in altitude in the troposphere over land than water (of the Northern Hemisphere in particular - as August is a summer month).

5.2.2   The Thermal Contrast from IASI

Defined as the difference between the surface temperature and the temperature of the first atmospheric layer, the thermal contrast plays an essential role in the sensitivity of thermal infrared instruments. In fact, with the Sun rise, the Earth starts to absorb ultra-violet radiations in a spectral region where the atmosphere is relatively transparent. When the day progresses, Earth and atmosphere absorb solar radiation. Land (more than water) can heat up and cool down faster than the atmosphere making the thermal contrast more pronounced during the day and over land. This thermal contrast depends as well on location, temperature, type of surface and time of the day. For a given thermal contrast, the spectral resolution and radiometric noise of the IR instrument determines the amount of vertical information that can be retrieved for a given species. Fig. 5.5 shows the surface temperature and thermal contrast on the 25th of April 2013, from MetOp-A and MetOp-B joined observations on the region surrounding Beijing (plotted with the cross).

One can notice several things in this figure:
1- Higher surface temperature during the day than during night, making the diurnal variation quite prominent.
2- Positive thermal contrast during the day (over land in general, but can be also negative), and both negative and positive thermal contrast during the night, though negative thermal contrast is more prominent.
3- Higher thermal contrast (in absolute value) during the day than the night.
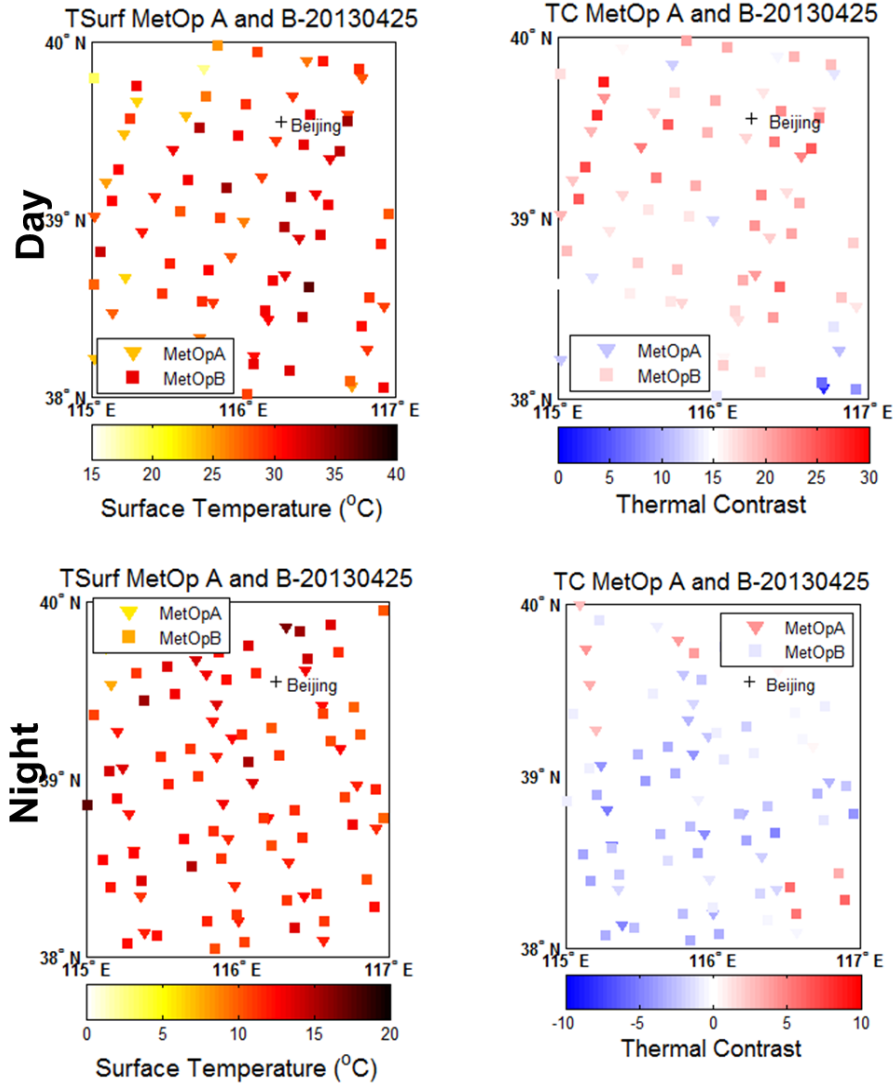
Figure 5.5: Surface temperature (TSurf) and thermal contrast (TC) during the day (upper panels) and night (lower panels) from IASI/MetOp-A (plotted with triangles) and IASI/MetOp-B (plotted with squares). Note that the colobar limits are different between day and night, implying larger TC (in absolute value) during the day.

5.2.3 Sensitivity to the Lower Troposphere with Thermal Contrast Change

In section 5.2.1 I showed how IASI sensitivity of tropospheric O_3 retrieval is highest in the altitude range 4-8 km and that the thermal contrast plays a role in the retrieval sensitivity in lower altitudes. What is this role, and how does it affect the information retrieved in

the troposphere? In order to answer this question, one should look at the averaging kernels (AK) functions with different thermal contrasts as the shape of the AK functions in the low troposphere will carry the answer.
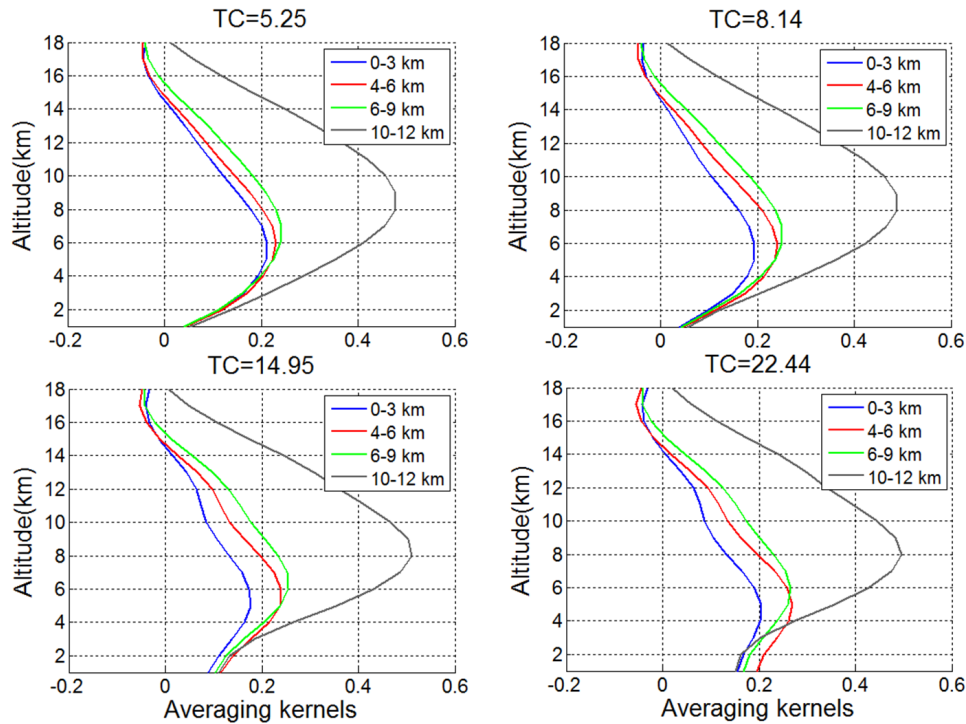
Figure 5.6: Averaging kernel functions for observations with different thermal contrast (TC). Higher thermal contrast tends to increase the sensitivity towards the surface.

Fig. 5.6 shows the relationship between the increase in thermal contrast (for randomly selected observations), and its effect on the shape of the averaging kernel functions of the O_3 retrieval. Though this relationship is not linear, one can see that when the thermal contrast increase, the AK tend to have higher values towards the surface with the peak shifted to lower altitudes. I note here that the [6-9] km or [10-12] km AK functions do not really depend on thermal contrast change as the figures show. In fact, in the mid and upper free troposphere, the ozone product from IASI is more robust, as it is less dependent on surface properties.

5.3 Global Seasonal Variation

The day-time seasonally averaged O_3 [0-8] km columns are shown in Fig. 5.7 for the year 2013. Day-time observation is chosen because as seen in section 5.2, the IASI sensitivity

to the troposphere is better during the day, where the thermal contrasts are usually higher. The unit used for O_3 is the *Dobson Unit* (DU), which is commonly used for the O_3 column concentration (total or tropospheric), with 1 DU=2.69×10^{16} molec.cm^{-2}. The DU notation will be used in all the O_3 plots in this thesis work. More information on the Dobson Unit and its physical meaning can be found in Appendix A.
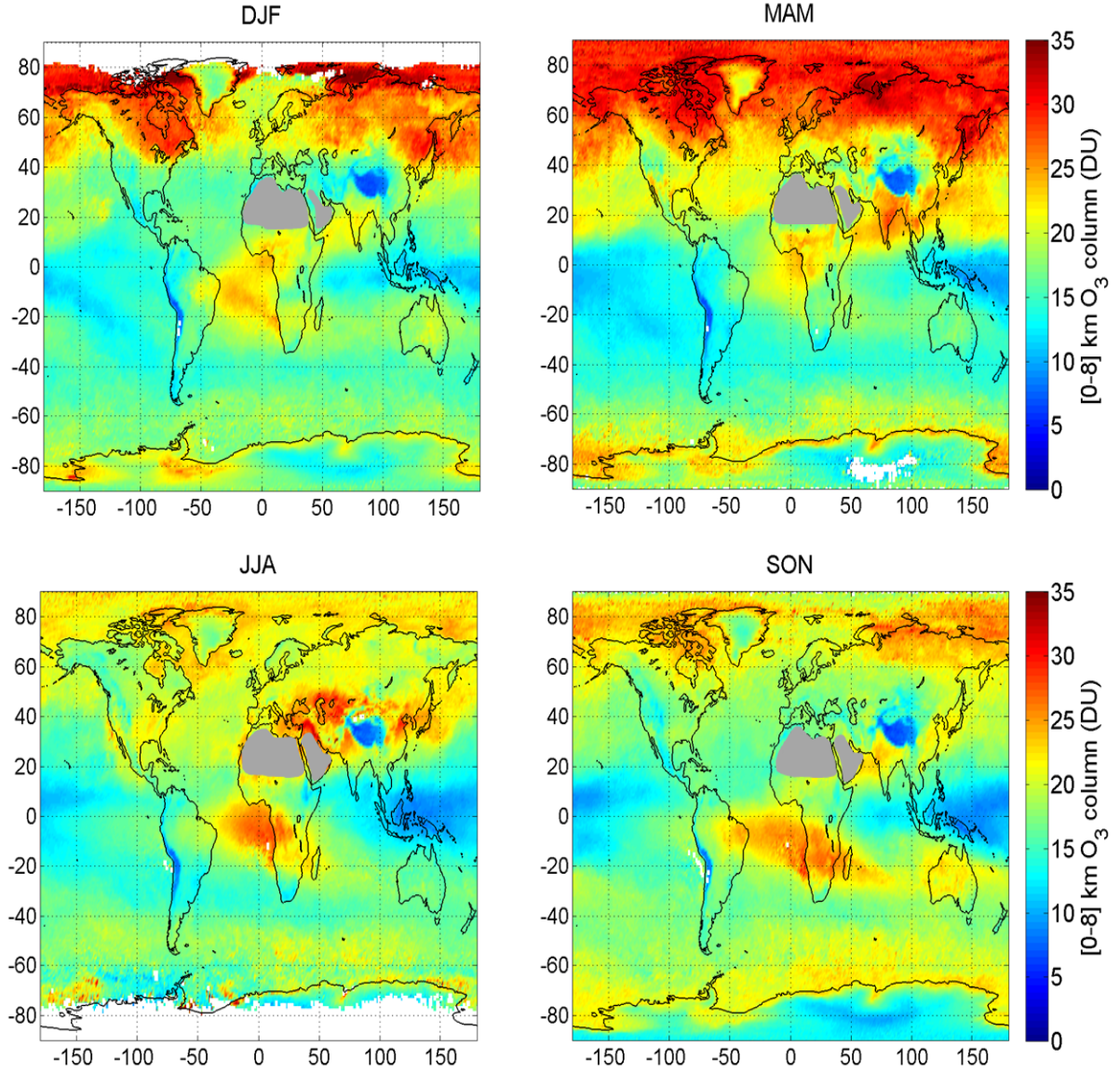
Figure 5.7: Day-time seasonally averaged tropospheric [0-8] km O_3 column for the year 2013. Grey pixels correspond to a flag due to emissivity issues in FORLI above the desert.

The seasonal variation of tropospheric O_3 is highlighted with lower values in winter and

increasing values in spring and summer due to the increase in photochemical activity. In general, the tropospheric O_3 observed in mid and high latitudes of the Southern Hemisphere are always smaller than those in the Northern Hemisphere. Over the desert regions in north Africa and Saudi Arabia, a filter is applied (with gray pixels in the figures) on poor spectral fits because of emissivity issues in FORLI.

High Latitudes

White pixels at high latitudes winter (DJF for northern high latitudes and JJA for southern high latitudes) correspond to no day-time observation during the winter months. The high values detected in the winter/spring of the northern high latitudes are explained by the integration of stratospheric air into the [0-8] km column due to lower tropopause height as well as residual stratospheric intrusions, which inject ozone-rich air from above the [0-8] km column during the whole year. Due to the ozone depletion in the Southern hemisphere and to the Brewer-Dobson circulation (section 1.1.2) that transports more O_3 to the Arctic, the same effect is not recorded in austral winter/spring.

Mid-Latitudes

Prominent values are mostly noticed in the mid-latitudes of the Northern Hemisphere. During summer, when the O_3 production is highest, high values are especially detected in East Asia and on the coasts of the US as well as in Eastern and Southern Europe coinciding with the highly populated areas and suggesting anthropogenic O_3 sources. Summertime O_3 maxima are also detected in the Mediterranean region. Transport of O_3 across the Atlantic and the Pacific is highlighted with high O_3 plumes between the continents, which are in accordance with the wind patterns analyzed in section 2.3. As seen in Fig. 5.4, the tropospheric O_3 product from IASI is sensitive in general in the free to upper troposphere. This makes the study of the transport processes in these atmospheric levels using the wind patterns coupled with the tropospheric [0-8] km O_3 column from IASI very efficient. Moreover, the East Asian plumes of pollution getting to the west coasts of North America, are clear in spring, less so in summer, in agreement with the winds at 500 hPa.

Tropics and Sub-Tropics

The O_3 minimum over the tropical/sub-tropical Pacific is due to the photochemical destruction of O_3 by ultraviolet light. Biomass burning is one of the major forcings of tropical tropospheric chemistry. This can be seen with the high values recorded above central Africa and the Amazon rainforest. Tropical Atlantic O_3 distribution is characterized by two maxima, the first in the lower troposphere, predominantly over the biomass burning region and just to the south of it, and a second in the mid troposphere in the southern tropical Atlantic [Edwards et al., 2003]. Since the maximum lightning influence is found in the Southern Hemisphere, O_3 availability over this part of the globe is suggested to be highly dependent on lighting NO_x [Lamarque et al., 1996a, Jacob et al., 1996]. In fact, lightning NO_x is shown to account for $> 39\%$ of the south Atlantic O_3 burden in DJF, and $> 30\%$ in JJA [Sauvage et al., 2007]. In absence of all tropical NO_x sources (from biomass burning and lightning), an important (though smaller) influence of background O_3 remains, reflecting transport and chemical production from extra-tropical sources [Sauvage et al., 2007].

5.4 IASI-A and IASI-B Comparison

Since two copies of the IASI instrument are on board of the two MetOp satellites, it is wise to compare the two instruments products. To accomplish this, I will take the average observation gridded on a 1x1 grid, both on a regional and global scale.

5.4.1 Regional Comparison

The location of the regions taken for this regional comparison is shown on Fig. 5.8. Day and night observations (using the *sza*) are shown in Fig. 5.9 for each of the box regions of Fig. 5.8.

The figure shows that in general, we have good agreement between the two products. It also highlights that on some occasions, one instrument might have a valid observation when the other doesn't. This is a great advantage when studying local pollution episodes that are usually accompanied with smog, making the retrieval of O_3 more challenging. However, more local sounding opportunities are offered with the two (and in the future three) IASI
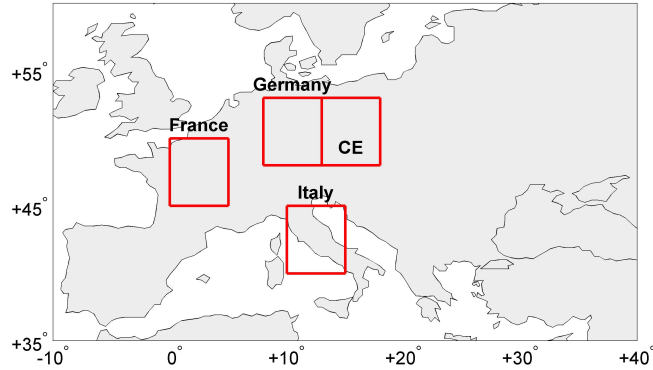
Figure 5.8: Location of the region used for comparison of the IASI-A and IASI-B products shown in Fig. 5.9
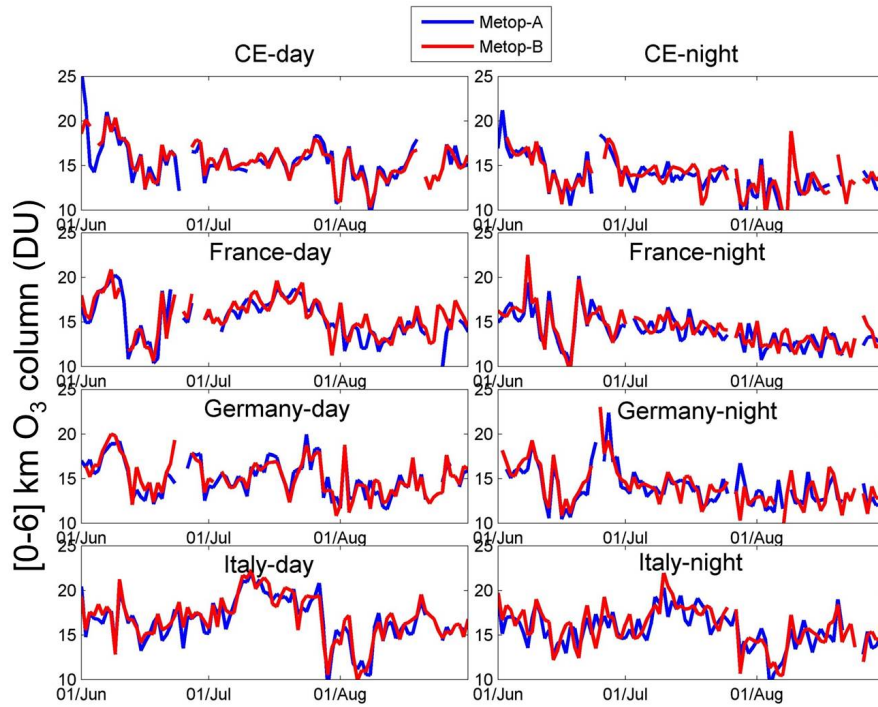
Figure 5.9: Comparison of the IASI-A and IASI-B products for the regions plotted in Fig. 5.8

instruments. During the day the two instruments are better correlated. They both capture same features (such as the peak during the first few days in August). Noticeable differences can also be seen, and are more frequent at night. In fact, as seen thus far, several factors play

a role in what is retrieved in the observation. Those are 1- related to the abundance of O_3 in the troposphere, and 2- the sensitivity of the instrument at the time and location of the observation. Besides chemistry, temperature, humidity and air movements play a significant role in the availability of O_3 locally. Moreover, during night, the thermal contrast is smaller, making the sensitivity of IASI (section 5.2.3) to the lower troposphere limited. All these factors might explain the differences seen during day as well as during the night.

5.4.2 Global Comparison
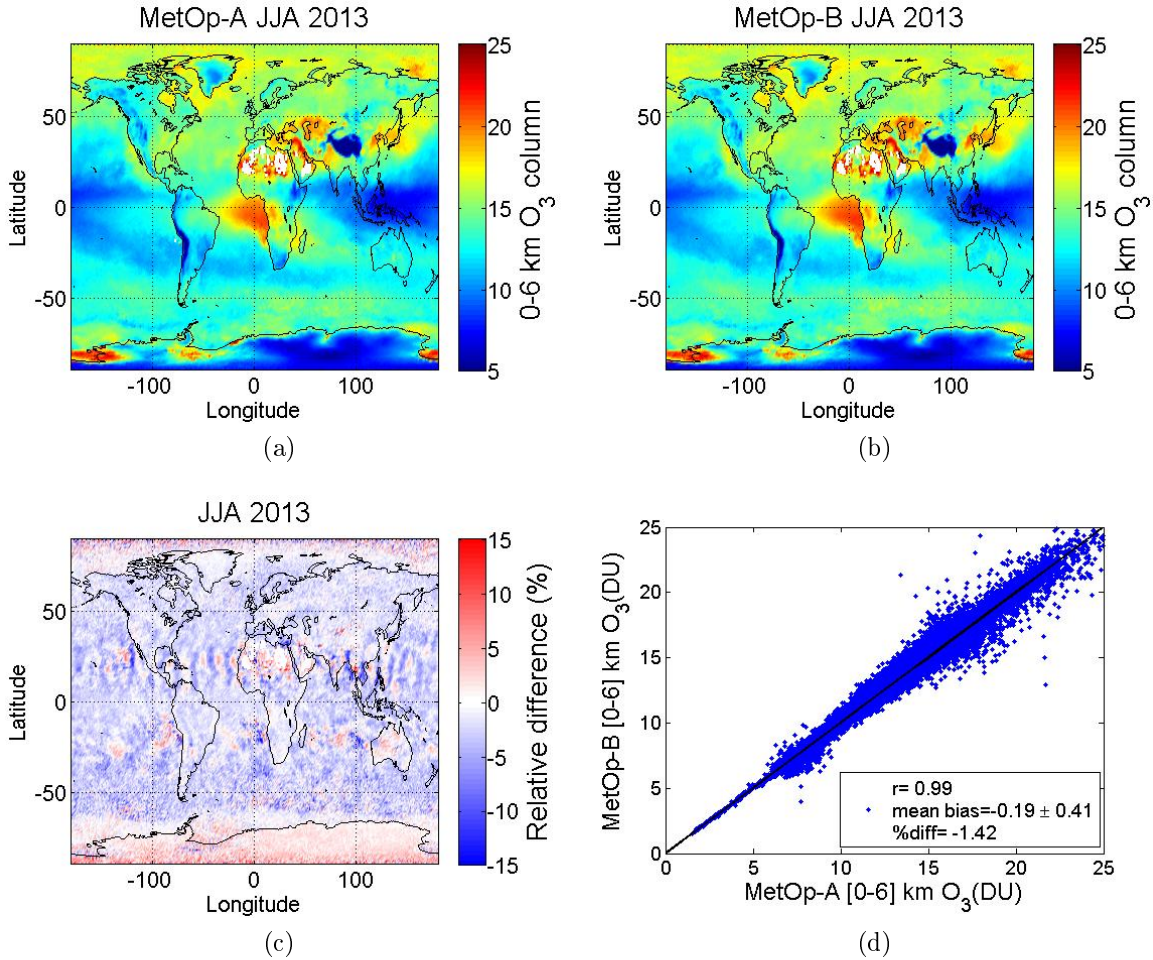
Figure 5.10: (a) June, July, August average of the [0-6] km O_3 column from IASI/MetOp-A and (b) IASI/MetOp-B. (c) The relative difference and (d) correlation between the two grids shown in (a) and (b).

Global comparison of the tropospheric O_3 products from the 2 IASI instruments taken

over a grid of 1x1 during a 3 month period is shown in Fig. 5.10. This global average, as opposed to the local average and plots shown previously, highlights the effect of averaging on eliminating the local differences. So globally speaking, one can say that the 2 IASI products show an excellent agreement, with a global mean bias over 3 months of around 1%.

5.5   Six-Year Time Series and Variability Analysis

I present here an analysis of the time development of tropospheric O_3 over the 6 year period (2008-2013) of the IASI-O_3 (MetOp-A) observations over different regions. The geographic location is the red box in the map attached to each of the panels of Figs. 5.11 and 5.13.
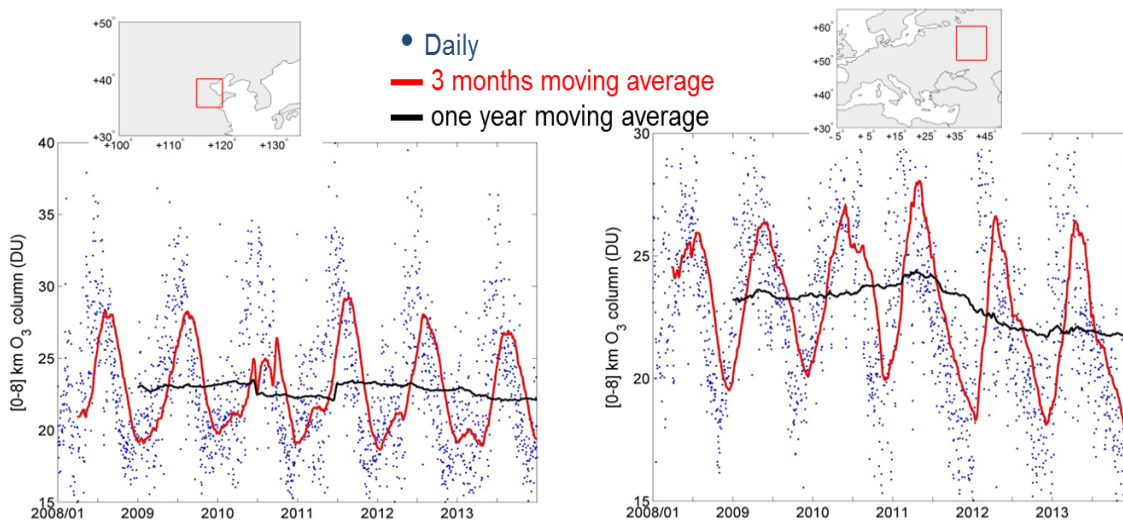
Figure 5.11: Time series of tropospheric O_3 column for the period 2008-2013 for each of the regions in the red box in the map above the plot. Daily, seasonally and yearly moving averages are shown.

The figures show the well-known seasonal cycle at mid-latitudes in the troposphere with maxima observed in spring-summer. Running 3-months mean and 1-year mean have been added to try to deduce a "trend". Despite the fact that more than 10 years of observations, corresponding to the large scale of solar cycle, is usually required to perform a trend analysis, I will make the assumption that statistically relevant information might be derived from the

six years of the available IASI observations.

In the tropospheric [0-8] km column, one can see that the variability based on daily observations are highly depending on the region of interest and season, with the seasonal variation discussed in section 5.3. Few features are noticeable in Fig 5.11: in the Chinese region, during summer 2010, the summer peaks are reduced in comparison with the other years. South East Asia witnessed in 2010 an unusual strong monsoon. Floods in North Korea and northeast China buried farmland and destroyed homes, factories, railroads, and bridges. And in northwest China, rain triggered a massive landslide that left 702 dead with 1,042 missing as different news sources reported. All of these disasters occurred as a result of unusually heavy monsoon rains, depicted in Fig. 5.12. If we look at the Russian region during the same period, we can see that during summer 2010, a second peak appears, that is not seen during the other years. This is due to the Russian heat wave, that persisted starting late June which had catastrophic effects, and lead to massive fires. In Moscow alone, an estimated 300 people a day have died.
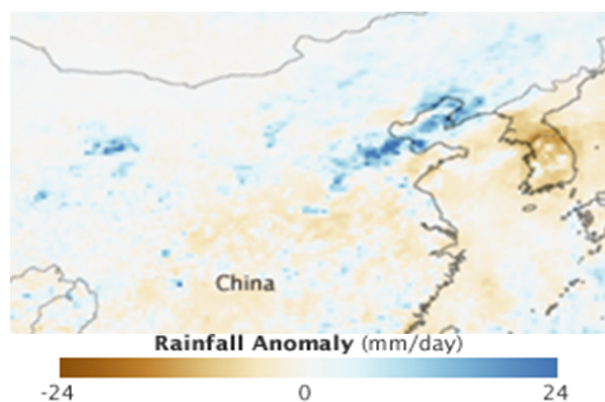
Figure 5.12: Rain rates (the intensity with which rain was falling) between August 1 and August 9, 2010, compared to average rain rates for the same period. Blue reveals areas where rain was much more intense than normal, while brown points to less intense rain. Figure from http://earthobservatory.nasa.gov/NaturalHazards/view.php?id=45177.

One would ask if these 2 events are actually linked. A study by Trenberth and Fasullo [2012] shows that record high surface sea temperatures were recorded in the Northern Indian Ocean in May 2010 which provided a source of unusual abundant atmospheric moisture for the monsoon. The result was an anomalous diabatic heating forcing quasi-stationary Rossby

waves [1] which altered the monsoon strength, extended to Europe and Russia where it created a persistent anti-cyclonic [2] regime creating a heat wave.

If we look now to Fig. 5.13, over the East coat of the US, a summer peak during 2010 (for the 3-month average) is detected. In fact, this could be related to the same reason, as the region was under the influence of the same Rossby wave that extended to Europe and Russia. If we look also closely, one can notice how the west coast of the US, over the same period shows an increase O_3 concentrations in summer. This could suggest effective transport of pollution from East Asia to the west coast due to the high monsoon power, though more detailed analysis, that I do not present here, is required to confirm it. As for the other regions' variability, Northern Hemisphere regions presented here present a slight downward "trend", that is clear with the 1-year moving average, with the exception of China. Downwind the US, this decrease is the most clear (Fig. 5.13, middle panel). Given that this area is subjected to mainly the transport from North America (as explained in the transatlantic transport of pollution) it is an interesting area for the study of the effect of reduction in O_3 precursor emissions on the transatlantic transport. Over this region, the average O_3 column was of 19.8 DU, and is plotted as a dashed line. Even though the decrease is small, it does nevertheless show a promising downward slope in the 1-year moving average of around 1 DU or 5% during the 6-year period. The downward variability seen over the different regions, especially those in Europe, are in agreement with the study by Logan et al. [2012] that showed that over Alpine stations, O_3 is actually decreasing in summer of the 2000's with no significant trend in other seasons. Such tropospheric O_3 trends remain difficult to interpret but they are generally linked -as seen thus far- to the change in anthropogenic emissions of O_3 precursors, to long-range transport and to STE processes.

---

1. In planetary atmospheres, Rossby waves are due to the variation in the Coriolis effect with latitude.

2. Anticyclones are stable areas of high pressure. High pressure at the surface of Earth results from air that is descending from high in the atmosphere and is stable. Descending air discourages condensation so there will be little cloud cover. Anticyclonic conditions in summer bring clear skies, sunshine, low wind speeds, high temperatures and dry weather.
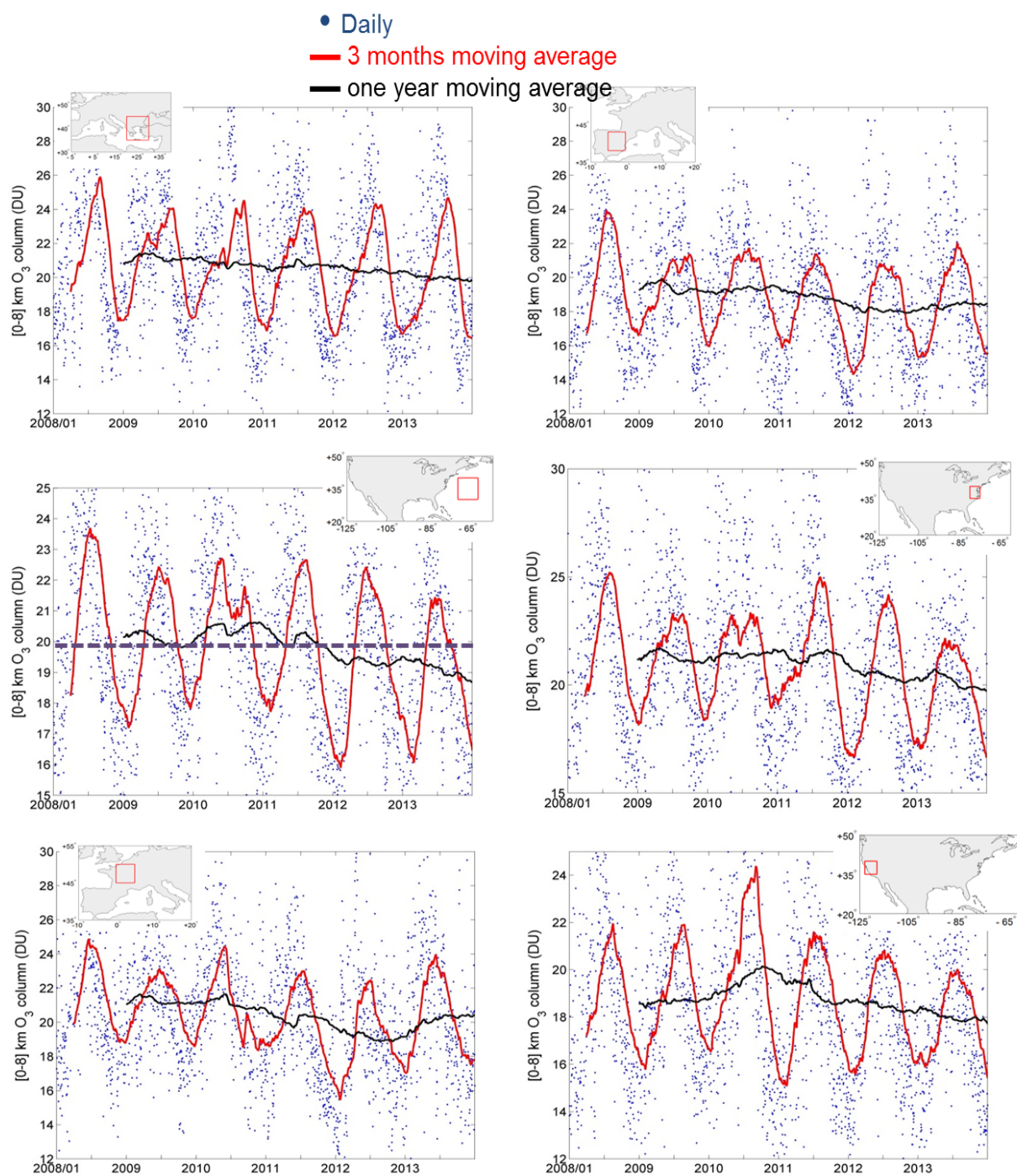
Figure 5.13: Same as for Fig. 5.11, but for different regions.

Chapter 6

Tropospheric Ozone and Nitrogen Dioxide Measurements In Urban and Rural Areas As Seen By IASI And GOME-2

6.1 Motivation

As seen in the introduction, the present day atmosphere is more complex due to human activity, notably in urban areas giving rise to spatially and temporally varying inorganic and organic gases whose mixing ratios are small but vary in time and space. Table 6.1 lists the concentrations of the principle gases that might be expected in the clean and polluted (urban) troposphere. When one tries to compare a clean and a polluted atmosphere, many of the pollutants concentrations increase up to 2 orders of magnitude.

Pollutants can be transported from their urban sources by winds, depending on their lifetime. O$_3$ lifetime in the troposphere depends on several factors, but in many cases, it can survive in pollution plumes or even get formed in them. In fact, and in contrast to other pollutants, O$_3$ levels in downwind plumes can be higher than in the surrounding urban area during meteorological conditions that favor its formation (high sunlight and warm temperatures) [Miller et al., 1978, Sillman, 1999, Xu et al., 2011, Pires et al., 2012, Cooper et al., 2012] (among many others). In urban centers, and at short distances from strong

Table 6.1: Volume mixing ratios (VMR) of some spatially and temporally varying gases [Jacobson, 2012]

	Gas name	Chemical	Clean trop. VMR(ppbv)	Polluted trop. VMR(ppbv)
Inorganic				
	Water vapor	$H_2O(g)$	$3000\text{-}4\text{x}10^6$	$5\text{x}10^6\text{-}4\text{x}10^7$
	Carbon monoxide	$CO(g)$	40-200	2000-10000
	Ozone	$O_3(g)$	10-100	10-350
	Sulfur dioxide	$SO_2(g)$	0.02-1	1-30
	Nitric oxide	$NO(g)$	0.005-0.1	0.05-300
	Nitrogen dioxide	$NO_2(g)$	0.01-0.3	0.2-200
Organic				
	Methane	$CH_4(g)$	1850	1850-2500
	Ethane	$C_2H_6(g)$	0-2.5	1-50
	Ethene	$C_2H_4(g)$	0-1	1-30
	Formaldehyde	$HCHO(g)$	0.1-1	1-200

NO_x sources, O_3 is depleted through titration by the freshly emitted NO (typically, 90% or more of total NO_x emitted) which reacts rapidly with O_3 to produce NO_2 (see section 2.1). In situations with significant O_3 production (including most urban and polluted rural areas during meteorological conditions favorable to O_3 formation) this removal of O_3 is small compared to the rate of its production. The process of NO_x titration can only remove at most one O_3 per emitted NO, whereas the process of O_3 formation typically produces four or more O_3 per emitted NO_x.

Thus the importance of the study of the difference between urban and rural O_3 and its relationship to its precursors. As an O_3 precursor, NO_2 from space is a well defined product from different instruments such as GOME (1996-2003), SCanning Imaging Absorption spectroMeter for Atmospheric CHartographY (SCIAMACHY) (2002-2012), OMI (2004-present), GOME-2 on MetOp-A (2007-present) and GOME-2 on MetOp-B (2013-present). GOME-2 and IASI are therefore on the same platform offering a good opportunity to study the relationship between NO_2 and O_3 with the same overpass time. If we want to study the urban and rural relationship in terms of pollution from space, a well defined geo-localisation is required. Given the resolution of the instruments on board of the satellite, the rural area defined should therefore be away from its corresponding urban region by at least the spatial resolution of the instrument. In this study, the rural areas were chosen this way. The exact

direction with respect of the urban region is found by studying the wind patterns from the ERA-interim reanalysis. The resulting study assessing O_3 and NO_2 in urban and rural regions was published in 2013 in the Journal of Geophysical Research-Atmospheres and can be found attached in section 6.3.

6.2   Wind Pattern Analysis

The cities studied can be located in Fig.   6.1.   After testing different locations, those were chosen because they have high anthropogenic emissions (when looking at NO_2 maps), good seasonal variability and good thermal contrast near the ground allowing the detection of O_3 in the low troposphere.   The wind patterns were those blowing from the city during the study period which is from 2008-2011. The wind patterns have various diurnal, seasonal, and vertical variations so that in this study I had to choose a "prevailing" wind direction. Monthly averaged wind directions were extracted and a general wind pattern was chosen. The wind roses for different cities are shown in Fig. 6.2. Tehran and Istanbul are the 2 cities for which the winds take frequent completely opposite wind directions, where the assumption of a prevailing wind direction was based on the highest frequency of occurrence.

Figure 6.1: Location of the cities used in this study.
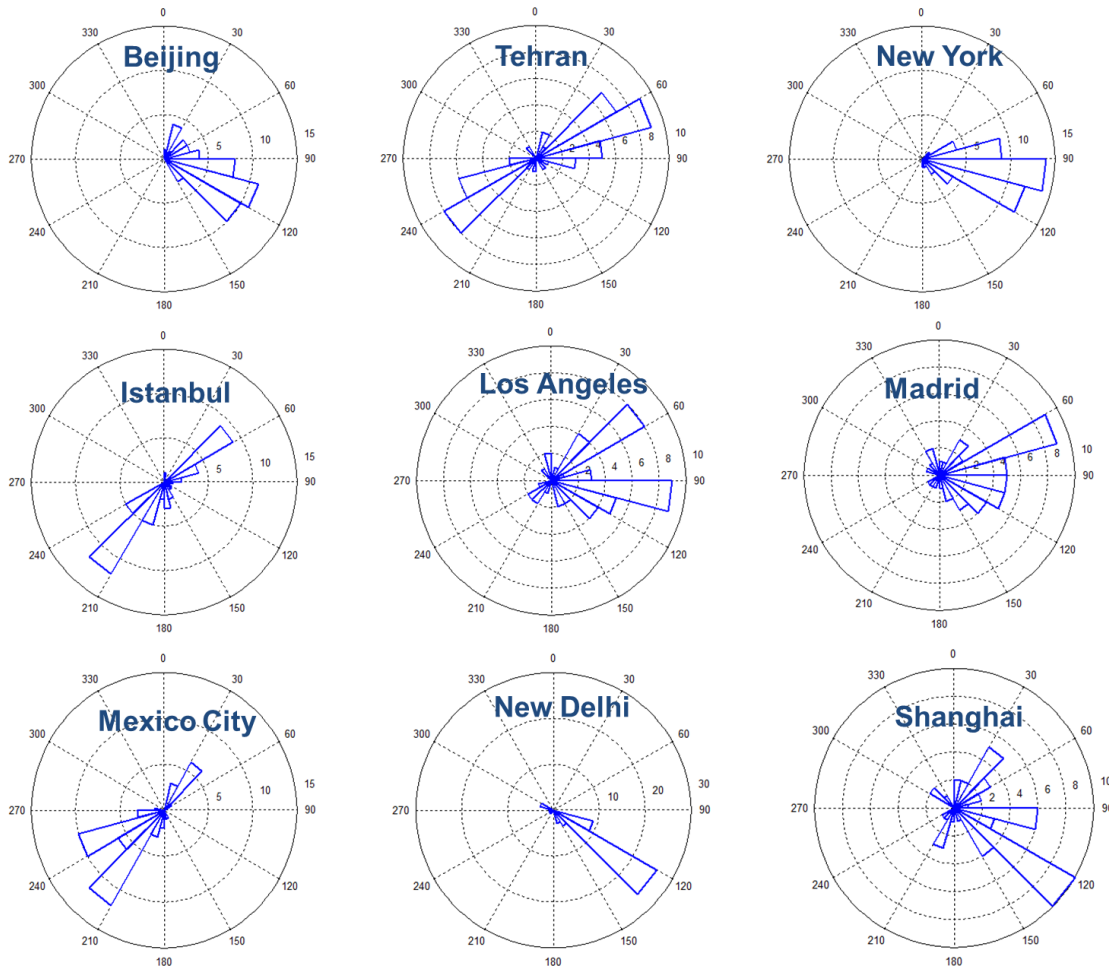
Figure 6.2: The average 1000-750 hPa wind rose, for the monthly averaged observation of the 4-year study (48 observations for each city).

6.3   Published Article

In this attached article, I present more detailed analysis of the IASI-O_3 product coupled with the GOME-2/NO_2 product. I present seasonal variability of tropospheric O_3 and NO_2 as well as the complex relationship joining them. A case study of the Olympic games of summer 2008 in Beijing is presented to highlight the non-linear relationship between O_3 and NO_2. As a summary, the results of this paper show that in contrast with NO_2, O_3 can be transported by winds to downwind rural regions where its values can be of the same order of magnitude to those found in urban centers. The study also shows that it might be possible to draw a relationship between rural O_3 and NO_2 assuming a NO_x limited regime, though

further detailed analysis is required to confirm this claim. The analysis of the Beijing Olympic games of summer 2008 shows a significant decrease in the NO_2 tropospheric column up to 54%, while the O_3 tropospheric columns during the same period do not follow the same trend and even show an increase of 12% during the month of July.

Due to copyright infringement issues, attached here is the final version of the published article of Safieddine et al. [2013].

Tropospheric ozone and nitrogen dioxide measurements in urban and rural regions as seen by IASI and GOME-2

S. Safieddine[1], C. Clerbaux[1,2], M. George[1], J. Hadji-Lazaro[1], D. Hurtmans[2], P.-F. Coheur[2], C. Wespes[2], D. Loyola[3], P. Valks[3] and N. Hao[3]

[1]UPMC Univ. Paris 06; Université Versailles St-Quentin; CNRS/INSU, LATMOS-IPSL, Paris, France

[2]Spectroscopie de l'Atmosphère, Chimie Quantique et Photophysique, Université Libre de Bruxelles (U.L.B.), Brussels, Belgium

[3]German Aerospace Center (DLR), Remote Sensing Technology Institute (IMF), Oberpfaffenhofen, Germany

Abstract

Tropospheric ozone (O_3) columns in urban and rural regions as seen by the infrared sounder IASI are analyzed along with GOME-2 tropospheric nitrogen dioxide (NO_2) columns. Results over nine cities of the Northern Hemisphere for the period 2008-2011 show a typical seasonal behavior of tropospheric O_3, with a first maximum reached in late spring because of stratospheric intrusion mainly, and a continuous rise till the summer because of the anthropogenic based ozone production. Over the East Asian cities, a decrease in the O_3 tropospheric column is detected during monsoon period. Seasonal cycling of tropospheric NO_2 shows consistent higher values during winter because of the higher anthropogenic sources and longer lifetime. In rural regions, a complex relation between the O_3 and NO_2 column is found, with good correlation in summer and winter. O_3 concentrations in rural sites are found to be comparable to those closest to the anthropogenic emission sources, with peak values in spring and summer. Furthermore, the effect of the reduction of pollutant emissions in Beijing region during the Olympic Games of 2008 compared to the same summer period in the following three years is studied. GOME-2 NO_2 measurements show a reduction up to 54% above Beijing during this period compared to the following three years. IASI O_3 measurements show an increase of 12% during July 2008 followed by a decrease of 5-6% during the months of August and September.

1. Introduction

Global monitoring of tropospheric O_3 is essential as it is an important greenhouse gas and air pollutant [*Jacobson*, 2012]. It is a significant absorber of infrared and ultraviolet radiation, and a primary source of the most important oxidant in the atmosphere, the hydroxyl radical OH, that is highly reactive with organic and inorganic compounds [*Levy et al.,* 1985; *Finlayson-Pitts and Pitts*, 1997; *Jacob*, 2000]. Exposure to high levels of O_3 is associated with pulmonary and chronic respiratory diseases as well as premature mortality [*Bell et al.,* 2004, 2007; *Ito et al.,* 2005; *Ebi and McGregor,* 2008]. Economic concerns are also raised because of the negative effect of O_3 on vegetation, ecosystems, crops production and yield [*Reich,* 1983; *Chappelka et al.,* 1999; *Collins et al.,* 2000; *Fuhrer and Booker,* 2003; *Schaub et al.,* 2005; *Karnosky et al.,* 2007]. Sources of O_3 in the troposphere are either due to natural intrusion from the stratosphere, where most of the O_3 resides, or to photochemical production from precursors. These precursors are pollutants emitted mainly during anthropogenic urban activities and include carbon monoxide (CO), peroxy radicals generated by the photochemical oxidation of VOCs (such as hydrocarbons and aldehydes) and nitrogen oxides (

1

$NO_x = NO + NO_2$). The main sources of NO_x are either anthropogenic such as the result of the combustion of fossil fuels and biomass burning, or natural from wildfires, soil emissions and lighting. Most of the NO_2 in urban air results from the rapid oxidation of NO which is the major nitrogenous product emitted from combustion [*Finlayson-Pitts and Pitts,* 1997; *Klonecki and Levy,* 1997; *Jacob,* 2000; *Seinfeld and Pandis,* 2006; *Jacobson,* 2012]. One can distinguish 2 regimes with different O_3-NO_x-VOC sensitivity. The first one is the NO_x-limited regime where O_3 concentrations increase with increasing NO_x; and the second one is the VOC-limited (NO_x-saturated) regime, where O_3 production rate increases with increasing VOCs concentrations. Generally, urban centers are found to be in a VOC limited regime while   rural regions downwind are found to be in a NOx-limited regime [*Milford et al.,* 1989, 1994; *Sillman,* 1999; *Duncan et al,* 2010]. In fact, O_3 concentrations in rural sites are frequently found to be higher than the values found near anthropogenic activity, with peak values in spring and summer [*Logan*, 1985, 1989; *Sillman et al.,* 1990]. The measurement of tropospheric O_3 and NO_2 by satellite is shown to be efficient since it provides a good way to get regional and global information on O_3 and NO_2 distribution, transport and variability [*Tie et al.,* 2007]. Tropospheric O_3 retrievals from satellites have been possible by subtracting the stratospheric O_3 column with UV sounders [e.g. *Fishman and Larsen*., 1987; *Schoeberl et al.,* 2007], directly from measurements in the UV [*Liu et al.,* 2006] and from high resolution infrared sounders like IMG (Interferometric Monitor for Greenhouse gases), TES (Tropospheric Emission Spectrometer) and IASI (Infrared Atmospheric Sounding Interferometer) [*Coheur et al.,* 2005; *Worden et al.,* 2007; *Eremenko et al.,* 2008].

In this paper we analyze the seasonal variations of O_3 and NO_2 in the troposphere, over 4 years (2008-2011) above specific urban and rural areas of the Northern Hemisphere (NH), using data provided by IASI and GOME-2 (Global Ozone Monitoring Experiment) instruments on the MetOp-A (Meteorological Operational) satellite along with wind patterns provided by ECMWF (European Centre for Medium-Range Weather Forecasts) ReAnalysis (ERA). Section 2 details the study area selection and how measurements data are collocated above cities. In section 3 we explain the method used to extract wind directions, the tropospheric O_3 retrieval from the IASI mission as well as GOME-2 retrievals of the tropospheric NO_2 columns. We discuss the results in section 4 and list our conclusions in section 5.

2. Study Area Selection

In order to understand the effect of local pollution, we chose to focus in this study on a selected set of big cities, listed in Table 1, known for their high anthropogenic emissions in different locations in the NH and over three continents: North America, Europe and Asia. Over the period from January 2008 to December 2011, monthly averaged gridded tropospheric O_3 and NO_2 columns were calculated, over a grid size of 0.25^{o}x0.25^o. The corresponding rural area for each city was defined as the area downwind the city (see section 3.1).

Table 1. Cities Location Used in this Study and the Corresponding Rural Areas (the Latter According to the Prevailing Wind Directions from the Urban Center).

Urban Region				Rural Region	
City	Latitude range (^{o}N)	Longitude range (^{o}E)	Wind direction	Latitude range (^{o}N)	Longitude range (^{o}E)
Mexico City	19 19.75	-99.5 -98.75	SW	18.25 19	-100.25 -99.5
Los Angeles	33.5 34.25	-118.5 -117.75	E	33.5 34.25	-117.75 -117
Istanbul	40.75 41.5	28.75 29.5	SW	40 40.75	28 28.75
Madrid	40 40.75	-4 -3.25	E	40 40.75	-3.25 -2.5
New York	40.25 41	-74.5 -73.75	E	40.25 41	-73.75 -73
Tehran	35.25 36	51 51.75	NE	36 36.75	51.75 52.5
New Delhi	28.25 29	77 77.75	SE	27.5 28.25	77.75 78.5
Shanghai	30.75 31.5	121 121.75	SE	30 30.75	121.75 122.5
Beijing	39.5 40.25	116 116.75	SE	38.75 39.5	116.75 117.5

3. Measurements

High pollution episodes are notably detected above and around cities. During such events, elevated values of NO_2 and O_3 can be observed by satellite in the troposphere [e.g. *Tie et al.,* 2007; *Dufour et al.,* 2010]. In this study we aim at investigating the relation between O_3 and NO_2 pollution over cities and their corresponding rural areas using satellite data: we use in particular IASI tropospheric O_3 column and GOME-2 tropospheric NO_2 column data. In addition we use wind fields from ECMWF reanalysis to locate the rural areas where the formation or transport of O_3 is important.

3.1. Wind Directions

Wind direction patterns used in this study are from ERA-Interim archive at ECMWF (*u-* and *v*-components of horizontal wind). The data assimilation produces 4 analyses per day at 00, 06, 12 and 18 UTC at 37 pressure levels from 1000 to 1 hPa with a Gaussian grid with a resolution of 0.7^o at the Equator. Data Services associated with wind data sets apply an interpolation scheme to make it adaptable to requested resolutions and representation forms [*Berrisford et al.,* 2009; *Dee et al.,* 2011]. In the ERA-Interim database, monthly means of wind directions patterns are interpolated and extracted over a grid size of 0.75^o x 0.75^o. In this study, we attempt to analyze the prevailing wind directions from each studied urban city of Table 1. We averaged monthly wind patterns over the 4-year period of the study in the boundary layer (surface to 750 hPa) where the production and transport of pollutants is the most important. The result is inserted in as "rural" region in Table 1.

3.2. IASI Ozone Measurements

3.2.1. Instrumentation

The IASI instrument launched on board the MetOp-A platform on 19 October 2006, is a nadir looking Fourier transform spectrometer that probes the Earth's atmosphere in the thermal infrared spectral range between 645 and 2760 cm^{-1}, with a spectral resolution of 0.5 cm^{-1} (apodized) and a 0.25 cm^{-1} spectral sampling. Three IASI instruments have been assigned for a span of at least 15 years. The second one was launched on 17 September 2012 on board of MetOp-B and a third instrument is scheduled for 2016-2017. IASI footprint is a matrix of 2x2 pixels, each with 12 km diameter at nadir. IASI monitors the atmospheric composition at any location two times per day with a swath width of 2200 km corresponding to a total of 120 views. IASI can as well measure many of the chemical components that play a key role in the climate system and are responsible of atmospheric pollution [*Clerbaux et al.,* 2009; *Coheur et al.,* 2009; *Turquety et al.,* 2009; *Clarisse et al.,* 2011]. As far as O_3 is concerned, vertical information has been demonstrated to be sufficient to study separately stratospheric O_3 [*Scannell et al.,* 2012], O_3 in the upper troposphere/lower stratosphere [*Barret et al.,* 2011] and O_3 in the troposphere [*Boynard et al.,* 2009; *Dufour et al.,* 2010; *Wespes et al.,* 2012].

3.2.2. Retrievals

The IASI level 1C radiance data (1.3 million spectra per day) are distributed by EumetCast, the EUMETSAT's Data Distribution system and global distributions of O_3 vertical profiles are retrieved in near real time using an exclusive radiative transfer and retrieval software for the IASI O_3 product, the Fast Optimal Retrievals on Layers for IASI (FORLI-O_3) [*Hurtmans et al.,* 2012]. FORLI radiative transfer model uses pre-calculated tables of absorbance of the O_3 band (1025–1075 cm^{-1}) at different pressures and temperatures. It provides profiles over 39 layers from the surface up to 39 km based on the inversion scheme of the Optimal Estimation Theory [*Rodgers,* 2000]. Details and description of FORLI are given by *Hurtmans et al.* [2012] and a comparison of performances with other retrieval algorithms is provided by *Dufour et al.* [2012]. The IASI FORLI-O_3 observations are selected for scenes with cloud coverage below 13%, and with RMS of the spectral fit residual lower than 3.5 x10^{-8} W/cm^2.sr.cm^{-1}. The O_3 apriori profile (plotted in black in Figure 1) and associated apriori covariance matrix are constructed from the McPeters/Labow/Logan climatology of O_3 profiles, which combines long term satellite limb measurements and measurements from ozone sondes [*Turner,* 2004; *Hurtmans et al.,* 2012]. The constraint on the measurement has an average value of 2 x 10^{-8} W/(cm^2.sr.cm^{-1}) which is close to the instrumental noise. Profiles and partial column products have been validated and compared with available ground-based, aircraft, O_3 sonde and other satellite observations [*Anton et al.,* 2011; *Gazeaux et al.,* 2012; *Parrington et al.,* 2012; *Pommier et al.,* 2012]. These analysis show a good agreement in the troposphere (below 10 km) and middle stratosphere (25–40 km), where the differences are lower than 10% on average. However a significant positive bias of about 10–26% is found between 10 and 25 km. The same bias is reported when using different retrieval algorithms [*Dufour et al.,* 2012].

Interestingly, *Eremenko et al.* [2008] have shown that it was possible to study, with infrared sounders, the variation of the tropospheric O_3 column around cities in particular since high thermal contrast (the temperature difference between that of the surface and that of the first atmospheric layer), and thus more information in the boundary layer, is usually associated to the spring-summer photochemical pollution events.

We plot in Figure 1 O_3 vertical profiles (panel (a)) and the corresponding averaging kernel functions for the merged 0-8 km columns (panel (b)) for IASI observations recorded during

4

January and June 2011 above the urban regions of Table 1. Vertical profiles in panel (a), show an expected higher O_3 mixing ratio values in June than in January. A significant increase in surface O_3 values between January and June is recorded for all the cities, reflecting high surface O_3 production in summer along with a high thermal contrast. In this study, we use IASI day observations of the 0-8 km tropospheric O_3 column since the information content of IASI data is shown to be higher during the day [*Clerbaux et al.,* 2009].
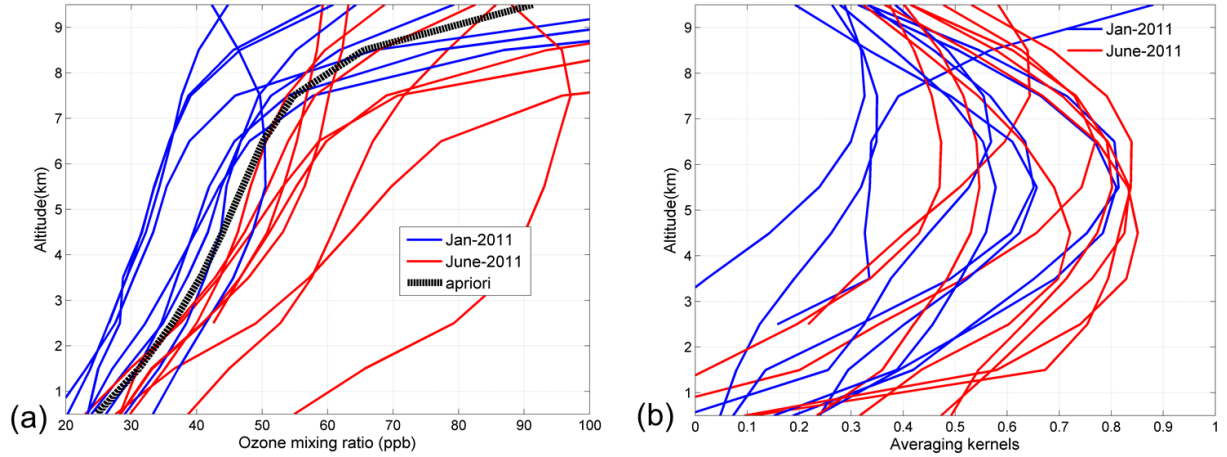
Figure 1. (a) IASI mean O_3 mixing ratio (ppb) profile for the urban cities listed in Table 1 during January 2011 (in blue) and June 2011 (in red), with the apriori profile plotted in black. (b) Averaging kernel functions for the merged 0-8 km IASI O_3 partial columns for the same locations and period. Note that some cities have altitudes > 0.

Panel (b) shows that the averaging kernels are more sensitive to the lower troposphere in summer because of higher surface temperature and better thermal contrast, leading to a smaller contribution of the apriori to the retrieved profiles. We chose the 0-8 km column because it provides above 0.5 degrees of freedom (the trace of the averaging kernel matrix) in the troposphere and avoids having to define a variable tropopause height, which impacts on quantifying the O_3 content in the troposphere [*Held,* 1981; *Bethan et al.,* 1996; *Hoinka,* 1997; *Reichler et al.,* 2003]: since the cities selected for this study (see Table 1) fall in a latitude range between 19° and 41^oN, this choice thus provides a good mean to maximize the tropospheric information content while minimizing the stratospheric contamination.
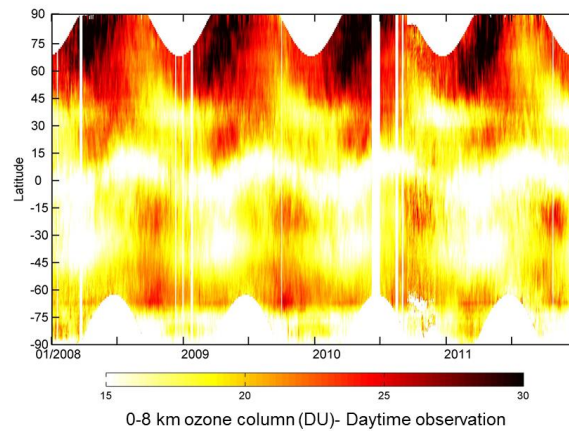
Figure 2. Latitude-time plot of zonally-averaged 0-8 km O_3 column between 2008 and 2011 for the IASI day time observations. White vertical lines correspond to days with no data.

Figure 2 shows the latitudinal variation of the 0-8 km O_3 column over the 4 years of the study. It shows that the selected 0-8 km O_3 column captures well the signature of tropospheric O_3 at mid-latitudes. The high values detected in the northern high latitudes are explained by the integration of stratospheric air into the 0-8 km column due to lower tropopause height especially in winter as well as residual stratospheric intrusions, which injects O_3 rich-air below 8 km column the rest of the year. High concentrations are found in the latitudes between $0°$ and $45°N$, where the main anthropogenic sources of tropospheric O_3 are located. On the other hand, the high values detected between $0°$ and $45°S$, correspond likely to the biomass burning source of O_3. The Figure also shows that the magnitude of the seasonal variation of the O_3 column over the period 2008-2011 is smaller for the Southern Hemisphere (SH) in comparison with the NH all year long. The highest detected O_3 values in the two hemispheres are in spring (March-April-May for NH and September-October-November for SH) for the 4 year span of 2008-2011, which coincides to the period where the intrusions from the stratosphere are the highest.

The O_3 column changes according to the latitude and season. High values are especially detected in populated areas in mid-latitudes due to the high emission of O_3 precursors and the photochemical production of O_3, as seen in Figure 3, which represents the monthly averaged 0-8 km O_3 column over a grid of $0.5°x0.5°$. The weakest values for the O_3 tropospheric column are observed in the high and mid-latitudes of the SH as well as around the tropics, all year long except when fires occur. For the months of January and June, high O_3 concentrations are observed in high latitudes of the NH, corresponding to the stratospheric intrusion into the 0-8 km column. Photochemical production of O_3 is better highlighted during the month of June, notably in mid-latitudes of the NH. The Figure also shows the transport of O_3, between Northern America and Europe, Southern America and Africa, as well as the transport of pollution from China to North America.
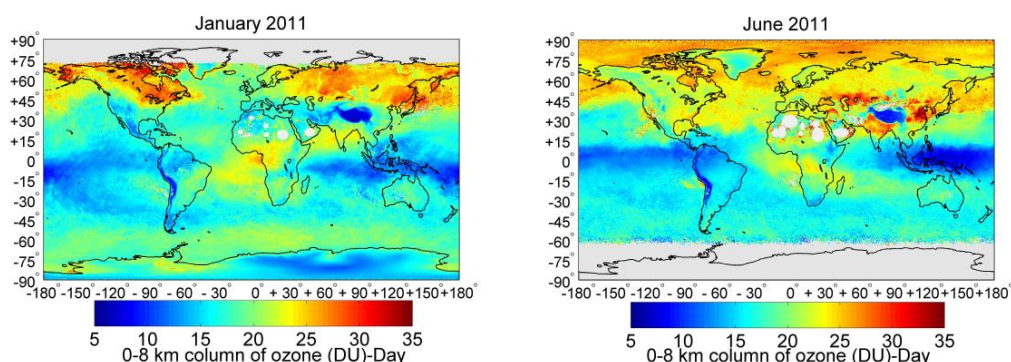
Figure 3. IASI day-time tropospheric O_3 column averaged over a grid of $0.5°x0.5°$ for the months of January and June 2011. The white areas over the desert in North Africa and Saudi Arabia correspond to a filter applied on poor spectral fits, because of emissivity issues in the FORLI radiative transfer.

3.3. GOME-2 Nitrogen Dioxide Measurements

3.3.1. Instrumentation

In this study, we analyze the relationship between the tropospheric O_3 columns retrieved from IASI and GOME-2 NO_2 tropospheric columns in a polluted environment. We use GOME-2 data since it is on board of the MetOp-A platform as well, and offer one of the first opportunities to study the O_3-NO_2 relationship with coincident measurements. GOME-2 is a

nadir-scanning UV/visible spectrometer with a swath width of 1920 km with a nominal ground pixel size of 80x40 km^2 which allows global coverage every 1.5 days. The spectral range covered by the GOME-2 instrument is from 240 to 790 nm distributed on 4 main optical channels, with a spectral resolution between 0.26 nm and 0.51 nm [*Munro et al.,* 2006; *Valks et al.,* 2011].
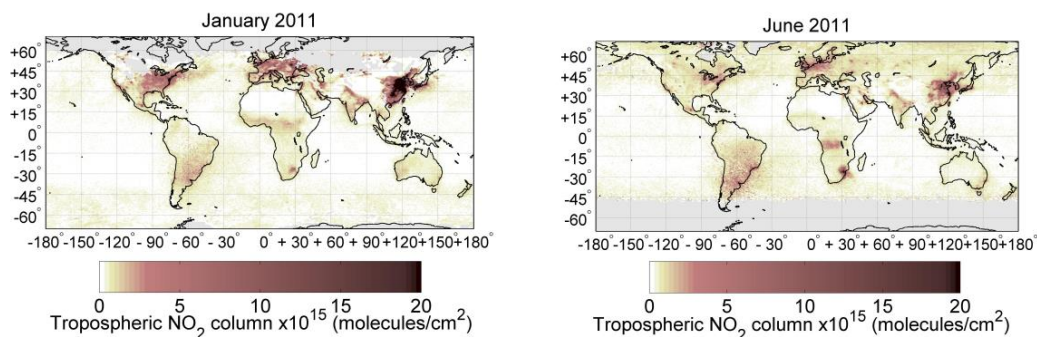
Figure 4. Monthly averaged NO$_2$ tropospheric column over a 0.25^{o}x0.25^o grid for January and June 2011 as seen by GOME-2.

3.3.2. Retrievals

The operational tropospheric NO$_2$ product is provided by the German Aerospace center, in the framework of the EUMETSAT O3M-SAF (Satellite Application Facility on Ozone and Atmospheric Chemistry Monitoring). The differential optical absorption spectroscopy (DOAS) method is used to determine NO$_2$ slant columns from GOME-2 (ir)radiance data in the 425-450 nm range. Initial total NO$_2$ columns are computed using stratospheric air mass factors, and GOME-2 derived cloud properties are used to calculate the air mass factors for scenarios in the presence of clouds. To obtain the stratospheric NO$_2$ component, a spatial filtering approach is used. Tropospheric air mass factors are computed using monthly averaged NO$_2$ profiles from the MOZART-2 chemistry transport model [*Valks et al.,* 2011]. Figure 4 shows the GOME-2 tropospheric NO$_2$ column during January and June 2011. Anthropogenic sources of NO$_2$ are notably detected in mid-latitudes especially near populated regions with high anthropogenic activity such as in Northern America, Europe, and Eastern Asia. In comparing the two Hemispheres, we note that the NH has in both months larger NO$_2$ concentrations. This is also seen in Figure 5 that shows the seasonal variation over the 4 years of the study in the NH and SH. The magnitude of the tropospheric NO$_2$ column is larger in the NH than in the SH, all year long, for the 4 year-period. The highest values are detected in winter for each Hemisphere, while the lowest values are in summer. Moreover, the Figure highlights the yearly increase in the NO$_2$ column from 2008 to 2011: while the NO$_2$ emission sources are expected to be reduced in industrialized countries, the rapid economic growth, in some countries such as China is leading to an increase in the NO$_2$ emissions [*Richter et al.,* 2005].
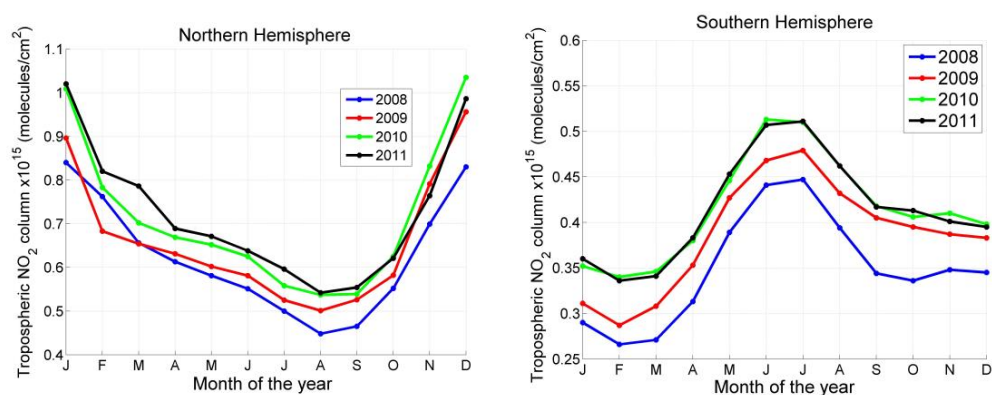
Figure 5. Seasonal variation of the tropospheric NO_2 column for the years of 2008 to 2011 in the Northern and Southern Hemispheres.

4. Results

4.1. Seasonal Cycling of Ozone in Urban Regions

O_3 in the troposphere shows a slower photochemistry in winter and faster in spring and summer [*Levy et al.,* 1985; *Klonecki and Levy,* 1997]. Figure 6 illustrates the seasonal variation of the 0-8 km O_3 column over the nine cities listed in Table 1. Both panel (a) and (b) show a typical seasonal behavior with increasing values of O_3 in late spring (April-May) that could be associated with the transport of O_3 from the lower stratosphere to the troposphere [*Logan,* 1985]. Cities located at high latitudes are subject to larger stratospheric contamination. This can be seen in winter for the first 3 cities in panel (a): Mexico City with latitude defined between 19° and 19.75^oN, has a smaller winter O_3 values than Los Angeles which location is defined between 33.5^o and 34.25^oN which in turn has a smaller winter column than Istanbul located at higher latitude (40.75^o-41.5^oN). The second prominent peak, seen for example in the cities of Los Angeles and Istanbul in summer, is likely due to high anthropogenic activity. Madrid, New York and Tehran exhibit a slightly shifted seasonal behavior, with increasing O_3 values from spring till summer and reaching its maximum in July and August where the solar activity is at its peak. Lower summer-time values of O_3 such as in Los Angeles and New York could be due to the photochemical destruction of O_3, phenomena that is less prominent in spring than summer [*Derwent et al.,* 1998]. Higher values are likely associated with increase in production of O_3 by its precursors and seen for example in Mexico City, Istanbul, Madrid and Tehran. Panel (b) shows cities where the summer season is the rainy one, such as in New Delhi, Shanghai and Beijing. In magnitude, the two Chinese cities presented, Shanghai and Beijing, have the highest tropospheric O_3 values, reaching 33 DU over Shanghai for the month of June 2011. The cities in panel (b), in particular New Delhi and Shanghai, are characterized by a strong depletion of O_3 values (around 8-9 DU) respectively between June on one hand and July and August on the other hand. This could be attributed to the summer monsoon, which brings clean air masses with lower values of tropospheric O_3, as well as slower photochemical activity because of clouds and the wet scavenging of O_3 precursors by rains. In New Delhi, the monsoon starts in mid June and lasts until end of August [*Varshney and Aggarwal,* 1992]. In Beijing and Shanghai, the East Asian summer monsoon falls in July-August and mid June-mid July respectively [*Wang et al.,* 2008].
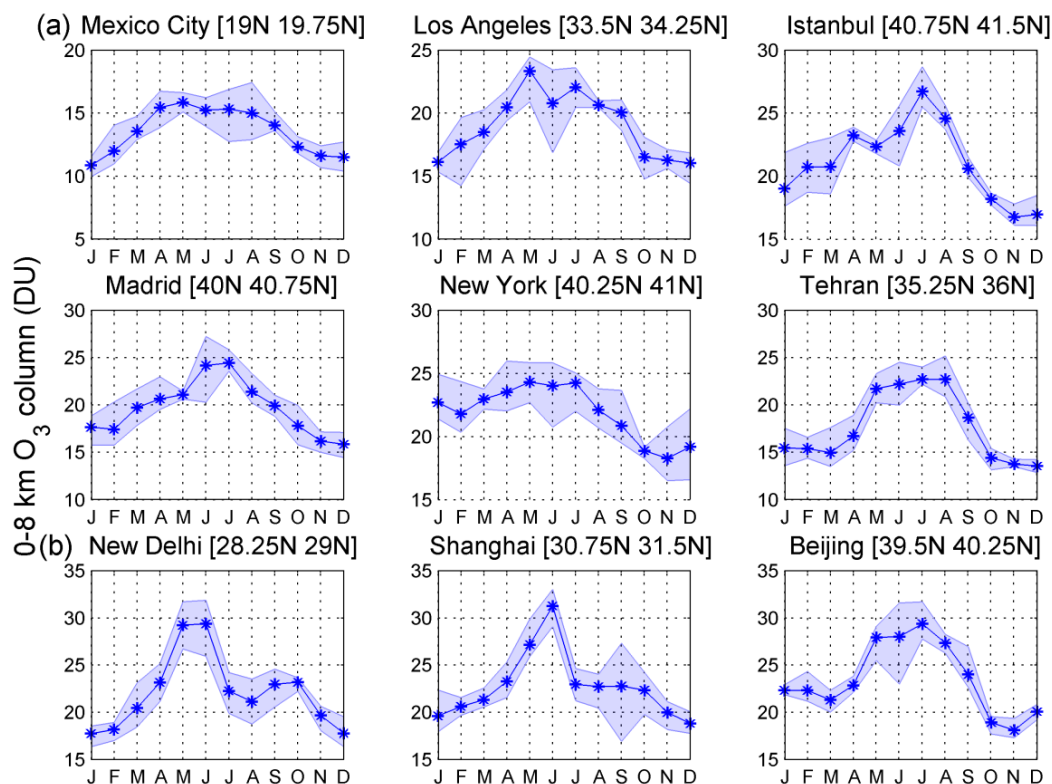
Figure 6. Seasonal distribution of the IASI 0-8 km tropospheric O_3 in selected urban regions. Results are shown for the period 2008-2011. The shaded regions show the minimum and maximum values recorded during this period.

The drop observed is latitude dependent: since New Delhi and Shanghai lie closer to tropical latitudes, the intensity of the drop is larger than the one in Beijing which is on the other hand, more susceptible to stratospheric contamination [*Dufour et al.,* 2010].

4.2. Seasonal Cycling of Nitrogen Dioxide in Urban Regions

The NO_2 lifetime is shorter than the one for O_3 and depends on many factors such as meteorological conditions and OH concentrations. Sunlight triggers OH production, causing NO_2 to be removed from the atmosphere [*Jacobs,* 2000; *Van der A et al.,* 2006]. All cities plotted in Figure 7 show indeed a minima in summer since anthropogenic NO_2 is destroyed when exposed to sunlight. On the other hand, higher values of NO_2 are expected in winter, when the days are shorter and the solar activity and OH concentrations are lower. Moreover, winter is the season with the strongest anthropogenic emissions in the NH because of heating. For all the cities, we notice that the NO_2 values are relatively higher in winter than summer. For both tropospheric O_3 and NO_2, we notice that the columns are the highest in the economic centers of China with the highest industrial activity: Shanghai and Beijing, with average values over the 4 years of 31.2 and 29.3 DU for O_3 in June and 32.2 x 10^{15} and 24.5 x 10^{15} molecules/cm^2 for NO_2 in December, respectively. It is important to note that over highly polluted regions, most of the tropospheric NO_2 accumulates in the boundary layer [*Ma et al.,* 2006], while the 0-8 km O_3 column accounts for the boundary layer contribution as well as the contribution from the long range transport in the free troposphere.
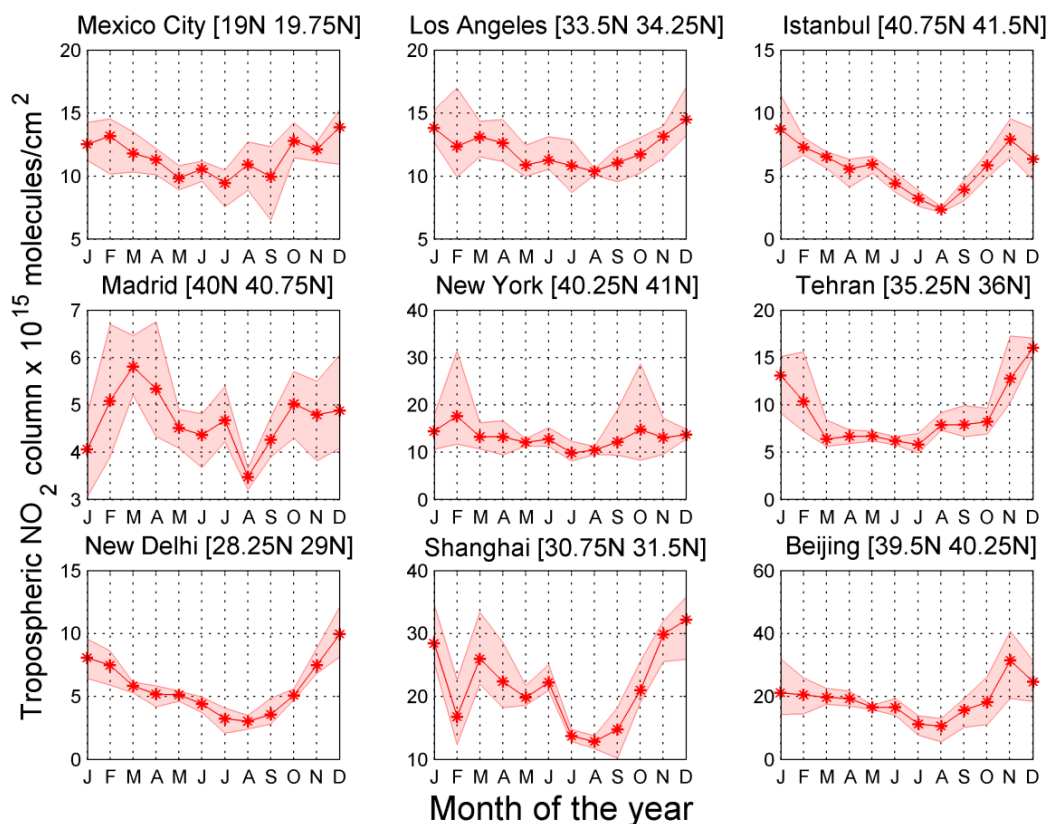
Figure 7. Same as Figure 8 but for GOME-2 tropospheric NO_2 column.

4.3. Tropospheric Ozone and Nitrogen Dioxide in Rural Regions

As explained in section 1, production of O_3 is directly related to the presence of NO_x. For low NO_x values observed in rural areas, an increase in NO_x values leads to an increase in O_3 production. This effect is better in Figure 8, which shows the O_3 0-8 km column versus the tropospheric NO_2 column over rural areas surrounding the different cities of the study for the span of 2008 to 2011.
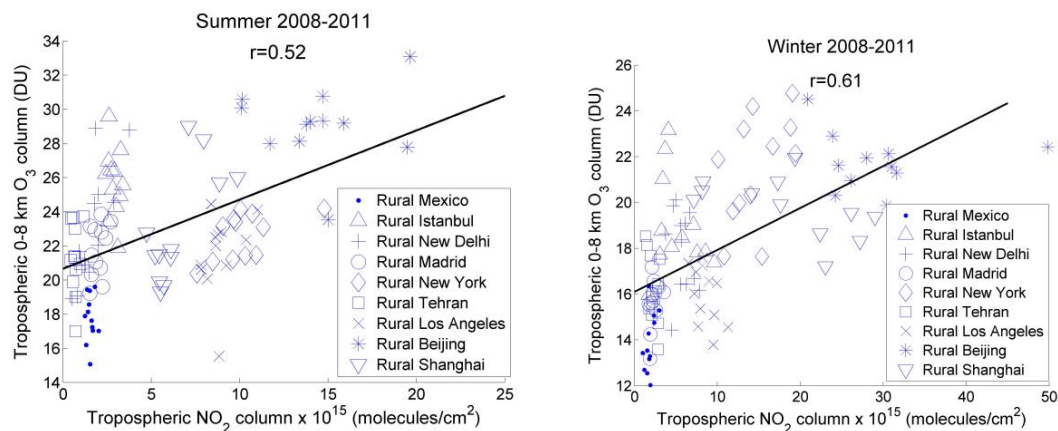
Figure 8. Summertime (June 1 to August 31) and wintertime (December 1 to February 28) O_3 and NO_2 relationship observed at rural sites for the years of 2008-2011.

The figure shows a reasonably linear behavior with a Pearson correlation coefficient of 0.52 in summer and 0.61 in winter where O_3 increases as NO_2 increases. Note that the scatter in the data is likely due in part to the difference in lifetime between the two gases: NO_2 in rural areas reflects generally local sources while O_3 is influenced by photochemical formation from NO_2, the transport from urban regions and the long range transport in the free troposphere that is integrated in the 0-8 km column, add to that the error on IASI and GOME-2 measurements and on wind directions. In fact, the approach used to determine the rural region using the prevailing wind direction may cause further uncertainties since the boundary layer winds can have strong diurnal and seasonal variations [*Lin et al.,* 2008, *Lin et al.,* 2009]. The figure represents the NOx-limited regime (section 1) since in these regions the O_3 production is partially dependent and limited by the availability of NO_2, and increases with increasing NO_2 values.

Figure 9 shows the time series from 2008 to 2011 of urban and rural tropospheric O_3 and NO_2 in the cities of Table 1. Over the 4 years, IASI observations (on the left) show a consistent seasonal behavior for O_3, both in urban and rural areas with maxima around spring-summer. Rural values observed are comparable to urban values, and exceeding the urban values (up to 7.3 DU in May 2011 in Shanghai city) several times during the study period for all the cities. GOME-2 observations (on the right) show a less marked seasonal behavior for NO_2 in the nine cities, with relatively higher winter values in comparison with summer ones. During the whole study period, rural NO_2 values were observed to be lower than urban ones, except for Beijing (due perhaps to the transport by strong winds or the availability of important local emissions). The urban-rural detected difference could be due to the absence of local NO_2 sources leading to a decrease in the rural concentrations. The largest difference is seen in New York City, where the difference reached 20.4×10^{15} molecules/cm^2 in November 2011.

4.4. Case Study of the Beijing Olympic Games of 2008
In this part of the study, we focus on the analysis of the tropospheric NO_2 and O_3 column within China by studying the case of the Olympic Games (8–24 August 2008) and the Paralympics (9–17 September 2008). Previous studies have shown, at different background sites, up to 200 km away from urban centers in China, a significant transport of O_3 and enhancement in the surface O_3 [*Xu et al.,* 2008]. For the past few decades, Chinese cities, such as Beijing, have been suffering from deterioration of air quality, because of the massive population and industrial growth [*Hao and Wang,* 2005]. Strict emissions control measures on vehicles and industries have been implemented between July and September 2008 for the summer Olympics and Paralympics games in Beijing. The World Health Organization 2000 Air Quality Guidelines were used as standards for the Beijing's strategy to control air quality [*UNEP,* 2009]. From July 1 to September 20, these standards were applied on circulating vehicles and traffic was reduced by 22% during the Olympics [*Wang et al.,* 2009]. Strict restrictions were applied on polluting industries in Beijing and surrounding provinces, starting August 8th, the first day of the Olympics [*Li et al.,* 2009]. These standards do not include surface O_3 limitations, however because of the limitations on NO_2, O_3 values were expected to be indirectly affected. During this period, the Ozone Monitoring Instrument showed a significant decrease of around 60% in NO_2 concentrations [*Mijling et al.,* 2009]. After the Olympic Games, NO_2 values were observed to return comparable to the years before [*Witte et al.,* 2011].
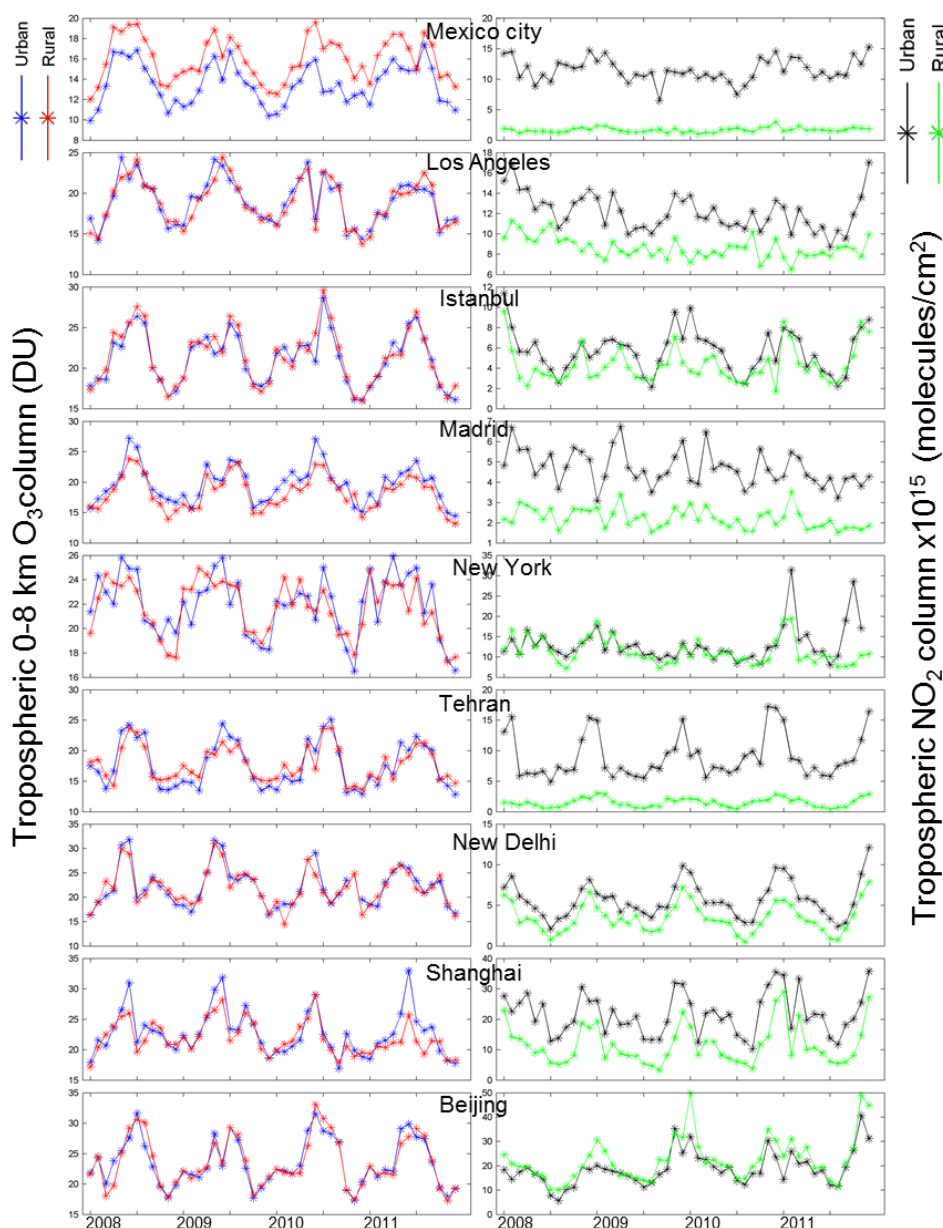
Figure 9. Time series (January 2008-December 2011) for urban and rural tropospheric O_3 (left) and NO_2 (right) columns for cities listed in Table 1. Tropospheric O_3 in rural areas persists whereas the rural tropospheric NO_2 is lower.

Worden et al. [2012] also detected a significant decrease in CO between summer of 2007 and 2008 using MOPITT satellite retrievals and WRF-chem model. Upon comparing August 2006 and 2007 with the one of 2008, *Wang et al.* [2009] found a reduction of daytime O_3, SO_2, CO, and NO_y by 20%, 61%, 25%, and 21%, respectively at a rural site 100 km downwind Beijing. *Wang et al.* [2010] reported an increase of 16% in the mixing ratio of O_3 in downtown Beijing, when comparing it with the period before the restrictions on traffic emissions. *Chou et al.* [2011] found an increase of 42.2% of the averaged mixing ratio of O_3 in August 2008 compared to the one of 2006.

In this study, we compare the O_3 and NO_2 contents in summer 2008 to those of the 3 following years during the same period. Figure 10 shows the percentage difference between

2008 and the average of the years 2009, 2010 and 2011, in the tropospheric NO_2 column (on the left) and the 0-8 km column of O_3 (on the right) for the different months where the restrictions were applied. It is noted that while the effect of the air quality control for NO_2 is local and direct and shows considerable decrease in the area above Beijing, up to 54.3 % in August (see Table 2), the effect on the O_3 column is not similar. In fact, an increase of around 12% is observed in the month of July, and a slight decrease of around 5 and 6% for the months of August and September. The increase in July could be interpreted as either the O_3 was transported by winds from nearby polluted areas such as the North China Plain [*Wang et al.,* 2009, 2010], or the fact that O_3 was formed in the boundary layer since the photostationary state of the nitrogen cycle was perturbed and the reduction of the emitted NO led to an accumulation of O_3 [*Wang and Xie*, 2009].
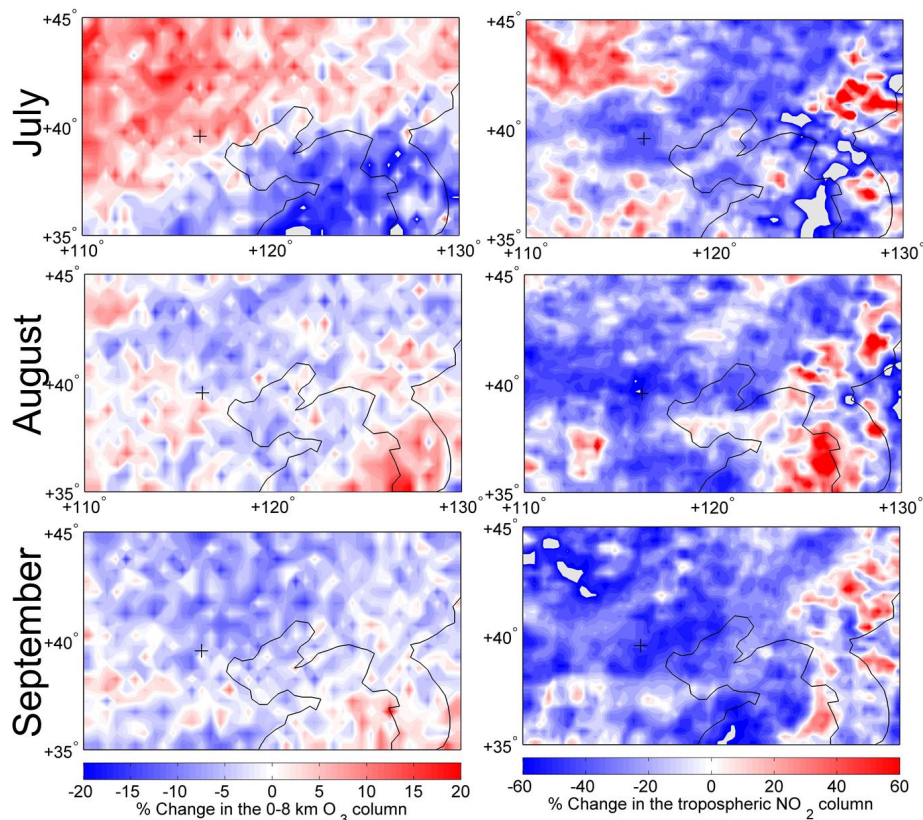
Figure 10. Percentage change in the tropospheric O_3 (left) and NO_2 (right) column between 2008 and the average of the years 2009, 2010 and 2011. Large decrease in NO_2 is detected directly above Beijing (indicated with a "+" marker) while the same effect is not detected for O_3.

Table 2. Percentage Change Between 2008 and the Average of 2009-2011 for the Area Above Beijing Which Location is Given in Table 1.

	% change of O_3	% change of NO_2
July	+11.8	-37.7
August	-5.1	-54.3
September	-6.1	-41.3

13

5. Conclusions and perspectives

In this work 4 years of tropospheric O_3 observations provided by the IASI mission are analyzed. Our results show that latitudinal and seasonal variations can be observed at the city scale. This dataset was studied along with the NO_2 product provided by the GOME-2 mission flying on the same platform, both over urban and rural regions. Our data shows that the assessment of tropospheric O_3 and NO_2 budgets in urban cities and rural regions is not straightforward and depends on complex photochemistry and transport processes. Tropospheric O_3 in different cities in the Northern Hemisphere shows a consistent seasonal behavior over the 4 years. Main features correspond to a peak in spring due to stratospheric intrusion and another higher one in summer due to the photochemical production of O_3 by its precursors. The seasonal variations of the 0-8 km O_3 column over New Delhi, Shanghai and Beijing show the influence of the Asian summer monsoon that brings clean air masses from the Pacific. Tropospheric NO_2 over the same cities shows a different seasonal behavior with higher values during winter, and lower during summer. A reasonable correlation is detected in summer and winter between O_3 and NO_2. We anticipate that analyzing the effect of VOCs on the formation of O_3 would help to better explain and assess this relationship.

By studying the case of Olympic Games of summer 2008 in Beijing, we show that even when the concentration of NO_2 was well decreased in the city and its vicinity, no significant decrease of tropospheric O_3 was observed. We also suggest to compare the IASI observations with atmospheric chemistry models to see if the spatial and temporal variability agree with the satellite observations, such as the comparison made by *Wespes et al.* [2012].

More generally, the results presented in this paper, which focus on the analyses of the 0-8 km O_3 columns, further confirm that IASI is able to discriminate the tropospheric O_3 column from the total O_3. While tropospheric O_3 forecasts nowadays rely solely on regional modeling and ground based measurements, this work is thus a new step showing that infrared satellite spectrometers, such as IASI, are capable to track pollution by tropospheric O_3 on a city scale and provide relevant information for air quality studies. From 2014 and onwards, the FORLI-O_3 profile and partial column products will be operationally distributed through the EumetCast near real time data distribution service in the framework of the O3M-SAF project.

References

Anton, M., D. Loyola, C. Clerbaux, M. Lopez, J. Vilaplana, M. Banon, J. Hadji-Lazaro, P. Valks, N. Hao, W. Zimmer, P. Coheur, D. Hurtmans, and L. Alados-Arboledas (2011), Validation of the Metop-A total ozone data from GOME-2 and IASI using reference ground-based measurements at the Iberian peninsula, Remote Sensing of Environment, 115, 1380-1386.

Barret, B., E. LeFlochmoen, B. Sauvage, E. Pavelin, M. Matricardi, and J. Cammas (2011), The detection of post-monsoon tropospheric ozone variability over south Asia using IASI data, Atmos. Chem. Phys., 11, 9533-9548, doi:10.5194/acp-11-9533-2011.

Bell, M., A. McDermott, S. Zeger, J. Samet, and F. Dominici (2004), Ozone and mortality in 95 US urban communities, 1987 to 2000, Journal of the American Medical Association, 292, 2372-2378.

Bell, M., R. Goldberg, C. Hogrefe, P. Kinney, K. Knowlton, L. B., J. Rosenthal, C. Rosenzweig, and J. Patz (2007), Climate change, ambient ozone, and health in 50 US cities, Climate Change, 82, 61-76.

Berrisford, P., D. Dee, K. Fielding, M. Fuentes, P. Kallberg, S. Kobayashi, and S. Uppala (2009), The ERA-Interim archive. ERA report series, no.1, Tech. rep., ECMWF: Reading, UK.

Bethan, S., G. Vaughan, and S. Reid (1996), A comparison of ozone and thermal tropopause heights and the impact of tropopause definition on quantifying the ozone content of the troposphere, Q. J. R. Meteorol. Soc., 122, 926-944.

Boynard, A., C. Clerbaux, P.-F. Coheur, D. Hurtmans, S. Turquety, M. George, J. Hadji-Lazaro, C. Keim, and J. Meyer-Arnek (2009), Measurements of total and tropospheric ozone from IASI: comparison with correlative satellite, ground-based and ozonesonde observations, Atmos. Chem. Phys., 9, 6255-6271.

Chappelka, A., J. Skelly, G. Somers, R. Renfro, and E. Hildebrand (1999), Mature black cherry used as a bioindicator of ozone injury, Water Air and Soil Pollution, 116 (1-2), 261-266.

Chou, C. C.-K., C.-Y. Tsai, C.-C. Chang, P.-H. Lin, S. C. Liu, and T. Zhu (2011), Photochemical production of ozone in Beijing during the 2008 Olympic games, Atmos. Chem. Phys., 11, 9825-9837, doi:10.5194/acp-11-9825-2011.

Clarisse, L., Y. RHoni, P. Coheur, D. Hurtmans, and C. Clerbaux (2011), Thermal infrared nadir observations of 24 atmospheric gases, Geophys. Res. Lett., 38, L10,802, doi:10.1029/2011GL047271.

Clerbaux, C., A. Boynard, L. Clarisse, M. George, J. Hadji-Lazaro, H. Herbin, D. Hurtmans, M. Pommier, A. Razavi, S. Turquety, C. Wespes, and P.-F. Coheur (2009), Monitoring of atmospheric composition using the thermal infrared IASI/MetOp sounder, Atmos. Chem. Phys., 9, 6041-6054.

Coheur, P.-F., B. Barret, S. Turquety, D. Hurtmans, J. Hadji-Lazaro, and C. Clerbaux (2005), Retrieval and characterization of ozone vertical profiles from a thermal infrared nadir sounder, J. Geophys. Res., 110, D24,303, doi:10.1029/2005JD005845.

Coheur, P.-F., L. Clarisse, S. Turquety, D. Hurtmans, and C. Clerbaux (2009), IASI measurements of reactive trace species in biomass burning plumes, Atmos. Chem. Phys., 9, 5655-5667.

Collins, W., D. Stevenson, C. Johnson, and R. Derwent (2000), The European regional ozone distribution and its links with the global scale for the years 1992 and 2015, Atmos. Environ., 34, 255-267.

Dee, D., S. Uppala, A. Simmons, P. Berrisford, P. Poli, S. Kobayashi, U. Andrae, M. Balmaseda, G. Balsamo, P. Bauer, P. Bechtold, A. Beljaars, L. van de Berg, J. Bidlot, N. Bormann, C. Delsol, R. Dragani, M. Fuentes, A. Geer, L. Haimberger, S. Healy, H. Hersbach, E. Holm, L. Isaksen, P. Kallberg, M. Kohler, M. Matricardi, A. McNally, B. Monge-Sanz, J.-J. Morcrette, B.-K. Park, C. Peubey, P. de Rosnay, C. Tavolato, J.-N. Thepaut, and F. Vitart (2011), The ERA-Interim reanalysis: configuration and performance of the data assimilation system, Q. J. R. Meteorol. Soc., 137, 553-597, doi:10.1002/qj.828.

Derwent, R., P. Simmonds, S. Seuring, and C. Dimmer (1998), Observation and interpretation of the seasonal cycles in the surface concentrations of ozone and carbon monoxide at Mace Head, Ireland from 1990 to 1994, Atmos. Environ., 32, 145-157.

Dufour, G., M. Eremenko, J. Orphal, and J.-M. Flaud (2010), IASI observations of seasonal and day-to-day variations of tropospheric ozone over three highly populated areas of China: Beijing, Shanghai, and Hong Kong, Atmos. Chem. Phys., 10, 3787-3801.

Dufour, G., M. Eremenko, A. Griesfeller, B. Barret, E. LeFlochmoen, C. Clerbaux, J. Hadji-Lazaro, P.-F. Coheur, and D. Hurtmans (2012), Validation of three different scientific ozone products retrieved from IASI spectra using ozonesondes, Atmos. Meas. Tech., 5, 611-630.

Duncan, B., Y. Yoshida, J. Olson, S. Sillman, C. Retscher, R. Martin, L. Lamsal, Y. Hu, K. Pickering, C. Retscher, D. Allen and J. Crawford (2010), Application of OMI observations to a space-based indicator of NOx and VOC controls on surface ozone formation, Atmos. Environ. 44, 2213-2223.

Ebi, K., and G. McGregor (2008), Climate change, tropospheric ozone and particulate matter, and health impacts, Environ. Health Perspectives, 116, 1449-1455.

Eremenko, M., G. Dufour, G. Foret, C. Keim, J. Orphal, M. Beekmann, G. Bergametti, and J.-M. Flaud (2008), Tropospheric ozone distributions over Europe during the heat wave in July 2007 observed from infrared nadir spectra recorded by IASI, Geophys. Res. Lett., 35, L18,805, doi:10.1029/2008GL034803.

Fishman, J. and J. Larsen (1987)., Distribution of total ozone and stratospheric ozone in the tropics: Implications for the distribution of tropospheric ozone. , J. Geophys. Res., 92(D6).

Finlayson-Pitts, B., and J. Pitts (1997), Tropospheric air pollution: Ozone, airborne toxics, polycyclic aromatic hydrocarbons, and particles, Science, 276, 1045-1050.

Fuhrer, J., and F. Booker (2003), Ecological issues related to ozone: agricultural issues, Environment International, 29, 141-154.

Gazeaux, J., C. Clerbaux, M. George, J. Hadji-Lazaro, J. Kuttippurath, P.-F. Coheur, D. Hurtmans, T. Deshler, M. Kovilakam, P. Campbell, V. Guidard, F. Rabier, and J.-N. Thepaut (2012), Intercomparison of polar ozone profiles by IASI/Metop sounder with 2010 concordiasi ozonesonde observations, Atmos. Meas. Tech., 5, 7923-7944.

Hao, J., and L. Wang (2005), Improving urban air quality in China: Beijing case study, J. Air Waste Manage. Assoc., 55, 1298-1305.

Held, I. (1981), On the height of the tropopause and the static stability of the troposphere, Journal of the Atmospheric Sciences, 39, 412-417.

Hoinka, K. P. (1997), The tropopause: discovery, definition and demarcation, Meteor. Z., 6, 281-303.

Hurtmans, D., P. Coheur, C.Wespes, L. Clarisse, O. Scharf, C. Clerbaux, J. Hadji-Lazaro, M. George, and S. Turquety (2012), FORLI radiative transfer and retrieval code for IASI, Journal of Quantitative Spectroscopy and Radiative Transfer, 113, 1391-1408.

Ito, K., S. De Leon, and M. Lippmann (2005), Associations between ozone and daily mortality: analysis and meta-analysis, Epidemiology, 16, 446-457.

Jacob, D. (2000), Heterogeneous chemistry and tropospheric ozone, Atmos. Environ., 34, 2131-2159.

Jacobson, M. Z. (2012), Air Pollution and Global Warming: History, Science, and Solutions, Cambridge University Press, second edition.

Karnosky, D., J. Skelly, K. Percy, and A. Chappelka (2007), Perspectives regarding 50 years of research on effects of tropospheric ozone air pollution on US forests, Environmental Pollution, 147, 489-506.

Klonecki, A., and H. Levy (1997), Tropospheric chemical ozone tendencies in CO-CH4-NOy-H2O system: Their sensitivity to variations in environmental parameters and their application to a global chemistry transport model study, J. Geophys. Res., 102, 21221-21237.

Levy, H., J. Mahlman, and W. Moxim (1985), Tropospheric ozone: The role of transport, J. Geophys. Res., 90, 3753-3772.

Li, Y., W. Wang, H. Kan, X. Xu, and B. Chen (2009), Air quality and outpatient visits for asthma in adults during the 2008 summer Olympic games in Beijing, Science of the Total Environment, 408 (5), 1226-1227.

Lin, W. , X. Xu, X. Zhang, and J. Tang (2008), Contributions of pollutants from North China Plain to surface ozone at the Shangdianzi GAW Station, Atmos. Chem. Phys., 8, 5889–5898.

Lin, W., X. Xu, B. Ge and X. Zhang (2009), Characteristics of gaseous pollutants at Gucheng, a rural site southwest of Beijing, J. Geophys. Res., 144 D2, doi: 10.1029/2008JD010339.

Liu, X., K. Chance, C. Sioris, T. Kurosu, R. Spurr, R. Martin, T. Fu, J. A. Logan, D. J. Jacob, P. Palmer, M. Newchurch, I. Megretskaia, and R. Chatfield (2006), First directly retrieved global distribution of tropospheric column ozone from GOME: Comparison with the geos-chem model, J. Geophys. Res., 111, D02,308, doi:10.1029/2005JD006564.

Logan, J. (1985), Tropospheric ozone: seasonal behavior, trends, and anthropogenic influence, J. Geophys. Res., 90, 10463-10482.

Logan, J. (1989), Ozone in rural areas of the united states, J. Geophys. Res., 94, 8511-8532.

Ma, J., A. Richter, J. Burrows, H. N Nüß, and J. A. van Aardenne (2006), Comparison of model-simulated tropospheric NO2 over China with GOME-satellite data, Atmos. Environ., 40, 593–604.

Mijling, B., R. van der A, K. Boersma, M. Van Roozendael, I. De Smedt, and H. Kelder (2009), Reductions of NO2 detected from space during the 2008 Beijing Olympic games, J. Geophys. Res., 36, L13,801, doi:10.1029/2009GL038943.

Milford, J., A. Russell and G. McRae (1989), A new approach to photochemical pollution control: implications of spatial patterns in pollutant responses to reductions in nitrogen oxides and reactive organic gas emissions, Environmental Science & Technology 23, 1290-1301.

Milford, J., D. Gao, S. Sillman, P. Blossey and A. Russell (1994), Total reactive nitrogen (NOy) as an indicator for the sensitivity of ozone to NOx and hydrocarbons. J. Geophys. Res., 99, 3533-3542.

Munro, R., M. Eisenger, C. Anderson, J. Callies, E. Carpaccioli, R. Lang, A. Lefebvre, Y. Livschitz, and A. Albinana (2006), GOME-2 on MetOp: From in-orbit verification to routine operations, in The 2006 EUMETSAT Meteorological Satellite Conference, Helsinki, Finland, EUMETSAT (pp. 48).

Parrington, M., P. I. Palmer, D. K. Henze, D. W. Tarasick, E. J. Hyer, R. C. Owen, D. Helmig, C. Clerbaux, K. W. Bowman, M. N. Deeter, E. M. Barratt, P.-F. Coheur, D. Hurtmans, Z. Jiang1, M. George, and J. R. Worden (2012), The influence of boreal biomass burning emissions on the distribution of tropospheric ozone over north America and the north Atlantic during 2010, Atmos. Chem. Phys., 12, 2077-2098, doi: 10.5194/acp-12-2077-2012.

Pommier, M., C. Clerbaux, K. S. Law, G. Ancellet, P. Bernath, P.-F. Coheur, J. Hadji- Lazaro, D. Hurtmans, P. Nedelec, J.-D. Paris, F. Ravetta, T. B. Ryerson, H. Schlager, and A. J.Weinheimer (2012), Analysis of IASI tropospheric O3 data over the arctic during POLARCAT campaigns in 2008, Atmos. Chem. Phys., 12, 7371-7389, doi:doi:10.5194/acp-12-7371-2012.

Reich, P. (1983), Effects of low concentrations of O3 on net photosynthesis, dark respiration, and chlorophyll contents in aging hybrid poplar leaves, Plant Physiology, 73, 291-296.

Reichler, T., M. Dameris, and R. Sausen (2003), Determining the tropopause height from gridded data, Geophys. Res. Lett., 30 (2), 2042, doi:10.1029/2003GL018240.

Richter, A., J. Burrows, H. Nu, C. Granier, and U. Niemeier (2005), Increase in tropospheric nitrogen dioxide over China observed from space, Letters to Nature, 437, 129-132.

Rodgers, C. (2000), Inverse methods for atmospheric sounding : Theory and Practice, Series on Atmospheric, Oceanic and Planetary Physics Vol. 2, World Scientific.

Scannell, C., D. Hurtmans, A. Boynard, J. Hadji-Lazaro, M. George, A. Delcloo, A. Tuinder, P.F. Coheur, and C. Clerbaux (2012), Antarctic ozone hole as observed by IASI/MetOp for 2008-2010, Atmos. Meas. Tech., 5, 123-139.

Schaub, M., J. Skelly, J. Zhang, J. Ferdinand, J. Savage, R. Stevenson, D. Davis, and K. Steiner (2005), Physiological and foliar symptom response in the crowns of prunus serotina, fraxinus americana and acer rubrum canopy trees to ambient ozone under forest conditions, Environmental Pollution, 133, 553-567.

Schoeberl, M. R., J. R. Ziemke, B. Bojkov, N. Livesey, B. Duncan, S. Strahan, L. Froidevaux, S. Kulawik, P. Bhartia, S. Chandra, P. Levelt, J. Witte, A. Thompson, E. Cuevas, A. Redondas, D. Tarasick, J. Davies, G. Bodeker, G. Hansen, B. Johnson, S. Oltmans, H. Vomel, M. Allaart, H. Kelder, M. Newchurch, S. Godin-Beekmann, G. Ancellet, S. Claude, H. Andersen, E. Kyro, M. Parrondos, M. Yela, G. Zablocki, D. Moore, H. Dier, P. von der Gathen, P. Viatte, R. Stubi, B. Calpini, P. Skrivankova, V. Dorokhov, H. de Backer, F. Schmidlin, G. Coetzee, M. Fujiwara, V. Thouret, F. Posny, G. Morris, J. Merrill, C. Leong, G. Koenig-Langlo, and E. Joseph (2007), A trajectory-based estimate of the tropospheric ozone column using the residual method, J. Geophys. Res., 112, D24S49, doi:10.1029/2007JD008773.

Seinfeld, J. H., and S. Pandis (2006), Atmospheric Chemistry and Physics From Air Pollution to Climate Change, second edition, John Wiley & Sons.

Sillman, S., J. Logan, and S. Wofsy (1990), The sensitivity of ozone to nitrogen oxides and hydrocarbons in regional ozone episodes, J. Geophys. Res., 95, 1837-1851.

Sillman,S. (1999), The relation between ozone, NOx and hydrocarbons in urban and polluted rural environments, Atmos. Env., 33, 1821-1845.

Tie, X., S. Chandra, J. R. Ziemke, C. Granier and G. P. Brasseur (2007), Satellite Measurements of Tropospheric Column O3 and NO2 in Eastern and Southeastern Asia:Comparison with a Global Model (MOZART-2), J. Atmos. Chem., 56:105-125,doi 10.1007/s10874-006-9045-7.

Turner, D. (2004), Systematic errors inherent in the current modeling of the reflected downward flux term used by remote sensing models, Appl. Opt., 43(11), 2369–2383, doi:10.1364/AO.43.002369

Turquety, S., D. Hurtmans, J. Hadji-Lazaro, P.-F. Coheur, C. Clerbaux, D. Josset, , and C. Tsamalis (2009), Tracking the emission and transport of pollution from wildfires using the IASI CO retrievals: analysis of the summer 2007 Greek fires, Atmos. Chem. Phys., 9, 4897-4913, doi:10.5194/acp-9-4897-2009.

(UNEP), U. N. E. P. (2009), Independent environmental assessment: Beijing 2008 Olympic games., isbn 978-92-807-2888-0.
Valks, P., G. Pinardi, A. Richter, J.-C. Lambert, N. Hao, D. Loyola, M. Van Roozendael, and S. Emmadi (2011), Operational total and tropospheric NO2 column retrieval for GOME-2, Atmos. Meas. Tech., 4, 1491-1514.

Van der A, R., D. Peters, H. Eskes, K. Boersma, M. Van Roozendael, I. De Smedt, and H. Kelder (2006), Detection of the trend and seasonal variation in tropospheric NO2 over China., J. Geophys. Res., 111, D12,317, doi:10.1029/2005JD006594.

Varshney, C., and M. Aggarwal (1992), Ozone pollution in the urban atmosphere of Delhi, Atmos. Environ., 26 (3), 291-294.

Wang, T., and S. Xie (2009), Assessment of traffic-related air pollution in the urban streets before and during the 2008 Beijing Olympic games traffic control period, Atmos. Environ., 43, 5682-5690, doi: http://dx.doi.org.biblioplanets.gate.inist.fr/10.1016/j.atmosenv.2009.07.034.

Wang, T., W. Nie, J. Gao, L. K. Xue, X. M. Gao, X. Wang, J. Qiu, C. N. Poon, S. Meinardi, D. Blake, S. L. Wang, D. A. J., F. H. Chai, Q. Z. Zhang, and W. X. Wang (2010), Air quality during the 2008 Beijing Olympics: secondary pollutants and regional impact, Atmos. Chem. Phys., 10, 7603-7615, doi:10.5194/acp-10-7603-2010.

Wang, W., Q. Ge, J. Hao, J.and Zheng, P. Zhang, and S. Sung (2008), Rainy season at Beijing and Shanghai since 1736, J. Meteor. Soc. Japan., 86 (5), 827-834.

Wang, Y., J. Hao, M. B. McElroy, J. W. Munger, H. Ma, D. Chen, and C. P. Nielsen (2009), Ozone air quality during the 2008 Beijing Olympics: effectiveness of emission restrictions, Atmos. Chem. Phys., 9, 5237-5251.

Wespes, C., L. Emmons, D. P. Edwards, J. Hannigan, D. Hurtmans, M. Saunois, P.-F. Coheur, C. Clerbaux, M. T. Coffey, R. L. Batchelor, R. Lindenmaier, K. Strong, A. J. Weinheimer, J. B. Nowak, T. B. Ryerson, J. D. Crounse, and P. O. Wennberg (2012), Analysis of ozone and nitric acid in spring and summer arctic pollution using aircraft, ground-based, satellite observations and mozart-4 model: source attribution and partitioning, Atmos. Chem. Phys., 12, 237-259.

Witte, J., B. Duncan, A. Douglas, T. Kurosu, K. Chance, and C. Retscher (2011), The unique OMI HCHO/NO2 feature during the 2008 Beijing Olympics: Implications for ozone production sensitivity, Atmos. Environ., 45, 3103-3111.

Worden, H., J. Logan, J. Worden, R. Beer, K. Bowman, A. Clough, S.and Eldering, B. Fisher, M. Gunson, R. Herman, S. S. Kulawik, M. Lampel, M. Luo, I. Megretskaia, G. Osterman, and S. M.W. (2007), Comparisons of tropospheric emission spectrometer (TES) ozone profiles to ozonesondes: Methods and initial results, J. Geophys. Res., 112, D03,309.

Worden, H., Y. Cheng, G. Pfister, G. Carmichael, Q. Zhang, D. Streets, M. Deeter, D. Edwards, J. Gille, and J. Worden (2012), Satellite-based estimates of reduced CO and CO2 emissions due to traffic restrictions during the 2008 Beijing Olympics, J. Geophys. Res., 39, L14,802, doi:10.1029/2012GL052395.

Xu, X., W. Lin, T.Wang, P. Yan, J. Tang, Z. Meng, and Y.Wang (2008), Long-term trend of surface ozone at a regional background station in Eastern China 1991-2006: enhanced variability, Atmos. Chem. Phys., 8, 2595-2607.

Chapter 7

Summertime Tropospheric Ozone Assessment over the Mediterranean Region

7.1   Motivation

Looking closely at the global maps of tropospheric O$_3$ plotted in Chapter 5, and here in Fig. 7.1, one can notice that the Mediterranean region in summer has an interesting tropospheric O$_3$ maxima. In fact, as I will present hereafter, these summertime (JJA) maxima are recorded over the whole IASI period. To investigate the dynamics and sources leading to the O$_3$ maximum above this region, we used both IASI and the Weather Research and Forecasting model coupled with Chemistry (WRF-Chem) model [Grell et al., 2005]. The latter was compared and validated using surface stations and IASI. The results were published in the Journal of Atmospheric Chemistry and Physics in 2014, in the paper attached with this chapter in section 7.7.

7.2   Tropospheric Ozone Seasonal Variation from EMEP and IASI

The European Monitoring and Evaluation Programme (EMEP) is a scientifically based and policy driven programme under the Convention on Long-range Transboundary Air Pollu-
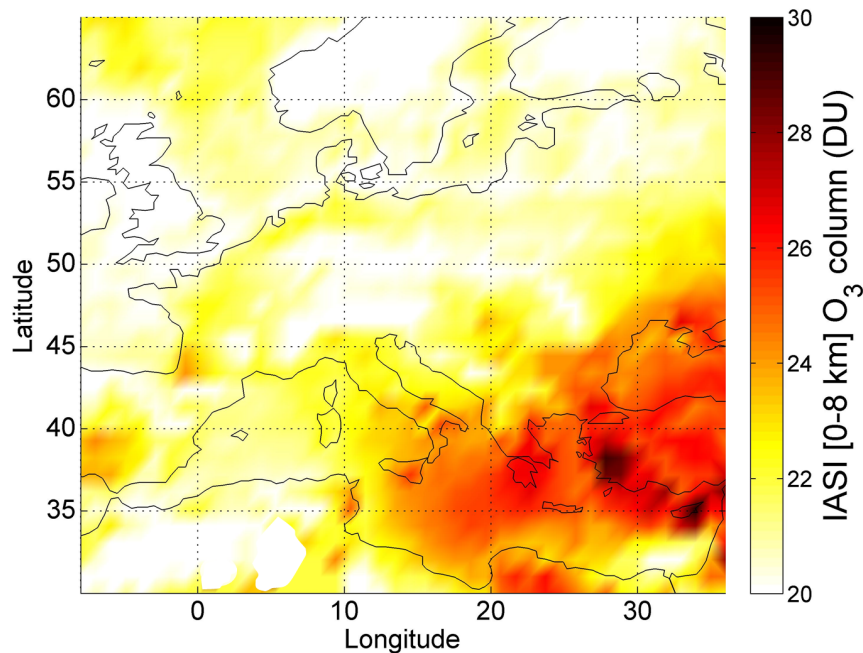
Figure 7.1: Tropospheric [0-8] km O_3 column during summer 2013. High values are recorded in the Mediterranean, especially to the east of it.

tion (CLRTAP) for international co-operation to solve transboundary air pollution problems. The stations used in this study are all rural and their location can be found in the upper panel of Fig. 7.2. The figure shows the ground O_3 as detected by the EMEP database (left axis). On the right axis, I plot the IASI [0-6] km columns. The two plots have clearly different units and are independent sets of data with different techniques, and I only want to compare them qualitatively. The EMEP data is at the ground, and the IASI data is a column, and was chosen to the nearest pixel at the same day (if available). Both show typical O_3 seasonal variation with lower values in winter and higher in spring and summer. What is interesting to note is that the 2 sets of data show parallel behavior especially in summer. Take for example the first panel: the EMEP data show a maximum in July. The same maximum is also captured by IASI, suggesting that during this period and above this area, IASI had a good sensitivity towards the surface and was able to capture the day to day variation in tropospheric O_3 column.
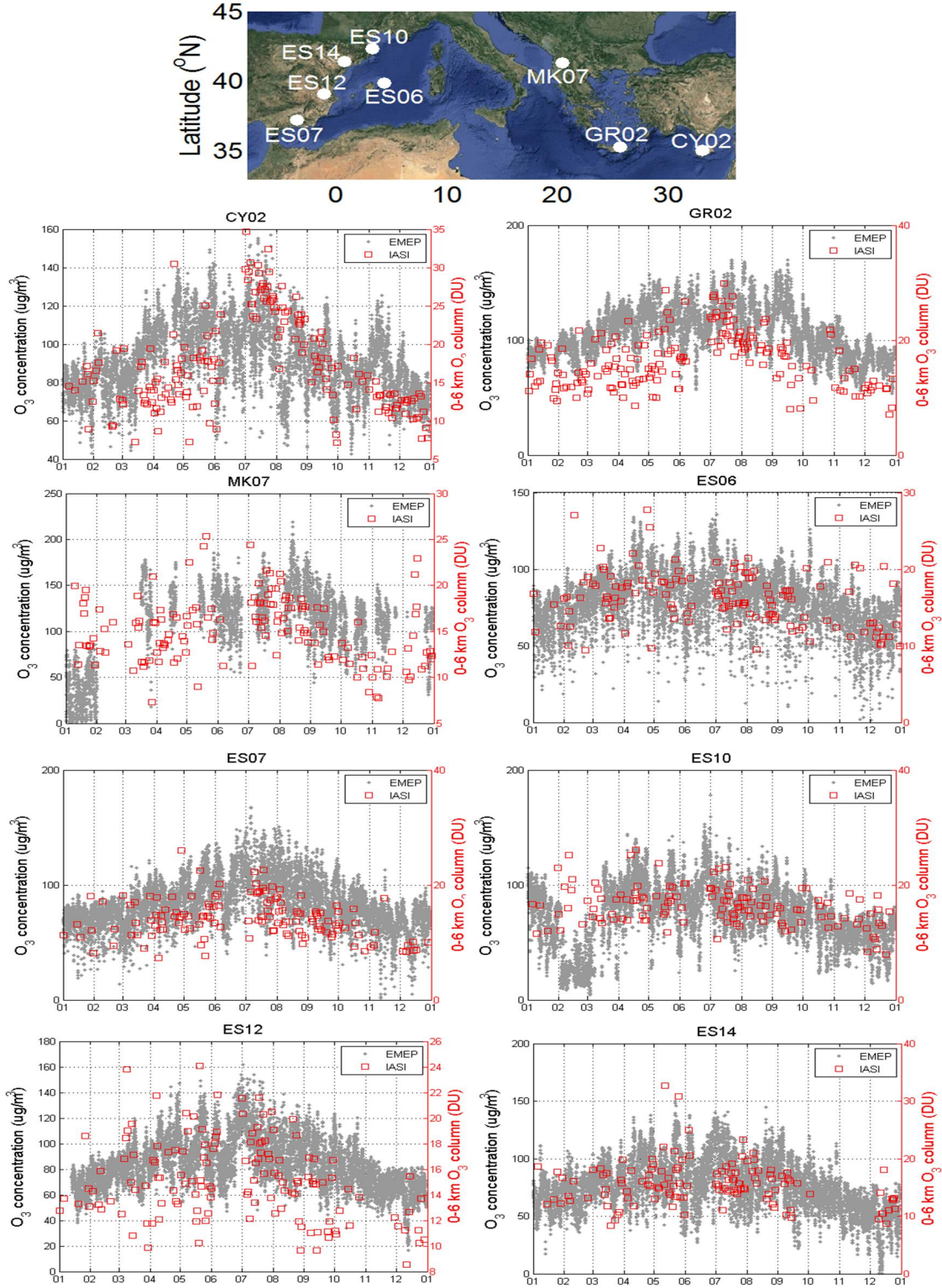
Figure 7.2: Seasonal variation during 2010 (the month number is on the x-axis) of: surface O$_3$ from the EMEP network in grey and IASI [0-6] km column in red.

7.3 Tropospheric Ozone and Nitrogen Dioxide Measurements

In order to have a closer look on the origins of the Mediterranean summer maxima, I plot in Figure 7.3 the tropospheric O_3 and NO_2 (from GOME-2) seasonal variation during 2010. For O_3, typical seasonal variation is observed. NO_2 shows the highest values in winter,
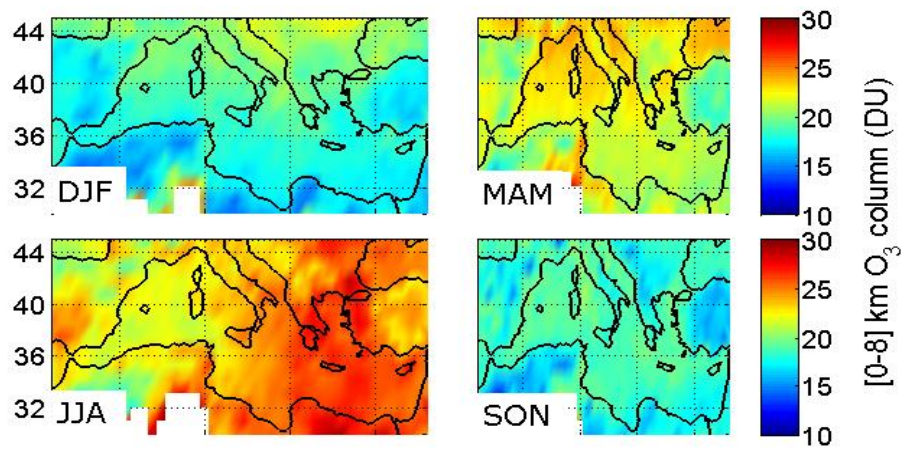
(a)
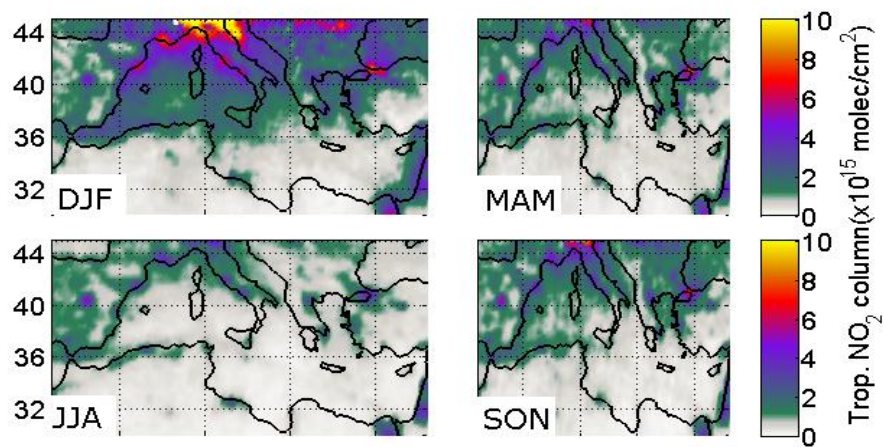
(b)

Figure 7.3: Seasonal variation during 2010 of O_3 tropospheric column as seen by IASI and NO_2 tropospheric column as seen by GOME-2

when its photochemical destruction is minimal and sources are larger. NO_2 plots are useful

to assess local anthropogenic sources of pollution in the boundary layer. One can notice that the Mediterranean region is surrounded with big cities, and also it lays close (and downwind) to Europe where the largest NO_2 sources are observed (as in DJF for latitudes above 40N). Comparing O_3 and NO_2 plots, once can see that the high O_3 values recorded in summer over the basin, are not in direct agreement with those of NO_2, suggesting that there are perhaps other sources or regimes responsible for the tropospheric O_3 increase during summer.

7.4   IASI Sensitivity above the Mediterranean

I plot in Fig. 7.4 the seasonal degrees of freedom of signal (DOFS) for the [0-8] km O_3 column, as well as the seasonal surface temperature.

Looking at the summer DOFS and surface temperature, one can see that the highest values are recorded in summer above land since summer is the season with the highest IASI sensitivity to the lower tropospheric O_3. However, over the sea, it is noticed that the DOFS above water, even in summer, are between 0.3 and 0.5, and less that 0.4 for the eastern part of the basin. Comparing averaging kernels functions (Figure 3 of the attached paper, not shown here) also shows that the IASI averaging kernels functions have the maximum sensitivity above land (in comparison with water). In fact, the air immediately above the water surface over the sea, will heat through the contact with the water. In summer the temperature is roughly constant with little variation and so is the temperature of the air just above the sea surface especially when there are no winds to change the air masses above it. This leads to a small thermal contrast and therefore lower sensitivity (and smaller DOFS in summer) in the troposphere. On the other hand in SON, for example, the temperature gradient from day to day is larger. The water heats up much more slowly than land, but air changes temperature faster than water. This leads to a larger thermal contrast, and hence larger DOFS in particular over the water.

The summertime plots with lower IASI sensitivity over the sea, led to the conclusion that in order to better analyze tropospheric O_3 especially in the lower troposphere and above the whole Mediterranean region, including the sea, one should resort to another independent set of data and for that the WRF-Chem model was used.
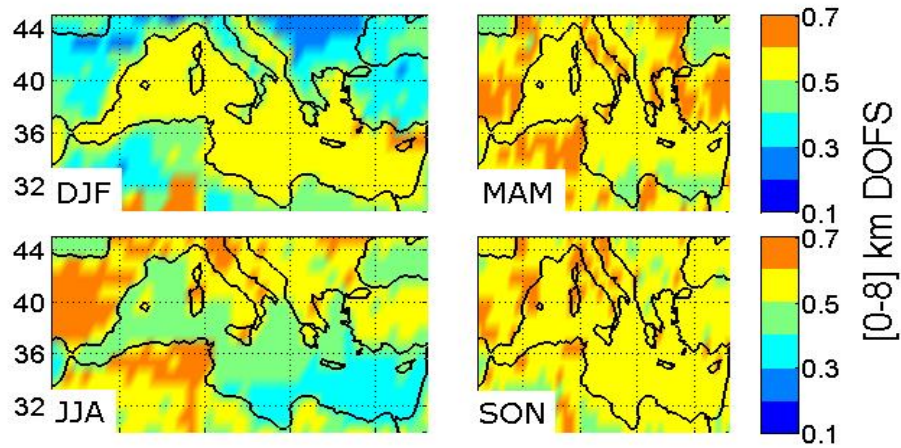
(a)
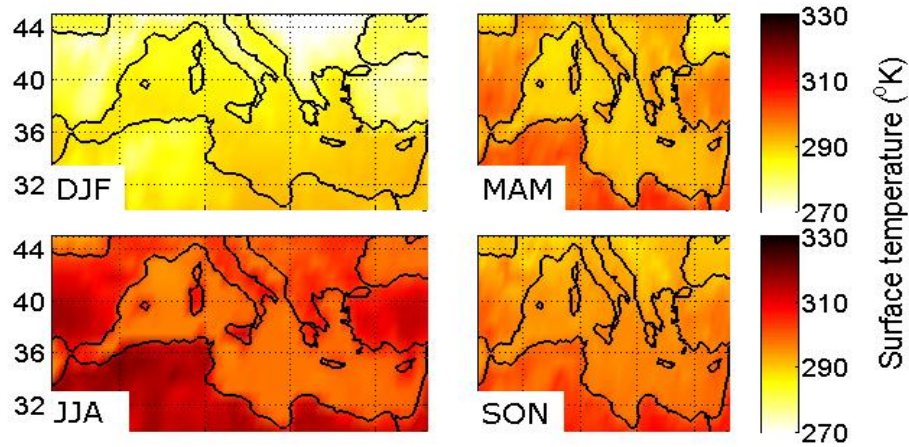
(b)

Figure 7.4: IASI seasonal variation during 2010 of the [0-8] km O$_3$ DOFS and surface temperature.

7.5 Evaluation of WRF-Chem with Meteorological Properties

The details about the WRF-Chem model, driven by analyzed fields based on assimilation of observations, are provided in the attached paper. However, the first step done to evaluate the model was to compare its outputs with meteorological properties, such as temperature, humidity, wind force and direction from surface stations. I used those of

National Oceanic and Atmospheric Administration (NOAA) available on the following url: http://gis.ncdc.noaa.gov/map/viewer/. The location of the stations used for the validation and the comparison with WRF-Chem is shown in Fig. 7.5.
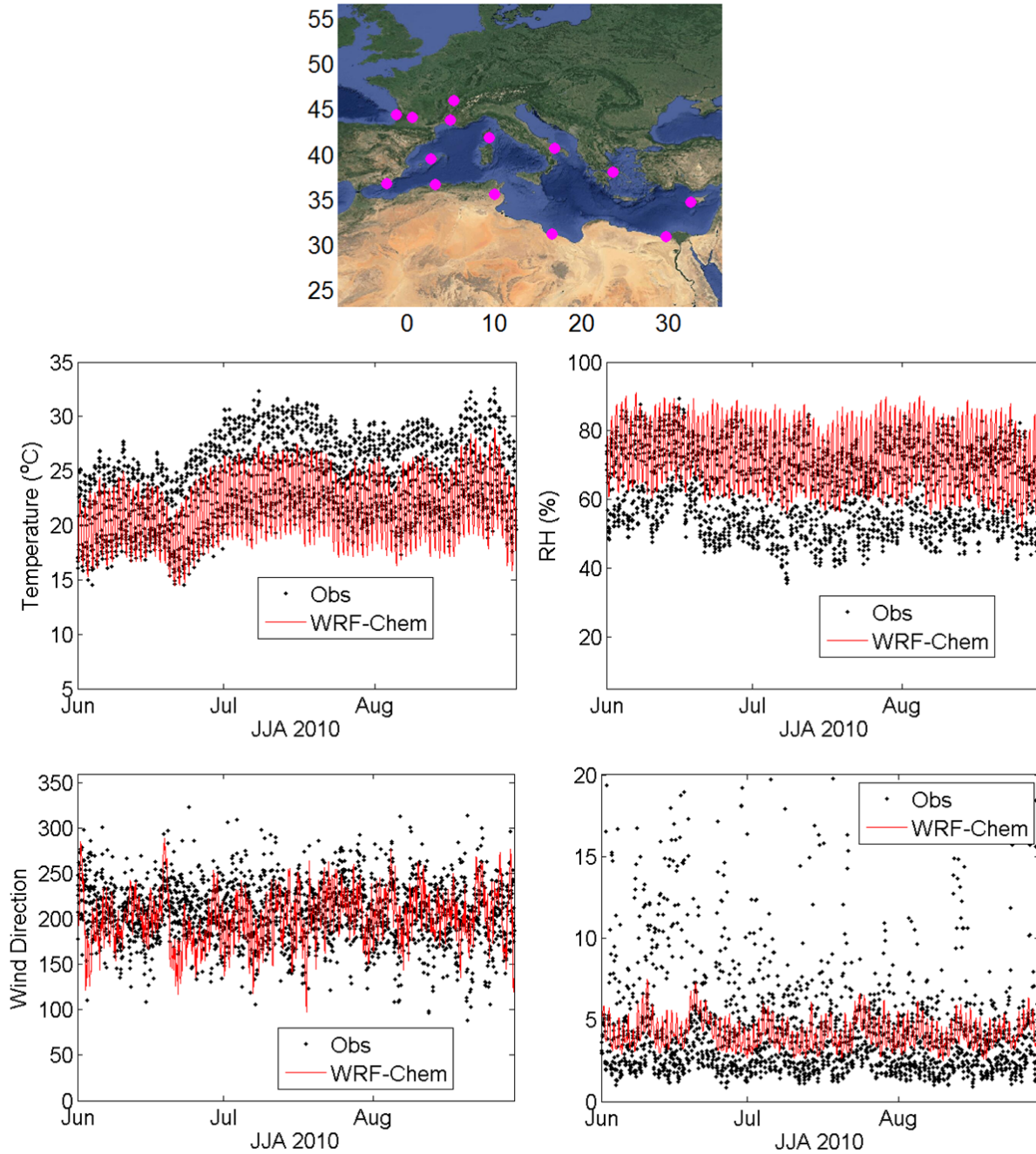
Figure 7.5: Validation of the WRF-Chem model with surface meteorological stations. The temperature, relative humidity, wind direction and speed shown here are the average of all the stations shown in the map above the plots.

The figure shows good agreement between the different stations averaged observations and WRF-Chem averaged outputs that are interpolated to the location of the stations. In general, one can deduce that the meteorological fields simulated by the model are of sufficient quality for use in chemical transport modeling. The validation of the model with the O_3 products from surface measurements and from IASI is shown in the next section.

7.6 Advantage of Using a Regional Model
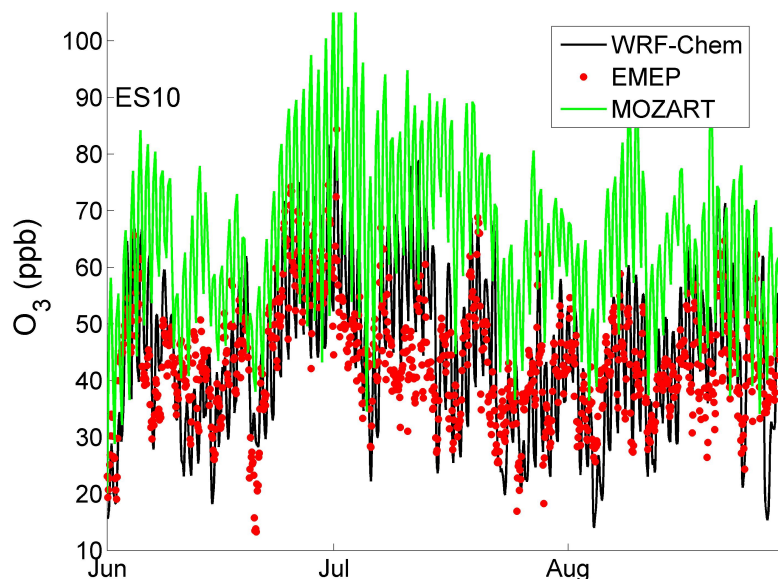
Figure 7.6: Comparison of surface O_3 from WRF-Chem, ground observation (from EMEP, station ES12 which location can be found in Fig. 2 of the published article attached to this chapter), and MOZART.

Regional models have the advantage of a finer vertical and spatial resolution. The spatial resolution chosen in the WRF-Chem run used in this study is chosen to be close to that of IASI. The finer vertical resolution allows a better representation of the boundary layer. Generally global models have 1-2 pressure levels in the boundary layer whereas in regional models, such as WRF-Chem, there are around 10. This leads to a better representation of the photochemistry in the lower troposphere with an effective representation of the pollution plumes and their transport and mixing in the boundary layer especially in an urban regime.

Moreover, when the model grid is finer the clouds are better resolved with a better representation of the complex terrain. To better see the advantage of using a regional model such as WRF-Chem, as compared a global model, I compare in Fig. 7.6 the surface O$_3$ distribution between the two, interpolated to the location of a ground O$_3$ station, taken as an example. The Model for OZone And Related chemical Tracers (MOZART) is the global chemical transport model that constrains the chemical initial and boundary conditions and provides the gas-phase chemical mechanism in the WRF-Chem model run used in this study. From this figure, one can see the advantage of using a regional model, where the local chemistry is better assessed. One can see in the figure how the WRF-Chem model is in better agreement with the EMEP ground station, and reproduces better O$_3$ at the surface than MOZART.

7.7   Published Article

The following attached article present more details on the tropospheric O$_3$ IASI columns over the period 2008-2013 with a focus on summer 2010, the period selected for the WRF-Chem run. The model run included tracers to assess the different sources of O$_3$ at different atmospheric levels. Validation analysis for the model is presented, along with an attempt to explain the sources for the summertime O$_3$ maxima in particular over the east side of the Mediterranean basin. Main results show that in the boundary layer, most of the O$_3$ is produced locally. On the other hand, in the free troposphere, the contribution of transported O$_3$ becomes more important. This O$_3$ can be either transported from outside the region at the different altitudes, or transported from the stratosphere. In fact, both IASI and WRF-Chem show evidence of stratospheric intrusions into the mid-upper troposphere over the Mediterranean, in particular to the east of it.

Summertime tropospheric ozone assessment over the Mediterranean region using the thermal infrared IASI/MetOp sounder and the WRF-Chem model

S. Safieddine[1], A. Boynard[1], P.-F. Coheur[2], D. Hurtmans[2], G. Pfister[3], B. Quennehen[1], J. L. Thomas[1], J.-C. Raut[1], K. S. Law[1], Z. Klimont[4], J. Hadji-Lazaro[1], M. George[1], and C. Clerbaux[1,2]

[1]Sorbonne Universités, UPMC Univ. Paris 06; Université Versailles St-Quentin; CNRS/INSU, LATMOS-IPSL, Paris, France
[2]Spectroscopie de l'Atmosphère, Chimie Quantique et Photophysique, Université Libre de Bruxelles (U.L.B.), Brussels, Belgium
[3]Atmospheric Chemistry Division, National Center for Atmospheric Research, Boulder, Colorado, USA
[4]International Institute for Applied Systems Analysis, Laxenburg 2361, Austria

Correspondence to: S. Safieddine (sarah.safieddine@latmos.ipsl.fr)

Abstract. Over the Mediterranean region, elevated tropospheric ozone (O$_3$) values are recorded, especially in summer. We use the thermal Infrared Atmospheric Sounding Interferometer (IASI) and the Weather Research and Forecasting Model with Chemistry (WRF-Chem) to understand and interpret the factors and emission sources responsible for the high O$_3$ concentrations observed in the Mediterranean troposphere. Six years (2008–2013) of IASI data have been analyzed and results show consistent maxima during summer, with an increase of up to 22 % in the [0–8] km O$_3$ column in the eastern part of the basin compared to the middle of the basin. We focus on summer 2010 to investigate the processes that contribute to these summer maxima. Using two modeled O$_3$ tracers (inflow to the model domain and local anthropogenic emissions), we show that, between the surface and 2 km, O$_3$ is mostly formed from anthropogenic emissions, while above 4 km it is mostly transported from outside the domain or from stratospheric origins. Evidence of stratosphere-to-troposphere exchange (STE) events in the eastern part of the basin is shown, and corresponds to a low water vapor mixing ratio and high potential vorticity.

1 Introduction

Tropospheric ozone (O$_3$) is a greenhouse gas, air pollutant, and a primary source of the hydroxyl radical (OH), the most important oxidant in the atmosphere (Chameides and Walker, 1973; Crutzen, 1973). Previous observations and studies have shown that tropospheric O$_3$ over the Mediterranean exhibits a significant increase during summertime, especially in the east of the basin (Kouvarakis et al., 2000; Im et al., 2011; Gerasopoulos et al., 2005, 2006a; Richards et al., 2013; Zanis et al., 2014). Meteorological conditions such as frequent clear-sky conditions (Fig. 1a) and high exposure to solar radiation (Fig. 1b) in summer enhance the formation of photochemical O$_3$ due to the availability of its precursors. These precursors include carbon monoxide (CO), peroxyl radicals generated by the photochemical oxidation of volatile organic compounds (VOCs) and nitrogen oxides (NO$_x$ = NO + NO$_2$). Locally, the eastern part of the basin is surrounded by megacities such as Cairo, Istanbul, and Athens that are large sources of local anthropogenic emissions. The geographic location of the basin makes it a receptor for anthropogenic pollution from Europe both in the boundary layer (Fig. 1c) and the mid-troposphere (Fig. 1d). The threshold O$_3$ value for air quality standards for the European Union (of daily maximum of running 8 h mean values of 60 ppbv) is exceeded on more than 25 days per year at a large number of stations across Europe, many of which are

Chapter 7. Summertime Trop. O$_3$ over the Mediterranean

10120   **S. Safieddine et al.: Summertime tropospheric ozone assessment over the Mediterranean region**

located to the south of Europe in the Mediterranean Basin (EEA, 2012). The dynamical processes of the summer circulation over the Mediterranean were previously attributed to the Hadley cell considered as the driver of the major subtropical dry zones. Rodwell and Hoskins (1996) argued that, during the June–August period, the zonal mean Hadley circulation has very little motion and cannot explain the dry season of North Africa and the Mediterranean. Rodwell and Hoskins (1996, 2001) suggested, through numerical simulations, that the Asian monsoon heating induces an equatorially trapped Rossby wave to its west that interacts with the midlatitude westerlies, producing a region of adiabatic descent and triggering subsidence. Long-term analysis of dP/dt (unit: $Pa\,s^{-1}$, used to represent subsidence) indeed shows a positive enhancement over the Mediterranean region (Ziv et al., 2004), making the South Asian monsoon a fundamental driver of the summer circulation over the eastern Mediterranean (Tyrlis et al., 2013). High O$_3$ values in the Mediterranean troposphere in the literature are attributed to different sources. Lelieveld et al. (2002) showed that, in the upper troposphere, Asian pollution is transported from the east by the monsoon across the Mediterranean tropopause into the lower stratosphere. Liu et al. (2011) showed with long-term model analysis that the dominant sources of O$_3$ in the Middle East (including the Mediterranean) are the transport from Asia and local production. On the other hand, Gerasopoulos et al. (2005) have shown that the mechanism that controls surface O$_3$ seasonal variability in the eastern basin during summer is mainly the transport from Europe. Using lidar measurements, Galani et al. (2003) detected an increase of 10 % of tropospheric O$_3$ between 4.5 and 6.5 km due to stratosphere-to-troposphere exchange (STE) events. Zbinden et al. (2013), using aircraft data from the MOZAIC (Measurements of OZone and water vapour by in-service AIrbus airCraft) program over 15 years (1994–2009), showed that the tropospheric O$_3$ columns in the east of the Mediterranean reached a maximum of 43.2 DU (Dobson units) during June–July. This recorded maximum exceeds the maximum recorded for Beijing for the same period, for example. Model calculation using WRF-Chem (Weather Research and Forecasting model coupled with Chemistry) and EMEP (European Monitoring and Evaluation Programme) MSC-W (Meteorological Synthesizing Centre – West) models of the eastern Mediterranean during heat waves in 2007 showed that the daily maximum near-surface O$_3$ is mostly sensitive to anthropogenic emissions of O$_3$ precursors (Hodnebrog et al., 2012). Im et al. (2011) found that the near-surface ozone mixing ratios increase almost linearly with temperature by 1.0 ± 0.1 ppb O$_3$ per kelvin. STE processes can affect the tropospheric O$_3$ budget and impact air quality if transported to the boundary layer (Fiore et al., 2002). Stratospheric intrusions have been detected in the Mediterranean region, especially on the eastern side (Galani et al., 2003; Zanis et al., 2014), because it lies to the south of the Northern Hemisphere polar jet flowing over midlatitudes (Stohl et al., 2000;
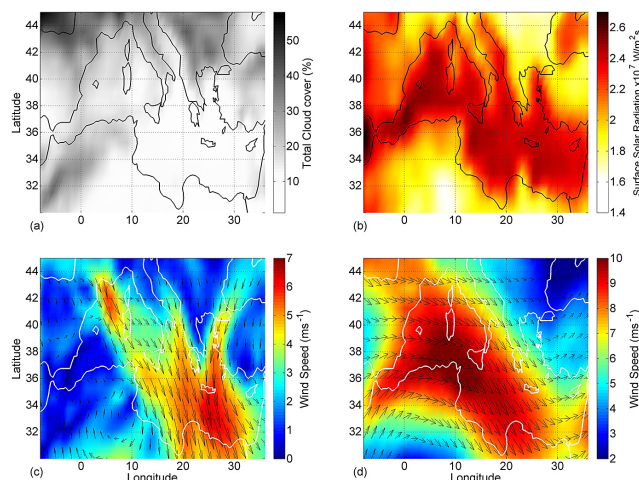
Figure 1. An example of the ECMWF (European Centre for Medium-Range Weather Forecasts) Reanalysis (ERA-Interim) for the period June-July-August (JJA) 2010 for **(a)** total cloud coverage, **(b)** 12:00 UTC solar radiation reaching the surface, **(c)** wind speed and direction averaged from the surface to 750 hPa, and **(d)** wind speed and direction averaged from 750 to 400 hPa.

Gerasopoulos et al., 2001). Understanding the factors that contribute to the O$_3$ maxima is important for developing control measures and preventing pollution buildup. In this study we analyze O$_3$ and its sources at different altitudes in the Mediterranean troposphere. Section 2 introduces the model and observations data sets used in this study. In Sect. 3, we analyze 6 years (2008–2013) of Infrared Atmospheric Sounding Interferometer (IASI) tropospheric [0–8] km O$_3$ column seasonal variation above the whole Mediterranean Basin as well as at 15 and 30° E, representative of what we henceforth refer to as "middle of the basin" and "east of the basin" respectively. In Sect. 4 we focus on summer 2010, as an example year, and validate the WRF-Chem model simulation with surface O$_3$ and IASI data, and then use the WRF-Chem model to assess the sources of O$_3$ in the troposphere. In Sect. 5, we use IASI and WRF-Chem free-tropospheric O$_3$ data to investigate potential STE events. Discussion and conclusions are given in Sect. 6.

2   Model and observational data

2.1   WRF-Chem model

In this study, we use the regional chemistry transport model WRF-Chem, version 3.2 (Grell et al., 2005), to assess the budget and spatiotemporal variability of O$_3$ over the Mediterranean during summer 2010. The model domain shown in Fig. 2a is over Europe and the Mediterranean Basin, the latter being the focus of this study (Fig. 2b). The horizontal resolution is of 50 km $\times$ 50 km and the vertical resolution is of 28 levels between the surface and 10 hPa. The

Atmos. Chem. Phys., 14, 10119–10131, 2014   **www.atmos-chem-phys.net/14/10119/2014/**

119

Chapter 7. Summertime Trop. O$_3$ over the Mediterranean

S. Safieddine et al.: Summertime tropospheric ozone assessment over the Mediterranean region   10121

Figure 2. (a) The enlarged WRF-Chem model run domain. **(b)** IASI and WRF-Chem domain used in this study. White dots correspond to the location of the EMEP ground stations and the orange strips correspond to the longitudinal transects used in Figs. 5 and 10.

meteorological initial and boundary conditions are based on the National Centers for Environmental Prediction (NCEP) Final (FNL) analyses with analysis nudging for wind, temperature, and humidity applied. Fields are provided every 6 h with 1° horizontal resolution and 27 vertical levels from the surface up to 10 hPa. The chemical initial and boundary conditions, spatially and temporally varying (6 h), are constrained by global chemical transport simulations from MOZART-4/GEOS-5 with 1.9° × 2.5° horizontal resolution (Emmons et al., 2010a). The WRF-Chem gas-phase chemical mechanism is that from Model for Ozone and Related Chemical Tracers, version 4 (MOZART-4) (Emmons et al., 2010a), which is coupled to the aerosol scheme Goddard Chemistry Aerosol Radiation and Transport (GOCART) model (Chin et al., 2002). The model also includes anthropogenic and fire emissions that are calculated offline. The anthropogenic emissions used within the WRF-Chem model were developed within the context of the ECLIPSE European project using the Greenhouse gas and Air pollution Interactions and Synerg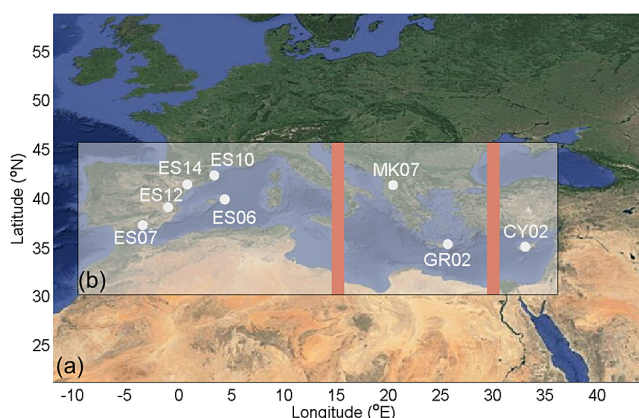ies (GAINS) model. In addition to the ECLIPSE V4.0 anthropogenic emissions, ship emissions from the RCP 6.0 scenario (Fujino et al., 2006; Hijioka et al., 2008) were used. Biomass burning emissions are obtained from the Fire Inventory from NCAR (FINN V1) (Wiedinmyer et al., 2011). Biogenic emissions are calculated online from the Model of Emissions of Gases and Aerosols from Nature (MEGAN) (Guenther et al., 2006). The WRF-Chem simulation outputs are saved every 2 h from 1 June until 31 August 2010.

In this study, we use a tagging method for O$_3$ (Emmons et al., 2012), which has been applied in global models for diagnosing contributions for individual sources to O$_3$ (e.g., Lamarque et al., 2005; Pfister et al., 2006, 2008; Emmons et al., 2010b; Wespes et al., 2012), as well as in other global and regional chemical transport models (Ma et al., 2002; Hess and Zbinden, 2013). Recently, this scheme was used for the

first time in the WRF-Chem model to quantify the contribution of transport on surface O$_3$ over California (Pfister et al., 2013). Here, we apply this scheme to keep track of the contribution of O$_3$ within the WRF-Chem domain. To determine O$_3$ sources, tagged NO$_x$ is traced through the odd nitrogen species (e.g., PAN, HNO$_3$, organic nitrates) to account for NO$_x$ recycling (Emmons et al., 2012). Two separate tracer runs were conducted with the same emissions and initial and boundary conditions. In the first one, the O$_{3\text{-ANTHRO}}$ tracer accounts for the anthropogenic regional tagged NO$_x$, while the second one, the O$_{3\text{-INFLOW}}$ tracer, accounts for tagged O$_3$ as well as all nitrogen species at the lateral boundaries of the regional model domain. The O$_{3\text{-INFLOW}}$ tracer includes O$_3$ and O$_3$ precursors from all natural (including lightning and stratospheric O$_3$) and anthropogenic sources outside the regional modeling domain. Within the regional modeling domain, O$_{3\text{-INFLOW}}$ undergoes transport and chemical processes but is not produced from sources other than from reactions including the tagged species. Since the stratospheric O$_3$ is controlled by the lateral boundaries in this version of WRF-Chem, O$_3$ from stratospheric intrusions within the regional domain would be labeled as O$_{3\text{-INFLOW}}$ as well. More details about the tagging scheme are provided in Emmons et al. (2012). Two more tracers are available to complete the O$_3$ budget: O$_3$ from biogenic sources and O$_3$ from fires. Given that their contribution to the total budget in comparison with the O$_{3\text{-INFLOW}}$ and O$_{3\text{-ANTHRO}}$ tracers is small ($< 10\,\%$), they are analyzed together in this study as "residuals" to the total budget and their contribution is defined as $100\,\% - (\text{O}_{3\text{-ANTHRO}}\,\% + \text{O}_{3\text{-INFLOW}}\,\%)$. We focus our analysis on summer 2010, which corresponds to the year of the anthropogenic emission inventory used in the model. During July–August 2010, a heat wave occurred in Russia that caused severe fires with high O$_3$ and O$_3$ precursor emissions that were probably transported to the Mediterranean region; this will be further investigated in this study.

2.2 EMEP data

The EMEP (European Monitoring and Evaluation Programme) O$_3$ hourly data (http://ebas.nilu.no/) are used to validate the WRF-Chem model at the surface. All ozone measurements within EMEP are done with UV monitors. In this study, measurements at eight ground rural background sites during the summer of 2010 are used. Details on the EMEP observation system can be found in Hjellbrekke et al. (2012). The geographic locations of the eight stations used for validation are plotted in Fig. 2, and the corresponding details are listed in Table 1. Two more station data sets were available, GR01-Aliartos (38.37° N, 23.11° E) and IT01-Montelibretti (42.1° N, 12.63° E), for the same period. We disregarded the data from these stations because they show a strong diurnal variation of 80–90 ppbv amplitude and recurrent near-zero O$_3$ concentrations throughout the period of the study, and were thus considered unreliable.

www.atmos-chem-phys.net/14/10119/2014/   Atmos. Chem. Phys., 14, 10119–10131, 2014

120

Table 1. List of geographic location of the EMEP O_3 monitoring ground stations used in this study, with the corresponding altitude above mean sea level.

Code	Station name	Latitude (° N)	Longitude (° E)	Altitude (m)
CY02	Ayia Marina	35.04	33.06	532
ES06	Mahón	39.87	4.32	78
ES07	Víznar	37.30	−3.53	1265
ES10	Cabo de Creus	42.32	3.32	23
ES12	Zarra	39.08	−1.10	885
ES14	Els Torms	41.39	0.73	470
GR02	Finokalia	35.31	25.66	250
MK07	Lazaropole	41.32	20.42	1332
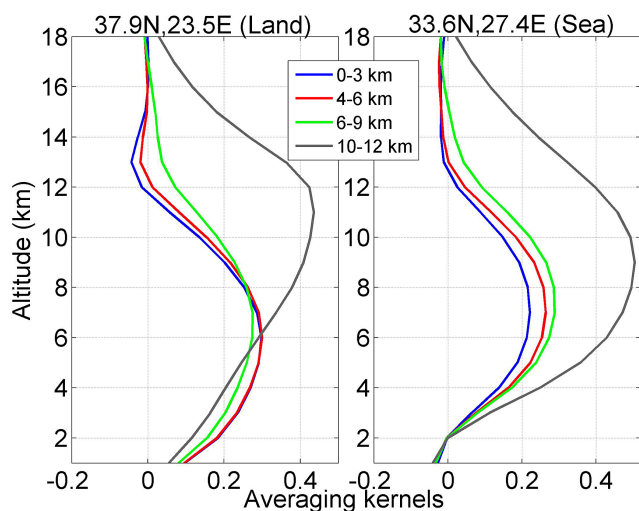
Figure 3. Random O_3 averaging kernels over the Mediterranean: the functions are for the [surface–3], [4–6], [6–9], and [10–12] km partial columns characterizing a retrieval for an observation chosen randomly above land (Greece, left panel) and above the sea (right panel) during June 2010.

2.3 IASI satellite measurements

The MetOp satellites, launched in October 2006 and September 2012, each carry an IASI instrument, which have been operationally sounding the atmosphere since June 2007 (IASI-1) and January 2013 (IASI-2). The IASI instruments are nadir-looking Fourier transform spectrometers that probe the Earth's atmosphere in the thermal infrared spectral range between 645 and 2760 cm^{-1}, with a spectral resolution of 0.5 cm^{-1} (apodized) and 0.25 cm^{-1} spectral sampling. Global distributions of O_3 vertical profiles are retrieved in near-real time using a dedicated radiative transfer and retrieval software for the IASI O_3 product, the Fast Optimal Retrievals on Layers for IASI (FORLI-O_3) (Hurtmans et al., 2012). The IASI FORLI-O_3 observations are selected for scenes with cloud coverage below 13 % and with root mean square (rms) of the spectral fit residual lower than 3.5×10^{-8} W cm^{-2} sr cm^{-1}. Details about the chemical com-

ponents that can be measured by IASI can be found in Clerbaux et al. (2009), Coheur et al. (2009), Turquety et al. (2009), and Clarisse et al. (2011). IASI has the highest O_3 sensitivity in the mid- to upper troposphere (Safieddine et al., 2013). Figure 3 shows the partial column averaging kernel function for two specific observations above land and sea during June 2010. It can be seen that the sensitivity to the O_3 profile is maximal around 4–10 km for both observations. IASI sensitivity near the surface is usually limited above the sea, as seen on the right panel of Fig. 3, and better over land, as seen in the left panel, and with corresponding better thermal contrast (7.8° above land, and 1.2° above sea). IASI is able to detect several pollutants (e.g., carbon monoxide, ammonia, sulfur dioxide, and ammonium sulfate aerosols), especially when a large thermal contrast is combined with stable meteorological conditions, leading to the accumulation of pollutants near the surface (Boynard et al., 2014).

3 Tropospheric O_3 seasonal variation as seen by IASI

To investigate the seasonal behavior of tropospheric O_3 above the Mediterranean, in Fig. 4 we plot the [0–8] km partial tropospheric O_3 column as seen by IASI during the period of 2008 to 2013. The data were averaged seasonally, and daytime observations were used since the information content of IASI O_3 data is shown to be higher during the day (Clerbaux et al., 2009). We observe a similar tropospheric O_3 seasonal behavior each year. The weakest values are observed in winter (DJF) and autumn (SON), when solar activity is minimal. Increasing values in spring (MAM) are due to the increase in O_3 production from photochemistry, buildup of winter O_3 and its precursors, transport, and/or from O_3 of stratospheric origin integrating into the troposphere. The [0–8] km column reaches a maximum in summer (JJA) due to high photochemical O_3 production, horizontal transport into the region, or STE, all of which will be investigated in detail in the following sections. Richards et al. (2013) detected a similar spatial distribution with the Global Ozone Monitoring Experiment-2 (GOME-2) during the summers of 2007 and 2008, with values exceeding 32 DU at the east of the

Atmos. Chem. Phys., 14, 10119–10131, 2014   **www.atmos-chem-phys.net/14/10119/2014/**

121
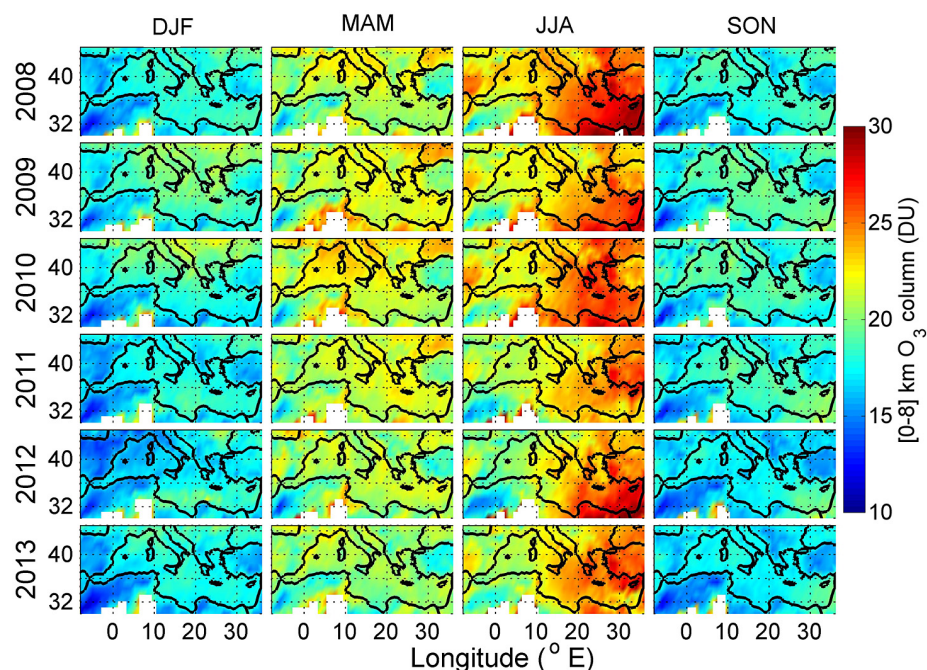
Figure 4. Six-year seasonal variation of [0–8] km integrated IASI O_3 column over the Mediterranean region for winter, spring, summer, and autumn. White pixels correspond to a filter applied to poor spectral fits because of emissivity issues in the FORLI radiative transfer above the Sahara.
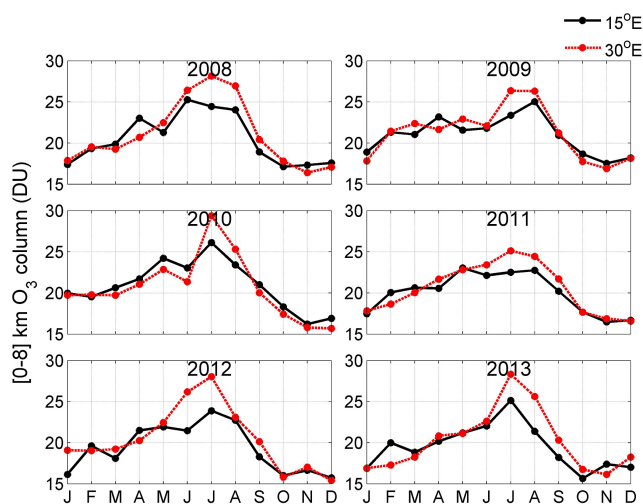
Figure 5. Six-year monthly variation of the integrated [0–8] km IASI O_3 column averaged over [30–45° N] at 15° E (in black) and 30° E (in red). Higher summer values are observed to the east of the basin at 30° E.

basin for the [0–6] km O_3 column. To further investigate the higher values detected to the east of the basin, we analyze longitudinal transects of 1° width along 15° E (representing the middle of the basin) and 30° E (representing the east of the basin), marked in orange in Fig. 2.

Figure 5 shows that, during the period of 2008 to 2013, the summers in the east of the basin, notably at 30° E (plotted in red), are marked by elevated tropospheric [0–8] km O_3 values. The difference between the two O_3 columns at the 2 different longitudes was highest (4.7 DU − 22 %) during June 2012. The highest recorded values were up to 30 DU in July 2010 at 30° E. This period coincides with the 2010 Russian heat wave (Schubert et al., 2011), which caused severe fires with high O_3 precursors emissions (R'Honi et al., 2013). Further discussion is provided in Sect. 4.2

4 O_3 budget from the WRF-Chem model during summer 2010

From this section onwards, we focus our analysis on summer 2010, the year of the anthropogenic emission inventory used in the model. We evaluate the model then we discuss the O_3 budget at different altitude levels in the Mediterranean troposphere.

4.1 Model evaluation: comparison to EMEP and IASI

The model is evaluated by comparing O_3 concentrations with ground O_3 data from the EMEP stations (Sect. 2.2) and then free-tropospheric O_3 data from IASI (Sect. 2.3).

Chapter 7. Summertime Trop. O$_3$ over the Mediterranean

10124   **S. Safieddine et al.: Summertime tropospheric ozone assessment over the Mediterranean region**

Figure 6. O$_3$ time series of EMEP and WRF-Chem data at the surface for the stations localized in Fig. 2 for the period JJA 2010.

4.1.1 Comparison to EMEP surface monitoring stations

Linear spatial interpolation was applied to WRF-Chem data in order to correlate the model outputs and the EMEP data that were averaged every 2 h to coincide with the model run output data. Figure 6 shows the individual time series of the data of the eight stations used for the validation. Table 2 shows the individual O$_3$ correlation and bias between WRF-Chem and the EMEP for each of the stations used in this study during JJA 2010. The model simulates the surface O$_3$ with a correlation ranging from 0.41 (ES06) to 0.80 (ES12) and a mean value of 0.52. Figure 6 and Table 2 show that the model reasonably well reproduces the average amplitude of the daily cycle seen in the observation. For all stations except ES06 and ES10, the model underestimates the ground observation during the summer period with a mean relative error between −23.9 and −6.4 %. The biases reported may be due to the resolution of the model resulting in a grid of around 50 km around the EMEP rural sites that may include other surface O$_3$ contributions. Other possible reasons include difficulties in simulating local flow patterns due to topography and land–sea circulation, as well as uncertainties in emissions and NO$_x$ concentrations (Pfister et al., 2013). Our results compare well with the study by Tuccella et al. (2012), which compared WRF-Chem to 75 EMEP stations over Europe during 2007 and found that hourly O$_3$ exhibits a correlation with observations ranging from 0.38 to 0.83. The largest discrepancy observed, with modeled O$_3$ values larger than

Table 2. Pearson correlation coefficient, bias and the corresponding mean relative error (MRE) of each EMEP and WRF-Chem ground station data localized in Fig. 2, for the period JJA 2010.

Station name	Corr. coeff. with WRF-Chem	Bias (ppbv)	MRE (%)
CY02	0.63	7.78	−14.2
ES06	0.41	+7.26	+20.9
ES07	0.77	−7.24	−13.4
ES10	0.72	+1.43	+3.6
ES12	0.80	−5.96	−12.7
ES14	0.78	−2.99	−6.4
GR02	0.62	−7.38	−11.3
MK07	0.57	−16.65	−23.9

80 ppbv, is for the station ES06-Mahon (39.87° N, 4.32° E), which might be due a particular uncertainty in the model emissions or dry deposition over this area.

4.1.2 Comparison to IASI observations

Averaged data for summer 2010 are used for the comparison of WRF-Chem and IASI O$_3$ [4–10] km free-tropospheric column. The modeled profile is first linearly interpolated to the time and location of the retrieval. Then, the averaging kernels associated with each IASI measurement and its a priori profile are applied to the interpolated modeled profile (of around seven layers between 4 and 10 km). Figure 7 shows

Atmos. Chem. Phys., 14, 10119–10131, 2014   **www.atmos-chem-phys.net/14/10119/2014/**

123

Chapter 7. Summertime Trop. O$_3$ over the Mediterranean

S. Safieddine et al.: Summertime tropospheric ozone assessment over the Mediterranean region 10125

Figure 7. Average [4–10] km O$_3$ column for JJA 2010 from IASI and WRF-Chem and their relative difference (%). White pixels correspond to a filter applied to poor spectral fits above the Sahara.
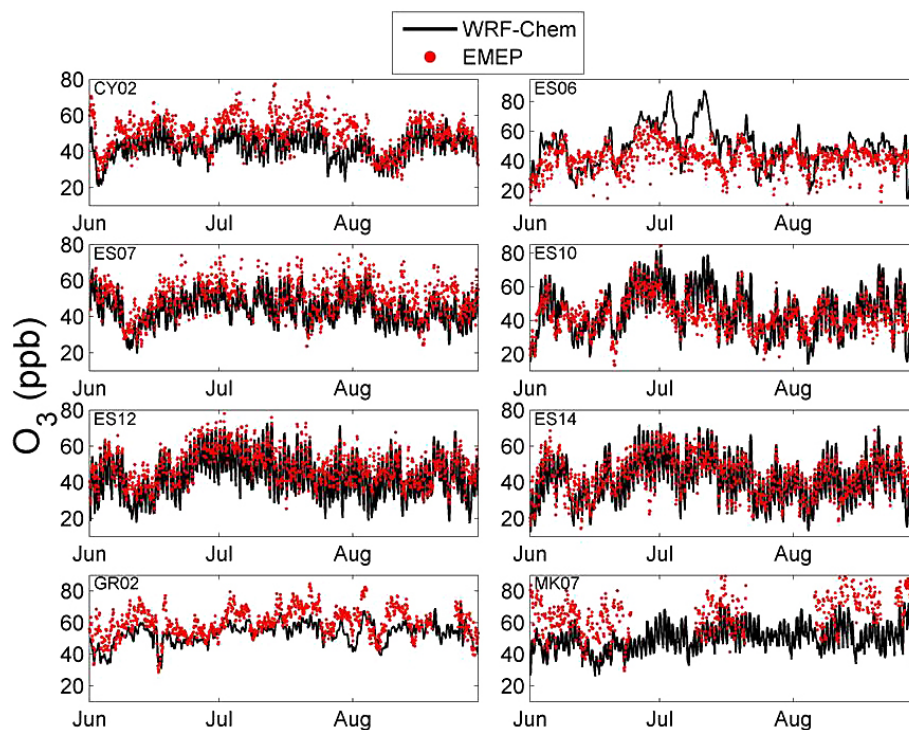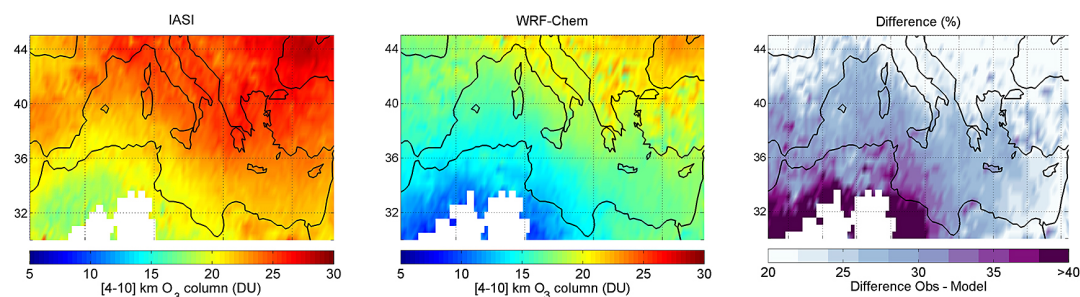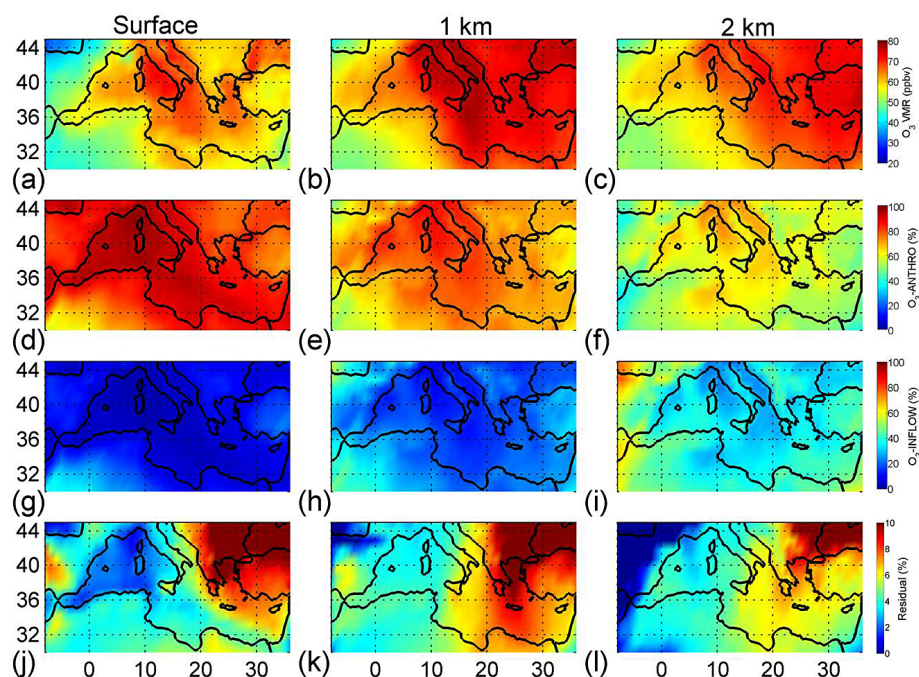

Figure 8. WRF-Chem spatial distributions of **(a–c)** O$_3$ mixing ratios (ppbv), **(d–f)** O$_3$ anthropogenic tracer relative contributions (%), **(g–i)** O$_3$ inflow tracer relative contribution, and **(j–l)** the residual $(100\% - (\text{O}_{3\text{-ANTHRO}}\% + \text{O}_{3\text{-INFLOW}}\%))$ averaged over the period JJA 2010 at the surface and 1 and 2 km. Note that the color bar for the residual plots is different.

the spatial distribution of the [4–10] km integrated IASI and WRF-Chem model O$_3$ column along with the relative differences. We chose to analyze this part of the atmosphere in particular because IASI has a better sensitivity between 4 and 10 km over both land and water as shown in Fig. 3. The model reproduces the spatial patterns seen by IASI during summer (JJA) 2010 well, with a correlation coefficient of about 0.93 and a summertime mean bias of 6.1 DU (25 %) (not shown). The model underestimation of the [4–10] km O$_3$ column might due to the difficulties in resolving the high O$_3$ concentrations observed in transported plumes over large distances (Pfister et al., 2013). On the other hand, the high discrepancies seen over northern Africa might be due to poor spectral fits from IASI above surfaces with sharp emissivity variations, particularly above the desert (Hurtmans et al.,

2012), leading to a possible overestimation of the real profile. We analyzed the IASI total retrieval error for the [4–10] km partial column (not shown here) and found that it is on average around 7 % in the model domain, and between 7 and 12 % where the discrepancies between the model and IASI are the highest.

4.2 Origins of boundary layer O$_3$ over the Mediterranean

Modeled O$_3$ concentrations are illustrated in Fig. 8a–c at the surface and 1 and 2 km during JJA 2010. At the surface, modeled O$_3$ exhibits the highest values downwind from the European continent. At 1 and 2 km the whole eastern part of the basin is characterized by high O$_3$ mixing ratios. In

Figure 9. Same as Fig. 8 but for 4, 6, and 8 km.

order to investigate possible sources of high O_3, we run the model with two different tracers of pollution, $O_{3\text{-ANTHRO}}$ and $O_{3\text{-INFLOW}}$, as described in Sect. 2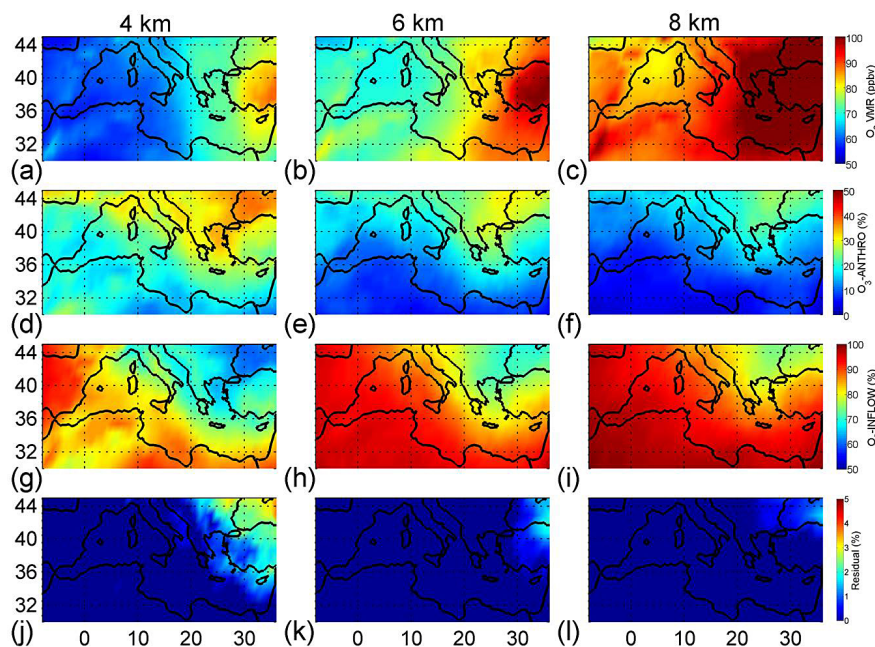.1. $O_{3\text{-ANTHRO}}$ (Fig. 8d–f) assesses the possible anthropogenic contribution of O_3 at different altitudes, while $O_{3\text{-INFLOW}}$ (Fig. 8g–i) provides an estimate of transport of O_3, including the stratosphere. The residual plots plotted in panels j–l show the completion of the O_3 budget, and represent the O_3 contribution from fires and biogenic sources. These plots show that the residual contribution is between 0 and 10 %, inferring that $O_{3\text{-ANTHRO}}$ and $O_{3\text{-INFLOW}}$ combined are responsible for 90 to 100 % of the total O_3 budget over the model domain at the different altitudes of Fig. 8. The surface shows a high contribution from the anthropogenic emission tracer ($O_{3\text{-ANTHRO}} > 85\,\%$), with almost zero contribution from the inflow tracer. This shows the importance of local emissions to the O_3 surface concentration. At 1 km, the highest contribution is also for the anthropogenic tracer (up to 75–80 %), whereas the result is mixed at 2 km between the two tracers (around 50–60 % for $O_{3\text{-ANTHRO}}$ and 40–50 % for $O_{3\text{-INFLOW}}$), suggesting that up to 50 % of the O_3 available at 2 km is being transported. The rest of the O_3 plotted in the residual plots (panels j–l) and decreasing with altitude is suggested to be from fire sources, as the extended domain (Fig. 2a) used in the study includes parts of the region hit by the Russian fires of summer 2010.

4.3 Origins of free-tropospheric O_3 over the Mediterranean

O_3 concentrations at 4, 6, and 8 km in Fig. 9a–c show that the eastern part of the basin is subject to much higher O_3 values, reaching up to 100 ppbv between 6 and 8 km (see further discussion in Sect. 5). The anthropogenic contribution decreases with altitude, whereas the O_3 inflow contribution increases. The northeastern corner of the modeled domain in panels d–f show anthropogenic contribution between 20 and 40 %. This might be due to important vertical transport and mixing in the free troposphere. These values can be correlated with the O_3 residuals plotted in panels j–l. These panels show an O_3 signature in the north eastern corner of the domain. This signature is probably related to the emitted O_3 precursors from fires sources in the model domain (Fig. 2) and lifted to the upper troposphere due to convective movements during the Russian fires of summer 2010. We can also suppose that certain anthropogenic O_3 precursors, like NO_x, near the fire sources were also transported with the same convective movements to the same part of the domain and eventually contributed to the production of anthropogenic O_3 in that region. Panels g–i show that 70 to 100 % of the available O_3 between 4 and 8 km does not come from local sources. The high values are likely due to long-range transport of pollution from outside the study region or transport of air masses from the stratosphere, which we will discuss in the following section. The low values recorded in the residual plots in panels j–l show that the O_3 budget in the free troposphere over this region is controlled almost exclusively by local anthropogenic sources and transport.

Atmos. Chem. Phys., 14, 10119–10131, 2014 **www.atmos-chem-phys.net/14/10119/2014/**

125

Chapter 7. Summertime Trop. O₃ over the Mediterranean

S. Safieddine et al.: Summertime tropospheric ozone assessment over the Mediterranean region 10127

5 WRF-Chem and IASI detection of STE events

Figures 4 and 5 and Fig. 9a–c showed that the eastern part of the Mediterranean Basin in summer is subject to high O₃ mixing ratios at 4, 6, and 8 km. In order to further investigate the sources and processes responsible for these enhancements, modeled and observed IASI O₃ vertical profiles in the troposphere were examined, during summer 2010, to try to detect possible STE events.

Figure 10 shows the tropospheric O₃ vertical distributions along 15° E (mid-Mediterranean) and 30° E (eastern Mediterranean) for IASI (panels a and b) and WRF-Chem, smoothed with the IASI averaging kernels (panels c and d) for JJA 2010. Between 4 and 8 km, panels b and d show higher values of O₃ in the eastern part of the basin (30° E), with concentrations ranging between 50 and 100 ppbv for IASI and 40 to 100 ppbv for WRF-Chem (WRF-Chem underestimates IASI as shown in Fig. 7).

Since stratospheric intrusions within the regional domain are included in the O₃-INFLOW tracer, it is useful to use other stratospheric tracers to distinguish the transport from the stratosphere. The potential vorticity (PV) and the water vapor mixing ratio (Q_{vap}) measurements can be used as markers of transport from the upper troposphere–lower stratosphere (UTLS) to the troposphere: elevated O₃ and PV, as well as low Q_{vap} values, would indicate that high free-tropospheric values are due to downward transport from the UTLS (Holton et al., 1995). Here, we study PV and Q_{vap} at 4, 6, 8, and 10 km calculated from the WRF-Chem model run parameters. Figure 11 shows that, starting at 4 km, higher PV and lower Q_{vap} values start to develop to the east of the basin. At 8 and 10 km, the highest PV values (1.5 to 2 potential vorticity units (pvu); 1 pvu = 10^{-6} m² K kg^{-1} s^{-1}) and the lowest Q_{vap} values (0–0.10 g kg^{-1}) are recorded to the east of the basin, in comparison with low PV values in the middle of and to the west of the basin (0.5–1) with high Q_{vap} values (0.1–0.15). The high PV/low Q_{vap} values to the east are in accordance with Figs. 9 and 10, strongly suggesting that this part of the basin is subject to transport from the UTLS into the free troposphere. In fact, at 30° E and around 37–39° N (panels b and d of Fig. 10), both IASI and the model suggest a stratospheric intrusion. This intrusion corresponds to PV values between 1.4 and 2 pvu at 8 km and Q_{vap} values around 0.05 g kg^{-1}. In a recent study, Zanis et al. (2014), using a 12-year climatology (1998–2009) of the ERA-interim reanalysis, also detected frequent events of STE with PV ranging between 0.4 and 1.4 pvu and specific humidity values between 0.01 and 2 g kg^{-1} between 700 and 250 hPa during July and August to the east of the basin, in accordance with our results for summer 2010 at 4, 6, and 8 km.
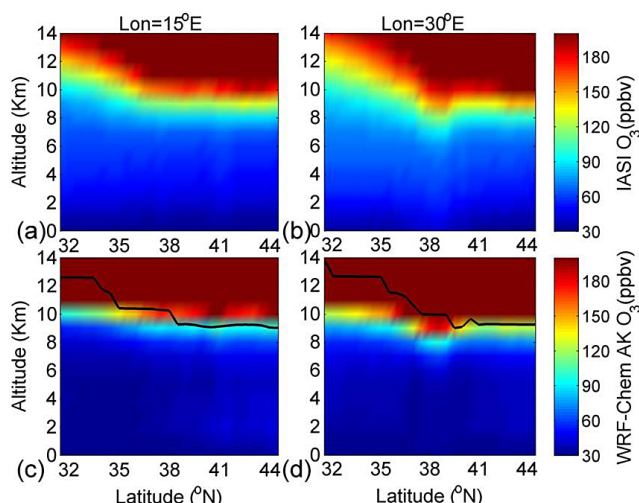

Figure 10. Mean latitude–altitude cross sections of IASI O₃ (a–b) and modeled O₃ (c–d) averaged over JJA 2010 at 15° E (left) and 30° E (right). The black line corresponds to the dynamical tropopause height.

6 Discussion and conclusions

Six years of tropospheric O₃ observations provided by the IASI mission above the Mediterranean are shown. Tropospheric [0–8] km O₃ columns show a consistent seasonal behavior over the period 2008–2013, with pronounced maxima in summer and with higher values to the east of the basin. A complementary study by Doche et al. (2014) using IASI data at 3 km height also showed 6-year recurrent O₃ summer maxima in July to the east of the basin. Since IASI has a lower sensitivity in the lower troposphere and above the sea, the anthropogenic emission contribution to the boundary layer O₃ is not well captured by the instrument. However, IASI is able to detect high tropospheric O₃ values in the free to upper troposphere, where its sensitivity is the highest, to the east of the basin during the 6 years. Focusing on summer 2010, we use IASI and the regional chemical transport model WRF-Chem to interpret these maxima. A tagging scheme is used to keep track of O₃ from anthropogenic sources in the domain (O₃-ANTHRO) and O₃ from inflow at the domain boundaries and stratosphere (O₃-INFLOW). Our results show that transport plays an essential role in the O₃ budget over the Mediterranean troposphere and that summer O₃ maxima over the region are especially recorded in the eastern part of the basin. Even though high local anthropogenic emissions are responsible for 60–100 % of O₃ in the boundary layer (surface–2 km), as demonstrated by the anthropogenic O₃ tracer of the WRF-Chem model, O₃ is mainly transported above 2 km. Kalabokas et al. (2007, 2013) showed that the highest ozone concentrations in the lower troposphere are associated with large-scale subsidence of ozone-rich air masses from the upper troposphere. However, Zanis et al. (2014), using model simulations, reported that long-distance transport and local
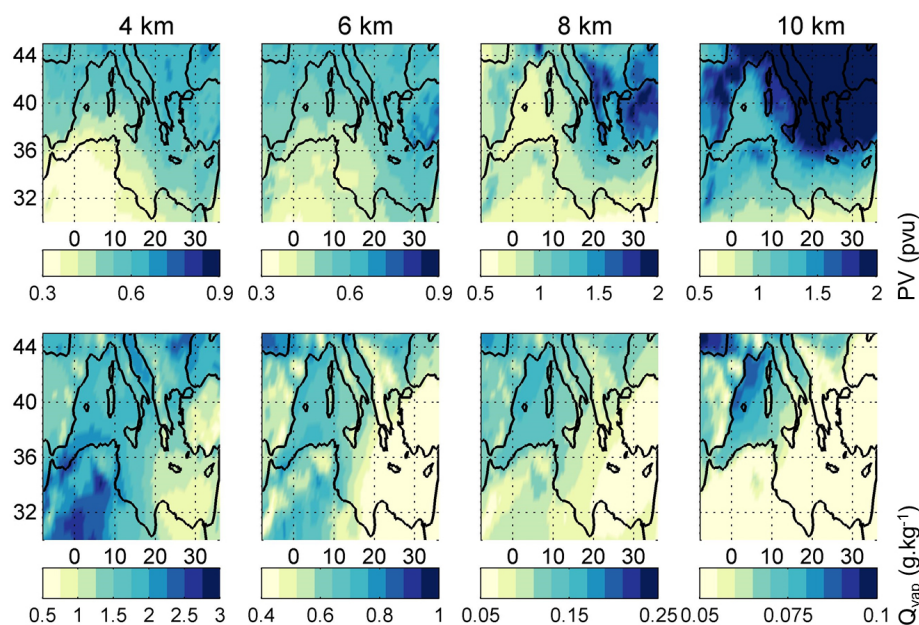
Chapter 7. Summertime Trop. O$_3$ over the Mediterranean

10128   S. Safieddine et al.: Summertime tropospheric ozone assessment over the Mediterranean region

Figure 11. WRF-Chem **(a)** potential vorticity (PV) at 4, 6, 8, and 10 km over the Mediterranean region for JJA 2010 and **(b)** the water vapor mixing ratio (Q_{vap}) for the same vertical levels and time period.

photochemical processes dominate at the low troposphere. In this study and in the free troposphere, WRF-Chem shows that vertical and lateral transport of O$_3$ (represented by the O$_{3\text{-INFLOW}}$ tracer) is responsible for 70–100 % of O$_3$ at 4, 6, and 8 km. In the eastern Mediterranean, Roelofs et al. (2003) showed important contributions to elevated O$_3$ in the middle troposphere by transport from the stratosphere. More recently, Hess and Zbinden (2013) showed that stratospheric interannual O$_3$ variability significantly drives the O$_3$ variability in the middle troposphere between 30 and 90° N, but not the overall trend, which is largely affected by transport processes. The increase in O$_3$ seen by the model and the IASI instrument in the eastern part of the Mediterranean Basin suggests that stratosphere-to-troposphere exchange (STE) events contribute to elevated ozone in the upper free troposphere. This is further shown in the WRF-Chem simulations that predict elevated potential vorticity (PV) and water vapor mixing ratio (Q_{vap}) over the same region. This result is in agreement with many previous studies (e.g., Butkovic et al., 1990; Kalabokas and Bartzis, 1998; Kalabokas et al., 2000, 2007; Kouvarakis et al., 2000; Lelieveld et al., 2002; Sprenger and Wernli, 2003; Papayannis et al., 2005; Gerasopoulos et al., 2006b; Akritidis et al., 2010; Zanis et al., 2014; Doche et al., 2014) that have shown the occurrence of STE events in the eastern Mediterranean region in summer. Since O$_3$ maxima have the potential to strongly impact regional air quality and climate (e.g., Hauglustaine and Brasseur, 2001), the present study further demonstrates the importance of quantifying and analyzing O$_3$ and its sources at different altitudes in the atmosphere. Quantification of long-term trends and distinguishing between the different sources are crucial. This

should be possible with observations and model runs over longer timescales with additional tracers to identify all O$_3$ sources.

Atmos. Chem. Phys., 14, 10119–10131, 2014   www.atmos-chem-phys.net/14/10119/2014/

127

References

Akritidis, D., Zanis, P., Pytharoulis, I., Mavrakis, A., and Kara-costas, T.: A deep stratospheric intrusion event down to the earth's surface of the megacity of Athens, Meteorol. Atmos. Phys., 109, 9–18, doi:10.1007/s00703-010-0096-6, 2010.

Boynard, A., Clerbaux, C., Clarisse, L., Safieddine, S., Pommier M., Van Damme, M., Bauduin, S., Oudot, C., Hadji-Lazaro, J., Hurt-mans, D., and Coheur, P.-F.: First simultaneous space measure-ments of atmospheric pollutants in the boundary layer from IASI: a case study in the North China Plain, Geophys. Res. Lett., 41, 645–651 doi:10.1002/2013GL058333, 2014.

Butkovic, V., Cvitas, T., and Klasinc, L.: Photochemical ozone in the Mediterranean, Sci. Total Environ., 99, 145–151, doi:10.1016/0048-9697(90)90219-k, 1990.

Chameides, W. and Walker, J. C. G.: A photochemical theory of tropospheric ozone, J. Geophys. Res., 78, 8751–8760, 1973.

Chin, M., Ginoux, P., Kinne, S., Torres, O., Holben, B. N., Duncan, B. N., Martin, R. V., Logan, J. A., Higurashi, A., and Nakajima, T.: Tropospheric aerosol optical thickness from the GOCART model and comparisons with satellite and Sun photometer mea-surements, J. Atmos. Sci., 59, 461–483, 2002.

Clarisse, L., R'Honi, Y., Coheur, P.-F., Hurtmans, D., and Clerbaux, C.: Thermal infrared nadir observations of 24 atmospheric gases, Geophys. Res. Lett., 38, L10802, doi:10.1029/2011GL047271, 2011.

Clerbaux, C., Boynard, A., Clarisse, L., George, M., Hadji-Lazaro, J., Herbin, H., Hurtmans, D., Pommier, M., Razavi, A., Turquety, S., Wespes, C., and Coheur, P.-F.: Monitoring of atmospheric composition using the thermal infrared IASI/MetOp sounder, At-mos. Chem. Phys., 9, 6041–6054, doi:10.5194/acp-9-6041-2009, 2009.

Coheur, P.-F., Clarisse, L., Turquety, S., Hurtmans, D., and Cler-baux, C.: IASI measurements of reactive trace species in biomass burning plumes, Atmos. Chem. Phys., 9, 5655–5667, doi:10.5194/acp-9-5655-2009, 2009.

Crutzen, P. J.: A discussion of the chemistry of some minor con-stituents in the stratosphere and troposphere, Pure Appl. Geo-phys., 106–108, 1385, 1973.

Doche, C., Dufour, G., Foret, G., Eremenko, M., Cuesta, J., Beekmann, M., and Kalabokas, P.: Summertime tropo-spheric ozone variability over the Mediterranean basin observed with IASI, Atmos. Chem. Phys. Discuss., 14, 13021–13058, doi:10.5194/acpd-14-13021-2014, 2014.

EEA: Air Quality in Europe – 2012 Report, European Environment Agency, ISBN:978-92-9213-328-3, Luxembourg, Office for Of-ficial Publications of the European Union, doi:10.2800/55823, 2012.

Emmons, L. K., Walters, S., Hess, P. G., Lamarque, J.-F., Pfister, G. G., Fillmore, D., Granier, C., Guenther, A., Kinnison, D., Laepple, T., Orlando, J., Tie, X., Tyndall, G., Wiedinmyer, C., Baughcum, S. L., and Kloster, S.: Description and evaluation of the Model for Ozone and Related chemical Tracers, version 4 (MOZART-4), Geosci. Model Dev., 3, 43–67, doi:10.5194/gmd-3-43-2010, 2010a.

Emmons, L. K., Apel, E. C., Lamarque, J.-F., Hess, P. G., Avery, M., Blake, D., Brune, W., Campos, T., Crawford, J., DeCarlo, P. F., Hall, S., Heikes, B., Holloway, J., Jimenez, J. L., Knapp, D. J., Kok, G., Mena-Carrasco, M., Olson, J., O'Sullivan, D., Sachse, G., Walega, J., Weibring, P., Weinheimer, A., and Wiedinmyer,

C.: Impact of Mexico City emissions on regional air quality from MOZART-4 simulations, Atmos. Chem. Phys., 10, 6195–6212, doi:10.5194/acp-10-6195-2010, 2010b.

Emmons, L. K., Hess, P. G., Lamarque, J.-F., and Pfister, G. G.: Tagged ozone mechanism for MOZART-4, CAM-chem and other chemical transport models, Geosci. Model Dev., 5, 1531–1542, doi:10.5194/gmd-5-1531-2012, 2012.

Fiore, A. M., Jacob, D. J., Bey, I., Yantosca, R. M., Field, B. D., Fusco, A. C., and Wilkinson, J. G.: Background ozone over the United States in summer: Origin, trend, and con-tribution to pollution episodes, J. Geophys. Res., 107, 4275, doi:10.1029/2001JD000982, 2002.

Fujino, J., Nair, R., Kainuma, M., Masui, T., and Matsuoka, Y.: Multi-gas mitigation analysis on stabilization scenarios using AIM global model, multigas mitigation and climate policy, En-erg. J., 27, 343–353, 2006.

Galani, E., Balis, D., Zanis, P., Zerefos, C., Papayannis, A., Wernli, H., and Gerasopoulos, E.: Observations of stratosphere-troposphere transport events over the eastern Mediterranean using a ground-based lidar system, J. Geophys. Res., 108, D128527, doi:10.1029/2002JD002596, 2003.

Gerasopoulos, E., Zanis, P., Stohl, A., Zerefos, C. S., Papastefanou, C., Ringer, W., Tobler, L., Huebener, S., Kanter, H. J., Tositti, L., and Sandrini, S.: A climatology of 7Be at four high-altitude sta-tions at the Alps and the Northern Apennines, Atmos. Environ., 35, 6347–6360, 2001.

Gerasopoulos, E., Kouvarakis, G., Vrekoussis, M., Kanakidou, M., Mihalopoulos, N.: Ozone variability in the marine boundary layer of the Eastern Mediterranean based on 7-year observations, J. Geophys. Res., 110, D15309, doi:10.1029/2005JD005991, 2005.

Gerasopoulos, E., Kouvarakis, G., Vrekoussis, M., Donoussis, C., Mihalopoulos, N., and Kanakidou, M.: Photochemical ozone production in the Eastern Mediterranean, Atmos. Environ., 40, 3057–3069, 2006a.

Gerasopoulos, E., Zanis, P., Papastefanou, C., Zerefos, C. S., Ioan-nidou, A., and Wernli, H.: A complex case study of down to the surface intrusions of persistent stratospheric air over the Eastern Mediterranean, Atmos. Environ., 40, 4113–4125, 2006b.

Grell, G. A., Peckham, S. E., Schmitz, R., McKeen, S. A., Frost, G., Skamarock, W. C., and Eder, B.: Fully coupled "online" chem-istry within the WRF model, Atmos. Environ., 39, 6957–6975, 2005.

Guenther, A., Karl, T., Harley, P., Wiedinmyer, C., Palmer, P. I., and Geron, C.: Estimates of global terrestrial isoprene emissions using MEGAN (Model of Emissions of Gases and Aerosols from Nature), Atmos. Chem. Phys., 6, 3181–3210, doi:10.5194/acp-6-3181-2006, 2006.

Hess, P. G. and Zbinden, R.: Stratospheric impact on tropospheric ozone variability and trends: 1990–2009, Atmos. Chem. Phys., 13, 649–674, doi:10.5194/acp-13-649-2013, 2013.

Hijioka, Y., Matsuoka, Y., Nishimoto, H., Matsui, M., and Kanuma, M.: Global GHG emissions scenarios under GHG concentration stabilization targets, Journal of Global Environmental Engineer-ing, 13, 97–108, 2008.

Hjellbrekke, A., Solberg, S., and Fjæraa, A. M.: Ozone mea-surements 2010 EMEP/CCC-Report 2/2012, available at: http://www.nilu.no/projects/ccc/reports/cccr2-2012.pdf (last access: 13 May 2014), 2012.

Chapter 7. Summertime Trop. O$_3$ over the Mediterranean

10130   **S. Safieddine et al.: Summertime tropospheric ozone assessment over the Mediterranean region**

Hodnebrog, Ø., Solberg, S., Stordal, F., Svendby, T. M., Simpson, D., Gauss, M., Hilboll, A., Pfister, G. G., Turquety, S., Richter, A., Burrows, J. P., and Denier van der Gon, H. A. C.: Impact of forest fires, biogenic emissions and high temperatures on the elevated Eastern Mediterranean ozone levels during the hot summer of 2007, Atmos. Chem. Phys., 12, 8727–8750, doi:10.5194/acp-12-8727-2012, 2012.

Hauglustaine, D. A. and Brasseur, G. P.: Evolution of tropospheric ozone under anthropogenic activities and associated radiative forcing of climate, J. Geophys. Res.-Atmos., 106, 32337–32360, doi:10.1029/2001jd900175, 2001.

Holton, J. R., Haynes, P. H., McIntyre, E. M., Douglass, A. R., Rood, R. B., and Pfister, L.: Stratosphere-troposphere exchange, Rev. Geophys., 33, 403–439, 1995.

Hurtmans, D., Coheur, P.-F., Wespes, C., Clarisse, L., Scharf, O., Clerbaux, C., Hadji-Lazaro, J., George, M., and Turquety, S.: FORLI radiative transfer and retrieval code for IASI, J. Quant. Spectrosc. Ra., 113, 1391–1408, 2012.

Im, U., Markakis, K., Poupkou, A., Melas, D., Unal, A., Gerasopoulos, E., Daskalakis, N., Kindap, T., and Kanakidou, M.: The impact of temperature changes on summer time ozone and its precursors in the Eastern Mediterranean, Atmos. Chem. Phys., 11, 3847–3864, doi:10.5194/acp-11-3847-2011, 2011.

Kalabokas, P. D. and Bartzis, J. G.: Photochemical air pollution characteristics at the station of the NCSR-Demokritos, during the MEDCAPHOT-TRACE campaign in Athens, Greece (20 August to 20 September 1994), Atmos. Environ., 32, 2123–2139, doi:10.1016/s1352-2310(97)00423-8, 1998.

Kalabokas, P. D., Viras, L. G., Bartzis, J. G., and Repapis, C. C.: Mediterranean rural ozone characteristics around the urban area of Athens, Atmos. Environ., 34, 5199–5208, doi:10.1016/s1352-2310(00)00298-3, 2000.

Kalabokas, P. D., Volz-Thomas, A., Brioude, J., Thouret, V., Cammas, J.-P., and Repapis, C. C.: Vertical ozone measurements in the troposphere over the Eastern Mediterranean and comparison with Central Europe, Atmos. Chem. Phys., 7, 3783–3790, doi:10.5194/acp-7-3783-2007, 2007.

Kalabokas, P. D., Cammas, J.-P., Thouret, V., Volz-Thomas, A., Boulanger, D., and Repapis, C. C.: Examination of the atmospheric conditions associated with high and low summer ozone levels in the lower troposphere over the eastern Mediterranean, Atmos. Chem. Phys., 13, 10339–10352, doi:10.5194/acp-13-10339-2013, 2013.

Kouvarakis, G., Tsigaridis, K., Kanakidou, M., and Mihalopoulos, N.: Temporal variations of surface regional background ozone over Crete Island in the southeast Mediterranean, J. Geophys. Res., 105, 4399–4407, 2000.

Lamarque, J.-F., Hess, P. G., Emmons, L., Buja, L., Washington, W., and Granier, C.: Tropospheric ozone evolution between 1890 and 1990, J. Geophys. Res., 110, D08304, doi:10.1029/2004JD005537, 2005.

Lelieveld, J., Berresheim, H., Borrmann, S., Crutzen, P. J., Dentener, F. J., Fischer, H., Feichter, J., Flatau, P. J., Heland, J., Holzinger, R., Korrmann, R., Lawrence, M. G., Levin, Z., Markowicz, K. M., Mihalopoulos, N., Minikin, A., Ramanathan, V., de Reus, M., Roelofs, G. J., Scheeren, H. A., Sciare, J., Schlager, H., Schultz, M., Siegmund, P., Steil, B., Stephanou, E. G., Stier, P., Traub, M., Warneke, C., Williams, J., and Ziereis, H.:

Global air pollution crossroads over the mediterranean, Science, 298, 794–799, doi:10.1126/science.1075457, 2002.

Liu, J., Jones, D. B. A., Zhang, S., and Kar, J.: Influence of interannual variations in transport on summertime abundances of ozone over the Middle East, J. Geophys. Res., 116, D20310, doi:10.1029/2011JD016188, 2011.

Ma, J., Zhou, X., and Hauglustaine, D.: Summertime tropospheric ozone over China simulated with a regional chemical transport model, Part 2. Source contribution and budget, J. Geophys. Res., 107, 4612, doi:10.1029/2001JD001355, 2002.

Papayannis, A., Balis, D., Zanis, P., Galani, E., Wernli, H., Zerefos, C., Stohl, A., Eckhardt, S., and Amiridis, V.: Sampling of an STT event over the Eastern Mediterranean region by lidar and electrochemical sonde, Ann. Geophys., 23, 2039–2050, doi:10.5194/angeo-23-2039-2005, 2005.

Pfister, G., Emmons, L. K., Hess, P. G., Honrath, R., Lamarque, J.-F., Val Martin, M., Owen, R. C., Avery, M., Browell, E. V., Holloway, J. S., Nedelec, P., Purvis, R., Ryerson, T. B., Sachse, G. W., and Schlager, H.: Ozone production from the 2004 North American boreal fires, J. Geophys. Res., 111, D24S07, doi:10.1029/2006JD007695, 2006.

Pfister, G. G., Emmons, L. K., Hess, P. G., Lamarque, J.-F., Thompson, A. M., and Yorks, J. E.: Analysis of the summer 2004 ozone budget over the United States using Intercontinental Transport Experiment Ozonesonde Network Study (IONS) observations and Model of Ozone and Related Tracers (MOZART-4) simulations, J. Geophys. Res., 113, D23306, doi:10.1029/2008JD010190, 2008.

Pfister, G. G., Walters, S., Emmons, L. K., Edwards, D. P., and Avise, J.: Quantifying the contribution of inflow on surface ozone over California during summer 2008, J. Geophys. Res. Atmos., 118, 12282–12299, doi:10.1002/2013JD020336, 2013.

R'Honi, Y., Clarisse, L., Clerbaux, C., Hurtmans, D., Duflot, V., Turquety, S., Ngadi, Y., and Coheur, P.-F.: Exceptional emissions of NH$_3$ and HCOOH in the 2010 Russian wildfires, Atmos. Chem. Phys., 13, 4171–4181, doi:10.5194/acp-13-4171-2013, 2013.

Richards, N. A. D., Arnold, S. R., Chipperfield, M. P., Miles, G., Rap, A., Siddans, R., Monks, S. A., and Hollaway, M. J.: The Mediterranean summertime ozone maximum: global emission sensitivities and radiative impacts, Atmos. Chem. Phys., 13, 2331–2345, doi:10.5194/acp-13-2331-2013, 2013.

Rodwell, M. J. and Hoskins, B. J.: Monsoons and the dynamics of deserts, Q. J. R. Meteorol. Soc., 122, 1385–1404, doi:10.1002/qj.49712253408, 1996.

Rodwell, M. J. and Hoskins, B. J.: Subtropical anticyclones and summer monsoons, J. Climate, 14, 3192–3211, 2001

Roelofs, G. J., Scheeren, H. A., Heland, J., Ziereis, H., and Lelieveld, J.: A model study of ozone in the eastern Mediterranean free troposphere during MINOS (August 2001), Atmos. Chem. Phys., 3, 1199–1210, doi:10.5194/acp-3-1199-2003, 2003.

Safieddine, S., Clerbaux, C., George, M., Hadji-Lazaro, J., Hurtmans, D., Coheur, P.-F., Wespes, C., Loyola, D., Valks, P., and Hao, N.: Tropospheric ozone and nitrogen dioxide measurements in urban and rural regions as seen by IASI and GOME-2, J. Geophys. Res.-Atmos., 118, 10555–10566, 2013.

Atmos. Chem. Phys., 14, 10119–10131, 2014   **www.atmos-chem-phys.net/14/10119/2014/**

129

Schubert, S., Wang, H., and Suarez, M.: Warm season sub-seasonal variability and climate extremes in the Northern Hemisphere: the role of stationary Rossby waves, J. Climate, 24, 4773–4792, 2011.

Sprenger, M. and Wernli, H.: A northern hemispheric climatology of cross-tropopause exchange for the ERA15 time period (1979–1993), J. Geophys. Res., 108, 8521, doi:10.1029/2002JD002636, 2003.

Stohl, A., Spichtinger-Rakowsky, N., Bonasoni, P., Feldmann, H., Memmesheimer, M., Scheel, H. E., Trickl, T., Hubener, S. H., Ringer, W., and Mandl, M.: The influence of stratospheric intrusions on alpine ozone concentrations, Atmos. Environ., 34, 1323–1354, 2000.

Tuccella, P., Curci, G., Visconti, G., Bessagnet, B., Menut, L., and Park, R. J.: Modeling of gas and aerosol with WRF/Chem over Europe: Evaluation and sensitivity study, J. Geophys. Res., 117, D03303, doi:10.1029/2011JD016302, 2012.

Turquety, S., Hurtmans, D., Hadji-Lazaro, J., Coheur, P.-F., Clerbaux, C., Josset, D., and Tsamalis, C.: Tracking the emission and transport of pollution from wildfires using the IASI CO retrievals: analysis of the summer 2007 Greek fires, Atmos. Chem. Phys., 9, 4897–4913, doi:10.5194/acp-9-4897-2009, 2009.

Tyrlis, E., Lelieveld, J., and Steil, B.: The summer circulation in the eastern Mediterranean and the Middle East: influence of the South Asian Monsoon, Clim. Dynam., 40, 1103–1123, doi:10.1007/s00382-012-1528-4, 2013.

Wespes, C., Emmons, L., Edwards, D. P., Hannigan, J., Hurtmans, D., Saunois, M., Coheur, P.-F., Clerbaux, C., Coffey, M. T., Batchelor, R. L., Lindenmaier, R., Strong, K., Weinheimer, A. J., Nowak, J. B., Ryerson, T. B., Crounse, J. D., and Wennberg, P. O.: Analysis of ozone and nitric acid in spring and summer Arctic pollution using aircraft, ground-based, satellite observations and MOZART-4 model: source attribution and partitioning, Atmos. Chem. Phys., 12, 237–259, doi:10.5194/acp-12-237-2012, 2012.

Wiedinmyer, C., Akagi, S. K., Yokelson, R. J., Emmons, L. K., Al-Saadi, J. A., Orlando, J. J., and Soja, A. J.: The Fire INventory from NCAR (FINN): a high resolution global model to estimate the emissions from open burning, Geosci. Model Dev., 4, 625–641, doi:10.5194/gmd-4-625-2011, 2011.

Zanis, P., Hadjinicolaou, P., Pozzer, A., Tyrlis, E., Dafka, S., Mihalopoulos, N., and Lelieveld, J.: Summertime free-tropospheric ozone pool over the eastern Mediterranean/Middle East, Atmos. Chem. Phys., 14, 115–132, doi:10.5194/acp-14-115-2014, 2014.

Zbinden, R. M., Thouret, V., Ricaud, P., Carminati, F., Cammas, J.-P., and Nédélec, P.: Climatology of pure tropospheric profiles and column contents of ozone and carbon monoxide using MOZAIC in the mid-northern latitudes (24° N to 50° N) from 1994 to 2009, Atmos. Chem. Phys., 13, 12363–12388, doi:10.5194/acp-13-12363-2013, 2013.

Ziv, B., Saaroni, H., and Alpert, P.: The factors governing the summer regime of the Eastern Mediterranean, Int. J. Climatol., 24, 1859–1871, 2004.

Chapter 8

Tropospheric O$_3$ from IASI during the East Asian Summer Monsoon

8.1   Motivation

Tropospheric O$_3$ concentrations over south and east Asia have significantly increased over the past few decades as a result of rapid industrialization in these regions, with important implications on regional and global air quality. Significant reductions in NO$_2$ from space are observed in Europe and part of the eastern coasts of the United States, while south and east Asian countries are experiencing increasing emissions of NO$_2$ as well as other pollutants, many of which are precursors of O$_3$ [Akimoto, 2003, Richter et al., 2005, Ohara et al., 2007]. For example, China shows an increase of NO$_2$ reaching 29% per year for the period 1996-2006 [van der A et al., 2008], and about 50% over the industrial areas of China over the period 1996-2004 [Richter et al., 2005]. Over most India, increasing trends in tropospheric O$_3$ are consistent with the observed trends in emissions (from NO$_x$ and CO as well as coal and petroleum consumption) [Lal et al., 2012]. I presented in section 2.3, how this region is affected by many dynamical processes, with mainly deep convection, pushing O$_3$ and its precursors to be uplifted to the middle and upper troposphere, with subsequent advection across large distances and thus affecting global air quality. Figure 8.1 shows tropospheric O$_3$ from IASI during summer 2013 over Asia and the population density for the year 2000.

One can see how the two plots relate, reflecting the high anthropogenic contribution to the regional pollution. The IASI plot has been calculated by taking only observations with |thermal contrast| > 8 kelvins, in order to highlight pollution in the boundary layer since the sensitivity towards the lower troposphere becomes higher for high thermal contrast especially over land. Shown here is a 3 month average since this method reduces considerably the number of points (by a factor of 4-5).
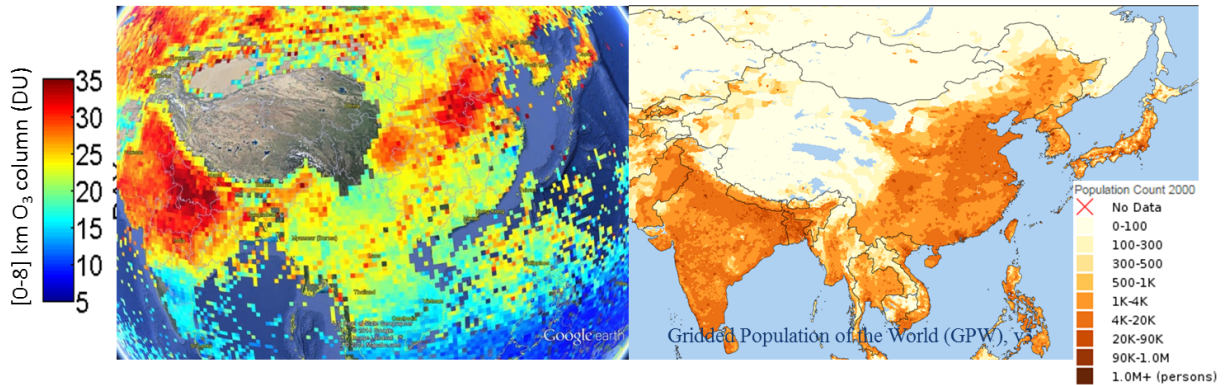

Figure 8.1: Left: Tropospheric O_3 from IASI. Right: population density over the same region, suggesting high anthropogenic sources of pollution.

From this figure, one can see the importance of the study of the sources, sinks, transport modes and dynamics affecting tropospheric O_3 over this region. One important dynamical system occurring every year is the east Asian monsoon, with local and global effects on the distribution of pollutants and with particular interest to this thesis work, the tropospheric O_3. This study was carried out in the framework of the "East Asian Monsoon and air quality" project, which is a part of the DRAGON program (https://dragon3.esa.int). It is a program led by the European Space Agency (ESA) and the Chinese Ministry of Science and Technology (MOST). It is also under the framework of the EU-FP7 PANDA project (http://www.marcopolo-panda.eu/), which is a support to the DRAGON project and is collaboration between European research groups and other research groups in China.

The main objective of this study is to understand the regional distribution of tropospheric O_3 during the monsoon period, using IASI and the effect of meteorological and dynamical parameters from the ECMWF Re-Analysis (ERA)-interim reanalysis model (winds, cloud cover, relative humidity and rainfall) on the tropospheric O_3 column. I will try first to look at the monsoon dynamics, then assess the monsoon effect on the tropospheric O_3 from IASI.

I add also the CO product from IASI to look at the effect of monsoon on pollutant's possible transport by winds. I will discuss the seasonal variation of tropospheric O$_3$ and CO over the whole IASI monsoon period, and then discuss some important features. Rainfall, cloud cover, relative humidity and wind analysis and their relationship to the drop in tropospheric O$_3$ will be discussed for the monsoon period of 2011. The second part of this chapter is dedicated to a WRF-Chem model run above this region for the monsoon period of 2011. This part is mainly a validation work for the model run with local surface O$_3$ measurements and IASI O$_3$ columns. I will present in the conclusion some perspectives on what could be later achieved with IASI, reanalaysis data and the WRF-Chem model to assess the tropospheric O$_3$ during the east Asian summer monsoon.

8.2 The East Asian Monsoon Dynamics

The Asian summer monsoon plays an important role in the weather and climate over the monsoon regions as well as in the global climate system. The classical definition of a monsoon is based on the annual reversal of surface winds [Ramage, 1972], though also extended to rainy season characteristics [Wang and Lin, 2002]. Numerous studies divide the Asian-Pacific summer monsoon system into three main subsystems: the Indian Summer Monsoon (ISM), the western North Pacific Summer Monsoon (WNPSM), and the East Asian Summer Monsoon (EASM) [Zhu, 1934, Yeh et al., 1959, Tao and Chen, 1987, Murakami and Matsumoto, 1994, Wang and Lin, 2002, Yihui and Chan, 2005, Ding, 2007] (among others). The three systems are plotted in Fig 8.2.

The ISM and WNPSM are tropical monsoons with an Indochinese "corridor"(also called Indochinese Peninsula) separating them. The EASM is a subtropical monsoon sharing a borderline with the WNPSM [Wang and Lin, 2002].

The three are independent yet closely linked to one another and they all take part in the global climate system and are therefore affected by many dynamical processes: the El Niño-Southern Oscillation (ENSO), the changes in Sea Surface Temperature (SST) in the western Pacific and Indian oceans, and the Tropospheric Biennial Oscillation (TBO) [Meehl, 1997, Meehl and Arblaster, 2001, 2002, Webster et al., 1998, Rasmusson and Carpenter, 1983] and
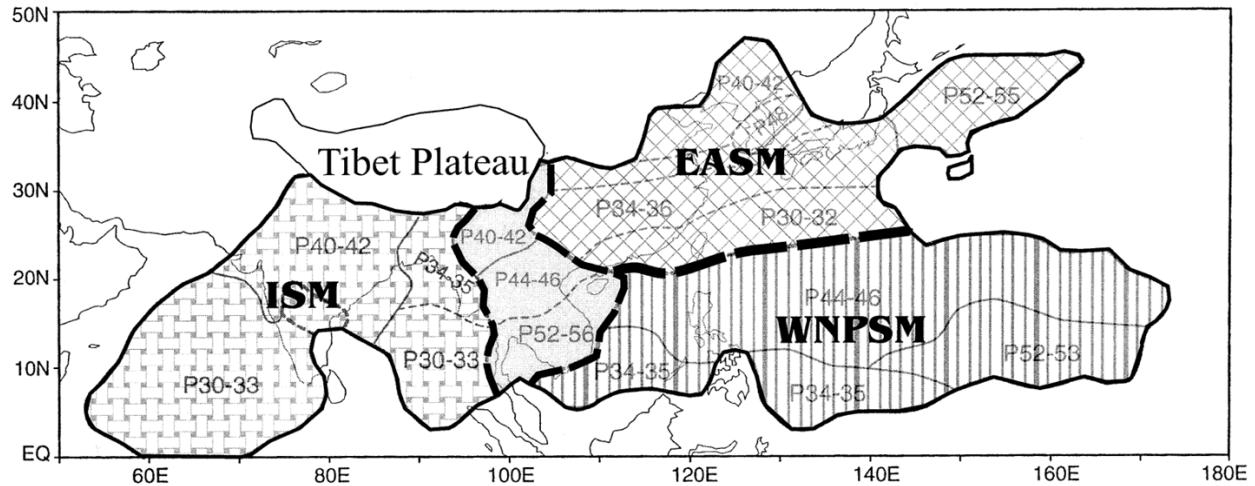
Figure 8.2: Asian-Pacific summer monsoon sub-systems. Figure from Wang and Lin [2002].

a more recent observed phenomena, the EQUatorial Indian Ocean Oscillation (EQUINOO) [Gadgil et al., 2004, Maity and Kumar, 2006]. Hereafter is a brief description of the role of each in the monsoon variability:

ENSO

The large scale displacement of heat sources from the tropics to the west is described by El Niño-Southern Oscillation (ENSO) [Shukla and Mooley, 1987]. It was previously thought that El Niño warm events tend to weaken the summer rainfall in the East Asian monsoons with lower-than-normal rainfall and opposite in case of a La Niña events [Pant and Parthasarathy, 1981, Rasmusson and Carpenter, 1983]. However, analysis over the last century shows that this inverse relationship has broken down in recent decades, starting 1988 [Kumar et al., 1999, 2002, Webster, 2006]. This is due to the increase in surface temperature over Eurasia in winter and spring, leading to a high land-ocean thermal gradient and thus favoring a strong monsoon. Moreover, the southeastward shift in the Walker circulation[1] anomalies associated with ENSO events may lead to a reduced subsidence over the Indian region, thus favoring normal monsoon conditions [Kumar et al., 1999]. Also, evidence that anomalously high winter/spring Eurasian snow cover is linked to weak rainfall in the following summer Indian monsoon [Vernekar et al., 1995].

---

1. The Walker circulation is seen at the surface as easterly trade winds which move water and air warmed by the sun towards the west. The western side of the equatorial Pacific is characterized by warm, wet and low pressure weather as the collected moisture is dumped in the form of typhoons and thunderstorms.

SST

Anomalies in Sea Surface Temperature (SST) in the oceans around the monsoon land regions may influence monsoon strength by affecting the moisture supply [Webster, 2006]. Studies have found a statistically significant relationship between SST and monsoon rainfall [Shukla, 1975, Sadhuram, 1997, Clark et al., 2000, Kucharski et al., 2006], with correlations reaching +0.8 between equatorial Indian ocean SST and Indian precipitation in the season prior to monsoon [Clark et al., 2000].

TBO

The Tropospheric Biennial Oscillation (TBO) is defined as the biennial variability of monsoon rainfall over monsoon regions defined with a tendency for a relatively strong monsoon to be followed by a relatively weak one, and vice versa [Meehl, 1997, Webster, 2006].

EQUINOO

The EQUatorial Indian Ocean Oscillation (EQUINOO) is related to the pressure gradients and the winds along the equator. The term "oscillation" refers to the changes in the convection anomalies in the equatorial Indian Ocean during the summer monsoon period. When the convection is enhanced over the western part of the equatorial Indian Ocean (50E-70E and 10S-10N), it leads to an anomalous surface pressure gradient to the west pushing surface winds along the equator to the east. The inverse effect is when the convection is suppressed leading to an easterly surface pressure gradient, and the anomalous surface winds along the equator becomes westerly [Gadgil et al., 2004].

8.3 Six-year Seasonal Variation

Given the six-year IASI data available so far, the first step to assess the monsoon strength is to look at spatio-temporal maps of pollutants concentrations over the monsoon period. In the following 2 sections, I will also add to the analysis the CO product from IASI. CO is formed during incomplete combustion of fossil-fuel or from fires. It is also produced in the atmosphere via the oxidation of methane and non-methane hydrocarbons by the hydroxyl radical (OH) [Duncan and Logan, 2008]. Because of its relatively long lifetime (a few weeks

to a few months depending on latitude and time of year), CO can therefore be used as an atmospheric tracer of transport and it can therefore provide some useful information on the transport of pollutants during the monsoon.

8.3.1 Tropospheric Ozone

To look at the general monthly variation of the monsoon on the IASI tropospheric O$_3$ product, I plot in Fig. 8.3 the average monthly variations (May-September) over the period 2008-2013.

IASI daytime observations are used, since as seen in Chapter 5, better thermal contrast, and hence better sensitivity in the lower troposphere, is usually recorded during the day. The IASI data show similar seasonal behavior over different months from one year to the other. Two effects play a role in the seasonal variability of O$_3$ over this region. First is the normal seasonal variability of O$_3$ and its photochemical production and availability with respect to its precursors. This can be summarized as an increase starting the end of the spring to reach a peak in summer and then decreasing values starting September (and was discussed thoroughly in previous chapters). The second effect is the summer Asian monsoon. The 3 different subsystems of the Asian monsoon have onset dates around the end of May-June. The definition of the monsoon onset date is the first Julian pentad (period of 5 days) in which monsoonal rainfall exceeds 5 mm/day Wang and Lin [2002]. In particular, the ISM arrives over the southern coasts of India around the end of May/beginning of June [Parthasarathy et al., 1994, Wang et al., 2009]. The EASM onset date is around mid-May [Yang and Lau, 1998]. The WNPSM onset date exhibits more inter-annual variability than the other monsoons [Murakami and Matsumoto, 1994], that might reach one month [Yan, 1997], with the earliest onset in mid-May [Wu and Wang, 2000]. It is worth noting here that Kajikawa et al. [2012] show that over the bay of Bengal[2], the Indochinese Peninsula and the western Pacific (120-140E), the monsoon onset date has shifted -10 to -15 days. Around 160E it shifted to +10 to +15 days in the previous 3 decades. With the dates all around May and June for the start of the different monsoon systems, one can see in

---

2. The bay of Bengal is the northeastern part of the Indian Ocean, bordered mostly by India and Sri Lanka to the west, Bangladesh to the north, and Burma/Myanmar to the east
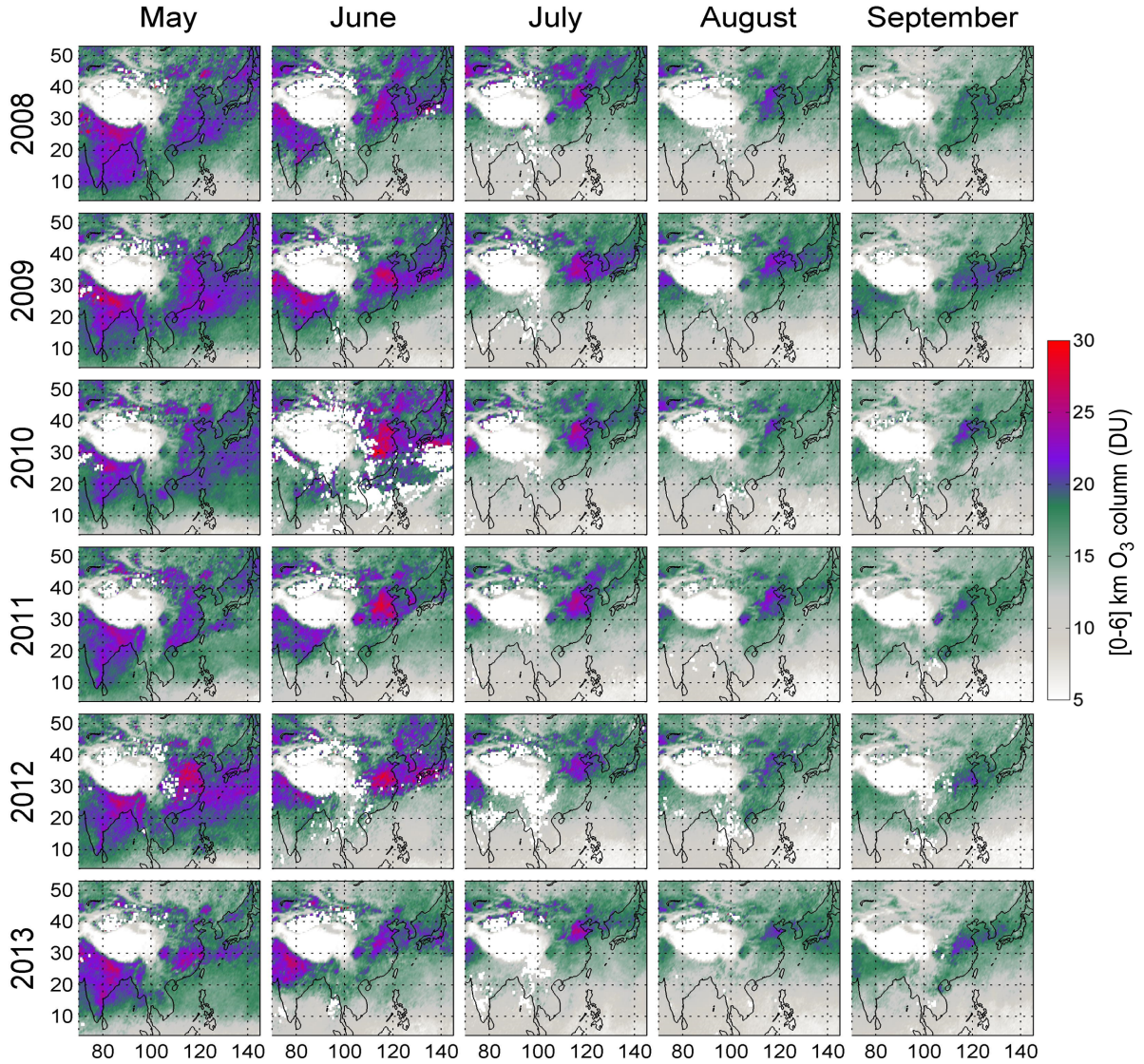
Figure 8.3: Monthly averaged daytime tropospheric [0-6] km O$_3$ column from IASI over the monsoon period (May-September) of the years 2008-2013. The decrease due to the monsoon is more prominent in the south, and is well reproduced from year to year.

Fig. 8.3, how after the settlement of the monsoon in May and June, the O$_3$ values start to decrease up to 50% of their May values starting the month of June. This is particularly seen over India, where high values up to 30 DU are recorded in May, then start decreasing afterward. Since the ISM starts at the south of India, the effect is most prominent there.

With the march of the monsoon north-east ward, the decrease becomes most prominent in July and August. To better understand the drop seen, one should couple the IASI data with monsoon characteristics, mainly cloud cover, rainfall, relative humidity and winds, which will be presented in a following section. On a closing note and as discussed in Chapter 5, summer 2010 was a year of a very strong monsoon. Notice how in June 2010 and over India in particular, the lowest O_3 values with respect to the other years are recorded. Due to the high cloud cover throughout the whole month, some areas were void of IASI retrievals (white pixels). Moreover, a high O_3 plume is spotted around 20-30N and 120-130E, that is not detected in the other years presented. Since this area is in the ocean and therefore with no local sources, the enhancement in the tropospheric O_3 column might be due to continental O_3 uplift of O_3 and O_3 precursors by deep convection (section 2.5) from the lower troposphere of polluted areas to the free troposphere. Once in the free troposphere, it is transported by winds over large distances.

8.3.2   CO Total Columns

I plot in Fig. 8.4 the time series of CO total columns over the same area and period of the previous section. The seasonal variation of CO is such that it is lowest in summer, starting the month of May, because of the destruction of CO by the OH radical in the presence of sunlight. Hence, one would *expect* a larger CO reduction (than that observed for O_3) during the monsoon months. The North China Plain is an area that is less affected by the monsoon (as I will show later) and thus shows the highest CO values recorded mainly from anthropogenic and fire sources. As Fig. 8.3 shows, the same region is characterized by high O_3 values as well. The areas under 30N show a decreasing signature from May to June, and then starting July to September, the CO total columns show little change, suggesting high CO emissions.

8.4   Monsoon Effect on the IASI Ozone and CO

In this section, I add to the analysis of O_3 and CO the wind field analysis and then the rainfall, cloud cover and relative humidity data in section 8.4.2 in order to better understand
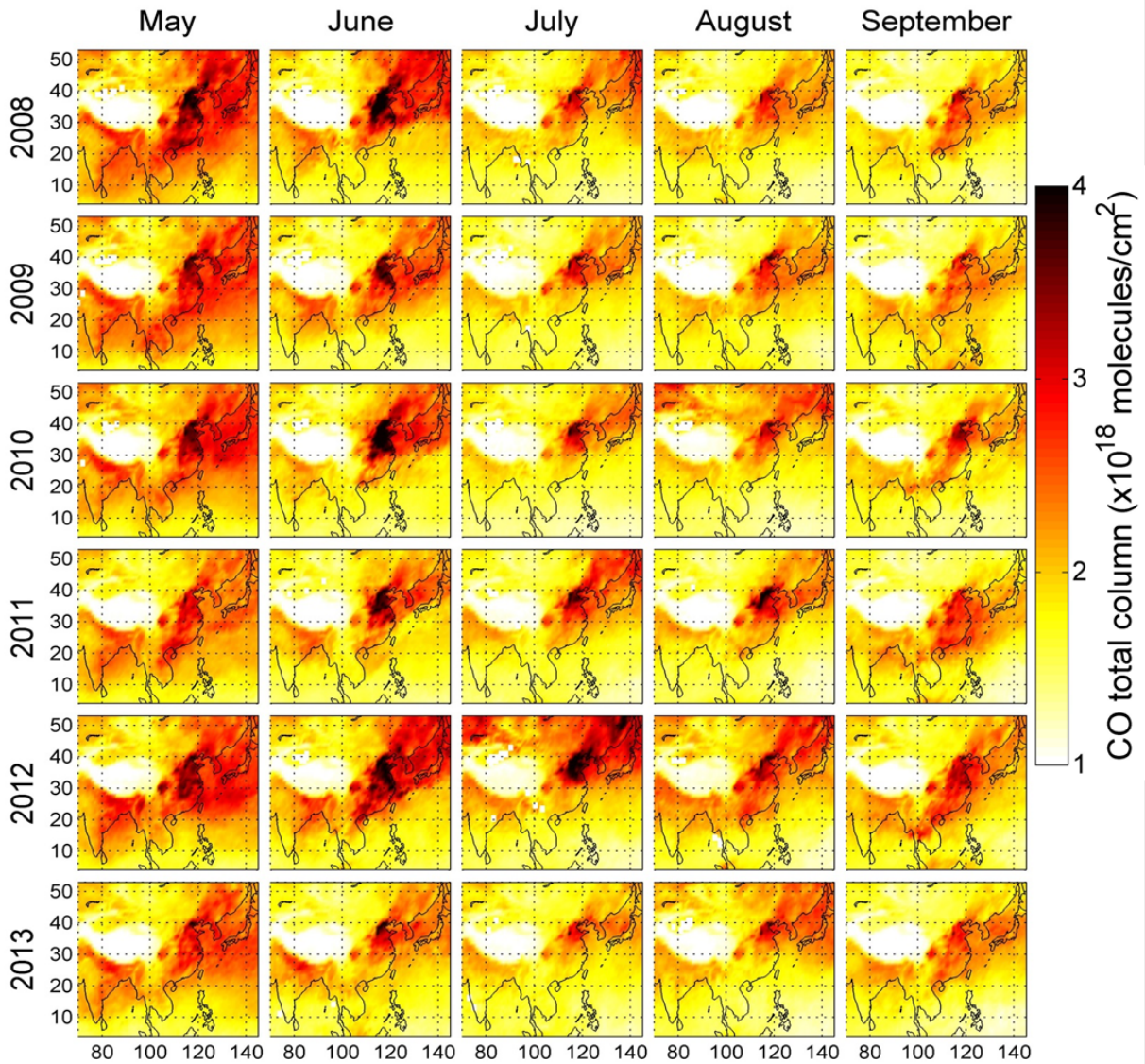
Figure 8.4: Monthly averaged daytime total CO columns from IASI over the monsoon period (May-September) and over the IASI period 2008-2013.

the meteorological and dynamical effects responsible for the decrease of O$_3$ and CO (though to a lower extent) detected in Figs. 8.3 and 8.4. The monthly averaged u- and v- winds fields, rainfall, cloud cover, and relative humidity data are from ERA-interim, and more details on this dataset was presented in Chapter 6.

8.4.1 Changes in Ozone and CO over Three Chinese Regions

To try to understand the relationship between wind force on one hand and O_3 and CO from IASI from the other hand, I plot in Fig. 8.5 the seasonal variation (May-August) of the averaged wind patterns and tropospheric O_3 and CO total columns during 2008-2013 and over three specific Chinese regions. These are the North China Plain (NCP, including among others, Beijing and Tianjin), the Yangtze River Delta (YRD, including among others, Shanghai and Nanjing) and the Pearl River Delta (PRD, including among others, Guangzhou and Hong Kong). The location of these "box" regions can be found in the first wind plot of Fig. 8.5 panel (a). The IASI data in panel (b) is calculated from the daily daytime average over this region, and the shaded color around the mean is the standard deviation of the 6-year daily observations.

Few features can be deduced while comparing O_3 and CO on one hand and the wind patterns on the other hand. Over the NCP region, the winds throughout the monsoon are weak. Looking at the O_3 and CO plots, one can see how they are relatively constant throughout the monsoon period. In fact this *constant* variability was also detected in Figs. 8.3 and 8.4, where both O_3 and CO persist above this region in summer. Low NCP variability might be also caused by higher impact of local sources from the Beijing area that are more constant through the summer. The YRD and PRD regions are more southern and thus the monsoon effect is higher as the winds are stronger. The YRD region shows high variability both for O_3 and CO, with a more prominent decrease starting June for both O_3 and CO. O_3 values are around 17 DU (in comparison to 22 DU in May), and CO values show a decrease of 0.5 x 10^{18} molecules/cm^2 from May to June-August with some occasional high peaks due probably to high local production or to transport by winds from other regions. The PRD region is the most affected by the monsoon. It shows the lowest variability suggesting similar effect from year to year (smallest standard deviation), O_3 values around 14 DU and CO values around 2 x 10^{18} molecules/cm^2 after June. The month of August shows interesting O_3 and CO peaks with a relatively small standard deviation suggesting a pattern of high O_3 and CO production or transport during this period. In their study, Dufour et al. [2010] showed the same seasonal variation of the [0-6] km O_3 column of IASI (with a different retrieval

(a)

(b)

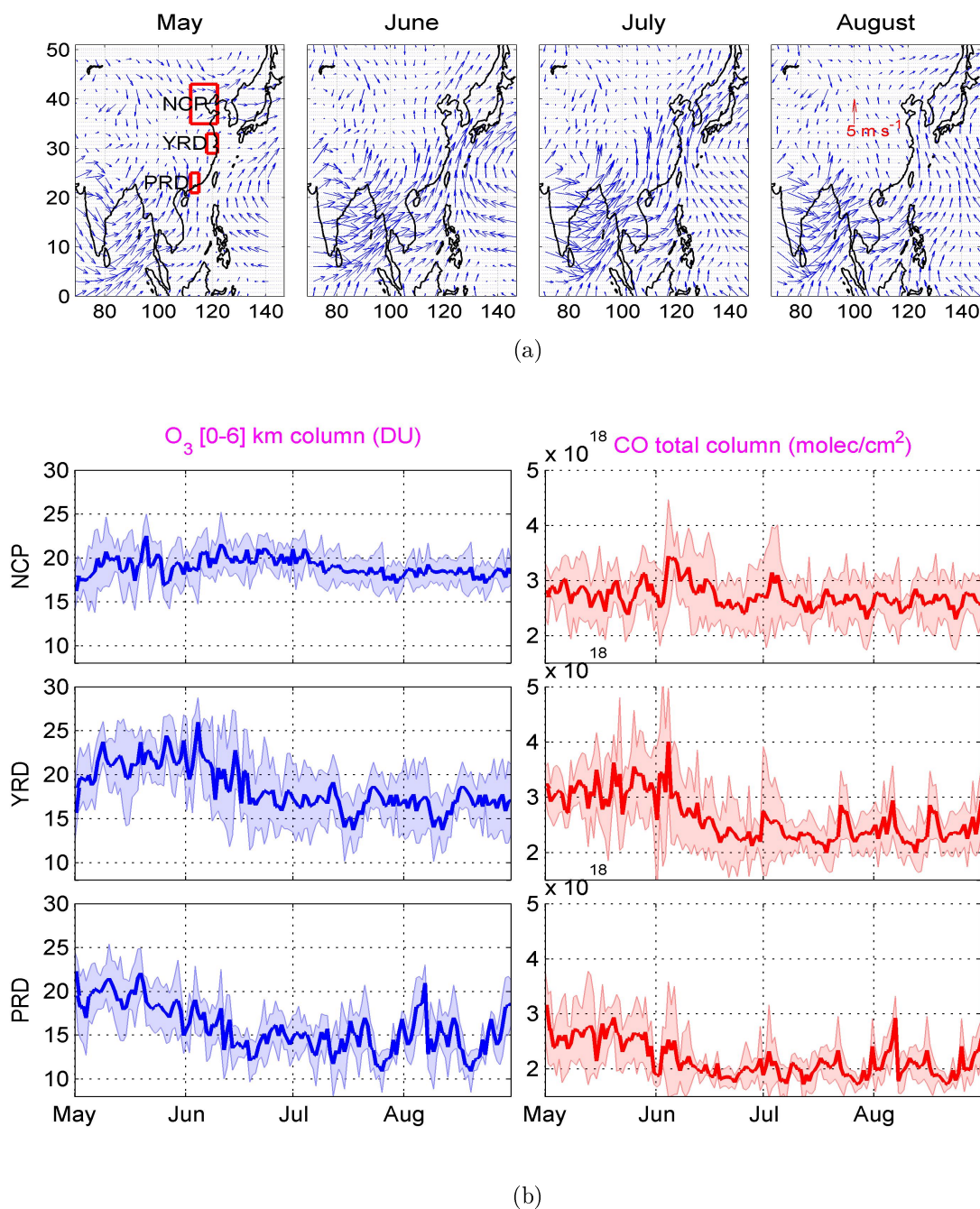Figure 8.5: Averaged seasonal variation during 2008-2013 of (a) ERA-interim wind patterns and (b) O$_3$ tropospheric columns and CO total columns as seen by IASI over the regions NCP, YRD and PRD which location can be found in the first plot of panel (a).

algorithm), and detected a more pronounced monsoon effect in Hong Kong and Shanghai than in Beijing for the year 2008, in agreement with what is presented here.

8.4.2   Case Study of the 2011 Monsoon

In order to look at the O_3 (mainly) and CO behavior during the monsoon, I show in Fig. 8.6 the monsoon period of 2011 taken as an example year. I also add different meteorological properties in order to study the relationship between change in meteorology and pollutant concentration. These are the total cloud cover that gives an insight on the photochemical activity in the troposphere; the relative humidity, since it is an important sink for tropospheric O_3; the rainfall which will help localizing high cloud cover and relative humidity regions and their effect on the tropospheric O_3 and CO columns locally; and lastly wind force and direction to assess monsoon strength and possible transport.

In May, and at the very southern tip of India, one can see the beginning of the rainy season, and the winds at 875 hPa start their march from India. Tropospheric O_3 values and CO total columns are therefore not yet affected. In June, the monsoon becomes stronger in India and also over the Yangtze River Valley region (with the green circle in the lowest panel) and Japan [3]. The cloud cover, relative humidity and rainfall are much larger especially in northern India and the Bay of Bengal as well as over the Yangtze River region, in accordance with the wind data (green circle). Tropospheric O_3 values in India and the Yangtze region decrease due to the clean marine air masses brought by winds which are coupled with high cloud cover and therefore lower photochemical activity. Moreover, with the presence of a high content in water vapor (as the relative humidity plots show) the production rate of the reaction $H_2O + O(^1D) \rightarrow 2OH$ increases, leading to higher production of the OH radical and therefore further destruction of O_3. In July and August, the monsoon reaches its maximal strength, rain falls over all the India, with a high cloud cover, winds are stronger and the tropospheric O_3 columns show a large decrease. The wind effect on O_3 has been detected before using IASI measurements (though for post-monsoon period), where elevated tropospheric O_3 values over central and southern India are shown to decrease significantly with the crossing of tropical storms [Barret et al., 2011]. Given that CO has a larger lifetime than that of O_3, the values of CO show a decrease in northern India where the monsoon is stronger, however, over China,

---

3. In China, the term "Meiyu" is used for the rainy season from mid-June to mid-July over the Yangtze River Valley. In Japan, the term "Baiu" is used both for the rainy season over Okinawa region from early May to mid-June and over the Japanese Main Islands from mid-June to mid-July.
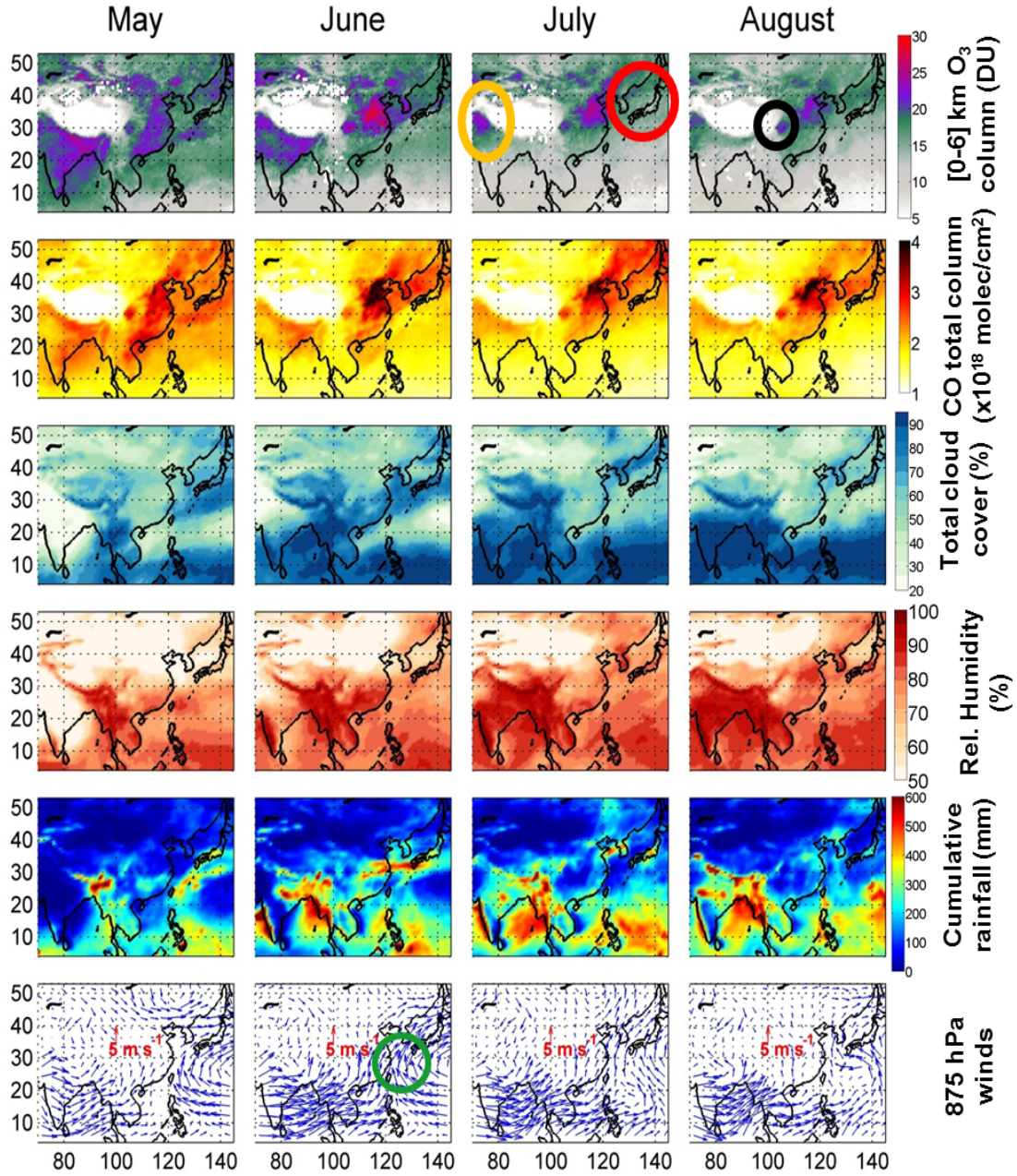
Figure 8.6: Monthly averaged tropospheric [0-6] km O$_3$ column, CO total columns both from IASI, total cloud cover, cumulative rainfall, relative humidity and winds at 875 hPa for each of the months of May to August 2011. Please refer to the text for the explanation of the different colored circles.

especially for latitudes > 20N, the monsoon effect on the CO total columns is less clear. While CO values remain of the same order of magnitude, tropospheric O$_3$ in Korea and Japan (with the red circle), show a decreasing effect, in particular in July for O$_3$ where a clear decrease is detected coinciding with the high cloud cover/relative humidity (and localized with the total rainfall) in July. On the other hand, over the yellow circled region, mainly north west of India and part of Pakistan, there was no or little cloud cover and weaker winds, leading to the persistence and the continuous production of the summer O$_3$ and CO over this region especially with the availability of high local precursor emissions. Looking at the winds plots over the different months, one can notice how the monsoon is stronger at the lower latitudes. Therefore the area of Beijing, Tianjin and the North China Plain are less affected by the monsoon and they show much weaker O$_3$ and CO decrease. The other interesting region in China that shows little or no change is the area between the Chongqing and Sichuan province (with the black circle in the month of August). One can notice how this region does not exhibit any monsoon characteristics with low cloud cover, relative humidity and weak winds. This region is also between 2 mountains (with low surface altitude as shown in Fig. 8.7 hereafter), making the persistence of O$_3$ and CO during summer favorable.

8.5   The WRF-Chem Model

In this study, we use the regional chemistry transport model WRF-Chem, version 3.4 [Grell et al., 2005], to simulate the meteorology and chemistry over the model domain shown in Fig. 8.7 during the Asian summer monsoon (May-August) of 2011 taken as a typical monsoon year, and the year for which we are able to get Chinese surface data to compare with the model. The horizontal resolution is of 50 km x 50 km and the vertical resolution is of 34 levels between the surface and 10hPa. The WRF-Chem simulation outputs are saved every 2h from 15 May until 31 August 2011 and more details on the model can be found in Chapter 7. Fig. 8.7 shows the *terrain height* variable of the model. In comparison to Figs. 8.1 and 8.3, this plot shows how the highly populated regions, and thus the most polluted ones, are where the surface height is the lowest and thus with better weather and agricultural conditions.

The WRF-Chem model has been used before over this region during and outside the monsoon period and was shown to capture well meteorology [Kumar et al., 2012a], tropospheric CO, O$_3$ and NO$_x$ [Kumar et al., 2012b, Ghude et al., 2013], aerosols and dust [Dipu et al., 2013, Kumar et al., 2014] over south Asia and the aerosols impact on precipitation over south and east Asia [Jiang et al., 2013, Wu and Su, 2013].
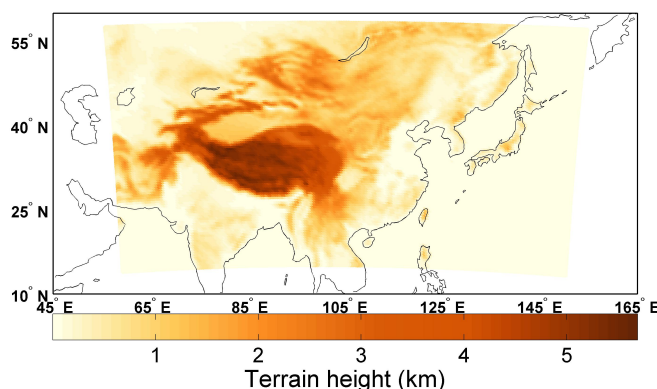

Figure 8.7: The WRF-Chem model domain used in this study with the altitude above sea level.

In order to establish the accuracy of the model's parameters, the WRF-Chem simulations were evaluated by comparing them with available meteorological and chemical observations.

8.5.1 Validation With Meteorology

The first step to assess the model outputs, would be to evaluate it with meteorological properties. For this end, I extracted from the NOAA website (http://gis.ncdc.noaa.gov/) the temperature, relative humidity, wind speed and direction of randomly selected few surface stations which locations are shown in Fig. 8.8.

Those were compared against the temperature and relative humidity at 2-m, wind speed and direction at 10-m from the WRF-Chem model. Geographic linear interpolation to the location of the stations was then applied to the model output. I analyzed different station data and I choose 2 cases (one *good* and one *bad*) that I plot in Fig. 8.9. The figure shows
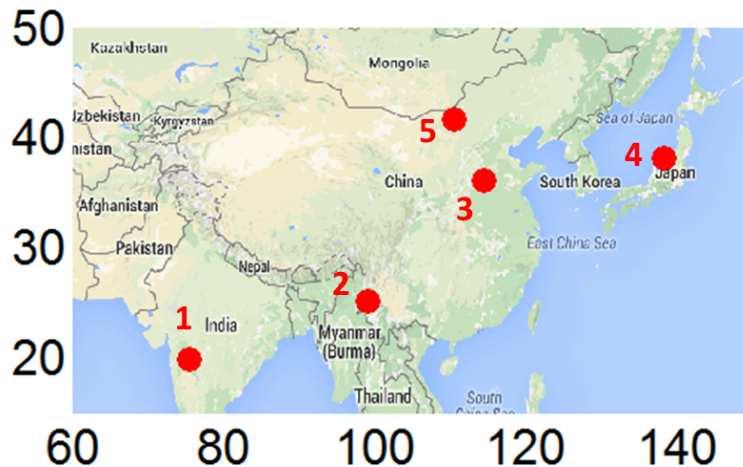
Figure 8.8: Location of the NOAA stations used for validation of meteorological properties.

the time series with bi-hourly measurements of stations *1* and *3* which location can be found in Fig. 8.8. Panel (a) is an example of a good case with excellent agreement and panel (b) is an example where wind speed is overestimated in the model. The plot shows the ability of the model to capture very well the important features of meteorological distributions. The only difference emerge from the wind speed where the model (as an example in panel (b)) overestimates it while the diurnal and seasonal cycle is well reproduced. This wind bias is mainly due to the fact that the wind direction at the ground stations takes discrete values (such as North, South etc.. in the ground data) leading to a bias in calculating the wind speed which will also take discrete values (as opposed to the model with continuous distribution of wind direction and speed). Moreover, one could also argue that due to the coarse grid resolution of 50 km used here, averaged representation of topography and land surface characteristics might lead to uncertainties. Nevertheless, the result of the comparison of the different stations is satisfying and show the ability of the model to reproduce meteorological parameters that might be useful in the monsoon dynamics analysis.

8.5.2 Validation With Surface Ozone Measurements

To evaluate the WRF-Chem O$_3$ data at the surface during the monsoon period May-August 2011, and to assess the effect of the monsoon on surface O$_3$, we use ground station data from 7 stations in North China plain (NCP), 13 in the Pearl River delta (PRD) and 10
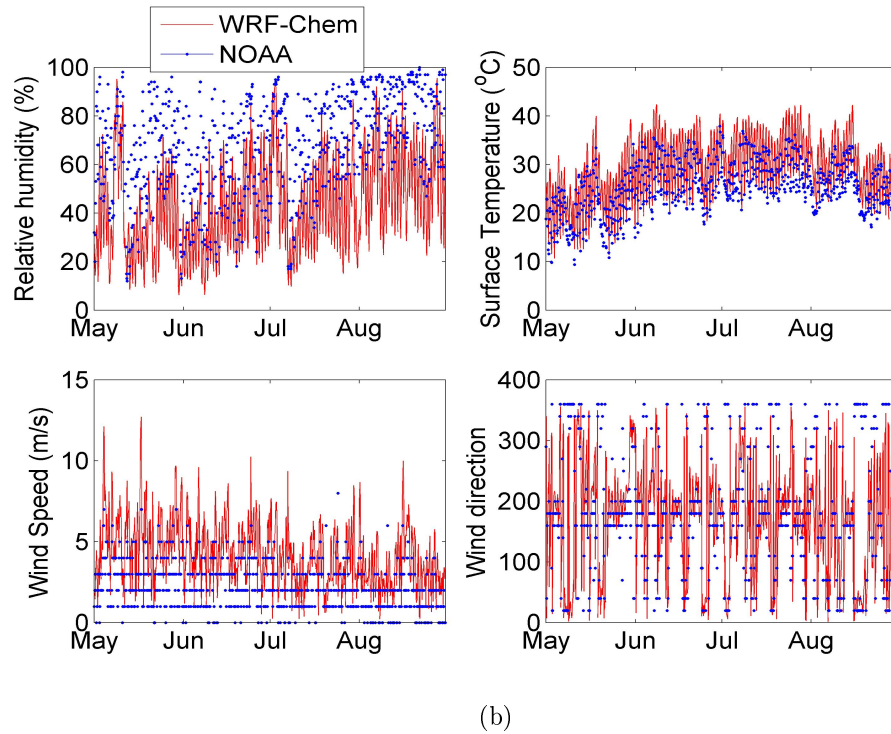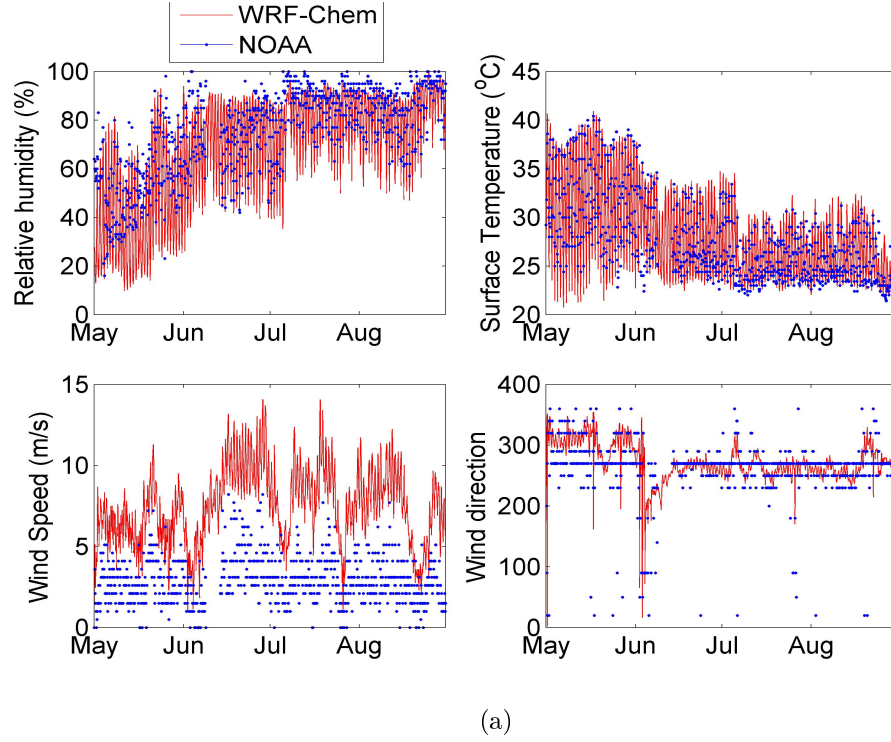
(a)

(b)

Figure 8.9: Validation of the WRF-Chem model temperature, relative humidity, wind speed and wind direction with the surface station *1* (a) and *3* (b). The location of these 2 stations can be found in Fig. 8.8

in Japan. The details and location of all stations can be found in Table 8.1.

Table 8.1: Ground stations used in the model validation: their location, type, correlation coefficient, root mean square error (rmse in ppbv) and the mean absolute percentage error (mape* in %).

Station label	Station name	Longitude	Latitude	Type	R	rmse	mape
N1	BD	115.52	38.87	urban	0.54	39.10	52.78
N2	CZ	116.81	38.28	urban	0.51	23.34	43.70
N3	TS	118.16	39.62	urban	0.59	33.35	44.58
N4	SJZ	114.54	38.03	urban	0.56	40.70	55.18
N5	BJ	116.37	39.97	urban	0.49	39.16	49.61
N6	LF	116.75	39.6	suburban	0.56	35.15	47.42
N7	XL	117.48	40.4	rural	0.25	34.41	45.80
P1	Chengzhong	112.47	23.05	Urban	0.39	23.47	77.83
P2	Jinjuzui	113.26	22.82	Urban	0.44	25.76	76.22
P3	Huijingcheng	113.10	23.00	Urban	0.42	24.60	80.18
P4	Donghu	113.08	22.59	Urban	0.37	28.35	83.34
P5	Zimaling	113.40	22.51	Urban	0.17	11.65	36.67
P6	Tangjia	113.63	22.42	Urban	0.42	22.54	55.86
P7	Haogangxiaoxue	113.77	23.00	Urban	0.43	29.41	93.79
P8	Jinguowan	114.38	22.94	Rural	0.49	26.09	81.91
P9	Xiapu	114.40	23.08	Urban	0.44	26.86	85.07
P10	Liyuan	114.09	22.55	Urban	0.49	20.05	62.10
P11	Luhugongyuan	113.27	23.15	Urban	0.39	31.63	98.56
P12	Nanshawanqingsha	113.62	22.72	Rural	0.42	29.85	76.79
P13	Tianhu	113.62	23.65	Rural	0.36	36.42	128.13
J1	Banryu	131.79	34.68	Urban	0.67	13.73	41.71
J2	Happo	137.79	36.69	Remote	0.46	23.61	57.80
J3	Hedo	128.25	26.86	Remote	0.84	10.22	55.48
J4	Ijira	136.69	35.57	Rural	0.56	17.47	59.46
J5	Ochiishi	145.49	43.16	Remote	0.60	13.22	26.46
J6	Ogasawara	142.21	27.09	Remote	0.87	6.21	36.75
J7	Oki	133.18	36.28	Remote	0.60	16.27	50.66
J8	Rishiri	140.20	45.12	Remote	0.47	16.54	27.61
J9	Sado-seki	138.40	38.25	Remote	0.52	17.12	39.78
J10	Yusuhara	132.93	33.38	Remote	0.82	9.73	34.54

*The *mape* is defined as: $\frac{1}{n}\sum_{t=1}^{n}\left|\frac{G_t - M_t}{G_t}\right|$ where G_t is the ground and M_t is the model value at t.

Linear interpolation is applied to the model output to the geographical locations of these stations. The location of these stations can be found on Fig. 8.10. All the stations provide hourly data and the result of the comparison for the different stations is plotted in Figs. 8.11 to 8.14 for the regions NCP (stations N1 to N9), PRD (stations P1 to P9) and Japan (stations J1 to J10). The correlation coefficient r, the root mean square error (rmse in ppbv) and the
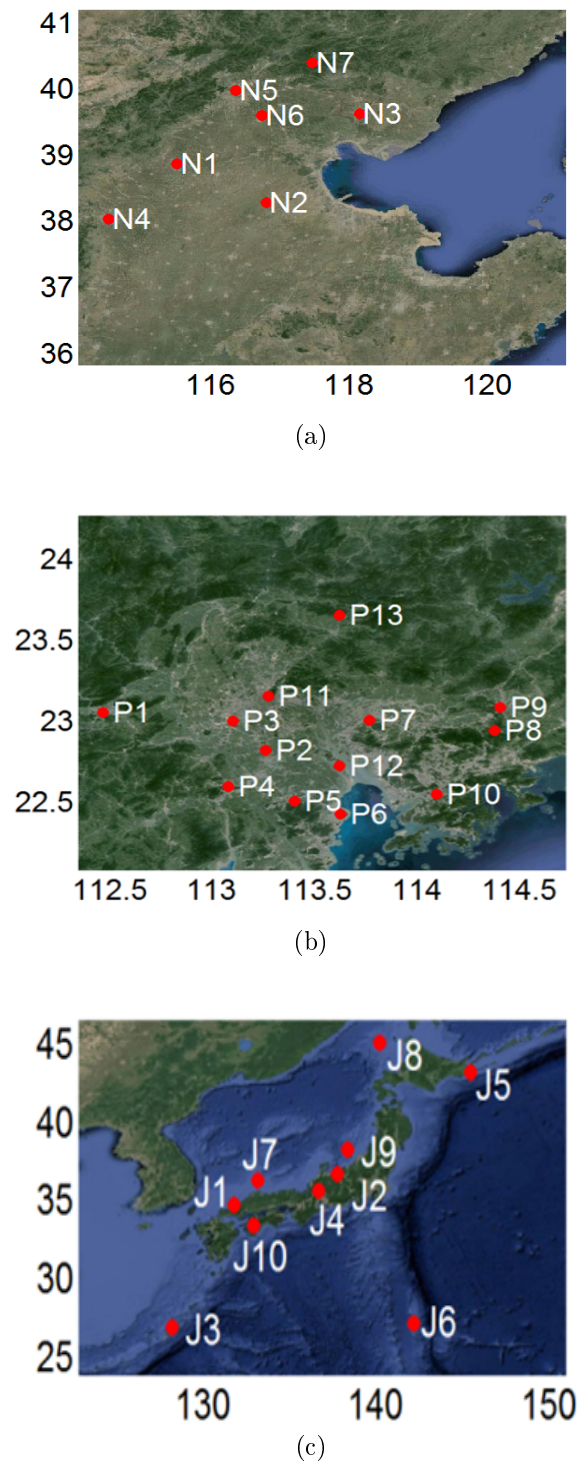
(a)

(b)

(c)

Figure 8.10: Location of the stations used to validate the model in: (a) North China Plain, (b) Pearl River Delta and (c) Japan.

mean absolute relative error (mare in %) can be found in Table 8.1. Getting these Chinese ground stations, even within the framework of the projects in which this study takes place,

was not an easy task and details of these stations are not always well known. Therefore the three different sets of stations belong to different organizations with different instruments and sensitivities, that should be known to better assess the error on the observation and whether the difference between model and observation is due to the model or rather to the observation itself.

Figure 8.11: O$_3$ time series of stations (in red) and WRF-Chem (in black) data at the surface for the period MJJA 2011 and for the stations in the North China Plain localized in panel (a) of Fig. 8.10.

Figs. 8.11 to 8.14 show in general that the model is able to reproduce fairly well the seasonal cycle of tropospheric O$_3$ at the surface. The figures also shows the seasonal behavior of tropospheric O$_3$ from model and ground measurements. What is interesting to note here, is that the drop in the tropospheric O$_3$ due to the monsoon at the surface is not always
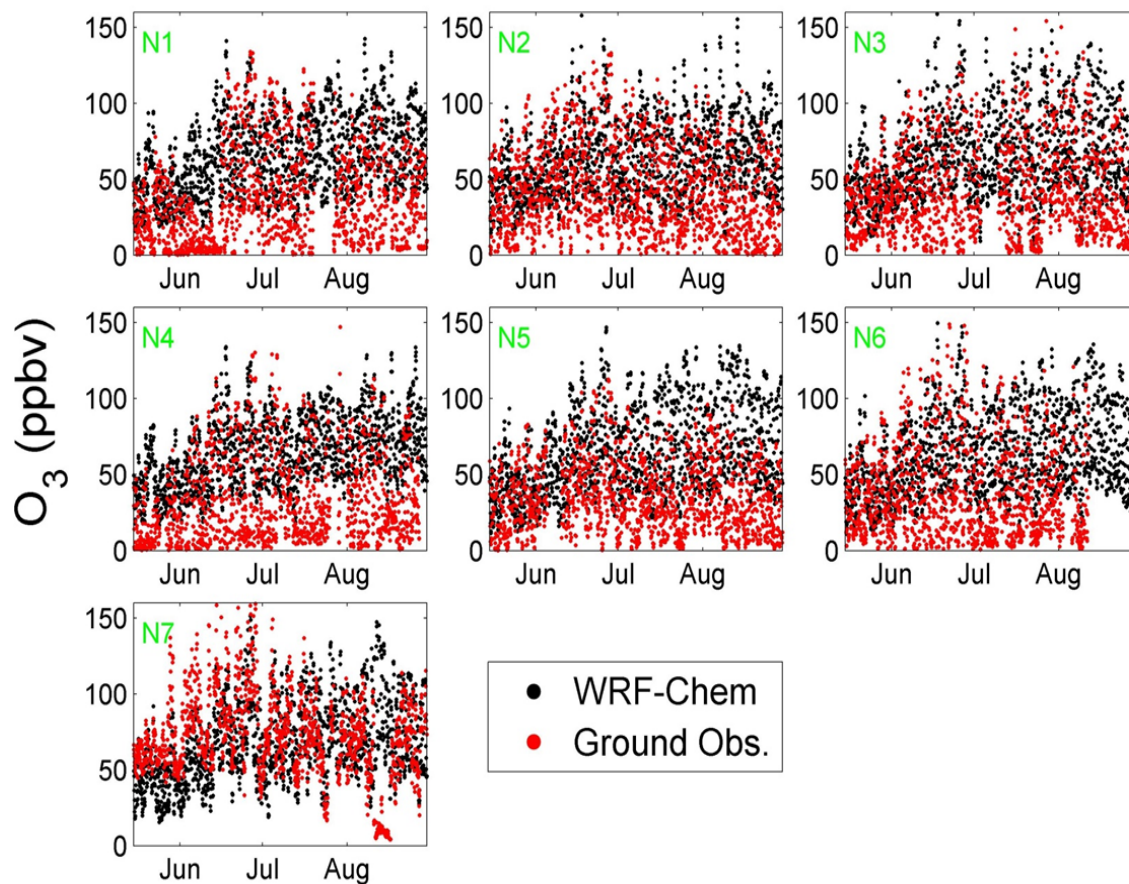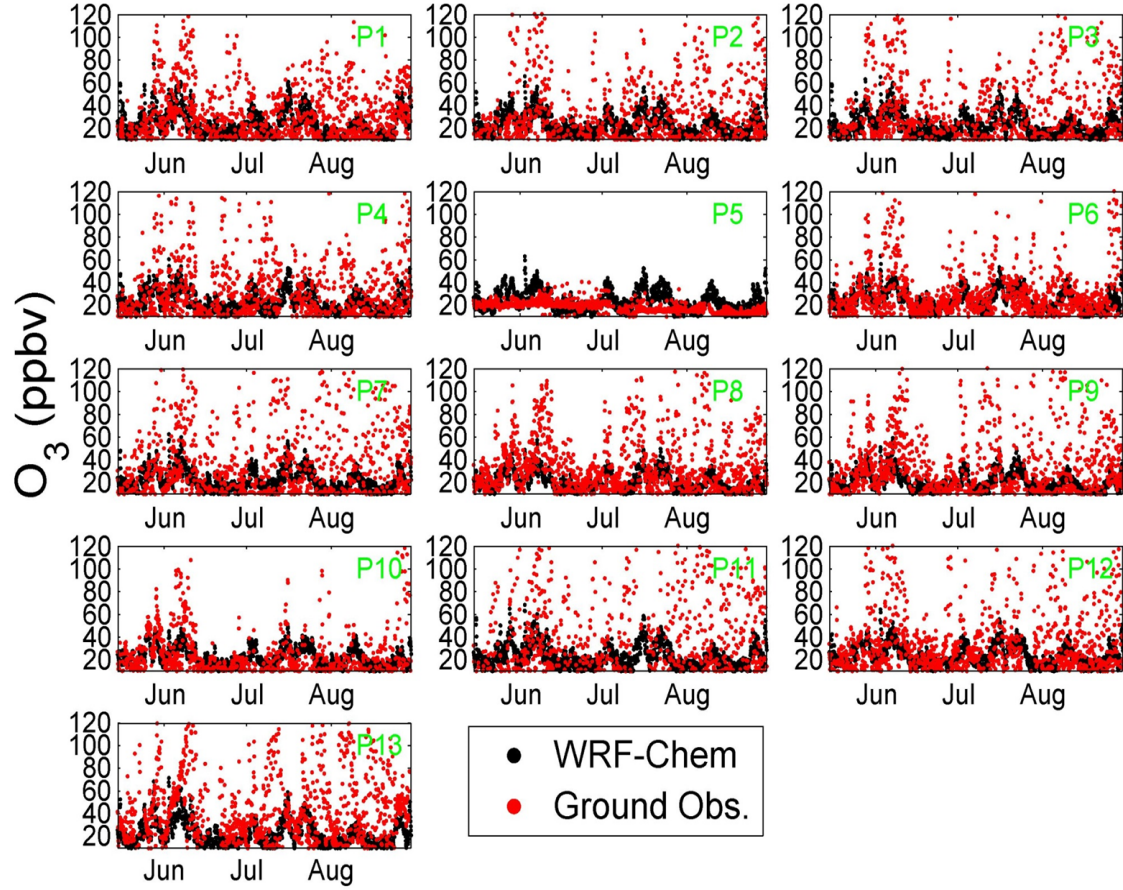
Figure 8.12: O₃ time series of stations (in red) and WRF-Chem (in black) data at the surface for the period MJJA 2011 and for the stations in Pearl River Delta localized in panel (b) of Fig. 8.10.

clear, with a drop most prominent over the stations in the west pacific (J3 and J6) since the monsoon strength depends on the location, and is stronger at lower latitudes. Generally, the biases reported may be due to the resolution of the model resulting in a grid of around 50 km around the station that may include other surface O₃ contributions. Many of the stations are close to one another, with a distance smaller than the WRF-Chem horizontal resolution. Other possible biases arise from difficulties in simulating local flow patterns due to topography and land-sea circulation, as well as uncertainties in emissions and NO$_x$ concentrations [Pfister et al., 2013]. In particular, the NCP stations (N1 to N7) have the highest variability, most affected by local emissions, and have correlation coefficients around 0.5. The surface stations
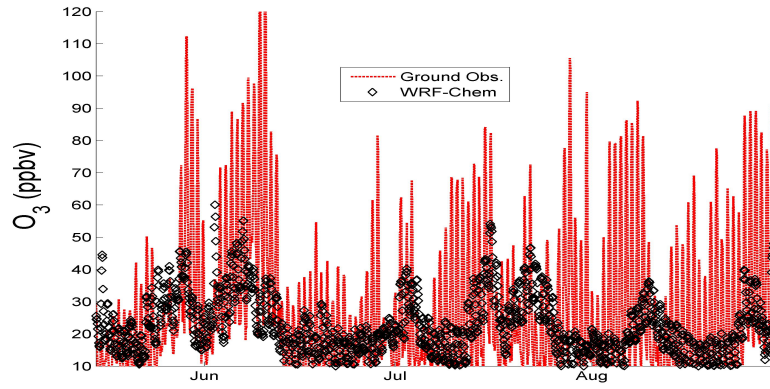
Figure 8.13: O₃ time series of stations (in red) and WRF-Chem (in black) data at the surface for the period MJJA 2011 and for the **average** of the stations in Pearl River Delta of Fig. 8.12.
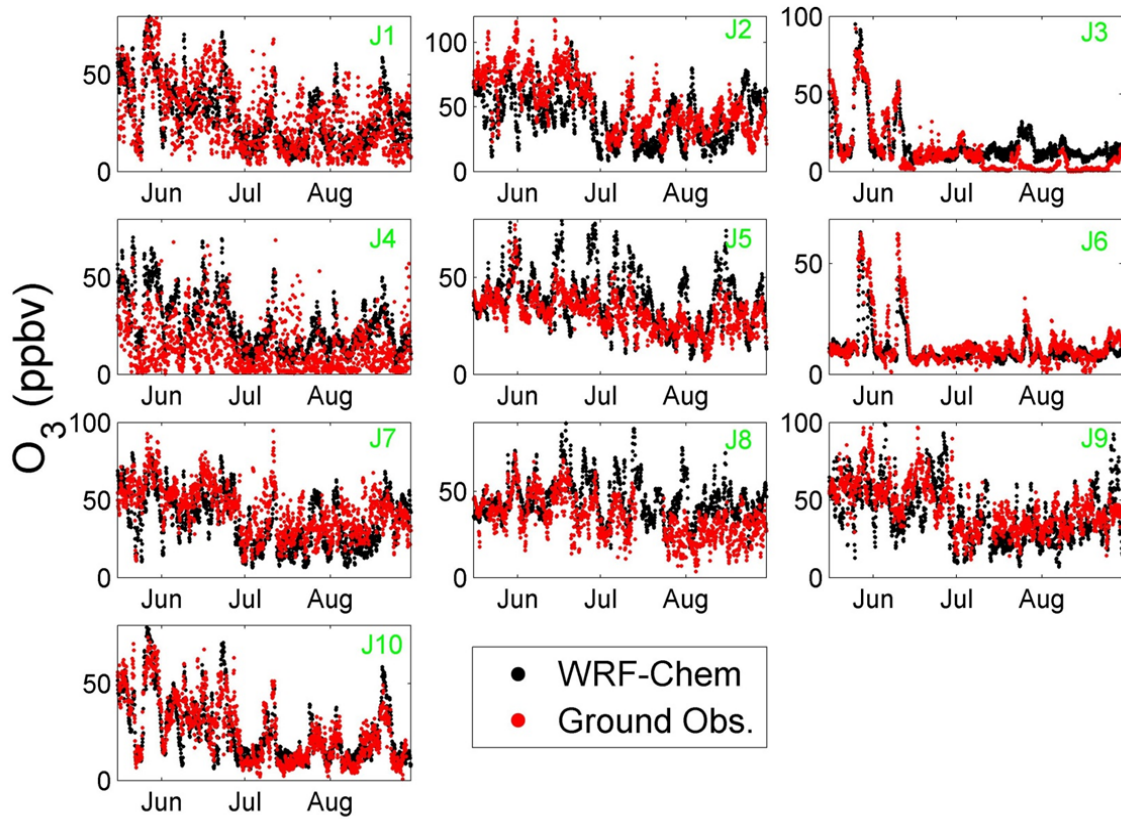

Figure 8.14: O₃ time series of stations (in red) and WRF-Chem (in black) data at the surface for the period MJJA 2011 and for the stations in Japan localized in panel (c) of Fig. 8.10.

have high diurnal variations with recurrent near-zero O$_3$ values suggesting high O$_3$ losses, most probably due to the fact that at short distances from NO$_x$ sources, as is the case at urban stations here, O$_3$ is depleted through titration by the freshly emitted NO, a process that is fast and not well captured by the model. In fact, this claim can be justified by looking at the station N7, which is the only rural station, and thus with lower emissions and NO$_x$ dependence. Both the model and the observation over N7 (except for few days in August), show better agreement than the rest of the stations though the correlation coefficient is not the highest since it is affected by the bias in August (probably due to a local effect such as rain over this region that is not captured by the model, given its coarse resolution). The ground observations of the PRD stations (P1 to P13) show frequent O$_3$ peaks, that are not captured by the model. Correlation coefficients are less than 0.5. The stations plotted here are very close to one another, making the model's ability to reproduce the observation quite limited due to its resolution. Nevertheless, the model is able to reproduce the diurnal variability of the observation. I plot in Fig. 8.13 the average of these stations from WRF-Chem and from the surface station, in order to deduce an average effective comparison. The model reproduces well the observation in May, June and beginning of July, but then it fails to capture the variability recorded. The correlation coefficient between the 2 averaged datasets is of 0.5, the *rmse*=19.65 ppbv and *mape*=58.6%.

Japanese stations (J1 to J10) show the best correlation with the model (0.46-0.87) suggesting that the anthropogenic emissions used within the WRF-Chem model over Japan are better than those over China. The model is able to reproduce well the diurnal O$_3$ variation. I note in particular the remote station J6, which is well off the pollution plumes from east Asia and therefore show the best correlation.

8.5.3   Validation With IASI

Unlike the comparison done with surface stations, satellite retrievals cannot be compared directly with the model output. The retrieval depends on the sensitivity of the instrument which can be described by the averaging kernel (AK) functions at the different altitudes (section 4.5.6). The modeled profile is first linearly interpolated to the time and location of the retrieval. Then, the averaging kernels associated with each IASI measurement and

its *apriori* profile are applied to the interpolated modeled profile (smoothing). Figure 8.15 shows the IASI and WRF-Chem (smoothed with IASI's AKs) [0-6] km O_3 column and their absolute difference in DU. To show the effect of applying the AK functions, I plot also the WRF-RAW, i.e. the direct model output without the application of the AK functions. The WRF-Chem AK accounts therefore for IASI sensitivity and vertical resolution. Focusing on the the last column of Fig. 8.15, one can see how the absolute difference is the largest around south of the domain which is the region where the monsoon starts and where it is the strongest (see section 8.4.2). This difference is smaller in May and June and becomes quite important after the well establishment of the monsoon (July-August). The model performs relatively well for all latitude above 30N. However, it systematically overestimates IASI over India, and south of 30N of about 10 DU during all the study period. This suggests that the O_3 local chemistry in the model is not accurately described since this region is the most affected by the monsoon (see section 8.4.2). In fact, any localized, intense convective events will be very difficult to reproduce at a 50 km grid spacing of the model and hence the O_3 lower production, or transport will be also not well captured.

The relative difference and correlation coefficient of the averaged 4 months observation and model data is shown in Fig. 8.16. The averaged correlation coefficient is of 0.91 indicating a good general model performance. The relative difference ranges between -30 to 30%, with the largest differences over the south of the domain, in accordance with Fig. 8.15.

8.6   Conclusions and Perspectives

Most of the world's population lives in regions that depend on monsoon rainfall for water and agricultural fertility. The monsoon also affects climate in other parts of the world as well via the effective transport of pollutants. The study of the dynamics and variability of the monsoon from space and model measurements provides therefore useful information on the distribution and losses of pollutants, in particular, tropospheric O_3. The latter is shown to have a particular seasonal variation over south and east Asia due to the monsoon. The monsoon variability is recorded and well captured over the different years of the IASI period (2008-2013). The IASI O_3 data show decreasing values starting May of each year,
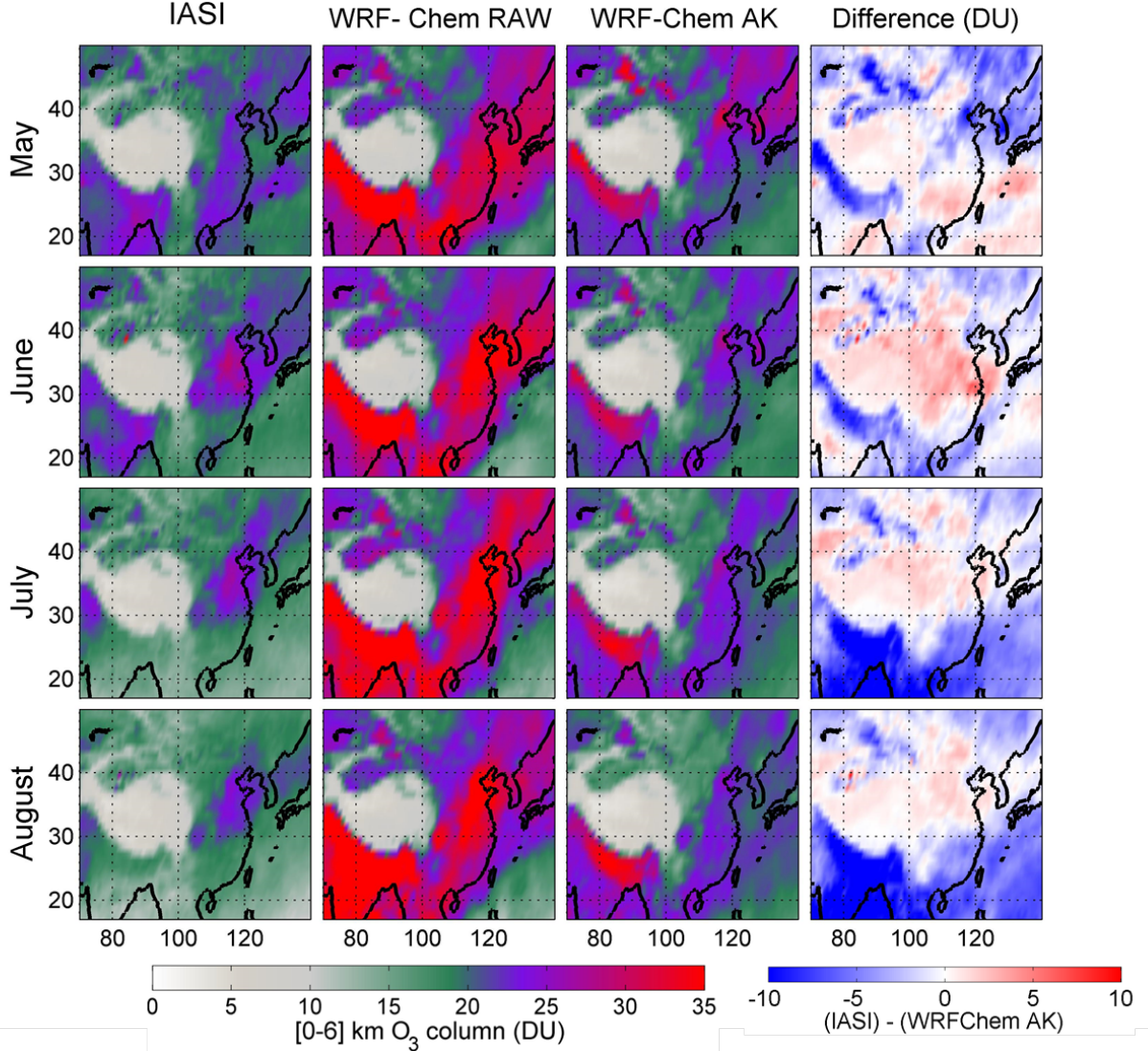
Figure 8.15: [0–6] km O$_3$ column for the period MJJA 2011 from IASI and WRF-Chem (both raw data and those smoothed with IASI's averaging kernel functions, and their absolute difference (in DU).

and reach a minimum in July-August which is mostly prominent in south Asia where the monsoon is stronger. CO monthly variation does not show the same strong decreasing pattern. Given that the lifetime of CO is larger and that the seasonal variation of CO is such that it decreases in summer, the analysis of the monsoon effect on the CO total columns is not straightforward. The rather constant CO total columns values during the monsoon suggest that CO is not locally removed. For surface O$_3$, both the ground stations and the
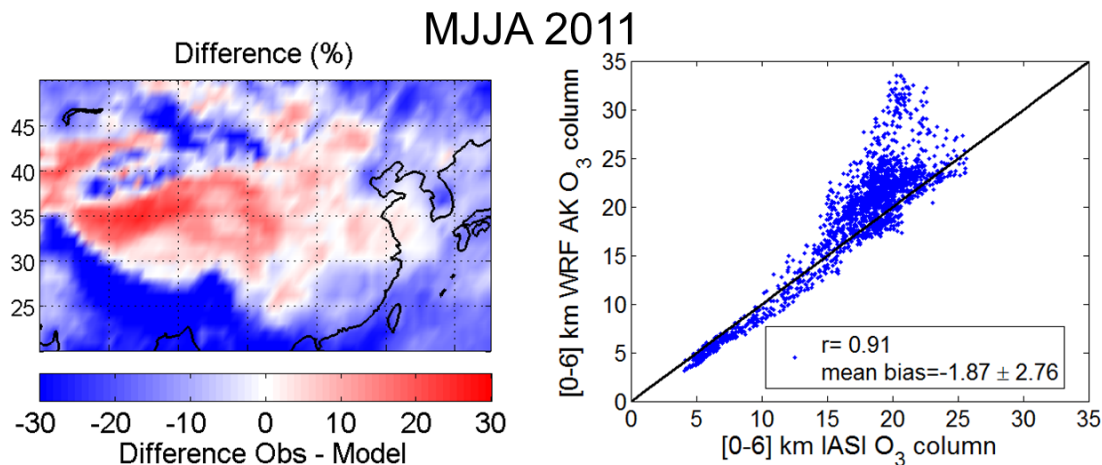
Figure 8.16: Relative difference (%) (left) and correlation (right) of the [0–6] km O$_3$ column for the averaged period MJJA 2011 from IASI and WRF-Chem (smoothed with IASI's averaging kernel functions.

model data in China in particular show no clear signature due to the monsoon, suggesting that near-surface pollution sources do not correlate with the monsoon strength, except few stations in the north west Pacific. In order to assess the monsoon strength on tropospheric O$_3$ and CO, I compare tropospheric O$_3$ and total CO columns to meteorological parameters from the ERA interim database during the monsoon of 2011. Using the [0-6] km O$_3$ column from IASI, clear inverse relationship is seen between tropospheric O$_3$ on one hand, and cloud cover/relative humidity/winds on the other hand, suggesting that free tropospheric O$_3$ production is decreased during the monsoon or that O$_3$ is transported. In fact, the high cloud cover that the monsoon generates, accompanied with a lot of rain and therefore high relative humidity in the troposphere lead to a lower production rate since the photochemical activity will be much lower and relative humidity is a sink of O$_3$. On the other hand, the winds are also strong during the monsoon and O$_3$ during this period can be transported either vertically due to deep convection to above the [0-6] km column, or horizontally to the Pacific and the globe. The last part of this chapter shows that the WRF-Chem model captures the diurnal and seasonal variation of tropospheric O$_3$ better at the surface than in the whole [0-6] km column, though good correlations were seen with IASI for latitudes above 25N, where the monsoon is less strong. This study thus shows the need of studying the monsoon over finer

resolutions in order to well assess and capture losses mechanisms and transport of pollutants. My work for this study is not completed yet, and I plan to look at different other aspects of the monsoon notably:

– Statistical and sensitivity analysis on the IASI daily data. Since these are provided with a cloud flag, and given that high rainfall would be accompanied with high cloud cover, it sounds counter-intuitive to use IASI data with cloud cover less than 13(24)<% for O_3(CO), to compare with high cloud cover reanalysis data. However, even if rain is associated with high cloud cover and low IASI observation count, the IASI observation taken at relatively clear cloud scenes, will reflect the status of the clean atmosphere after the rain. So roughly my approach in this study is valid but could be made better. I will choose days where IASI data are available, and pick the corresponding days (or day before and after the observation is taken) for rainfall, and then compare to find (better) correlations between the two products.

– Vertical transport of pollutants as seen by IASI. This will be done using altitude-latitude (zonal) plots and profile analysis to track possible vertical transport of O_3 and CO from the boundary layer to the free troposphere. I will also study the [6-12] km O_3 column and check if the O_3 column exhibits a decrease (due to transport by winds during the monsoon) or an increase (due to deep convection pushing air masses from the lower and middle troposphere to the upper troposphere).

– Add NO_2 product from GOME-2. In order to look at the near-surface pollutants decrease in concentration, it is best if one looks at a short-lived species such as NO_2 that is also mostly found in the boundary layer.

– Include O_3 and O_3 precursors tracers in the WRF-Chem model to assess transport. This would be done in a similar manner than that done in section 7.7 to assess sources of O_3 at different altitudes to try to find how the variations in the monsoon re-distribute surface emissions into the free troposphere, i.e. is there a pulse of increased O_3 production after the monsoon due to lifting of non-soluble O_3 precursors into the free troposphere? Or do the precursors get there via other mechanisms? Even if there was a lot of good vertical mixing and uplift of O_3 precursors, it would be also counter-acted by the transport of O_3 itself as well as its non-soluble precursors from elsewhere given that the winds

are stronger in the free troposphere, especially during the monsoon period. Even if we see with IASI a pulse of increased O_3 production in the free troposphere, could it be STE, long range transport or vertical mixing? Here we could also see the advantage of working with different sets of input data and model to complement the observations. Another question is derived from this previous point: does the monsoon itself decrease the global background free tropospheric O_3 values or does it increase it due to the uplifting of its precursors as mentioned above, or the two effects cancel one another?

Chapter 9

General Conclusions and Discussion

Reducing tropospheric ozone values in the boundary layer in particular, will help improve air quality and public health [WHO, 2005]. The complexity in controlling O_3 concentrations lies in the difficulty in attributing it to a source region, due to the interplay of the different processes that governs its production, loss, and transport. Background O_3 in the Northern Hemisphere from observation data is shown to be increasing, although estimates are variable, some even revealing little change e.g. [Vingarzan, 2004, Oltmans et al., 2006, Derwent et al., 2007], despite the efforts (mainly in Europe and the US) for improving local and regional air quality by strict control of precursors emissions [Yienger et al., 2000, Collins et al., 2000, Dentener et al., 2005, Szopa et al., 2006]. For example, by 2030, Dentener et al. [2006] suggest an average O_3 surface concentration from 40 to 50 ppbv over large parts of North America, Southern Europe, and Asia.

Uncertainties in O_3 precursors and transport estimates are still a main challenge that hinder the complete rightful assessment of its budget. Current policies to reduce tropospheric O_3 levels, focus on reducing the traditional O_3 precursors such as NO_x, NMVOC and CO. This is effective on the short term with hours-to-weeks response. However and as discussed in Chapter 2, the hydroxyl radical plays a crucial role in the production of O_3. Altering the concentrations of OH, will perturb the emissions of the O_3 precursors and also affect the lifetime of methane, which is particularly the first precursor of O_3 in the remote troposphere as it is the most abundant atmospheric VOC [Crutzen, 1973, Derwent et al., 2001, Fiore

et al., 2009]. Since the methane lifetime is quite long (and changes considerably in each new IPCC report), this will result in a long-term influence on tropospheric O_3 values. On a shorter timescale, NO_x, an important precursor of O_3, as seen in this thesis, controls the tropospheric O_3 budget. However, NO_x emission from lightning remains highly uncertain, with estimates ranging from 1 to 20 Tg N yr^{-1} [Lee et al., 1997, Boersma et al., 2005]. Another source of uncertainty lies in the budget of O_3 transported from STE influx. Jacob [1999] suggested a wide range of STE influx from 400 to 1100 Tg O3 yr^{-1}.

Here lies the importance of the study of tropospheric O_3 from a local to a global scale as well as its relationship to its precursors and transport modes to eventually well assess its effect on global air quality. For this end, I present in this thesis work an overview on what could be accomplished with IASI and other supporting datasets to study the seasonal cycle of tropospheric O_3 at a city scale (9 cities in the Northern Hemisphere), regional scale (Mediterranean, south and east Asia) and on a global scale, over a period of 4-6 years.

9.1 General Conclusions

My analysis show that on a city scale, tropospheric O_3 is transported to downwind rural regions which might suggest serious public health issues, even well away from pollution emission sources. This study shows the importance of the right quantification of background O_3 both locally and globally to study its consequences on health and ecosystems. Since O_3 can be either produced locally or transported by winds or by STEs, the Mediterranean region, and in particular the east side of it, show the peculiarity of being subjected to all 3 processes. In my work it is demonstrated that: in the Mediterranean boundary layer, most of the O_3 is from local anthropogenic sources detected with the help of an anthropogenic O_3 tracer in the WRF-Chem model; in the free troposphere, using the transport (called *inflow*) tracer of the model, transport of pollutants is shown to be the main source of O_3 into the region; evidence of STE events are suggested by IASI as well as by the transport tracer and from the analysis of potential vorticity and relative humidity from the model. Since O_3 over the different cities studied and over the Mediterranean region is affected by transport, and since east and southeast Asian regions are the largest source of pollution by tropospheric O_3 (as well as different

other pollutants), the last study in this work focuses on this region, during a special season: the summer monsoon. In fact, the monsoon system acts like a cleaning factor through the lower photochemistry leading to a lower production of O_3 while larger water vapor content also acts as a sink. On the other hand, it can also act as a good mixing tool by uplifting the pollutants into the mid and upper troposphere where they can be transported over large distances and affecting downwind regions air quality. By taking a case study and analyzing the monsoon of 2011, tropospheric O_3 from IASI shows a dependency on the meteorological dynamics of the monsoon, leading to a direct inverse relationship between monsoon strength and tropospheric ozone.

9.2   Future Work

This thesis helped the understanding of the tropospheric O_3 over different regions and time scales, using different datasets to define its different sources and transport mechanisms. However, a lot should yet be done to complete this understanding especially in the future with the long time series of O_3 that IASI will be able to provide. Many countries have for decades, regulation to improve air quality by reducing O_3 precursors emissions. The financial cost of these regulations, counter-acted by the increase hemispheric background O_3 values is making an international approach to air quality management an attractive option which requires a deep understanding of the source-receptor relationships between countries and continents. With MetOp-C due to be launched in 2018, IASI data will be available till at least 2023. With the long-time series that will be available with the three IASI instruments (2007-2023), long-term changes in the global tropospheric O_3 and their response to changes in emissions will be better investigated in the future and trends will be deduced. Stratospheric O_3 recovery could be also better quantified. In fact, stratospheric recovery and climate change were found to contribute about equally to the increase in tropospheric O_3 during austral winter months [Zeng et al., 2010]. So with a long time-series of tropospheric O_3 from space, will the effect of stratospheric O_3 recovery on the increase in tropospheric O_3 columns in the Southern Hemisphere in particular, and on the rest of the globe in general, will be seen by satellite data?

At favorable conditions, IASI can detect the lowermost tropospheric O_3 but currently instrumental limitations stands in the way of sufficient vertical, spatial and temporal resolution to assess pollution events on a local scale. Monitoring air quality from space at all times is thus a valuable step towards a good understanding of pollution processes having an impact on the global climate system. This should be possible with the future Low Earth Orbit and Geostationary Earth Orbit missions offering more frequent observations with smaller footprints. Example of this mission is the Eumetsat's thermal InfraRed Sounder (IRS), embarked on the Meteosat Third Generation (MTG) satellite of the Sentinel-4 mission and due to be launched in 2021 [Clerbaux and Crevoisier, 2013].

In polar orbit, IASI-NG on MetOp Second Generation satellites (as part of the EPS-Second Generation/Sentinel 5 program) is also due to be launched around 2022 and will offer global precise measurements. With the launch of three successive IASI-NG starting from 2022, more than 20 years of observations will be added to the 17 years from IASI. IASI-NG has a spectral resolution of 0.25 cm^{-1} after apodization (0.50 cm^{-1} for IASI) and a reduction of the radiometric noise by at least a factor of 2 as compared to IASI on MetOp [Crevoisier et al., 2014]. With these new improvements, IASI-NG will provide better information on the vertical distributions of trace gases which will therefore be a novel step towards the characterization of the lower part of the troposphere, and more generally, of the full atmospheric column. With the improved precision, tropospheric O_3 monitoring from space for local and global air quality assessment would be achieved. Retrievals of new species might be also possible, opening a new era in atmospheric detection from space.

Appendices

Appendix A

The Dobson Unit

Imagine that all the ozone in the vertical column of air reaching from the Earth's surface to the top of the atmosphere were concentrated in a single layer of pure O_3 at the surface of the Earth at 273 Kelvins and 1.013 x 10^5 Pascals. The thickness of that layer, measured in hundredths of a millimeter, is the column abundance of O_3 expressed in *Dobson units* (DU). The unit is named after G. M. B. Dobson, who produced the first O_3 spectrometer in 1923. It detects O_3 concentrations from the ground by measuring the intensity of solar UV radiation at four wavelenghths: two are absorbed by O_3, and two are not. One DU is equivalent to 2.69 x 10^{16} molecules of O_3 cm^{-2}. A normal value of O_3 column abundance over the globe is about 300 DU, corresponding to a layer of pure O_3 at the surface only 3 mm thick. If the O_3 concentration as a function of altitude is n_{O_3} (z) (molecules cm^{-3}), the O_3 column burden is:

$$\bar{n}_{O_3} = \int_{\infty}^{0} n_{O_3}(z)dz \qquad (A.1)$$

To find what this $\bar{n}_{O_3}$ (unit=molecules cm^{-2}) translates into, in terms of DU, we need to determine the thickness of the layer of pure O_3 at 273 K and 1 atm corresponding to this burden. Over 1 cm^2 of area, this corresponds to $\bar{n}_{O_3}$ molecules of O_3. The volume (cm^3) occupied by this number of molecules of O_3 can be written as V = 1(cm^3) x h(cm). One DU corresponds to a thickness, h, of 0.01 mm (0.001 cm).

From the ideal-gas law:

$$V = \frac{(\bar{n}_{O_3}/N_A)RT}{P} \times 10^6 \tag{A.2}$$

Where $n_{\bar{O_3}}/N_A$ is the number of moles of O_3, and the factor 10^6 is needed to convert m^3 to cm^3. N_A is the Avogadro constant and is $= 6.02214129$ x 10^{23} mol^{-1} and R is the ideal gas constant and is $= 8.3144621$ J K^{-1}mol^{-1} .

At 273 K and 1 atm, the thickness of the layer of pure O_3 is:

$$\begin{aligned} h &= \frac{(\bar{n}_{O_3})(8.314)(273)}{(1.013 \times 10^5)(6.022 \times 10^{23})} \times 10^6 \\ &= 3.72 \times 10^{-20}\bar{n}_{O_3} \ (cm) \end{aligned} \tag{A.3}$$

for h=0.01 mm=10^{-3} cm, the column burden of O_3 is:

$$\bar{n}_{O_3} = 2.69 \times 10^{16} \ molecules.cm^{-2} \tag{A.4}$$

Appendix B

Spectral Lines Features

Almost each molecule has its own characteristic spectral signature in the infrared (that needs to be measured first in the laboratory). Hetero-nuclear diatomic molecules[1] such as CO or most of polyatomic molecules such as H_2O, CO_2, CH_4, N_2O, SO_2 etc... show good absorption in the thermal infrared. In order to predict the variation of the molecular spectra, it is essential to know the exact energy of the rotational-vibrational energy levels involved in the infrared transition (absorption or emission). For this purpose, quantum mechanical calculations are performed that provide these energy levels using theoretical models.

Basic properties to determine spectral features of an absorption line are: the central position of the line λ_0 or ν_0, the strength or intensity of the line, and shape factor or profile of the line.

Observed spectral lines are always broadened, partly due to the finite resolution of the spectrometer and partly due to intrinsic physical causes, which can have different sources: quantum mechanical uncertainty in the energy E of levels also referred as natural broadening, collisional or pressure broadening and thermal or Doppler broadening.

Natural Broadening   According to Heisenberg's Uncertainty Principle, as the time available for an energy measurement decreases, the inherent uncertainty of the result increases and electrons can make transitions from and to anywhere within "fuzzy" energy levels, pro-

---

1. In contrast to homo-nuclear diatomic molecules such as N_2 or O_2 that are not IR active, since their charges are distributed symmetrically and molecules only absorb in the IR if they have a permanent dipole moment or if the vibration generates a dipole moment

ducing an uncertainty in the wavelength of the photon absorbed or emitted in transition. Natural broadening is non-significant for ro-vibrational transitions in the IR.

Pressure-Collisional Broadening   At relatively high spectral resolution, individual molecular lines gets broadened when the total pressure increases in the Earth's atmosphere. The orbitals of an atom can be perturbed in a collision with a neutral atom or molecule or by a close encounter involving the electric field of an ion. The results is called pressure broadening and is largely dependent on the average time between collisions or encounters. It leads to a Lorentz profile with molecular linewidths of 0.2-0.4 cm^{-1}. The exact magnitude of this effect depends on the molecule and rotational quantum numbers and laboratory measurements and theoretical models are needed to determine the broadening. The values for natural and pressure broadening are of the same order, but the pressure profile could be wider.

Doppler/Thermal Broadening   In a gas, the individual atoms, elements or molecules are continuously moving in random directions, with an average speed proportional to the temperature of the gas: $\left\langle \frac{1}{2}mv^2 \right\rangle = \frac{3}{2}kT$. The term on the left-hand side is the mean kinetic energy. The individual gas particles (with mass m) follow a Maxwellian velocity distribution, resulting in a spread of velocities, v, about the average value. On the right hand side of the equation, T is the temperature of the gas and k the Stefan-Boltzmann constant. Compared to a stationary observer, any particular atom, element or molecule could be moving along the line-of-sight, perpendicular to the line-of-sight, or some combination of both. This means that every spectral line emitted is Doppler shifted relative to the observer, resulting in a small change in the observed wavelength. This spreading of a spectral line due to the temperature of the emitting medium is called "thermal Doppler broadening", which is significant at high altitudes in the atmosphere, where the pressure decrease and the temperature-generated thermal velocities of the molecules become significant.

Voigt Profile   In the IR, and in atmospheric regions from about 20 to 50 km, the line shapes are determined by both collisional and Doppler-broadening processes. which combination is called the Voigt line shape and is shown in Fig. B.1. The relative importance of each with respect to altitude is shown in Fig. B.2. Collisional broadening (with a Lorentz

profile) is mostly dominant at lower altitudes. At higher altitudes, the pressure is smaller and thus the thermal/Doppler broadening becomes important. When the Doppler and collisional broadening are of the same order, we get the Voigt profile. From here we can see how the shape of the spectral line includes information of the vertical distribution of the absorbing molecule.
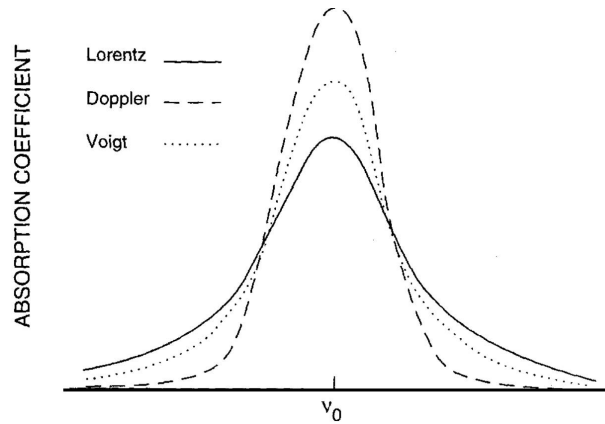

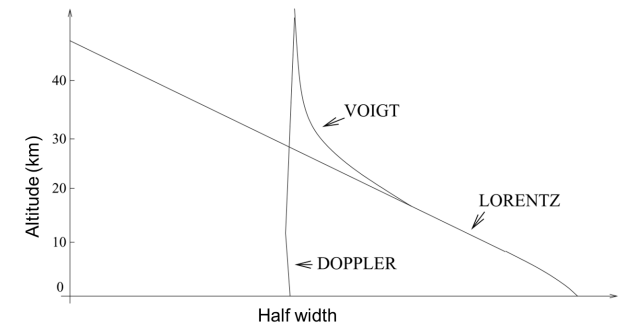Figure B.1: Lorentz, Doppler and Voigt line shape. Figure from Salby [1996].

Figure B.2: The importance of each of the line shapes with altitude. Figure from Turquety [2003]

References

H. Akimoto. Global air quality and pollution. *Science*, 302:1717–1719, 2003.

U. Amato, D. De Canditiis, and C. Serio. Effect of apodization on the retrieval of geophysical parameters from fourier-transform spectrometers. *Appl. Opt.*, 37(27):6537–6543, Sep 1998. doi: 10.1364/AO.37. 006537. URL http://ao.osa.org/abstract.cfm?URI=ao-37-27-6537.

G. Ancellet, M. Beekmann, and A. Papayannis. Impact of a cutoff low development on downward transport of ozone in the troposphere. *Journal of Geophysical Research: Atmospheres*, 99(D2):3451–3468, 1994. ISSN 2156-2202. doi: 10.1029/93JD02551. URL http://dx.doi.org/10.1029/93JD02551.

W. Attmannspacher, R. Hartmannsgruber, and P. Lang. Langzeit tendenzen des ozons der atmosphaere aufgrund der 1967 begonnenen ozon messreihen am meteorologischen observatorium hohenpeissenber. *Meteorol. Rundsch.*, 37:193–199, 1984.

T. August, D. Klaes, P. Schlüssel, T. Hultberg, M. Crapeau, A. Arriaga, A. O'Carroll, D. Coppens, R. Munro, and X. Calbet. IASI on Metop-A: Operational Level 2 retrievals after five years in orbit. *Journal of Quantitative Spectroscopy and Radiative Transfer*, 113(11):1340 – 1371, 2012. ISSN 0022-4073. doi: http://dx.doi.org/10.1016/j.jqsrt.2012.02.028. URL http://www.sciencedirect.com/science/article/pii/S0022407312000921.

H.H. Aumann, M.T. Chahine, C. Gautier, M.D. Goldberg, E. Kalnay, L.M. McMillin, H. Revercomb, P.W. Rosenkranz, W.L. Smith, D.H. Staelin, L.L. Strow, and J. Susskind. AIRS/AMSU/HSB on the Aqua mission: design, science objectives, data products, and processing systems. *Geoscience and Remote Sensing, IEEE Transactions on*, 41(2):253–264, Feb 2003. ISSN 0196-2892. doi: 10.1109/TGRS.2002.808356.

J. L. Baray, V. Daniel, G. Ancellet, and B. Legras. Planetary-scale tropopause folds in the southern subtropics. *Geophysical Research Letters*, 27(3):353–356, 2000. ISSN 1944-8007. doi: 10.1029/1999GL010788. URL http://dx.doi.org/10.1029/1999GL010788.

B. Barret, E. Le Flochmoen, B. Sauvage, E. Pavelin, M. Matricardi, and J. P. Cammas. The detection of post-monsoon tropospheric ozone variability over south Asia using IASI data. *Atmospheric Chemistry and Physics*, 11:9533–9548, 2011. doi: 10.5194/acp-11-9533-2011.

R. Beer. Tes on the aura mission: scientific objectives, measurements, and analysis overview. *Geoscience and Remote Sensing, IEEE Transactions on*, 44(5):1102–1105, May 2006. ISSN 0196-2892. doi: 10. 1109/TGRS.2005.863716.

S. Bethan, G. Vaughan, and S.J. Reid. A comparison of ozone and thermal tropopause heights and the impact of tropopause definition of quantifying the ozone content of the troposphere. *Q. J. R. Meteorol. Soc.*, 122:926–944, 1996.

K. F. Boersma, H. J. Eskes, E. W. Meijer, and H. M. Kelder. Estimates of lightning NO_x production from gome satellite observations. *Atmospheric Chemistry and Physics*, 5(9):2311–2331, 2005. doi: 10.5194/acp-5-2311-2005. URL http://www.atmos-chem-phys.net/5/2311/2005/.

K.W. Bowman, C.D. Rodgers, S.S. Kulawik, J. Worden, E. Sarkissian, G. Osterman, T. Steck, Ming Lou, A. Eldering, M. Shephard, H. Worden, M. Lampel, S. Clough, P. Brown, C. Rinsland, M. Gunson, and R. Beer. Tropospheric emission spectrometer: retrieval method and error analysis. *Geoscience and Remote Sensing, IEEE Transactions on*, 44(5):1297–1307, May 2006. ISSN 0196-2892. doi: 10.1109/ TGRS.2006.871234.

A. W. Brewer. Evidence for a world circulation provided by the measurements of helium and water vapour distribution in the stratosphere. *Quarterly Journal of the Royal Meteorological Society*, 75(326): 351–363, 1949. ISSN 1477-870X. doi: 10.1002/qj.49707532603. URL http://dx.doi.org/10.1002/ qj.49707532603.

J. Burrows, M. Weber, M. Buchwitz, V. Rozanov, A. Ladstatter-Weienmayer, A. Richter, R. Debeek, R. Hoogen, K. Bramstedt, K.-U. Eichmann, and M. Eisinger. The Global Ozone Monitoring Experiment (GOME): Mission concept and first scientific results. *Jounal of Atmospheric Sciences*, 56:151–175, 1999.

J.P. Burrows, U. Platt, and P. Borrell. *The Remote Sensing of Tropospheric Composition from Space*. Springer Verlag, Heidelberg, 2011.

M. Capderou. *Satellites: De Kepler au GPS*. Springer, 2012.

W. Chameides and J. C. G. Walker. A photochemical theory of tropospheric ozone. *Journal of Geophysical Research*, 78(36):8751–8760, 1973. ISSN 2156-2202. doi: 10.1029/JC078i036p08751. URL http://dx.doi.org/10.1029/JC078i036p08751.

C.-H. Chen, C.-C. Chan, B.-Y. Chen, T.-J. Cheng, and Y. L Guo. Effects of particulate air pollution and ozone on lung function in non-asthmatic children. *Environmental Research*, 137(0):40 − 48, 2015. ISSN 0013-9351. doi: http://dx.doi.org/10.1016/j.envres.2014.11.021. URL http://www.sciencedirect. com/science/article/pii/S0013935114004435.

L. Clarisse, D. Hurtmans, C. Clerbaux, J. Hadji-Lazaro, Y. Ngadi, and P.-F. Coheur. Retrieval of sulphur dioxide from the infrared atmospheric sounding interferometer (IASI). *Atmospheric Measurement Techniques*, 5:581–594, 2012. doi: 10.5194/amt-5-581-2012.

C.O. Clark, J.E. Cole, and P.J. Webster. Indian ocean SST and Indian summer rainfall: predictive relationships and their decadal variability. *J. Climate*, 13:2503–2519, 2000. doi: http://dx.doi.org/10. 1175/1520-0442(2000)013<2503:IOSAIS>2.0.CO;2.

C. Clerbaux and C. Crevoisier. New Directions: Infrared remote sensing of the troposphere from satellite: Less, but better. *Atmospheric Environment*, 72:24–26, June 2013. doi: 10.1016/j.atmosenv. 2013.01.057.

C. Clerbaux, A. Boynard, L. Clarisse, M. George, J. Hadji-Lazaro, H. Herbin, D. Hurtmans, M. Pommier, A. Razavi, S. Turquety, C. Wespes, and P.-F. Coheur. Monitoring of atmospheric composition using the thermal infrared IASI/MetOp sounder. *Atmospheric Chemistry and Physics*, 9:6041–6054, 2009.

S.A. Clough, M.W. Shephard, E.J. Mlawer, J.S. Delamere, M.J. Iacono, K. Cady-Pereira, S. Boukabara, and P.D. Brown. Atmospheric radiative transfer modeling: a summary of the AER codes. *Journal of Quantitative Spectroscopy and Radiative Transfer*, 91(2):233 – 244, 2005. ISSN 0022-4073. doi: http: //dx.doi.org/10.1016/j.jqsrt.2004.05.058. URL http://www.sciencedirect.com/science/article/ pii/S0022407304002158.

P.-F. Coheur, L. Clarisse, S. Turquety, D. Hurtmans, and C. Clerbaux. IASI measurements of reactive trace species in biomass burning plumes. *Atmospheric Chemistry and Physics Discussions*, 9(2):8757–8789, 2009. doi: 10.5194/acpd-9-8757-2009. URL http://www.atmos-chem-phys-discuss.net/9/ 8757/2009/.

W. J. Collins, R. G. Derwent, B. Garnier, C. E. Johnson, M. G. Sanderson, and D. S. Stevenson. Effect of stratosphere-troposphere exchange on the future tropospheric ozone trend. *Journal of Geophysical Research: Atmospheres*, 108(D12):n/a–n/a, 2003. ISSN 2156-2202. doi: 10.1029/2002JD002617. URL http://dx.doi.org/10.1029/2002JD002617.

W.J. Collins, D.S. Stevenson, C.E. Johnson, and R.G. Derwent. The european regional ozone distribution and its links with the global scale for the years 1992 and 2015. *Atmospheric Environment*, 34: 255–267, 2000.

O. R. Cooper, J. L. Moody, D. D. Parrish, M. Trainer, J. S. Holloway, G. Hübler, F. C. Fehsenfeld, and A. Stohl. Trace gas composition of midlatitude cyclones over the western north atlantic ocean: A seasonal comparison of O_3 and CO. *Journal of Geophysical Research: Atmospheres*, 107(D7):ACH 2–1–ACH 2–12, 2002. ISSN 2156-2202. doi: 10.1029/2001JD000902. URL http://dx.doi.org/10. 1029/2001JD000902.

O. R. Cooper, R. Gao, D. Tarasick, T. Leblanc, and C. Sweeney. Long-term ozone trends at rural ozone monitoring sites across the United States, 1990–2010. *Journal of Geophysical Research: Atmospheres*, 117(D22):n/a–n/a, 2012. ISSN 2156-2202. doi: 10.1029/2012JD018261. URL http://dx.doi.org/ 10.1029/2012JD018261.

J. K. Creilson, J. Fishman, and A. E. Wozniak. Intercontinental transport of tropospheric ozone: a study of its seasonal variability across the North Atlantic utilizing tropospheric ozone residuals and its relationship to the North Atlantic Oscillation. *Atmospheric Chemistry and Physics*, 3:2053–2066, 2003.

C. Crevoisier, C. Clerbaux, V. Guidard, T. Phulpin, R. Armante, B. Barret, C. Camy-Peyret, J.-P. Chaboureau, P.-F. Coheur, L. Crépeau, G. Dufour, L. Labonnote, L. Lavanant, J. Hadji-Lazaro, H. Herbin, N. Jacquinet-Husson, S. Payan, E. Péquignot, C. Pierangelo, P. Sellitto, and C. Stubenrauch. Towards IASI-New Generation (IASI-NG): impact of improved spectral resolution and radiometric noise on the retrieval of thermodynamic, chemistry and climate variables. *Atmospheric Measurement Techniques*, 7(12):4367–4385, 2014. doi: 10.5194/amt-7-4367-2014. URL http://www.atmos-meas-tech.net/7/4367/2014/.

P. Crutzen. A discussion of the chemistry of some minor constituents in the stratosphere and troposphere. *Pure Appl. Geophys.*, 106-108:1385–1399, 1973. doi: 10.1007/BF00881092.

P. Crutzen. Photochemical reactions initiated by and influencing ozone in unpolluted tropospheric air. *Tellus*, 26(1-2):47–57, 1974. ISSN 2153-3490. doi: 10.1111/j.2153-3490.1974.tb01951.x. URL http://dx.doi.org/10.1111/j.2153-3490.1974.tb01951.x.

E. F. Danielsen, R. S. Hipskind, S. E. Gaines, G. W. Sachse, G. L. Gregory, and G. F. Hill. Three-dimensional analysis of potential vorticity associated with tropopause folds and observed variations of ozone and carbon monoxide. *Journal of Geophysical Research: Atmospheres*, 92(D2):2103–2111, 1987. ISSN 2156-2202. doi: 10.1029/JD092iD02p02103. URL http://dx.doi.org/10.1029/JD092iD02p02103.

F. Dentener, D. Stevenson, J. Cofala, R. Mechler, M. Amann, P. Bergamaschi, F. Raes, and R. Derwent. The impact of air pollutant and methane emission controls on tropospheric ozone and radiative forcing: CTM calculations for the period 1990-2030. *Atmospheric Chemistry and Physics*, 5(7):1731–1755, 2005. doi: 10.5194/acp-5-1731-2005. URL http://www.atmos-chem-phys.net/5/1731/2005/.

F. Dentener, D. Stevenson, K. Ellingsen, T. van Noije, M. Schultz, M. Amann, C. Atherton, N. Bell, D. Bergmann, I. Bey, L. Bouwman, T. Butler, J. Cofala, B. Collins, J. Drevet, R. Doherty, B. Eickhout, H. Eskes, A. Fiore, M. Gauss, D. Hauglustaine, L. Horowitz, I. S. A. Isaksen, B. Josse, M. Lawrence, M. Krol, J. F. Lamarque, V. Montanaro, J. F. Müller, V. H. Peuch, G. Pitari, J. Pyle, S. Rast, J. Rodriguez, M. Sanderson, N. H. Savage, D. Shindell, S. Strahan, S. Szopa, K. Sudo, R. Van Dingenen, O. Wild, and G. Zeng. The global atmospheric environment for the next generation. *Environmental Science & Technology*, 40(11):3586–3594, 2006. doi: 10.1021/es0523845. URL http://dx.doi.org/10.1021/es0523845. PMID: 16786698.

R. G. Derwent, W. J. Collins, C. E. Johnson, and D. S. Stevenson. Transient behaviour of tropospheric ozone precursors in a global 3-d ctm and their indirect greenhouse effects. *Clim. Change*, 49:463–487, 2001. doi: 10.1023/A:1010648913655.

R.G. Derwent, D.S. Stevenson, W.J. Collins, and C.E. Johnson. Intercontinental transport and the origins of the ozone observed at surface sites in europe. *Atmospheric Environment*, 38(13):1891 – 1901, 2004. ISSN 1352-2310. doi: http://dx.doi.org/10.1016/j.atmosenv.2004.01.008. URL http://www.sciencedirect.com/science/article/pii/S1352231004000603.

R.G. Derwent, P.G. Simmonds, A.J. Manning, and T.G. Spain. Trends over a 20-year period from 1987 to 2007 in surface ozone at the atmospheric research station, Mace Head, Ireland. *Atmospheric Environment*, 41(39):9091 – 9098, 2007. ISSN 1352-2310. doi: http://dx.doi.org/10.1016/j.atmosenv.2007.08.008. URL http://www.sciencedirect.com/science/article/pii/S1352231007006978.

Y. Ding. The variability of the Asian Summer Monsoon. *Journal of the Meteorological Society of Japan. Ser. II*, 85B:21–54, 2007. doi: 10.2151/jmsj.85B.21.

S. Dipu, T. V. Prabha, G. Pandithurai, J. Dudhia, G. Pfister, K. Rajesh, and B.N. Goswami. Impact of elevated aerosol layer on the cloud macrophysical properties prior to monsoon onset. *Atmospheric Environment*, 70(0):454 – 467, 2013. ISSN 1352-2310. doi: http://dx.doi.org/10.1016/j.atmosenv.2012.12.036. URL http://www.sciencedirect.com/science/article/pii/S1352231013000034.

G. M. B. Dobson. Origin and distribution of the polyatomic molecules in the atmosphere. *Royal Society of London Proceedings Series A*, 236:187–193, August 1956. doi: 10.1098/rspa.1956.0127.

R. M. Doherty, D. S. Stevenson, W. J. Collins, and M. G. Sanderson. Influence of convective transport on tropospheric ozone and its precursors in a chemistry-climate model. *Atmospheric Chemistry and Physics*, 5(12):3205–3218, 2005. doi: 10.5194/acp-5-3205-2005. URL http://www.atmos-chem-phys.net/5/3205/2005/.

G. Dufour, M. Eremenko, J. Orphal, and J.-M. Flaud. IASI observations of seasonal and day-to-day variations of tropospheric ozone over three highly populated areas of china: Beijing, shanghai, and hong kong. *Atmospheric Chemistry and Physics*, 10:3787–3801, 2010.

G. Dufour, M. Eremenko, A. Griesfeller, B. Barret, E. Le Flochmoen, C. Clerbaux, J. Hadji-Lazaro, P.-F. Coheur, and D. Hurtmans. Validation of three different scientific ozone products retrieved from IASI spectra using ozonesondes. *Atmospheric Measurement Techniques*, 5:611–630, 2012. doi: 10.5194/amt-5-611-2012.

B. N. Duncan and J. A. Logan. Model analysis of the factors regulating the trends and variability of carbon monoxide between 1988 and 1997. *Atmospheric Chemistry and Physics*, 8(24):7389–7403, 2008. doi: 10.5194/acp-8-7389-2008. URL http://www.atmos-chem-phys.net/8/7389/2008/.

K.L. Ebi and G. McGregor. Climate change, tropospheric ozone and particulate matter, and health impacts. *Environmental Health Perspectives*, 116:1449–1455, 2008.

D. P. Edwards, J.-F. Lamarque, J.-L. Attié, L. K. Emmons, A. Richter, J.-P. Cammas, J. C. Gille, G. L. Francis, M. N. Deeter, J. Warner, D. C. Ziskin, L. V. Lyjak, J. R. Drummond, and J. P. Burrows. Tropospheric ozone over the tropical Atlantic: A satellite perspective. *Journal of Geophysical*

Research: Atmospheres, 108(D8):n/a–n/a, 2003. ISSN 2156-2202. doi: 10.1029/2002JD002927. URL http://dx.doi.org/10.1029/2002JD002927.

EEA. Air quality in europe - 2012 report. Technical Report ISBN 978-92-9213-328-3, European Environment Agency, Offce for Offcial Publications of the European Union, Luxembourg, 2012.

EMEP. Transboundary acidification, eutrophication and ground level ozone in europe in 2009. EMEP Status Report 2011, Norwegian Meteorological Institute, 2011.

J.C. Farman, B.G. Gardiner, and J.D. Shanklin. Large losses of total ozone in antarctica reveal seasonal ClO_x/NO_x interaction. *Nature*, 315:207 –210, 1985. doi: 10.1038/315207a0.

Z. Feng, J. Sun, W. Wan, E. Hu, and V. Calatayud. Evidence of widespread ozone-induced visible injury on plants in beijing, china. *Environmental Pollution*, 193(0):296 − 301, 2014. ISSN 0269-7491. doi: http://dx.doi.org/10.1016/j.envpol.2014.06.004. URL http://www.sciencedirect.com/science/article/pii/S0269749114002322.

B.J. Finlayson-Pitts and J.N. Pitts. Tropospheric air pollution: Ozone, airborne toxics, polycyclic aromatic hydrocarbons, and particles. *Science*, 276:1045–1050, 1997.

A. M. Fiore, D. J. Jacob, I. Bey, R. M. Yantosca, B. D. Field, A. C. Fusco, and J. G. Wilkinson. Background ozone over the United States in summer: Origin, trend, and contribution to pollution episodes. *Journal of Geophysical Research: Atmospheres*, 107(D15):ACH 11–1–ACH 11–25, 2002. ISSN 2156-2202. doi: 10.1029/2001JD000982. URL http://dx.doi.org/10.1029/2001JD000982.

A. M. Fiore, F. J. Dentener, O. Wild, C. Cuvelier, M. G. Schultz, P. Hess, C. Textor, M. Schulz, R. M. Doherty, L. W. Horowitz, I. A. MacKenzie, M. G. Sanderson, D. T. Shindell, D. S. Stevenson, S. Szopa, R. Van Dingenen, G. Zeng, C. Atherton, D. Bergmann, I. Bey, G. Carmichael, W. J. Collins, B. N. Duncan, G. Faluvegi, G. Folberth, M. Gauss, S. Gong, D. Hauglustaine, T. Holloway, I. S. A. Isaksen, D. J. Jacob, J. E. Jonson, J. W. Kaminski, T. J. Keating, A. Lupu, E. Marmer, V. Montanaro, R. J. Park, G. Pitari, K. J. Pringle, J. A. Pyle, S. Schroeder, M. G. Vivanco, P. Wind, G. Wojcik, S. Wu, and A. Zuber. Multimodel estimates of intercontinental source-receptor relationships for ozone pollution. *Journal of Geophysical Research: Atmospheres*, 114(D4):n/a–n/a, 2009. ISSN 2156-2202. doi: 10.1029/2008JD010816. URL http://dx.doi.org/10.1029/2008JD010816.

J. Fuhrer and F. Booker. Ecological issues related to ozone: agricultural issues. *Environment International*, 29:141–154, 2003.

Sulochana Gadgil, P. N. Vinayachandran, P. A. Francis, and Siddhartha Gadgil. Extremes of the Indian summer monsoon rainfall, ENSO and equatorial Indian Ocean oscillation. *Geophysical Research Letters*, 31:12, 2004. ISSN 1944-8007. doi: 10.1029/2004GL019733. URL http://dx.doi.org/10.1029/2004GL019733.

J. Gazeaux, C. Clerbaux, M. George, J. Hadji-Lazaro, J. Kuttippurath, P.-F. Coheur, D. Hurtmans, T. Deshler, M. Kovilakam, P. Campbell, V. Guidard, F. Rabier, and J.-N. Thepaut. Intercompari-

son of polar ozone profiles by IASI/MetOp sounder with 2010 concordiasi ozonesonde observations. *Atmospheric Measurement Techniques*, 5:7923–7944, 2012. doi: 10.5194/amtd-5-7923-2012.

S. D. Ghude, G. G. Pfister, C. Jena, R.J. van der A, L. K. Emmons, and R. Kumar. Satellite constraints of nitrogen oxide (NO_x) emissions from India based on OMI observations and WRF-Chem simulations. *Geophysical Research Letters*, 40(2):423–428, 2013. ISSN 1944-8007. doi: 10.1002/grl.50065. URL http://dx.doi.org/10.1002/grl.50065.

G. A. Grell, S. E. Peckham, R. Schmitz, S. A. McKeen, G. Frost, W. C. Skamarock, and B. Eder. Fully coupled "online" chemistry within the WRF model. *Atmospheric Environment*, 39:6957–6975, 2005. doi: 10.1016/j.atmosenv.2005.04.027.

A. Guenther, C. N. Hewitt, D. Erickson, R. Fall, C. Geron, T. Graedel, P. Harley, L. Klinger, M. Lerdau, W. A. Mckay, T. Pierce, B. Scholes, R. Steinbrecher, R. Tallamraju, J. Taylor, and P. Zimmerman. A global model of natural volatile organic compound emissions. *Journal of Geophysical Research: Atmospheres*, 100(D5):8873–8892, 1995. ISSN 2156-2202. doi: 10.1029/94JD02950. URL http://dx.doi.org/10.1029/94JD02950.

A. Guenther, T. Karl, P. Harley, C. Wiedinmyer, P. I. Palmer, and C. Geron. Estimates of global terrestrial isoprene emissions using MEGAN (Model of Emissions of Gases and Aerosols from Nature). *Atmospheric Chemistry and Physics*, 6(111):3181–3210, 2006. doi: 10.5194/acp-6-3181-2006. URL http://www.atmos-chem-phys.net/6/3181/2006/.

B. Hamelin, F. E. Grousset, P. E. Biscaye, A. Zindler, and J. M. Prospero. Lead isotopes in trade wind aerosols at Barbados: The influence of European emissions over the North Atlantic. *Journal of Geophysical Research: Oceans*, 94(C11):16243–16250, 1989. ISSN 2156-2202. doi: 10.1029/JC094iC11p16243. URL http://dx.doi.org/10.1029/JC094iC11p16243.

C. L. Heald, D. J. Jacob, A. M. Fiore, L. K. Emmons, J. C. Gille, M. N. Deeter, J. Warner, D. P. Edwards, J. H. Crawford, A. J. Hamlin, G. W. Sachse, E. V. Browell, M. A. Avery, S. A. Vay, D. J. Westberg, D. R. Blake, H. B. Singh, S. T. Sandholm, R. W. Talbot, and H. E. Fuelberg. Asian outflow and trans-pacific transport of carbon monoxide and ozone pollution: An integrated satellite, aircraft, and model perspective. *Journal of Geophysical Research: Atmospheres*, 108(D24):n/a–n/a, 2003. ISSN 2156-2202. doi: 10.1029/2003JD003507. URL http://dx.doi.org/10.1029/2003JD003507.

D. F. Heath, A. J. Krueger, H. A. Roeder, and B. D. Henderson. The Solar Backscatter Ultraviolet and Total Ozone Mapping Spectrometer (SBUV/TOMS) for NIMBUS G. *Optical Engineering*, 14(4):144323–144323–, 1975. doi: 10.1117/12.7971839. URL http://dx.doi.org/10.1117/12.7971839.

K. P. Hoinka. The tropopause: discovery, definition and demarcation. *Meteorologische Zeitschrift*, 6:281–303, 1997.

J. R. Holton, P. H. Haynes, M. E. McIntyre, A. R. Douglass, R. B. Rood, and L. Pfister. Stratosphere-

troposphere exchange. *Reviews of Geophysics*, 33(4):403–439, 1995. ISSN 1944-9208. doi: 10.1029/ 95RG02097. URL http://dx.doi.org/10.1029/95RG02097.

HTAP. *HTAP: Hemispheric Transport of Air Pollution (2010) Executive Summary, Task Force on Hemispheric Transport of Air Pollution, see www.htap.org.*, 2010.

R. C. Hudman, D. J. Jacob, O. R. Cooper, M. J. Evans, C. L. Heald, R. J. Park, F. Fehsenfeld, F. Flocke, J. Holloway, G. Hübler, K. Kita, M. Koike, Y. Kondo, A. Neuman, J. Nowak, S. Oltmans, D. Parrish, J. M. Roberts, and T. Ryerson. Ozone production in transpacific asian pollution plumes and implications for ozone air quality in california. *Journal of Geophysical Research: Atmospheres*, 109 (D23):n/a–n/a, 2004. ISSN 2156-2202. doi: 10.1029/2004JD004974. URL http://dx.doi.org/10. 1029/2004JD004974.

J. W. Hurrell. Decadal trends in the north atlantic oscillation: Regional temperatures and precipitation. *Science*, 269(5224):676–679, 1995. doi: 10.1126/science.269.5224.676. URL http://www.sciencemag. org/content/269/5224/676.abstract.

D. Hurtmans, P.F. Coheur, C. Wespes, L. Clarisse, O. Scharf, C. Clerbaux, J. Hadji-Lazaro, M. George, and S. Turquety. FORLI radiative transfer and retrieval code for IASI. *Journal of Quantitative Spectroscopy and Radiative Transfer*, 113:1391–1408, 2012. doi: 10.1016/j.jqsrt.2012.02.036.

IPCC. Climate change 2007: The physical science basis. Contribution of Working Group I to the Fourth Assessment Report (AR4) of the Intergovernmental Panel on Climate Change, Intergovernmental Panel on Climate Change, 2007.

IPCC. Climate change 2013: The physical science basis. Contribution of Working Group I to the Fifth Assessment Report (AR5) of the Intergovernmental Panel on Climate Change, Intergovernmental Panel on Climate Change, 2013.

D. J Jacob. *Introduction to atmospheric chemistry*. Princeton University Press, Princeton, NJ, USA, 1999.

D. J. Jacob, J. A. Logan, G. M. Gardner, R. M. Yevich, C. M. Spivakovsky, S. C. Wofsy, S. Sillman, and M. J. Prather. Factors regulating ozone over the United States and its export to the global atmosphere. *Journal of Geophysical Research: Atmospheres*, 98(D8):14817–14826, 1993. ISSN 2156- 2202. doi: 10.1029/98JD01224. URL http://dx.doi.org/10.1029/98JD01224.

D. J. Jacob, E. G. Heikes, S.-M. Fan, J. A. Logan, D. L. Mauzerall, J. D. Bradshaw, H. B. Singh, G. L. Gregory, R. W. Talbot, D. R. Blake, and G. W. Sachse. Origin of ozone and NOx in the tropical troposphere: A photochemical analysis of aircraft observations over the South Atlantic basin. *Journal of Geophysical Research: Atmospheres*, 101(D19):24235–24250, 1996. ISSN 2156-2202. doi: 10.1029/96JD00336. URL http://dx.doi.org/10.1029/96JD00336.

D. J. Jacob, J. A. Logan, and P. P. Murti. Effect of rising Asian emissions on surface ozone in the

United States. *Geophysical Research Letters*, 26(14):2175–2178, 1999. ISSN 1944-8007. doi: 10.1029/ 1999GL900450. URL http://dx.doi.org/10.1029/1999GL900450.

D.J. Jacob. Heterogeneous chemistry and tropospheric ozone. *Atmospheric Environment*, 34:2131–2159, 2000.

M. Z. Jacobson. *Fundamentals of Atmospheric Modeling*. Cambridge University Press, 2nd edition, 2005.

M. Z. Jacobson. *Air Pollution and Global Warming: History, Science, and Solutions*. Cambridge University Press,2nd edition, 2012.

I. Jhun, N. Fann, A. Zanobetti, and B. Hubbell. Effect modification of ozone-related mortality risks by temperature in 97 {US} cities. *Environment International*, 73(0):128 – 134, 2014. ISSN 0160-4120. doi: http://dx.doi.org/10.1016/j.envint.2014.07.009. URL http://www.sciencedirect.com/ science/article/pii/S0160412014002141.

X. Jiang, M. C. Barth, C. Wiedinmyer, and S. T. Massie. Influence of anthropogenic aerosols on the Asian monsoon: a case study using the WRF-Chem model. *Atmospheric Chemistry and Physics Discussions*, 13(8):21383–21425, 2013. doi: 10.5194/acpd-13-21383-2013. URL http://www. atmos-chem-phys-discuss.net/13/21383/2013/.

J.E Jonson, J.K Sundet, and L Tarrasón. Model calculations of present and future levels of ozone and ozone precursors with a global and a regional model. *Atmospheric Environment*, 35(3):525 – 537, 2001. ISSN 1352-2310. doi: http://dx.doi.org/10.1016/S1352-2310(00)00314-9. URL http://www. sciencedirect.com/science/article/pii/S1352231000003149.

Y. Kajikawa, T. Yasunari, S. Yoshida, and H. Fujinami. Advanced Asian summer monsoon onset in recent decades. *Geophysical Research Letters*, 39(3):n/a–n/a, 2012. ISSN 1944-8007. doi: 10.1029/ 2011GL050540. URL http://dx.doi.org/10.1029/2011GL050540.

D. F. Karnosky, J. M. Skelly, K. E. Percy, and A. H. Chappelka. Perspectives regarding 50 years of research on effects of tropospheric ozone air pollution on US forests. *Environmental Pollution*, 147: 489–506, 2007.

M.S. Kim, J.E. McMurtrey, C.L. Mulchi, C.S.T. Daughtry, E.W. Chappelle, and Y.R. Chen. Steady-state multispectral fluorescence imaging system for plant leaves. *Applied Optics*, 40:157–166, 2001.

A. Klonecki and H. Levy. Tropospheric chemical ozone tendencies in CO-CH_4-NO_y-H_2O system: their sensitivity to variations in environmental parameters and their application to a global chemistry transport model study. *Journal of Geophysical Research*, 102:21221–21237, 1997.

F. Kucharski, F. Molteni, and J. H. Yoo. SST forcing of decadal Indian Monsoon rainfall variability. *Geophysical Research Letters*, 33(3):n/a–n/a, 2006. ISSN 1944-8007. doi: 10.1029/2005GL025371. URL http://dx.doi.org/10.1029/2005GL025371.

K. K. Kumar, B. Rajagopalan, and M. A. Cane. On the weakening relationship between the indian monsoon and ENSO. *Science*, 284(5423):2156–2159, 1999. doi: 10.1126/science.284.5423.2156. URL http://www.sciencemag.org/content/284/5423/2156.abstract.

R. Kumar, M. Naja, G. G. Pfister, M. C. Barth, and G. P. Brasseur. Simulations over South Asia using the Weather Research and Forecasting model with Chemistry (WRF-Chem): set-up and meteorological evaluation. *Geoscientific Model Development*, 5(2):321–343, 2012a. doi: 10.5194/gmd-5-321-2012. URL http://www.geosci-model-dev.net/5/321/2012/.

R. Kumar, M. Naja, G. G. Pfister, M. C. Barth, C. Wiedinmyer, and G. P. Brasseur. Simulations over South Asia using the Weather Research and Forecasting model with Chemistry (WRF-Chem): chemistry evaluation and initial results. *Geoscientific Model Development*, 5(3):619–648, 2012b. doi: 10.5194/gmd-5-619-2012. URL http://www.geosci-model-dev.net/5/619/2012/.

R. Kumar, M. C. Barth, G. G. Pfister, M. Naja, and G. P. Brasseur. WRF-Chem simulations of a typical pre-monsoon dust storm in northern India: influences on aerosol optical properties and radiation budget. *Atmospheric Chemistry and Physics*, 14(5):2431–2446, 2014. doi: 10.5194/acp-14-2431-2014. URL http://www.atmos-chem-phys.net/14/2431/2014/.

R. R. Kumar, K. K. Kumar, R. G. Ashrit, S. K. Patwardhan, and G. B. Pant. *Climate Change in India 24-75 pp.* Tata McGraw Hill, New Delhi, India, 2002.

D.M. Lal, D. G. Sachin, S.D. Patil, S.H. Kulkarni, C. Jena, S. Tiwari, and M. K. Srivastava. Tropospheric ozone and aerosol long-term trends over the Indo-Gangetic Plain (IGP), India. *Atmospheric Research*, 116(0):82 – 92, 2012. ISSN 0169-8095. doi: http://dx.doi.org/10.1016/j.atmosres.2012.02.014. URL http://www.sciencedirect.com/science/article/pii/S0169809512000543. Remote Sensing of Clouds and Aerosols: Techniques and Applications - Atmospheric Research.

J-F. Lamarque and P. G. Hess. Cross-tropopause mass exchange and potential vorticity budget in a simulated tropopause folding. *J. Atmos. Sci.*, 51:2246–2269, 1994. doi: http://dx.doi.org/10.1175/1520-0469(1994)051<2246:CTMEAP>2.0.CO;2.

J.-F. Lamarque, G. P. Brasseur, P. G. Hess, and J.-F. Müller. Three-dimensional study of the relative contributions of the different nitrogen sources in the troposphere. *Journal of Geophysical Research: Atmospheres*, 101(D17):22955–22968, 1996a. ISSN 2156-2202. doi: 10.1029/96JD02160. URL http://dx.doi.org/10.1029/96JD02160.

J.-F. Lamarque, A. O. Langford, and M. H. Proffitt. Cross-tropopause mixing of ozone through gravity wave breaking: Observation and modeling. *Journal of Geophysical Research: Atmospheres*, 101(D17):22969–22976, 1996b. ISSN 2156-2202. doi: 10.1029/96JD02442. URL http://dx.doi.org/10.1029/96JD02442.

A. O. Langford, M. H. Proffitt, T. E. VanZandt, and J.-F. Lamarque. Modulation of tropospheric ozone

by a propagating gravity wave. *Journal of Geophysical Research: Atmospheres*, 101(D21):26605–26613, 1996. ISSN 2156-2202. doi: 10.1029/96JD02424. URL http://dx.doi.org/10.1029/96JD02424.

Mark G. Lawrence, Rolf von Kuhlmann, Marc Salzmann, and Philip J. Rasch. The balance of effects of deep convective mixing on tropospheric ozone. *Geophysical Research Letters*, 30(18):n/a–n/a, 2003. ISSN 1944-8007. doi: 10.1029/2003GL017644. URL http://dx.doi.org/10.1029/2003GL017644.

T. Leblanc, S. McDermid, Marion Müller, Franz Immler, Otto Schrems, K. Stebel, G. Hansen, W. Steinbrecht, H. Claude, A. Pazmino, S. Godin-Beekmann, G. Ancellet, J. L. Baray, H. Bencherif, Y. Meijer, D. Swart, L. Twigg, T. McGee, J. Thayer, J. Livingston, P. Keckhut, A. Hauchcorne, J. E. Barnes, and Peter von der Gathen. The NDSC ozone and temperature lidar algorithm intercomparison initiative (A2I): project overview. In *Reviewed and revised papers presented at the 22nd International Laser Radar Conference (ILRC 2004) : 12 - 16 July 2004, Matera, Italy / European Space Agency. Gelsomina Pappalardo, eds., II. (ESA SP ; 561, Buch)*, volume 881, 2004.

D.S. Lee, I. Köhler, E. Grobler, F. Rohrer, R. Sausen, L. Gallardo-Klenner, J.G.J. Olivier, F.J. Dentener, and A.F. Bouwman. Estimations of global NO emissions and their uncertainties. *Atmospheric Environment*, 31(12):1735 − 1749, 1997. ISSN 1352-2310. doi: http://dx.doi.org/10.1016/S1352-2310(96) 00327-5. URL http://www.sciencedirect.com/science/article/pii/S1352231096003275.

J. Lenoble. *Atmospheric radiative transfer*. A. Deepak Publishing, Hampton, VA, 1993.

P.F. Levelt, G.H.J. van den Oord, M.R. Dobber, A. Malkki, Huib Visser, J. de Vries, P. Stammes, J.O.V. Lundell, and H. Saari. The ozone monitoring instrument. *Geoscience and Remote Sensing, IEEE Transactions on*, 44(5):1093–1101, May 2006. ISSN 0196-2892. doi: 10.1109/TGRS.2006.872333.

Q. Li, D. J. Jacob, I. Bey, P. I. Palmer, B. N. Duncan, B. D. Field, R. V. Martin, A. M. Fiore, R. M. Yantosca, D. D. Parrish, P. G. Simmonds, and S. J. Oltmans. Transatlantic transport of pollution and its effects on surface ozone in Europe and North America. *Journal of Geophysical Research: Atmospheres*, 107(D13):ACH 4–1–ACH 4–21, 2002. ISSN 2156-2202. doi: 10.1029/2001JD001422. URL http://dx.doi.org/10.1029/2001JD001422.

Q. Liang, L. Jaeglé, R. C. Hudman, S. Turquety, D. J. Jacob, M. A. Avery, E. V. Browell, G. W. Sachse, D. R. Blake, W. Brune, X. Ren, R. C. Cohen, J. E. Dibb, A. Fried, H. Fuelberg, M. Porter, B. G. Heikes, G. Huey, H. B. Singh, and P. O. Wennberg. Summertime influence of asian pollution in the free troposphere over north america. *Journal of Geophysical Research: Atmospheres*, 112(D12): n/a–n/a, 2007. ISSN 2156-2202. doi: 10.1029/2006JD007919. URL http://dx.doi.org/10.1029/2006JD007919.

H. Liu, D. J. Jacob, I. Bey, R. M. Yantosca, B. N. Duncan, and G. W. Sachse. Transport pathways for Asian pollution outflow over the Pacific: Interannual and seasonal variations. *Journal of Geophysical Research: Atmospheres*, 108(D20):n/a–n/a, 2003. ISSN 2156-2202. doi: 10.1029/2002JD003102. URL http://dx.doi.org/10.1029/2002JD003102.

J. Liu and D. L. Mauzerall. Estimating the average time for inter-continental transport of air pollutants. *Geophysical Research Letters*, 32(11):n/a–n/a, 2005. ISSN 1944-8007. doi: 10.1029/2005GL022619. URL http://dx.doi.org/10.1029/2005GL022619.

X. Liu, P. K. Bhartia, K. Chance, R. J. D. Spurr, and T. P. Kurosu. Ozone profile retrievals from the ozone monitoring instrument. *Atmospheric Chemistry and Physics*, 10(5):2521–2537, 2010. doi: 10.5194/acp-10-2521-2010. URL http://www.atmos-chem-phys.net/10/2521/2010/.

J. A. Logan, J. Staehelin, I. A. Megretskaia, J.-P. Cammas, V. Thouret, H. Claude, H. De Backer, M. Steinbacher, H.-E. Scheel, R. Stübi, M. Fröhlich, and R. Derwent. Changes in ozone over Europe: Analysis of ozone measurements from sondes, regular aircraft (MOZAIC) and alpine surface sites. *Journal of Geophysical Research: Atmospheres*, 117(D9):n/a–n/a, 2012. ISSN 2156-2202. doi: 10. 1029/2011JD016952. URL http://dx.doi.org/10.1029/2011JD016952.

D. G. Loyola, M. E. Koukouli, P. Valks, D. S. Balis, N. Hao, M. Van Roozendael, R. J. D. Spurr, W. Zimmer, S. Kiemle, C. Lerot, and J.-C. Lambert. The GOME-2 total column ozone product: Retrieval algorithm and ground-based validation. *Journal of Geophysical Research: Atmospheres*, 116 (D7):n/a–n/a, 2011. ISSN 2156-2202. doi: 10.1029/2010JD014675. URL http://dx.doi.org/10. 1029/2010JD014675.

R. Maity and N. D. Kumar. Bayesian dynamic modeling for monthly Indian summer monsoon rainfall using El Niño–Southern Oscillation (ENSO) and Equatorial Indian Ocean Oscillation (EQUINOO). *Journal of Geophysical Research: Atmospheres*, 111(D7):n/a–n/a, 2006. ISSN 2156-2202. doi: 10. 1029/2005JD006539. URL http://dx.doi.org/10.1029/2005JD006539.

E. J. McCartney. *Absorption and emission by atmospheric gases - The physical processes*. New York, John Wiley and Sons, 331 p., 1983.

R. D. McPeters, G. J. Labow, and J. A. Logan. Ozone climatological profiles for satellite retrieval algorithms. *Journal of Geophysical Research: Atmospheres*, 112:D5, 2007. ISSN 2156-2202. doi: 10.1029/2005JD006823. URL http://dx.doi.org/10.1029/2005JD006823.

G. A. Meehl. The south Asian monsoon and the tropospheric biennial oscillation. *J. Climate*, 10: 1921–1943, 1997.

G. A. Meehl and J. M. Arblaster. The tropospheric biennial oscillation and indian monsoon rainfall. *Geophysical Research Letters*, 28(9):1731–1734, 2001. ISSN 1944-8007. doi: 10.1029/2000GL012283. URL http://dx.doi.org/10.1029/2000GL012283.

G. A. Meehl and J. M. Arblaster. Indian Monsoon GCM sensitivity experiments testing tropospheric biennial oscillation transition conditions. *J. Climate*, 15:923–944, 2002. doi: http://dx.doi.org/10. 1175/1520-0442(2002)015<0923:IMGSET>2.0.CO;2.

D. F. Miller, A. J. Alkezweeny, J. M. Hales, and R. N. Lee. Ozone formation related to power plant

emissions. *Science*, 202(4373):1186–1188, 1978. doi: 10.1126/science.202.4373.1186. URL http://www.sciencemag.org/content/202/4373/1186.abstract.

L. T. Molina and M. J. Molina. Production of cl_2o_2 from the self-reaction of the clo radical. *J. Phys. Chem.*, 91:433–436, 1987.

M.J. Molina and F. S. Rowland. Stratospheric sink for chlorofluoromethanes: chlorine atom-catalysed destruction of ozone. *Nature*, 249:810 – 812, 1974. doi: 10.1038/249810a0.

P. S. Monks. Gas-phase radical chemistry in the troposphere,. *Chem. Soc. Rev.*, 34:376–395, 2005.

R. Munro, R. Siddans, W. J. Reburn, and B Kerridge. Direct measurement of tropospheric ozone from space. *Nature*, 392:168–171, 1998. doi: 10.1038/32392,1998.

T. Murakami and J. Matsumoto. Summer monsoon over the Asian continent and western north Pacific. *J. Meteor. Soc. Japan*, 72:719–745, 1994.

T. Ohara, H. Akimoto, J. Kurokawa, N. Horii, K. Yamaji, X. Yan, and T. Hayasaka. An asian emission inventory of anthropogenic emission sources for the period 1980-2020. *Atmospheric Chemistry and Physics*, 7(16):4419–4444, 2007. doi: 10.5194/acp-7-4419-2007. URL http://www.atmos-chem-phys.net/7/4419/2007/.

S. Oltmans and H. Levy. Seasonal cycle of surface ozone over the western North Atlantic. *Letters to Nature*, 358:392–394, 1992.

S.J. Oltmans, A.S. Lefohn, J.M. Harris, I. Galbally, H.E. Scheel, G. Bodeker, E. Brunke, H. Claude, D. Tarasick, B.J. Johnson, P. Simmonds, D. Shadwick, K. Anlauf, K. Hayden, F. Schmidlin, T. Fujimoto, K. Akagi, C. Meyer, S. Nichol, J. Davies, A. Redondas, and E. Cuevas. Long-term changes in tropospheric ozone. *Atmospheric Environment*, 40(17):3156 – 3173, 2006. ISSN 1352-2310. doi: http://dx.doi.org/10.1016/j.atmosenv.2006.01.029. URL http://www.sciencedirect.com/science/article/pii/S1352231006001233.

E. Palmén. Origin and structure of high-level cyclones south of the: Maximum westerlies. *Tellus*, 1(1): 22–31, 1949. ISSN 2153-3490. doi: 10.1111/j.2153-3490.1949.tb01925.x. URL http://dx.doi.org/10.1111/j.2153-3490.1949.tb01925.x.

G.B. Pant and B. Parthasarathy. Some aspects of an association between the southern oscillation and indian summer monsoon. *Archives for meteorology, geophysics, and bioclimatology, Series B*, 29 (3):245–252, 1981. ISSN 0066-6424. doi: 10.1007/BF02263246. URL http://dx.doi.org/10.1007/BF02263246.

D. D. Parrish, J. S. Holloway, M. Trainer, P. C. Murphy, F. C. Fehsenfeld, and G. L. Forbes. Export of North American ozonepollution to the North Atlantic Ocean. *Science*, 259(5100):1436–1439, 1993. doi: 10.1126/science.259.5100.1436. URL http://www.sciencemag.org/content/259/5100/1436.abstract.

B. Parthasarathy, A.A. Munot, and D.R. Kothawale. All-India monthly and seasonal rainfall series: 1871–1993. *Theoretical and Applied Climatology*, 49(4):217–224, 1994. ISSN 0177-798X. doi: 10.1007/BF00867461. URL http://dx.doi.org/10.1007/BF00867461.

F. S. R. Pausata, L. Pozzoli, E. Vignati, and F. J. Dentener. North Atlantic Oscillation and tropospheric ozone variability in Europe: model analysis and measurements intercomparison. *Atmospheric Chemistry and Physics*, 12:6357–6376, 2012. doi: 10.5194/acp-12-6357-2012.

G. G. Pfister, S. Walters, L. K. Emmons, D. P. Edwards, and J. Avise. Quantifying the contribution of inflow on surface ozone over California during summer 2008. *Journal of Geophysical Research: Atmospheres*, 118(21):12,282–12,299, 2013. ISSN 2169-8996. doi: 10.1002/2013JD020336. URL http://dx.doi.org/10.1002/2013JD020336.

K. E. Pickering, A. M. Thompson, R. R. Dickerson, W. T. Luke, D. P. McNamara, J. P. Greenberg, and P. R. Zimmerman. Model calculations of tropospheric ozone production potential following observed convective events. *Journal of Geophysical Research: Atmospheres*, 95(D9):14049–14062, 1990. ISSN 2156-2202. doi: 10.1029/JD095iD09p14049. URL http://dx.doi.org/10.1029/JD095iD09p14049.

J.C.M. Pires, M.C.M. Alvim-Ferraz, and F.G. Martins. Surface ozone behaviour at rural sites in Portugal. *Atmospheric Research*, 104–105(0):164 – 171, 2012. ISSN 0169-8095. doi: http://dx.doi.org/10.1016/j.atmosres.2011.10.001. URL http://www.sciencedirect.com/science/article/pii/S0169809511003280.

M. Pommier, C. Clerbaux, K. S. Law, G. Ancellet, P. Bernath, P.-F. Coheur, J. Hadji-Lazaro, D. Hurtmans, P. Nedelec, J.-D. Paris, F. Ravetta, T. B. Ryerson, H. Schlager, and A. J. Weinheimer. Analysis of IASI tropospheric O_3 data over the Arctic during POLARCAT campaigns in 2008. *Atmospheric Chemistry and Physics*, 12:7371–7389, 2012. doi: doi:10.5194/acp-12-7371-2012.

O. Poulida, R. R. Dickerson, and A. Heymsfield. Stratosphere-troposphere exchange in a midlatitude mesoscale convective complex: 1. observations. *Journal of Geophysical Research: Atmospheres*, 101(D3):6823–6836, 1996. ISSN 2156-2202. doi: 10.1029/95JD03523. URL http://dx.doi.org/10.1029/95JD03523.

C. S. Ramage. *Monsoon Meteorology*. Academic Press, 296pp, 1972.

E.M. Rasmusson and T. H. Carpenter. The relationship between Eastern Equatorial Pacific sea surface temperatures and rainfall over India and Sri Lanka. *Mon. Wea. Rev.*, 111:517–528, 1983. doi: http://dx.doi.org/10.1175/1520-0493(1983)111<0517:TRBEEP>2.0.CO;2.

A. Richter, J. P. Burrows, H. Nu, C. Granier, and U. Niemeier. Increase in tropospheric nitrogen dioxide over China observed from space. *Letters to Nature*, 437:129–132, 2005. doi: 10.1038/nature04092.

C. Rodgers. *Inverse methods for atmospheric sounding: Theory and Practice, Series on Atmospheric, Oceanic and Planetary Physics*, volume 2. World Scientific, 2000.

L.S. Rothman, D. Jacquemart, A. Barbe, D. Chris Benner, M. Birk, L.R. Brown, M.R. Carleer, C. Chackerian Jr., K. Chance, L.H. Coudert, V. Dana, V.M. Devi, J.-M. Flaud, R.R. Gamache, A. Goldman, J.-M. Hartmann, K.W. Jucks, A.G. Maki, J.-Y. Mandin, S.T. Massie, J. Orphal, A. Perrin, C.P. Rinsland, M.A.H. Smith, J. Tennyson, R.N. Tolchenov, R.A. Toth, J. Vander Auwera, P. Varanasi, and G. Wagner. The HITRAN 2004 molecular spectroscopic database. *Journal of Quantitative Spectroscopy and Radiative Transfer*, 96(2):139 – 204, 2005. ISSN 0022-4073. doi: http://dx.doi.org/10.1016/j.jqsrt. 2004.10.008. URL http://www.sciencedirect.com/science/article/pii/S0022407305001081.

Y. Sadhuram. Predicting monsoon rainfall and pressure indices from sea surface temperature. *Current Science*, 72:166–168, 1997.

S. Safieddine, C. Clerbaux, M. George, J. Hadji-Lazaro, D. Hurtmans, P.-F. Coheur, C. Wespes, D. Loyola, P. Valks, and N. Hao. Tropospheric ozone and nitrogen dioxide measurements in urban and rural regions as seen by IASI and GOME-2. *Journal of Geophysical Research: Atmospheres*, 118(18): 10,555–10,566, 2013. ISSN 2169-8996. doi: 10.1002/jgrd.50669. URL http://dx.doi.org/10.1002/jgrd.50669.

M. L. Salby. *Fundamentals of Atmospheric Physics*. Academic Press, San Diego, 1996.

B. Sauvage, Randall V. Martin, A. van Donkelaar, and J. R. Ziemke. Quantification of the factors controlling tropical tropospheric ozone and the south atlantic maximum. *Journal of Geophysical Research: Atmospheres*, 112(D11):n/a–n/a, 2007. ISSN 2156-2202. doi: 10.1029/2006JD008008. URL http://dx.doi.org/10.1029/2006JD008008.

C. Scannell, D. Hurtmans, A. Boynard, J. Hadji-Lazaro, M. George, A. Delcloo, A. Tuinder, P.-F. Coheur, and C. Clerbaux. Antarctic ozone hole as observed by IASI/MetOp for 2008-2010. *Atmospheric Measurement Techniques*, 5:123–139, 2012. doi: 10.5194/amt-5-123-2012.

M. Schaub, J.M. Skelly, J.W. Zhang, J.A. Ferdinand, J.E. Savage, R.E. Stevenson, D.D. Davis, and K.C. Steiner. Physiological and foliar symptom response in the crowns of Prunus serotina, Fraxinus americana and Acer rubrum canopy trees to ambient ozone under forest conditions. *Environmental Pollution*, 133:553–567, 2005.

P. Schlüssel, T. H. Hultberg, P. L. Phillips, T. August, and X. Calbet. The operational IASI level 2 processor. *Advances in Space Research*, 36(5):982 – 988, 2005. ISSN 0273-1177. doi: http://dx.doi.org/10.1016/j.asr.2005.03.008. URL http://www.sciencedirect.com/science/article/pii/S0273117705002838. Atmospheric Remote Sensing: Earth's Surface, Troposphere, Stratosphere and Mesosphere- I.

C. F. Schoenbein. On the odour accompanying electricity, and on the probability of its dependence on the presence of a new substrate. *Philosophical Magazine*, 17:293–294, 1840.

J. H. Seinfeld and S.N. Pandis. *Atmospheric Chemistry and Physics From Air Pollution to Climate Change*. John Wiley & Sons, Inc, second edition edition, 2006.

J. Shukla. Effect of Arabian sea-surface temperature anomaly on Indian summer monsoon: a numerical experiment with the GFDL model. *J. Atmos. Sci.*, 32:503–511, 1975. doi: http://dx.doi.org/10.1175/1520-0469(1975)032<0503:EOASST>2.0.CO;2.

J. Shukla and D.A. Mooley. Empirical prediction of the summer monsoon rainfall over India. *Mon. Wea. Rev.*, 115:695–704, 1987. doi: http://dx.doi.org/10.1175/1520-0493(1987)115<0695:EPOTSM>2.0.CO;2.

S. Sillman. The relation between ozone, NO_x and hydrocarbons in urban and polluted rural environments. *Atmospheric Environment*, 33(12):1821 – 1845, 1999. ISSN 1352-2310. doi: http://dx.doi.org/10.1016/S1352-2310(98)00345-8. URL http://www.sciencedirect.com/science/article/pii/S1352231098003458.

D. Simeoni, P. Astruc, D. Miras, C. Alis, O. Andreis, D. Scheidel, C. Degrelle, P. Nicol, B. Bailly, P.e Guiard, A. Clauss, D. Blumstein, T. Maciaszek, G. Chalon, T. Carlier, and G. Kayal. Design and development of IASI instrument. *Proc. SPIE*, 5543:208–219, 2004. doi: 10.1117/12.561090. URL http://dx.doi.org/10.1117/12.561090.

S. Solomon, R. R. Garcia, F. S. Rowland, and D. J. Wuebbles. On the depletion of Antarctic ozone. *Nature*, 321:755–758, 1986.

D. S. Stevenson, F. J. Dentener, M. G. Schultz, K. Ellingsen, T. P. C. van Noije, O. Wild, G. Zeng, M. Amann, C. S. Atherton, N. Bell, D. J. Bergmann, I. Bey, T. Butler, J. Cofala, W. J. Collins, R. G. Derwent, R. M. Doherty, J. Drevet, H. J. Eskes, A. M. Fiore, M. Gauss, D. A. Hauglustaine, L. W. Horowitz, I. S. A. Isaksen, M. C. Krol, J.-F. Lamarque, M. G. Lawrence, V. Montanaro, J.-F. Müller, G. Pitari, M. J. Prather, J. A. Pyle, S. Rast, J. M. Rodriguez, M. G. Sanderson, N. H. Savage, D. T. Shindell, S. E. Strahan, K. Sudo, and S. Szopa. Multimodel ensemble simulations of present-day and near-future tropospheric ozone. *Journal of Geophysical Research: Atmospheres*, 111(D8):n/a–n/a, 2006. ISSN 2156-2202. doi: 10.1029/2005JD006338. URL http://dx.doi.org/10.1029/2005JD006338.

A. Stohl. A 1-year Lagrangian "climatology" of airstreams in the Northern Hemisphere troposphere and lowermost stratosphere. *Journal of Geophysical Research*, 106:7263–7279, 2001.

A. Stohl, S. Eckhardt, C. Forster, P. James, and N. Spichtinger. On the pathways and timescales of intercontinental air pollution transport. *Journal of Geophysical Research*, 107, D23:4684, 2002. doi: 10.1029/2001JD001396.

A. Stohl, P. Bonasoni, P. Cristofanelli, W. Collins, J. Feichter, A. Frank, C. Forster, E. Gerasopoulos, H. Gäggeler, P. James, T. Kentarchos, H. Kromp-Kolb, B. Krüger, C. Land, J. Meloen, A. Papayannis, A. Priller, P. Seibert, M. Sprenger, G. J. Roelofs, H. E. Scheel, C. Schnabel, P. Siegmund, L. Tobler, T. Trickl, H. Wernli, V. Wirth, P. Zanis, and C. Zerefos. Stratosphere-troposphere exchange: A review, and what we have learned from STACCATO. *Journal of Geophysical Research: Atmospheres*, 108(D12):

n/a–n/a, 2003. ISSN 2156-2202. doi: 10.1029/2002JD002490. URL http://dx.doi.org/10.1029/2002JD002490.

R. S. Stolarski and R. J. Cicerone. Stratospheric chlorine: a possible sink for ozone. *Canadian Journal of Chemistry*, 52(8):1610–1615, 1974. doi: 10.1139/v74-233. URL http://dx.doi.org/10.1139/v74-233.

S. Szopa, D. A. Hauglustaine, R. Vautard, and L. Menut. Future global tropospheric ozone changes and impact on European air quality. *Geophysical Research Letters*, 33(14):n/a–n/a, 2006. ISSN 1944-8007. doi: 10.1029/2006GL025860. URL http://dx.doi.org/10.1029/2006GL025860.

S. Tao and L. Chen. *A review of recent research on the East Asian summer monsoon. In: China, Monsoon meteorology.* Oxford University Press, 60-92, 1987.

A. M. Thompson, K. E. Pickering, R. R. Dickerson, W. G. Ellis, D. J. Jacob, J. R. Scala, W. Tao, D. P. McNamara, and J. Simpson. Convective transport over the central United States and its role in regional CO and ozone budgets. *Journal of Geophysical Research: Atmospheres*, 99(D9):18703–18711, 1994. ISSN 2156-2202. doi: 10.1029/94JD01244. URL http://dx.doi.org/10.1029/94JD01244.

A. M. Thompson, J. C. Witte, S. J. Oltmans, and F.J. Schmidlin. Shadoz-a tropical ozonesonde-radiosonde network for the atmospheric community. *Bull. Amer. Meteor. Soc.*, 85:1549–1564, 2004. doi: http://dx.doi.org/10.1175/BAMS-85-10-1549.

B. Tournier, D. Blumstein, and F.R. Cayla. IASI Level 0 and 1 processing algorithms description. In *Proceedings of the 12th International TOVS Working Group, held in Lorne.*, 2002.

K. E. Trenberth and J. T. Fasullo. Climate extremes and climate change: The Russian heat wave and other climate extremes of 2010. *Journal of Geophysical Research: Atmospheres*, 117(D17): n/a–n/a, 2012. ISSN 2156-2202. doi: 10.1029/2012JD018020. URL http://dx.doi.org/10.1029/2012JD018020.

G. B. Tucker and R. G. Barry. *Climates of the North Atlantic Ocean, in World Survey of Climatology, Climates of the Oceans*, volume 15, chapter 2, pages 193–262. Elsevier Sci., New York, 1984., 1984.

S. Turquety. *Mesures de l'ozone tropospherique a partir d'observations satellitaires dans le domaine de l'infrarouge thermique.* PhD thesis, Univ. Pierre et Marie Curie, 2003.

S. Turquety, J. Hadji-Lazaro, and C. Clerbaux. First satellite ozone distributions retrieved from nadir high-resolution infrared spectra. *Geophysical Research Letters*, 29(24):51–1–51–4, 2002. ISSN 1944-8007. doi: 10.1029/2002GL016431. URL http://dx.doi.org/10.1029/2002GL016431.

R. J. van der A, H. J. Eskes, K. F. Boersma, T. P. C. van Noije, M. Van Roozendael, I. De Smedt, D. H. M. U. Peters, and E. W. Meijer. Trends, seasonal variability and dominant NO_x source derived from a ten year record of NO_2 measured from space. *Journal of Geophysical Research: Atmospheres*, 113(D4):n/a–n/a, 2008. ISSN 2156-2202. doi: 10.1029/2007JD009021. URL http://dx.doi.org/10.1029/2007JD009021.

REFERENCES

H. van Loon and J. C. Rogers. The seesaw in winter temperatures between Greenland and Northern Europe. part I: general description. *Mon. Wea. Rev.*, 106:296–310, 1978. doi: http://dx.doi.org/10.1175/1520-0493(1978)106<0296:TSIWTB>2.0.CO;2.

A. D. Vernekar, J. Zhou, and J. Shukla. The effect of eurasian snow cover on the indian monsoon. *J. Climate*, 8:248–266, 1995. doi: http://dx.doi.org/10.1175/1520-0442(1995)008<0248:TEOESC>2.0.CO;2.

R. Vingarzan. A review of surface ozone background levels and trends. *Atmospheric Environment*, 38 (21):3431 – 3442, 2004. ISSN 1352-2310. doi: http://dx.doi.org/10.1016/j.atmosenv.2004.03.030. URL http://www.sciencedirect.com/science/article/pii/S1352231004002808.

A. Volz and D. Kley. Evaluation of the Montsouris series of ozone measurements made in the nineteenth century. *Nature*, 332:240 –242, 1988. doi: 10.1038/332240a0.

G. T. Walker and E. W. Bliss. World weather. *V. Mem. R. Meteorol. Soc.*, 4:53–83, 1932.

Z. Wan. New refinements and validation of the MODIS land-surface temperature/emissivity products. *Remote Sensing of Environment*, 112(1):59 – 74, 2008. ISSN 0034-4257. doi: http://dx.doi.org/10.1016/j.rse.2006.06.026. URL http://www.sciencedirect.com/science/article/pii/S0034425707003665.

B. Wang and H. Lin. Rainy season of the Asian-Pacific summer monsoon. *J. Climate*, 15:386–398, 2002. doi: http://dx.doi.org/10.1175/1520-0442(2002)015<0386:RSOTAP>2.0.CO;2.

B. Wang, Q. Ding, and P.V. Joseph. Objective definition of the indian summer monsoon onset. *J. Climate*, 22:3303–3316, 2009. doi: http://dx.doi.org/10.1175/2008JCLI2675.1.

P. J. Webster. *The coupled monsoon system. In The Asian Monsoon p 3-66*. Springer Berlin Heidelberg, 2006.

P. J. Webster, V. O. Magaña, T. N. Palmer, J. Shukla, R. A. Tomas, M. Yanai, and T. Yasunari. Monsoons: Processes, predictability, and the prospects for prediction. *Journal of Geophysical Research: Oceans*, 103(C7):14451–14510, 1998. ISSN 2156-2202. doi: 10.1029/97JC02719. URL http://dx.doi.org/10.1029/97JC02719.

C. Wespes, D. Hurtmans, C. Clerbaux, M. L. Santee, R. V. Martin, and P.-F. Coheur. Global distributions of nitric acid from IASI/MetOP measurements. *Atmospheric Chemistry and Physics*, 9: 7949–7962, 2009.

C. Wespes, L. Emmons, D. P. Edwards, J. Hannigan, D. Hurtmans, M. Saunois, P.-F. Coheur, C. Clerbaux, M. T. Coffey, R. L. Batchelor, R. Lindenmaier, K. Strong, A. J. Weinheimer, J. B. Nowak, T. B. Ryerson, J. D. Crounse, and P. O. Wennberg. Analysis of ozone and nitric acid in spring and summer Arctic pollution using aircraft, ground-based, satellite observations and MOZART-4 model: source attribution and partitioning. *Atmospheric Chemistry and Physics*, 12:237–259, 2012. doi: 10.5194/acp-12-237-2012.

WHO. *WHO air quality guidelines global update, report on a working group meeting Rep. E87950.* World Health Organization, 2005.

O. Wild and H. Akimoto. Intercontinental transport of ozone and its precursors in a three-dimensional global ctm. *Journal of Geophysical Research: Atmospheres*, 106(D21):27729–27744, 2001. ISSN 2156-2202. doi: 10.1029/2000JD000123. URL http://dx.doi.org/10.1029/2000JD000123.

WMO. *Atmospheric ozone 1985, WMO Global Ozone Res. and Monit. Proj. Rep. 20, Geneva.* World Meteorological Organization, 1986.

WMO. *Scientific Assessment of Ozone Depletion: 1994.* World Meteorological Organization, 1994.

WMO. *Scientific Assessment of Ozone Depletion: 2014.* World Meteorological Organization, 2014.

S. C. Wofsy, M. B. McElroy, and Y. L. Yung. The chemistry of atmospheric bromine. *Geophysical Research Letters*, 2(6):215–218, 1975. ISSN 1944-8007. doi: 10.1029/GL002i006p00215. URL http://dx.doi.org/10.1029/GL002i006p00215.

L. Wu and J. H. Su, H.and Jiang. Regional simulation of aerosol impacts on precipitation during the East Asian summer monsoon. *Journal of Geophysical Research: Atmospheres*, 118(12):6454–6467, 2013. ISSN 2169-8996. doi: 10.1002/jgrd.50527. URL http://dx.doi.org/10.1002/jgrd.50527.

R. Wu and B. Wang. Interannual variability of summer monsoon onset over the western north pacific and the underlying processes. *J. Climate*, 13:2483–2501, 2000. doi: http://dx.doi.org/10.1175/1520-0442(2000)013<2483:IVOSMO>2.0.CO;2.

J. Xu, J. Z. Ma, X. L. Zhang, X. B. Xu, X. F. Xu, W. L. Lin, Y. Wang, W. Meng, and Z. Q. Ma. Measurements of ozone and its precursors in Beijing during summertime: impact of urban plumes on ozone pollution in downwind rural areas. *Atmospheric Chemistry and Physics*, 11(23):12241–12252, 2011. doi: 10.5194/acp-11-12241-2011. URL http://www.atmos-chem-phys.net/11/12241/2011/.

J. Yan. Observational study on the onset of the south china sea southwest monsoon. *Advances in Atmospheric Sciences*, 14(2):277–287, 1997. ISSN 0256-1530. doi: 10.1007/s00376-997-0026-9. URL http://dx.doi.org/10.1007/s00376-997-0026-9.

S. Yang and K.-M. Lau. Influences of Sea Surface Temperature and Ground Wetness onAsian Summer Monsoon. *Journal of Climate*, 11:3230–3246, December 1998. doi: 10.1175/1520-0442(1998)011<3230:IOSSTA>2.0.CO;2.

T.C. Yeh, S.Y. Tao, and M.C. Li. *The abrupt change of circulation over the Northern Hemisphere during June and October. In: The atmosphere and the sea in motion (Bolin B, ed) pp 249-267.* New York: Rockefeller Inst. Press, 1959.

J.J. Yienger, M. Galanter, T.A. Holloway, M.J. Phadnis, S.K. Guttikun, G.R. Carmicha, W.J. Moxim, and H. Levy II. The episodic nature of air pollution transport from Asia to North America. *Journal of Geophysical Research*, 105(D22):26931–26945, 2000.

D. Yihui and J. C. L. Chan. The East Asian summer monsoon: an overview. *Meteorology and Atmospheric Physics*, 89(1-4):117–142, 2005. ISSN 0177-7971. doi: 10.1007/s00703-005-0125-z. URL http://dx.doi.org/10.1007/s00703-005-0125-z.

X. Yue and N. Unger. Ozone vegetation damage effects on gross primary productivity in the united states. *Atmospheric Chemistry and Physics*, 14(17):9137–9153, 2014. doi: 10.5194/acp-14-9137-2014. URL http://www.atmos-chem-phys.net/14/9137/2014/.

P. Zanis, T. Trickl, A. Stohl, H. Wernli, O. Cooper, C. Zerefos, H. Gaeggeler, C. Schnabel, L. Tobler, P. W. Kubik, A. Priller, H. E. Scheel, H. J. Kanter, P. Cristofanelli, C. Forster, P. James, E. Gerasopoulos, A. Delcloo, A. Papayannis, and H. Claude. Forecast, observation and modelling of a deep stratospheric intrusion event over Europe. *Atmospheric Chemistry and Physics Discussions*, 3(1): 1109–1138, February 2003. URL https://hal.archives-ouvertes.fr/hal-00300950.

G. Zeng, O. Morgenstern, P. Braesicke, and J. A. Pyle. Impact of stratospheric ozone recovery on tropospheric ozone and its budget. *Geophysical Research Letters*, 37(9):n/a–n/a, 2010. ISSN 1944-8007. doi: 10.1029/2010GL042812. URL http://dx.doi.org/10.1029/2010GL042812.

L. Zhang, D. J. Jacob, K. F. Boersma, D. A. Jaffe, J. R. Olson, K. W. Bowman, J. R. Worden, A. M. Thompson, M. A. Avery, R. C. Cohen, J. E. Dibb, F. M. Flock, H. E. Fuelberg, L. G. Huey, W. W. McMillan, H. B. Singh, and A. J. Weinheimer. Transpacific transport of ozone pollution and the effect of recent Asian emission increases on air quality in North America: an integrated analysis using satellite, aircraft, ozonesonde, and surface observations. *Atmospheric Chemistry and Physics*, 8(20):6117–6136, 2008. doi: 10.5194/acp-8-6117-2008. URL http://www.atmos-chem-phys.net/8/6117/2008/.

D.K. Zhou, A.M. Larar, Xu Liu, W.L. Smith, L.L. Strow, Ping Yang, P Schlussel, and X. Calbet. Global land surface emissivity retrieved from satellite ultraspectral IR measurements. *Geoscience and Remote Sensing, IEEE Transactions*, 49(4):1277–1290, April 2011. ISSN 0196-2892. doi: 10.1109/ TGRS.2010.2051036.

K. Z. Zhu. Southeast monsoon and rainfall in China. *J. Chinese Geogr. Soc.*, 1:1–2 7, 1934.

List of Acronyms